Improving the world one monomer at a time

In silico and *on silica* investigations of polymerization reactions and polymers

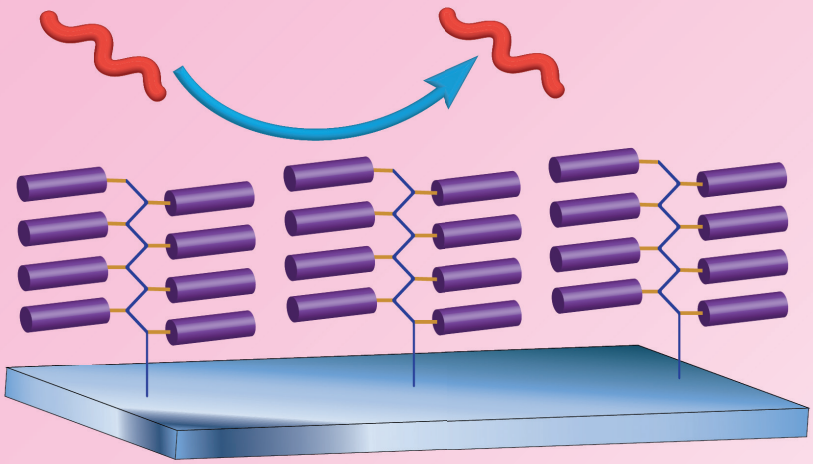

Annemieke van Dam

Propositions

1. Truly self-healing surfaces are a myth.
   (this thesis)

2. There are too many benchmark DFT functionals.
   (this thesis)

3. The Z/E ratio of the product of a Wittig reaction is caused by the size of the phosphine group.
   (Ge et al., *Sci. Adv.* **2023**, *9*, eadf8742.)

4. Although the PhD program leads up to a doctorate in philosophy, there is insufficient room for ethical and philosophical debate in a technical PhD.

5. It is a university's duty to stop gender discrimination by fully compensating chair-groups for any hinder caused by pregnant employees.

6. Having children during the Master study is the best way to start an academic career.

7. With the introduction of USB-C connections, the USB has lost its fourth dimension.

Propositions belonging to the thesis, entitled

Improving the world one monomer at a time: in silico and on silica investigations of polymerization reactions and polymers

Annemieke van Dam
Wageningen, 27 March 2024

Improving the world one monomer at a time:

in silico and on silica investigations of polymerization reactions and polymers

Annemieke Irene van Dam – Engelbert

Thesis committee

Promotor
Prof. Dr H. Zuilhof
Professor of Organic Chemistry
Wageningen University & Research

Co-promotor
Dr M.M.J. Smulders
Associate Professor at the Laboratory of Organic Chemistry
Wageningen University & Research

Other members
Prof. Dr F.A.M. Leermakers, Wageningen University & Research
Prof. Dr J.H. Bitter, Wageningen University & Research
Prof. Dr A. Palmans, Eindhoven University of Technology
Prof. Dr A.P.H.J. Schenning, Eindhoven University of Technology

This research was conducted under the auspices of VLAG Graduate School
(Biobased, Biomolecular, Chemical, Food and Nutrition Sciences).

Improving the world one monomer at a time:

in silico and on silica investigations of polymerization reactions and polymers

Annemieke Irene van Dam - Engelbert

Thesis
submitted in fulfilment of the requirements of the degree of doctor
at Wageningen University
by the authority of the Rector Magnificus,
Prof. Dr C Kroeze,
in the presence of the
Thesis Committee appointed by the Academic Board
to be defended in public
on Monday 6 May 2024
at 1.30 in the Omnia Auditorium.

Annemieke Irene van Dam - Engelbert
Improving the world one monomer at a time: in silico and on silica investigations of polymerization reactions and polymers
194 pages.

PhD thesis, Wageningen University, Wageningen, the Netherlands (2024)
With references, with summary in English
DOI: 10.18174/648574

Table of Content

Summary in English and Dutch

Summary

Surface modification is often used to enhance or adapt surface properties. In printing industries, heavily fluorinated materials are often applied as antifouling coating to prevent polymeric fouling of printhead nozzles. Such heavily fluorinated materials are toxic and will soon be prohibited in the European Union. A less toxic alternative is thus desired. Moreover, the durability of such a coating could be improved by rendering these coatings self-healing.

In **chapter 1** of this thesis, the current status of the field is explored. A general overview of grafting techniques for coatings is provided, and various polymerization techniques are discussed with a focus on polymer brushes. More specifically, antifouling and self-healing coatings are discussed. On the topic of bulk polymers, we touch upon dynamic covalent chemistry, SuFEx polymerization, and natural polymers such as lignin. A brief summary of the history of DFT and its current use, is provided as well.

In **chapter 2** of this thesis, the self-healing and antifouling properties of a range of partially fluorinated polymer brushes are reported. Eleven methacrylates are selected with linear side chains with varying degree of fluorination. After synthesis of six of the methacrylates, polymer brushes of all monomers are made by surface-initiated atom transfer radical polymerization (SI-ATRP). Characterization of the coatings is done with static contact angle measurements, ellipsometry, AFM and XPS, and the antifouling property of each coating is evaluated with confocal fluorescence microscopy. As expected, the polymer brushes with fully fluorinated side chains, be it short, medium or long, show excellent antifouling ability. With a decrease in the degree of fluorination, the antifouling capability decreases as well. Remarkably, the non-fluorinated side chains perform significantly better than their singly fluorinated counterparts. A correlation between the antifouling ability and the minimal surface tension of the polymer brushes is established. Furthermore, the self-healing ability is determined by repeated exposure to pH 3 solutions and a 120 °C atmosphere. Under these conditions, all coatings are found to be fully self-healing. Additionally, no damage is observed in the self-healing experiments of the longest non-fluorinated brushes.

To investigate the remarkable performance of the longest non-fluorinated side chain, we test a range of fluorine-free polymer brushes in the work described in **chapter 3**. Synthesis, polymerization, characterization and self-healing performance testing is similar to the work described in chapter 2. Polymer brushes with linear side chains of seven or less carbons display reversible damage, while polymer brushes with linear side chains of nine or more carbons are unharmed by repeated pH 3 exposure. We propose that longer side chains can pack tightly, preventing H_3O^+ reaching the ester bonds in the backbone of the polymer chain. Shorter chains cannot pack tightly enough, therefore acidic hydrolysis of the backbone will occur. To further support this hypothesis, we observe that coatings derived from polymers with branched side chains show reversible damage. Overall, the work in this chapter provides a promising basis for how fluorine-free coatings could still be made antifouling and/or self-healing.

In the age of the plastic soup and the energy transition, innovations for polymeric materials are in high demand. For example, although windmills contribute to cleaner energy production, the thermosets used in their construction cannot be recycled and generate enormous amounts of waste. A recyclable alternative to these thermosets would thus have a huge positive impact. In **chapter 4**, an investigation of the reactivity of the imine bond is described. This bond is a key moiety in covalent adaptable networks, which are currently seen as potential replacement of thermosets. With DFT calculations, we investigate the condensation and transimination reaction of an imine pincer that is coordinated to an iron(II) center. At first, we find the activation barriers of both reactions to be unrealistically high. When we adapt the system to allow two ethylamine molecules to mediate proton transfer, the activation barriers lowers to values matching experimental results. We thereby show that these proton shuttles are essential for the condensation and transimination of such coordinated imines. Furthermore, coordination of the imine to an iron(II)-center increases its reactivity.

DFT calculations are also applied in the investigation of chain-growth SuFEx polymerization, as reported in **chapter 5**. Recently, a homopolymer was produced with the SuFEx click reaction, whereas up to then, only ABAB-type polymers could be made. This new chain-growth SuFEx polymer uses monomers

with a silane-protected alcohol and a sulfur hub on the same aromatic ring, and an electron-withdrawing substituent to prevent self-polymerization in absence of the initiator. Only upon addition of the initiator will the monomers perform SuFEx reactions, creating well-defined polymers. With DFT calculations, we confirm the reactivity of the initiation and the propagation step of the chain growth polymerization. However, in contrast to the experimental report, our calculations cannot exclude self-polymerization under ambient conditions. Instead, we consistently find no effect of the electron-withdrawing substituent on the reactivity of the monomer. We propose that this inconsistency may be explained by the fact that our calculations did not include solvent interactions. This will need to be further studied, both computationally and experimentally.

While the aforementioned polymerizations were meant for creating a new polymer, in **chapter 6** an investigation of the degradation of a naturally produced polymer is described. Lignin is a major component of plant material and thereby a green source of chemical building blocks. To obtain these, the lignin must be degraded. However, in the degradation with laccase and a HBT mediator, oxidation is predominant over cleavage. In the research described in chapter 6, a range of pH values and buffer strengths is tested to improve the ratio of cleavage to oxidation. A rationale of the results is provided by DFT calculations. We propose that cleavage is enhanced by hydrogen bonding of the lignin and buffer anions, which is more likely to occur in stronger buffers or at higher pH.

The general discussion in **chapter 7** remarks on the industrial applicability of polymer brushes such as those studied in chapters 2 and 3. Furthermore, the desired reduction in the use of fluorine-containing compounds and materials is discussed, as well as the attempts of the chemical academic society to both comply and stall measures that are being taken towards this goal. Lastly, the added value of DFT calculations for materials chemistry is considered.

In all, the research reported in the various chapters of this thesis gains insight in a broad range of polymerization reactions. With this knowledge, the transition towards non-toxic polymerizations and thereby to a more sustainable society is one step closer.

Samenvatting

Oppervlaktemodificatie wordt gebruikt om oppervlakte-eigenschappen te versterken of te bewerken. Zo worden in de printindustrie vaak zwaar gefluorineerde materialen toegepast als vuilafstotende coating om neerslag van polymeerdeeltjes in printkoppen te voorkomen. Zulke sterk gefluorineerde materialen zijn giftig en worden binnenkort verboden in de Europese Unie. Een minder giftig alternatief is dus gewenst. Daarnaast zou de levensduur van zulke coatings verbeterd kunnen worden door ze zelfhelende eigenschappen te geven.

Hoofdstuk 1 van dit proefschrift geeft een overzicht van de huidige stand van zaken van de chemische vakgebieden die in dit proefschrift zijn onderzocht. Er worden verscheidene hechtingsmethoden en polymerisatie-technieken besproken, met polymeerborstels als voornaamste onderwerp. Polymeerborstels zijn polymeren die aan een zijde verbonden zijn aan een oppervlak, waardoor zowel de manier waarop ze gemaakt en gekarakteriseerd kunnen worden, als ook hun eigenschappen, wezenlijk anders zijn dan bulkpolymeren. In het bijzonder worden vuilafstotende en zelfhelende coatings besproken. Op het gebied van bulkpolymeren worden dynamisch covalente chemie, polymeren op basis van SuFEx (een zwavel-fluor uitwisselingsreactie) en natuurlijke polymeren, zoals lignine, behandeld. Een korte geschiedenis en enkele huidige toepassingen worden behandeld van de chemische rekenmethode DFT (dichtheidsfunctionaaltheorie), welke gebruikt kan worden om chemische reacties te beschrijven.

In **hoofdstuk 2** van dit proefschrift worden de zelfhelende en vuilafstotende eigenschappen van een reeks polymeerborstels beschreven. Elf methacrylaat monomeren zijn gekozen met lineaire zijketens met verschillende hoeveelheden fluor. Na synthese van zes van deze monomeren, is SI-ATRP (oppervlakte-geïnitieerde atoomoverdracht radicaalpolymerisatie) gebruikt om elf polymeerborstels te maken. De coatings zijn geanalyseerd met statische contacthoekmetingen, ellipsometrie, AFM en XPS. De vuilafstotende eigenschappen van elke coating zijn bestudeerd met confocale fluorescentie microscopie. Zoals verwacht zijn de polymeerborstels met volledig gefluorineerde zijketens uitermate vuilafstotend, of ze nu kort, gemiddeld of lang zijn. Bij een afname in de fluorinatiegraad, neemt ook de mate van afstoting

af. Het is opmerkelijk dat de polymeerborstels met ongefluorineerde zijketens het significant beter doen dan de polymeerborstels met slechts één fluor atoom. We vinden een correlatie tussen de mate van afstoting en de minimale oppervlaktespanning van een polymeerborstel. Daarnaast is de zelfhelende eigenschap van alle polymeerborstels onderzocht door herhaalde blootstelling aan een pH 3 oplossing en een 120 °C atmosfeer. Alle coatings zijn volledig zelfhelend, waarbij moet worden opgemerkt dat er geen schade gezien wordt bij de polymeerborstel met de langste ongefluorineerde zijketen.

Om deze bijzondere eigenschap van de polymeerborstel met de langste ongefluorineerde zijketen verder te onderzoeken, is in het onderzoek dat is beschreven in **hoofdstuk 3** een reeks ongefluorineerde zijketens bestudeerd. Synthese, polymerisatie, karakterisering en het testen van de zelfhelende eigenschap is op dezelfde manier gedaan als uiteengezet in hoofdstuk 2. Polymeerborstels met lineaire zijketens van zeven of minder koolstoffen laten herstelbare schade zien, terwijl polymeerborstels met lineaire zijketens van negen of meer koolstoffen onbeschadigd blijven. We stellen dat langere lineaire zijketens dicht tegen elkaar aan zitten, waardoor H_3O^+ moleculen er niet tussendoor kunnen komen om de ruggengraat van het polymeer te verbreken (door hydrolyse). Kortere ketens kunnen niet strak genoeg tegen elkaar aan blijven zitten om de toegang te blokkeren, waardoor hydrolyse in die gevallen wel plaatsvindt. Om deze hypothese te toetsen, bestuderen we polymeerborstels met vertakte zijketens, want de vertakkingen zouden de dichte pakking ook verstoren. Deze polymeerborstels zijn inderdaad (herstelbaar) beschadigd door onderdompeling in pH 3. Het werk in dit hoofdstuk geeft een solide basis voor hoe ongefluorineerde coatings zelfhelend en/of vuilafstotend gemaakt kunnen worden.

In een tijd van plastic soep en de energietransitie zijn innovaties op polymeermaterialen erg wenselijk. Hoewel windmolens bijvoorbeeld bijdragen aan de productie van schone energie, kunnen de thermoharder materialen uit windmolens niet gerecycled worden en leveren ze enorme hoeveelheden afval op. Een recyclebaar alternatief voor thermoharders zou dus een grote positieve impact hebben. **Hoofdstuk 4** beschrijft onderzoek naar de reactiviteit van de imineverbinding. Deze verbinding is een centraal onderdeel van covalente aanpasbare netwerken, de potentiële recyclebare vervanger van thermo-

harders. Met DFT berekeningen onderzoeken we de condensatie en transiminering van een zogenaamde imine pincer dat gecoördineerd is aan een ijzer(II) ion. Onze eerste berekeningen leiden tot onrealistische hoge barrières. Door toevoeging van twee ethylamines om protonoverdracht mogelijk te maken, verkrijgen we realistische activatie energieën die overeenkomen met de gerapporteerde experimenten. We laten hierbij zien dat deze proton shuttles essentieel zijn voor condensatie en transiminering in zulke gecoördineerde imines. Daarnaast tonen we ook dat coördinatie aan een ijzer(II) ion de reactiviteit verhoogt.

Ook het onderzoek beschreven in **hoofdstuk 5** maakt gebruik van DFT berekeningen, in dit geval om ketenpolymerisatie van een zwavel–fluor uitwisselingsreactie (SuFEx) te bestuderen. Waar tot voor kort alleen ABAB-type polymeren met SuFEx gemaakt waren, is recent gebleken dat ook homo-polymeren gemaakt kunnen worden. Deze nieuwe SuFEx ketenpolymerisatie gebruikt monomeren waarbij de zwavelverbinding en de alcohol aan dezelfde aromatische ring zitten, alsook een elektronenzuigende groep om zelfpolymerisatie te voorkomen. Pas wanneer het monomeer in contact komt met een initiator, kan het alcohol reageren, waarna de zwavelkern van dat monomeer reactief wordt. Hierdoor ontstaan goed gedefinieerde polymeren. Met DFT berekeningen bevestigen we in hoofdstuk 5 de reactiviteit van de initiatiestap en propagatiestap van de ketenpolymerisatie. Echter, in tegenstelling tot de experimenten, laten onze berekeningen zien dat zelfpolymerisatie bij normale omstandigheden ook mogelijk is. Wij vinden geen enkel verschil tussen elektronenzuigende groepen. Er is dus meer onderzoek nodig om dit verschil te verklaren, bijvoorbeeld door oplosmiddel-interacties mee te nemen in de DFT berekeningen, of door de experimenten te herhalen in andere oplosmiddelen.

Waar de voorgaande onderzochte polymerisaties zich richtten op het creëren van nieuwe polymeren, richt het onderzoek in **hoofdstuk 6** zich op de afbraak van een natuurlijk polymeer. Lignine is een grote component van plantaardig materiaal en daarmee een groene bron van chemische bouwstenen. Om die bouwstenen te bemachtigen moet lignine afgebroken worden, maar bij de degradatie met laccase en HBT is oxidatie dominant over splitsing. In hoofdstuk 6 onderzoeken we een reeks pH's en buffersterktes om de verhouding van splitsing tot oxidatie te verbeteren. DFT berekeningen geven een verklaring voor

de gevonden resultaten. We stellen dat splitsing versterkt wordt door waterstofbruggen tussen de lignine en de bufferanionen, wat meer voorkomt in sterke buffers of bij hogere pH.

De algemene discussie in **hoofdstuk 7** gaat in op de industriële toepasbaarheid van de polymeerborstels beschreven in hoofdstukken 2 en 3. Ook de gewenste vermindering van het gebruik van gefluorineerde substanties wordt bediscussieerd, samen met de huidige inspanningen en opstelling van de academische gemeenschap op dit onderwerp, die zowel mee- als tegenwerken aan dit doel. Ten slotte wordt de toegevoegde waarde van DFT voor materiaalonderzoek besproken.

In totaal geven de beschreven onderzoeken in dit proefschrift meer inzicht in een wijd bereik van polymerisatiereacties en polymere materialen. Met deze kennis is de transitie naar milieuvriendelijke materialen, en daarmee naar een duurzamere samenleving, een stapje dichterbij.

Chapter 1
General Introduction

1.1 Polymer research

Plastics are all around. From lunch boxes to shoe soles, tables to windowsills, sunscreens to windmills. The average European citizen uses 150 kg plastic per year,[1] and the global plastic production of 2019 was 460 Mton[2] (Figure 1.1). It is safe to say that we live in a world that is addicted to plastic.

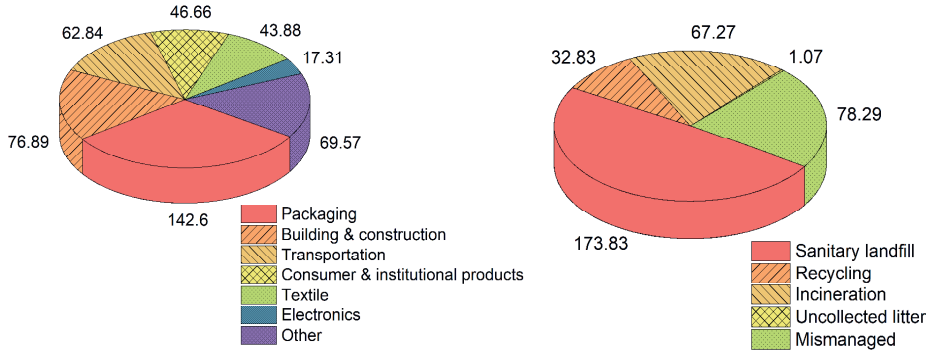

Figure 1.1: The global plastic production (left) and plastic waste (right) of 2019 in million tons, as reported by the Organization for Economic Co-operation and Development (OECD).[2]

Plastics, or polymers in general, have many beneficial properties that make them ideal for a variety of applications. In this, polymers are defined as long chains with repeating units, the monomers. These monomers can be combined in numerous ways, leading to homopolymers, block-copolymers, random copolymers, and many other varieties. They can be produced at will, in any shape or structure that one would like, are lightweight and electronically non-conducting. Transparency, stiffness, hardness, water and wind permeability, or any other material property can be tuned by taking the right polymer and combining it with the correct additives. Combinations with metals are easily produced, leading to the advanced products that we use and consume en masse.[3]

However, although polymers are easy to produce and use, current polymers do come with a number of limitations and disadvantages in their production and/or use. The most predominant synthetic polymers (polyethylene, polypropylene, polyvinylchloride, polystyrene) are produced from crude oil, which has been cheap and abundant for half a century. On the downside, distribution of oil has

caused ecological disasters like the one in the Gulf of Mexico in 2010,[4,5] and oil production continues to increase social inequality in for example Nigeria, Azerbaijan and Kazakhstan.[6–8] Natural polymers like rubber are harvested at increasing rates, leading to deforesting and growing social inequality in Latin America and South-East Asia.[9,10] Additionally, the end-of-life of most polymers is problematic. As most polymers are carbon-based, thermal degradation (by incineration) results in enormous CO_2 emissions, enhancing climate change. Recycling is only possible for pure thermoplastics, which composed 9% of all plastic waste in 2019.[2] Recovery of starting materials can be done with a few polymers, under specific conditions. To postpone this end-of-life problem, a significant amount of plastic is used as landfill [11,12] or washed into the ocean.[13] With 353 Mton of plastic waste in 2019 alone[2] (Figure 1.1), this cannot last. Research into polymers, especially in sustainable end-of-life techniques or non-polluting, biobased or biodegradable polymers, is thus highly desirable.

1.2 Coatings

Next to being bulk materials, polymers are also used as coatings in numerous applications, to alter surface properties while maintaining the bulk properties of the underlying material. In this manner, one can change for example color, texture, thermal stability, conductivity, hydrophobicity, antifouling capability, and wear resistance. A wide range of techniques has been developed to attach a polymer coating to a surface.[14] Depositing or spraying a polymeric coating onto a surface are popular methods, relying on hydrogen bonds[15] or ionic,[16,17] coordination,[18] π-π[19,20] or other non-covalent interactions[21] to connect the two materials. However, the coating holds strongest when covalent bonds are formed between the polymer and the surface.

1.2.1 Grafting methods

A polymer can interact with a surface in many configurations. Polyelectrolytes[22] often have multiple interaction sites, combining many weak interactions to strengthen the connection between the two materials. Crosslinked networks[23] use a few strong, covalent attachment points on the surface, to which the rest of the network is connected. Both result in full coverage of the surface with homogeneous surface properties. On the other hand, tethered polymers [24] are non-crosslinked polymer chains using a single attachment site, often connected

by only one[25] to three[26] covalent bonds. These chains can attach far apart or close together, which influences the surface properties from patchy functionalization to highly uniform,[27] and the resulting coatings have a typical thickness of 10 to 100 nm.[21]

The distance between anchoring points of these tethered polymers is the grafting density (σ).[28] When the distance between anchoring of individual polymer chains (D) is lower than the space each polymer chain occupies (as can be expressed by the radius of gyration, R_g), the grafting density is so low that the polymer chains have no interaction with each other. With a positive interaction with the surface, this leads to a pancake structure (situation A in Figure 1.2). If the surface repels the polymer chains, a mushroom structure is formed (situation B in Figure 1.2). When $D < R_g$, thus with higher grafting densities, the polymer chains undergo steric interactions, forcing them to stretch away from the surface, leading to a brush-like conformation (situation C in Figure 1.2).[29] As the functionality of pancake and mushroom polymer coatings is often patchy,[30] the more uniform polymer brushes are generally the desirable configuration.[27] In the development of polymer brush coatings, one thus typically aims for high grafting densities.

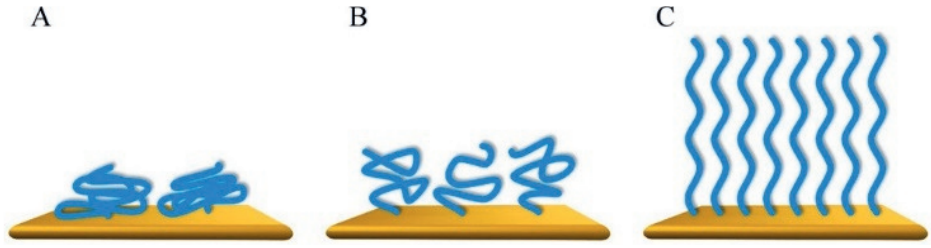

Figure 1.2: Schematic illustration of three different types of conformations of surface-attached polymers: (A) pancake, (B) mushroom, and (C) brush-type surface-anchored polymers. Reproduced from ref. 27.

Covalent bonding of the attachment point of a polymer to a surface can be mainly achieved in two ways: grafting-to and grafting-from.[27] In grafting-to methods, end-functionalized polymers and activated surfaces react to form a polymer brush (Figure 1.3, path A). Although the resulting coating is robust, the functionalized polymers may be poorly soluble, complicating the grafting

process. In addition, due to steric hindrance, the grafted-to coatings are generally thin (5 to 8 nm)[28] and have low grafting densities.[31–34]

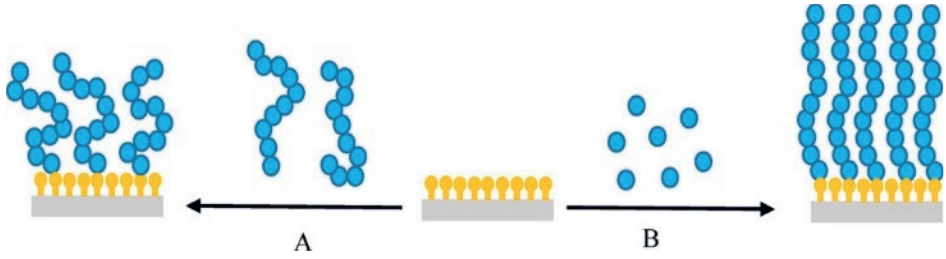

Figure 1.3: Schematic illustration of the preparation of polymer brushes via (A) the grafting to and (B) the grafting from strategy. Reproduced from ref. 27.

These drawbacks can be overcome by use of a grafting-from technique (Figure 1.3, path B).[35] First, an initiator is attached onto the surface. From the initiator, the polymer is grown with a suitable chain-growth polymerization technique. In these polymers, density, thickness (exceeding 100 nm) and functionality can accurately be tuned by control over the polymerization method. However, as the surface is exposed to the polymerization conditions, not all substrates are suited for grafting-from polymerization. Additionally, determination of polymer properties such as polydispersity, molecular weight and grafting density are complicated by the immediate attachment to the surface.[36]

1.2.2 Polymerization techniques

In chain-growth polymerizations, or living polymerizations, new monomers are added to the end of the polymer chain. This contrasts with step-growth polymerizations, where monomers are connected into short chains, after which those shorter chains connect to form longer chains. Step-growth polymerizations cannot be used to grow polymer brushes from a surface, as attachment to a surface will hamper the next growth step. Surface-initiated chain-growth polymerizations include ring-opening polymerization (ROP),[37] ring-opening metathesis polymerization (ROMP),[38,39] anionic polymerization,[40,41] cationic polymerization,[42] nitroxide-mediated polymerization (NMP),[43,44] reversible addition-fragmentation chain transfer polymerization (RAFT)[45] and atom transfer radical polymerization (ATRP). RAFT and ATRP are the most popular, with ATRP being used in this thesis.

In 1998, Fukuda *et al.*[46] first used ATRP to create a polymer with a narrow polydispersity. Matyjaszewski *et al.*[47] optimized the process of Fukuda by using a Cu(I) catalyst to minimize free polymerization. The reaction was then further optimized, for example to allow oxygen in the reaction vessel (Activator ReGenerated by Electron Transfer ATRP, or ARGET-ATRP),[48] or by using a photoinitiator.[49] ATRP can also be used to grow polymers from a surface, so-called surface-initiated ATRP (SI-ATRP, Figure 1.4). This method is used in chapters 2 and 3 of this thesis. The resulting polymer brushes know various applications. They can be used as antibiofouling coatings, either generally repelling [50,51] or by selectively connecting to one specific molecule while deflecting all else: a so-called "romantic surface".[52,53] In hydrophobic media, antifouling has been shown as well.[54] Polymers that show temperature-dependent hydrophilicity were made with poly(N-isopropylacrylamide) (PNIPAM) on gold, by using aqueous ATRP.[55] Patterns of polymer brushes on a gold surface were made with self-assembled microsphere monolayers (SMMs) as stamps for microcontact printing.[56] Furthermore, some polymer brushes have the ability to regain their surface properties after damage has been inflicted.[57,58]

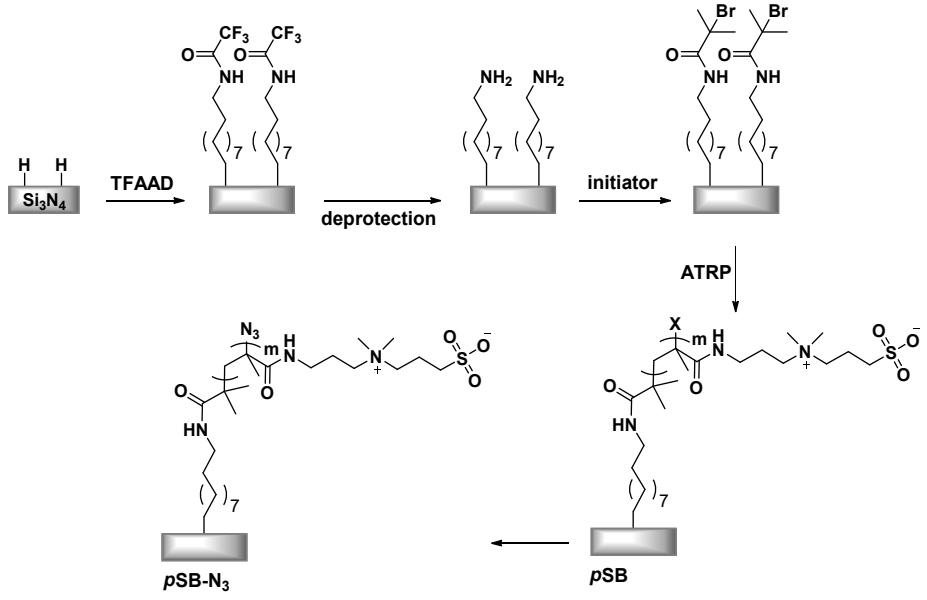

Figure 1.4. Zwitterionic polymer brushes grafted via surface-initiated atom transfer radical polymerization (SI-ATRP). Full synthetic details are available from ref. 59.

1.2.3 Antifouling coatings

Fouling is the unwanted deposition of a material onto a surface. When fouling occurs, there is a chance that the surface can no longer fully function in the intended way. Therefore, fouling can be a problem. For example, in the marine industry, fouling of mussels on the hulls of ships increases drag, thereby increasing the amount of fuel needed to move ships from A to B. Cleaning ship hulls is a difficult and time-consuming process, thus research into prevention of this type of fouling by an antifouling coating is worthwhile.

Most research of antifouling coatings is focussed on biological fouling: sedimentation of marine life,[60,61] fouling by bodily fluids on hospital instrumentation and protheses,[62,63] aqueous particles fouling of membranes,[64,65] etc. This has led to a deep understanding of the early stages of biofouling and the development hydrophilic antifouling coatings, such as zwitterionic polymer brushes.[66,67] These coatings have such high affinity for water, that a close water-shell is created, through which no fouling agent can penetrate. Thus, no fouling agent will reach the surface, and thus no fouling agent will stick to the surface.

In contrast, non-aqueous antifouling coatings employ a fully repelling mechanism, where the solvent is repelled as well as any fouling agent in the solvent. In order to repel all, non-aqueous antifouling coatings are generally highly fluorinated, as fluorocarbons are very hydrophobic, even more than normal hydrocarbons. Although this observation is old[68,69] and perfluorinated polymers like Teflon are widely used for almost a century,[70–78] a unified and concise explanation of this fluorophobic effect was only provided by Dalvi and Rossky in 2009.[79] In their computations, they discovered that although the strong electronegativity of fluorine provides a stronger dipole in a C—F bond than a normal C—H bond, fluorocarbons undergo hydrophobic interactions of similar strength as hydrocarbons when emerged in water. At the same time, the encapsulation of a fluorocarbon requires more water molecules than the encapsulation of a similar hydrocarbon, in other words: places a larger entropic demand on proper solvation. This “fatness” of fluorine as compared to hydrogen results in the more hydrophobic character of solvated fluorocarbons.

Fluorinated chains tethered to a surface cannot be completely encapsulated by a solvent, so supplementing calculations were performed on self-assembling

monolayers (SAMs) to assess their fluorophobic effect. These layers are formed by monomers attaching to a surface, arranging themselves in their most favorable fashion. Dalvi and Rossky discovered that also for the SAMs, the "fatness" is the main cause for the fluorophobic effect. Perfluorinated polymer strands require more space than similar fluorine-free SAMs, thereby offering a larger hydrophobic surface area and hence increasing the hydrophobicity. This results in highly hydrophobic and oleophobic coatings, having affinity to nothing and thus display excellent antifouling performance.

However, next to being excellent in antifouling, fluorinated compounds are also toxic, carcinogenic and disrupting the reproductive system.[80–82] Their persistency in nature poses long-term threats to the environment and humans, which urged the European Union to ban all perfluorinated chemicals from 2027 onwards.[83] The current coatings must thus soon be replaced by non-fluorinated hydrophobic antifouling coatings, for example those discussed in chapter 3.

1.2.4 Self-healing antifouling coatings

Practical applications of antifouling coatings can be seriously hindered by the short durability of their antifouling property. Exposure to sunlight or scratching by loose particles decreases the lifespan of these coatings, especially because

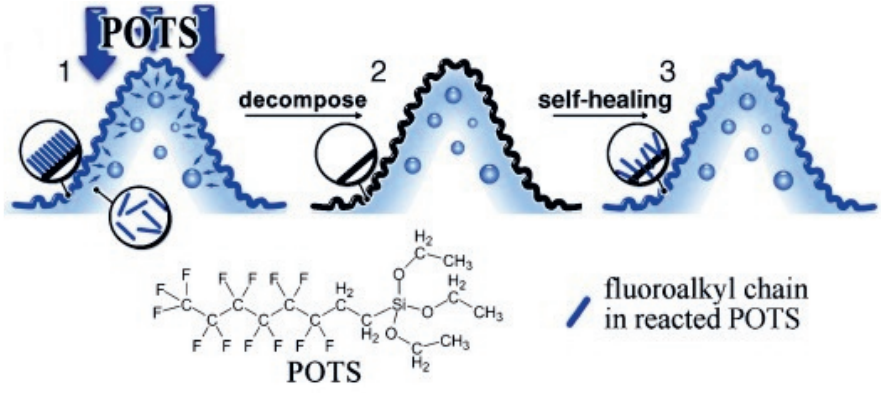

Figure 1.5: Working principle of self-healing super-hydrophobic coatings, as published by ref. 85: 1) the porous polymer coating with micro- and nanoscaled hierarchical structures can preserve an abundance of healing agent units of reacted fluoroalkylsilanes; 2) the top fluoroalkylsilane layer is decomposed and the coating loses its super hydrophobicity; 3) the preserved healing agents can migrate to the coating surface and heal the super hydrophobicity.

the antifouling property is usually based on having a low surface energy. Integrating self-healing properties into the antifouling coating could solve these problems, and various approaches have been employed.[84] Li and Sun[85] have attached fluoroalkylsilanes onto a porous polymer coating and buried a reserve of the fluoroalkylsilanes under it. When the top layer is scratched and the polymer becomes humid, some of the buried fluoroalkylsilanes migrate through the pores to the surface, re-enforcing the antifouling property (Figure 1.5). Alternatively, catechol-mediated hydrogen bonding interactions and aromatic interactions,[86] flexible polymers,[87] and liquids captured within nanostructures[88] have been used to implement self-healing properties in coatings.

1.3 Bulk Polymers

Although polymers are valuable when applied to a surface, most polymers are used in bulk. For the most common polymer streams, production processes are well established, and ongoing research focuses on finetuning.89,90 However, as stated before, if we want to battle the ever-increasing amount of polymer waste, we need radically different ideas. As such, we will discuss dynamic covalent chemistry (a smarter polymer design), SuFEx polymerization (a new polymerization technique) and natural polymers (a non-fossil resource).

1.3.1 Dynamic Covalent Chemistry

Until recently, polymers could be divided into two categories based on their chemical structure: thermoplastics and thermosets (Figure 1.6). In thermoplastics, individual strings of polymer exist next to each other, being held together by weak, non-covalent interactions. This makes the material flexible, and by heating or dissolving, the individual strands can be regained, and a new

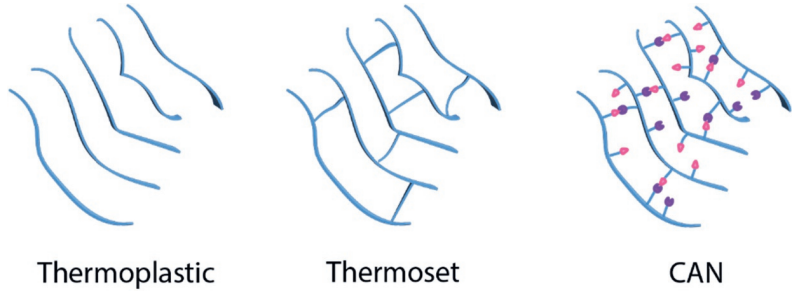

Figure 1.6: Schematic representation of three types of polymers: thermoplastics, thermosets, and covalent adaptable networks (CANs).

shape can be formed: the material is recyclable. In thermosets, no recycling is possible, as the polymer chains crosslink to form one strong network. These crosslinks make the polymer stiff and strong, but unable to assume any other shape than the original one. This severely limits the possibilities to reprocess or recycle thermoset materials.

In 2011, a new type of polymer was invented: the covalent adaptable network (CAN).[91] In these dynamic covalent networks, monomers are covalently bound in polymeric chains, yet some of the monomers can undergo reversible crosslinking. This provides the strength and stiffness of thermosets, while the reversibility of the crosslinks allows malleability and recyclability, like thermoplastics. Due to this dynamic nature of the material, CANs are self-healing, meaning that they can repair themselves after physical damage into a chemically pristine material. Motifs like furan-maleimide Diels–Alder adducts,[92-94] boronic esters,[95,96] disulfides,[97] sterically hindered urethanes,[98] and imines[99] are frequently used to create dynamic materials.[100,101]

In contrast to the previously described coatings with static functionalities, smart coatings can adapt to changes in their environment. Thermo-responsive polymer brushes such as PNIPAM[102,103] or PNMEP (poly(N-2-(methacryloyl-oxy)ethyl pyrrolidone))[104] change thickness and functionality when exposed to different temperatures. A catch-and-release coating can trap a specific biomolecule in one condition and release the biomolecule when, for example, a mild current is applied,[105] or when another chemical is added.[106] In dynamic coatings, the material is not just rearranging to adapt to environmental changes, but actually forming and breaking covalent bonds. Du Prez and co-workers have produced recyclable epoxy coatings in this fashion,[107] and Li and Huang and co-workers have applied two types of dynamic covalent interactions in a layer-by-layer approach to smart antibacterial coatings.[108] When using an external stimulus, dynamic covalent bonds can repair damage to a coating.[109] The flexibility of dynamic coatings is highly interesting from an environmental and industrial point of view. As such, it is worthwhile to investigate dynamic covalent chemistry as a whole.

1.3.2 SuFEx polymerization

Next to the living polymerization techniques described in section 1.2.2, many other reactions exist to perform step-growth polymerization. The most successful reactions are high yielding, stereospecific, require mild conditions, produce inoffensive byproducts and a easy to purify. In other words, they are click reactions.[110] Kolb, Finn and Sharpless invented the term click chemistry in 2001 to describe a group of reactions that can be used to efficiently connect separate building blocks without side reactions or loss of material. These characteristics make click reactions perfect for polymerization, and they have been used abundantly.[111–113]

When a promising chemical reaction is brought to the attention, as Sharpless did in 2014 with the sulfur(IV) fluoride exchange (SuFEx) reaction,[114] chemists worldwide promptly set out to explore all its possibilities.[115–117] It was quickly discovered that the SuFEx reaction, behaving like a click reaction,[110] was well-suited for step-growth polymerization.[118,119] As it is orthogonal to other chemistries, it can be used as handle to further functionalize polymers made with another technique,[120–122] or vice versa.[123] Polymer brushes have been grafted onto surfaces as well.[124,125]

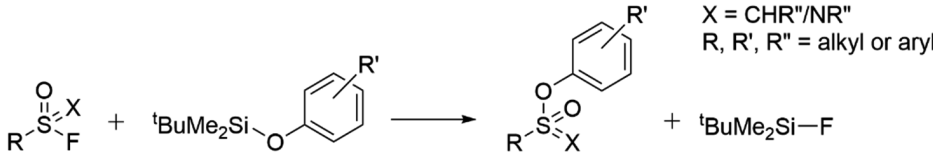

Figure 1.7: General scheme of the SuFEx reaction.

In the SuFEx reaction (Figure 1.7), a phenolate or amine group attacks a sulfonyl fluoride group, eliminating the fluoride and forming a sulfate or sulfonamide moiety. The fluoride is commonly captured by a silicon group, forming the extremely stable Si—F bond, although both silicon-free[126] and fluorine-free[127] SuFEx adaptations have been reported. The SuFEx reaction proceeds readily at room temperature and under ambient conditions, in contrast to most other click reactions.

Recently, Wu and Sharpless have produced a SuFEx polymer in a chain-growth manner (Figure 1.8).[128] By making an electron-poor monomer, they were able to

prevent step-growth polymerization, while maintaining reactivity with an initiator and the polymer chain. A chain-growth reaction is thus the result. As this would open the door to surface-initiated SuFEx polymerization, this specific reaction is potentially relevant to the field of surface chemistry.

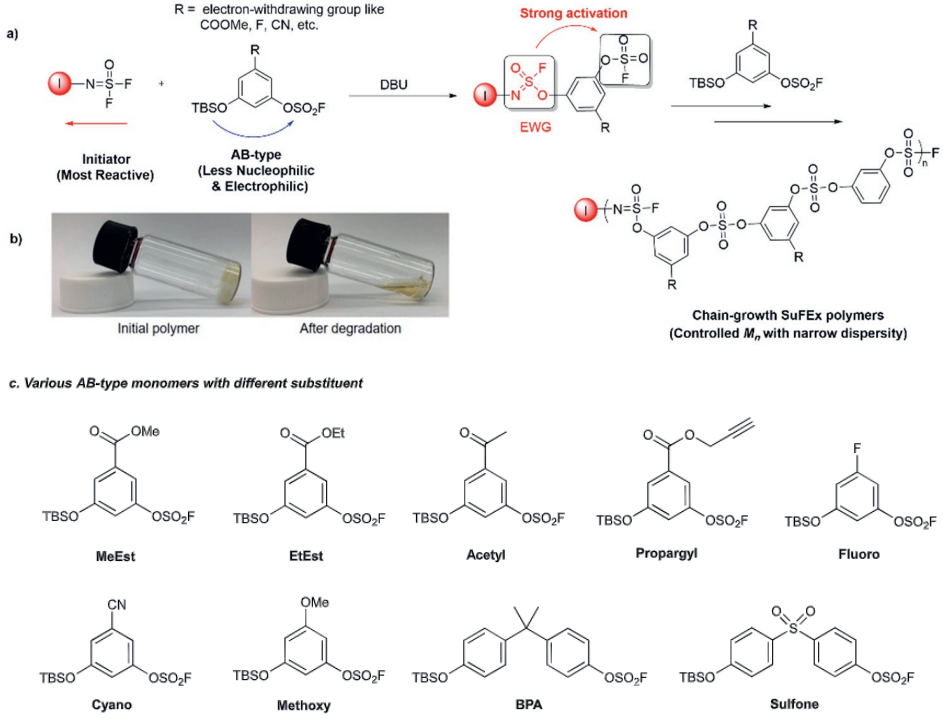

Figure 1.8: (a) Chain-growth polymerization of aryl silyl ether-fluorosulfates, as performed by ref. 128. (b) Pictures of gels that, upon degradation, transition from rigid to fluid. (c) Monomers used in the chain-growth polymerization, with varying degrees of electron-withdrawing ability.

1.3.3 Natural polymers

One of the most famous natural polymers is rubber, tapped as isoprene or latex from a rubber tree and purified or vulcanized before forming one of the many applications. Silk and wool are other natural polymers, produced by animals and harvested by man to be used as fabrics. Plants also mainly consist of polymers: cellulose, pectin and lignin provide strength and stability to stand, starch is used as energy storage, DNA and RNA as information storage, and proteins fulfil many other functionalities both in- and outside a living cell.

While pectin, starch, DNA, RNA, and proteins can be degraded by animals and humans, our capabilities of reducing the strongly crosslinked polymers cellulose and lignin are limited. We therefore aim to use these non-edible polymers for many other applications. At the same time, using natural materials is an excellent way to reduce our oil and gas consumption, thereby reducing our carbon footprint and environmental impact. Especially lignin is increasingly used as feedstock for aromatic chemicals, carbon fibers and resins.[129] For this purpose, lignin must be degraded into small subunits, both phenolic (10–30 % of the lignin composition) and non-phenolic (70–90 %). Efficient degradation processes of lignin are thus essential for feasible industrial applicability.

In biorefinery, lignin is degraded into monomeric components to be used as alternatives to fossil-derived chemicals. Thermochemical treatment is the common method for lignin degradation, being effective and fast, yet energy consuming.[130,131] A greener alternative for lignin degradation is the use of bacteria[132–135] that produce enzymes such as lignin- or Mn-peroxidase or laccase. These enzymes are often well-suited for depolymerizing the phenolic subunits of lignin, but do not reach high enough potentials to degrade the non-phenolic majority of the lignin. For the degradation of the non-phenolic subunits, combining laccase with a mediator such as TEMPO((2,2,6,6-tetramethylpiperidin-1-yl)oxyl), ABTS (2,2'-azino-bis(3-ethylbenzothiazoline-6-sulfonic acid)) or HBT (1-hydroxybenzotriazole) is promising.[136] In such a laccase/mediator system, the mediator depolymerizes the subunits, while laccase regenerates the mediator. However, not only depolymerization but also oxidation is possible. The mode of operation of the mediator differs per mediator[136–138] and per reaction condition.[139] Investigating various reaction conditions is thus desirable to find the optimal conditions where depolymerization is favored over oxidation.

1.4 Theoretical chemistry

Where polymer coatings are studied with surface techniques and bulk polymers are studied with bulk polymer techniques, their fundamental chemical interactions can best be studied computationally. Accurate descriptions of chemical interactions are crucial in understanding chemical reactions. Quantum chemistry is the field that explores these interactions, in which these days Density Functional Theory (DFT) is its most practical tool. In DFT calculations,

ideal geometries of starting molecules and transition states are found, as well as values for energy barriers, enthalpic and entropic factors and solvation energies. Choosing the right combination of functional (the method of calculating electron density) and basis set (the method of describing orbitals for those electrons) is vital, as an incorrect model often leads to incorrect results.[140,141]

With the Hohenberg-Sham theorems [142] and the introduction of the Nobel prize-winning self-consistent field equations by Kohn and Sham,[143] a strong foundation for DFT was laid in the 1960s. When proper models of the exchange and correlation interactions were made in the late '80s and '90s,[144–146] the field of quantum chemistry took off, with 94 publications in 1990, over 16,000 in 2015,[147] and 24,831 in 2022.[148] DFT calculations have been used to shed light on the origins of life on Earth,[149] to elucidate complex biological reactions,[150] or simply to verify and explain experimental observations of basic chemical reactions.[151]

In materials chemistry, the design, production, characterization and functioning of a material is central. Although the design process often involves a lot of chemical theory, theoretical chemistry is rarely included. In cases where computations are combined with materials chemistry, like self-consistent field theory[152] or Monte Carlo simulations,[153,154] physical interactions between entire building blocks are the foundation and small-scale chemical interactions are omitted. As a result, the obtained values are often only valid for those materials whose chemical properties are 'standard'. Fluorophobic effects are rarely included, as are dynamic bonds.

1.5 In this thesis

This thesis investigates a range of promising polymer reactions. In chapter 2, partially fluorinated polymer brushes covalently bound to a silicon surface are examined with regard to their self-healing and antifouling abilities. For this, the synthesis of six monomers and the surface-initiated ATRP of eleven polymers are described, along with the detailed characterization of their products. It is shown that more heavily fluorinated polymer brushes have better antifouling properties, yet do not perform better in self-healing. Upon determination of the minimal surface tension of all polymer brushes, a correlation with antifouling

performance is established. Interestingly, the non-fluorinated poly(decyl methacrylate) polymer brush displays the highest stability, being unaffected by repeated exposure to pH 3.

This potential to achieve great brush properties without involving fluorine lead to chapter 3, which describes a systematic study of non-fluorinated polymer brushes, to understand which side chain length is needed to withstand damage from pH 3 exposure. Five monomers are synthesized, and fourteen polymer brushes are created with SI-ATRP and characterized with XPS, ellipsometry and static water contact angle measurements. Side chains of at least nine carbon atoms show no damage upon repeated exposure, while side chains with six or less carbons, or non-linear side chains, are significantly affected by acid. In all cases, full self-healing is displayed.

The remaining chapters of this thesis involve DFT calculations. Chapter 4 describes the condensation and transimination reaction of an iron(II)-coordinated imine pincer. Although imine chemistry is well-established in the field of dynamic polymers and multiple publications of DFT research on condensation and transimination reactions exist,[155–157] the effect of iron(II)-coordination was never incorporated. We show that the barriers for proton-transfers remain at unrealistic heights when four-membered transition states are considered, as was proposed earlier,[155] regardless of the coordination to iron(II) or zinc(II) or the absence of any metal. However, if two ethylamine molecules are used as shuttles in the proton transfers, plausible energy barriers are found, with iron(II)-coordination increasing the required activation energies for hydrolysis and transimination. This supports the general knowledge of experimental imine chemists that metal coordination improves the stability of imines, and can be used to guide the further development of (metal-stabilized) imine polymers.

Where the field of imine chemistry is well-established, the possibilities of the SuFEx reaction are still being explored at rapid pace. To support the more interesting applications of SuFEx with DFT calculations, chapter 5 of this thesis reports simulations of a chain-growth SuFEx polymerization reaction that was first described by Sharpless and Wu in 2021.[128] In contrast to experimental findings, chapter 5 shows that chain growth polymerization and self-

polymerization are both feasible reactions for all four studied monomers, regardless of the electron-withdrawing nature of their meta-substituents. The three operational SuFEx reactions (initiation, propagation and self-polymerization) are described in detail, and suggestions are given on how to bring theory and experiments closer together.

Chapter 6 is a combination of experimental and theoretical work. The reaction conditions for the degradation of a *β*-O-4′ linked lignin model dimer are optimized towards ether cleavage over C_α-oxidation, using unconventionally highly concentrated buffers at higher pHs. A rationale of the success of these buffers is provided by DFT calculations.

In the general discussion in chapter 7, the industrial applicability of polymer brushes and their polymerization strategies are discussed. A reflection on the use of fluorinated chemicals in academic research is provided, as well as a contemplation of the use of DFT in materials chemistry.

1.6 References

(1) https://plasticseurope.org/wp-content/uploads/2021/09/Plastics_the_facts-WEB-2020_versionJun21_final.pdf.
(2) https://www.oecd.org/environment/plastics/.
(3) Thompson, R. C.; Swan, S. H.; Moore, C. J.; Vom Saal, F. S. *Phil. Trans. Royal Soc. B: Biol. Sci*. **2009**, *164*, 1973–1976.
(4) Fodrie, F. J.; Heck, K. L. *PLoS One* **2011**, *6* (7).
(5) Kotsakis, A.; Boukli, A. *Transn. Env. Law* **2023**, *12* (1), 71–94.
(6) Ruggiero, V.; South, N. *Int. J. Crime Just. Soc. Democ.* **2013**, *2* (2), 12–26.
(7) Obi, C. *Extr. Ind. Soc.* **2014**, *1* (2), 147–153.
(8) Karl, T. L. Covering Oil: A Reporter's Guide to Energy and Development **2005**, Revenue Watch, Open Society Institute: New York.
(9) Traldi, R.; Silva, J. A.; Potapov, P.; Tyukavina, A.; Epprecht, M.; Gore, M. L.; Phompila, C. *World Dev.* **2023**, *170*, 106312.
(10) Bou Dib, J.; Krishna, V. V.; Alamsyah, Z.; Qaim, M. *Land use policy* **2018**, *76*, 828–838.
(11) Diez-Cañamero, B.; Mendoza, J. M. F. *Waste Management* **2023**, *164*, 94–105.
(12) Liu, P.; Barlow, C. Y. *Waste Management* **2017**, *62*, 229–240.
(13) https://theoceancleanup.com/.
(14) Zhao, B.; Brittain, W. J. *Prog. Polym. Sci.* **2000**, *25* (5), 677–710.
(15) Du, Y.; Qiu, W. Z.; Wu, Z. L.; Ren, P. F.; Zheng, Q.; Xu, Z. K. *Adv. Mater. Interfaces* **2016**, *3* (15).
(16) Etienne, O.; Gasnier, C.; Taddei, C.; Voegel, J. C.; Aunis, D.; Schaaf, P.; Metz-Boutigue, M. H.; Bolcato-Bellemin, A. L.; Egles, C. *Biomaterials* **2005**, *26* (33), 6704–6712.
(17) Schaaf, P.; Voegel, J. C.; Jierry, L.; Boulmedais, F. *Adv. Mater.* **2012**, *24* (8), 1001–1016.
(18) Tanaka, D.; Aketa, N.; Tanaka, H.; Tamaki, T.; Inose, T.; Akai, T.; Toyama, H.; Sakata, O.; Tajiri, H.; Ogawa, T. *Chem. Commun.* **2014**, *50* (70), 10074–10077.

(19) Jo, J. W.; Jung, J. W.; Lee, J. U.; Jo, W. H. *ACS Nano* **2010**, *4* (9), 5382–5388.
(20) Hassan, B. M.; Li, H.; McKeown, N. B. *J. Mater. Chem.* **2000**, *10* (1), 39–45.
(21) Buhl, K. B.; Agergaard, A. H.; Lillethorup, M.; Nikolajsen, J. P.; Pedersen, S. U.; Daasbjerg, K. *Polymers* **2020**, *12* (7), 1475.
(22) Guzmán, E.; Rubio, R. G.; Ortega, F. *Adv. Coll. Interf. Sci.* **2020**, *282*, 102197.
(23) Nielsen, L. E. *J. Macromol. Sci. C* **1969**, *3* (1), 69–103.
(24) Azzaroni, O.; Szleifer, I. Polymer and Biopolymer Brushes, **2017**, John Wiley & Sons, ISBN 9781119455042.
(25) Yang, W. J.; Cai, T.; Neoh, K. G.; Kang, E. T.; Teo, S. L. M.; Rittschof, D. *Biomacromolecules* **2013**, *14* (6), 2041–2051.
(26) Methling, R.; Dückmann, O.; Simon, F.; Wolf-Brandstetter, C.; Kuckling, D. *Macromol. Mater. Eng.* **2023**, 2200665.
(27) Zoppe, J. O.; Ataman, N. C.; Mocny, P.; Wang, J.; Moraes, J.; Klok, H. A. *Chem. Rev.* **2017**, *117* (3), 1105–1318.
(28) Brittain, W. J.; Minko, S. *J. Polym. Sci. A* **2007**, *45* (16), 3505–3512.
(29) Liu, G.; Cheng, H.; Yan, L.; Zhang, G. *J. Phys. Chem. B* **2005**, *109* (47), 22603–22607.
(30) Yang, W.; Zhang, R.; Wu, Y.; Pei, X.; Liu, Y.; Zhou, F. *J. Appl. Polym. Sci.* **2018**, *135* (22).
(31) Bergbreiter, D. E.; Tao, G.; Franchina, J. G.; Sussman, L. *Macromolecules* **2001**, *34* (9), 3018–3023.
(32) Ginzburg, M.; Galloro, J.; Jakle, F.; Power-Billard, K. N.; Yang, S.; Sokolov, I.; Lam, C. N. C.; Neumann, A. W.; Manners, I.; Ozin, G. A. *Langmuir* **2000**, *16* (24), 9609–9614.
(33) Ebata, K.; Furukawa, K.; Matsumoto, N. *J. Am. Chem. Soc.* **1998**, *120* (29), 7367–7368.
(34) Crooks, R. M.; Ricco, A. J. *Acc. Chem. Res.* **1998**, *31* (5), 219–227.
(35) Edmondson, S.; Osborne, V. L.; Huck, W. T. S. *Chem. Soc. Rev.* **2004**, *33* (1), 14–22.
(36) Michalek, L.; Barner, L.; Barner-Kowollik, C. *Adv. Mater.* **2018**, 1706321.
(37) Foucher, D. a.; Tang, B.-Z.; Manners, I. *J. Am. Chem. Soc.* **1992**, *114* (14), 6246–6248.
(38) Bielawski, C. W.; Grubbs, R. H. *Angew. Chem. Int. Ed.* **2000**, *39* (16), 2903–2906.
(39) Nguyen, S. B. T.; Johnson, L. K.; Grubbs, R. H. *J. Am. Chem. Soc.* **1992**, *114* (8), 3974–3975.
(40) Advincula, R.; Zhou, Q.; Park, M.; Wang, S.; Mays, J.; Sakellariou, G.; Pispas, S.; Hadjichristidis, N. *Langmuir* **2002**, *18* (22), 8672–8684.
(41) Jordan, R.; Ulman, a; Kang, J. F.; Rafailovich, M. H.; Sokolov, J. *J. Am. Chem. Soc.* **1999**, *121* (5), 1016–1022.
(42) Zhao, B.; Brittain, W. J. *Macromolecules* **2000**, *33* (2), 342–348.
(43) Blomberg, S.; Ostberg, S.; Harth, E.; Bosman, A. W.; Van Horn, B.; Hawker, C. J. *J. Polym. Sci. A* **2002**, *40* (9), 1309–1320.
(44) Husseman, M.; Malmström, E. E.; McNamara, M.; Mate, M.; Mecerreyes, D.; Benoit, D. G.; Hedrick, J. L.; Mansky, P.; Huang, E.; Russell, T. P.; Hawker, C. J. *Macromolecules* **1999**, *32* (5), 1424–1431.
(45) Baum, M.; Brittain, W. J. *Macromolecules* **2002**, *35* (3), 610–615.
(46) Ejaz, M.; Yamamoto, S.; Ohno, K.; Tsujii, Y.; Fukuda, T. *Macromolecules* **1998**, *31* (17), 5934–5936.
(47) Matyjaszewski, K.; Miller, P. J.; Shukla, N.; Immaraporn, B.; Gelman, A.; Luokala, B. B.; Siclovan, T. M.; Kickelbick, G.; Vallant, T.; Hoffmann, H.; Pakula, T. *Macromolecules* **1999**, *32* (26), 8716–8724.
(48) Matyjaszewski, K.; Hongchen, D.; Jakubowski, W.; Pietrasik, J.; Kusumo, A. *Langmuir* **2007**, *23* (8), 4528–4531.

(49) Anastasaki, A.; Nikolaou, V.; Zhang, Q.; Burns, J.; Samanta, S. R.; Waldron, C.; Haddleton, A. J.; McHale, R.; Fox, D.; Percec, V.; Wilson, P.; Haddleton, D. M. *J. Am. Chem. Soc.* **2014**, *136* (3), 1141–1149.
(50) Van Andel, E.; Lange, S. C.; Pujari, S. P.; Tijhaar, E. J.; Smulders, M. M. J.; Savelkoul, H. F. J.; Zuilhof, H. *Langmuir* **2019**, *35* (5), 1181–1191.
(51) Kuzmyn, A. R.; Teunissen, L. W.; Fritz, P.; van Lagen, B.; Smulders, M. M. J.; Zuilhof, H. *Adv. Mater. Interfaces* **2021**, *2101784*, 1–12.
(52) Baggerman, J.; Smulders, M. M. J.; Zuilhof, H. *Langmuir* **2019**, *35* (5), 1072–1084.
(53) Van Andel, E.; De Bus, I.; Tijhaar, E. J.; Smulders, M. M. J.; Savelkoul, H. F. J.; Zuilhof, H. *ACS Appl. Mater. Interfaces* **2017**, *9* (44), 38211–38221.
(54) Wang, Z.; Zuilhof, H. *J. Mater. Chem. A* **2016**, *4* (7), 2408–2412.
(55) Jones, D. M.; Smith, J. R.; Huck, W. T. S.; Alexander, C. *Adv. Mater.* **2002**, *14* (16), 1130–1134.
(56) Chen, T.; Jordan, R.; Zauscher, S. *Soft Matter* **2011**, *7* (12), 5532–5535.
(57) Wang, Z.; Zuilhof, H. *Langmuir* **2016**, *32* (25), 6310–6318.
(58) van Dam, A.; Smulders, M. M. J.; Zuilhof, H. *Appl. Surf. Sci.* **2022**, *579*, 152264.
(59) Lange, S. C.; van Andel, E.; Smulders, M. M. J.; Zuilhof, H. *Langmuir* **2016**, *32* (40), 10199–10205.
(60) Scardino, A. J.; de Nys, R. *Biofouling* **2011**, *27* (1), 73–86.
(61) Yebra, D. M.; Kiil, S.; Dam-Johansen, K. *Prog. Org. Coat.* **2004**, *50* (2), 75–104.
(62) Blaszykowski, C.; Sheikh, S.; Thompson, M. *Chem. Soc. Rev.* **2012**, *41* (17), 5599–5612.
(63) Krishnan, S.; Weinman, C. J.; Ober, C. K. *J. Mater. Chem.* **2008**, *18* (1), 3405–3413.
(64) Gan, D.; Mueller, A.; Wooley, K. L. *J. Polym. Sci. A* **2003**, *41* (22), 3531–3540.
(65) Rana, D.; Matsuura, T. *Chem. Rev.* **2010**, *110* (4), 2448–2471.
(66) Jiang, S.; Cao, Z. *Adv. Mater.* **2010**, *22* (9), 920–932.
(67) Shao, Q.; Jiang, S. *Adv. Mater.* **2015**, *27* (1), 15–26.
(68) Scott, R. L. *J. Am. Chem. Soc.* **1948**, *70* (12), 4090–4093.
(69) Hildebrand, J. H.; Cochran, D. R. F. *J. Am. Chem. Soc.* **1978**, *71* (1), 22–25.
(70) Banks, R. E.; Smart, B. E.; Tatlow, J. C. In Organofluorine Chemistry: Principles and Commercial Applications; Plenum, New York, **1994**.
(71) Tada, H.; Nagayama, H. *Langmuir* **1995**, *11* (1), 136–142.
(72) Tadanaga, K.; Katata, N.; Minami, T. *J. Am. Ceramic Soc.* **1997**, *80* (12), 3213–3216.
(73) Chen, W.; Fadeev, A. Y.; Hsieh, M. C.; Öner, D.; Youngblood, J.; McCarthy, T. J. *Langmuir* **1999**, *15* (10), 3395–3399.
(74) Feng, L.; Li, S. H.; Li, Y. S.; Li, H. J.; Zhang, L. J.; Zhai, J.; Song, Y. L.; Liu, B. Q.; Jiang, L.; Feng, L.; Li, S. H.; Li, Y. S.; Li, H. J.; Zhang, L. J.; Zhai, J.; Song, Y. L.; Liu, B. Q.; Jiang, L.; Zhu, D. B. *Adv. Mater.* **2002**, *14* (24), 1857–1860.
(75) Feng, L.; Li, S.; Li, H.; Zhai, J.; Song, Y.; Jiang, L.; Zhu, D. *Angew. Chem. Int. Ed.* **2002**, *41* (7), 1221–1223.
(76) Li, X.; Chen, G.; Ma, Y.; Feng, L.; Zhao, H.; Jiang, L.; Wang, F. *Polymer* **2006**, *47* (2), 506–509.
(77) Tsujii, K.; Yamamoto, T.; Onda, T.; Shibuichi, S. *Angew. Chem. Int. Ed.* **1997**, *36* (9), 1011–1012.
(78) Feng, L.; Zhang, Z.; Mai, Z.; Ma, Y.; Liu, B.; Jiang, L.; Zhu, D. *Angew. Chem. Int. Ed.* **2004**, *43* (15), 2012–2014.
(79) Dalvi, V. H.; Rossky, P. J. *Proc. Natl. Acad. Sci. U.S.A.* **2010**, *107* (31), 13603–13607.
(80) Hekster, F. M.; Laane, R. W. P. M.; de Voogt, P. Environmental and Toxicity Effects of Perfluoroalkylated Substances; 2003; 99–121.

(81) Fenton, S. E.; Ducatman, A.; Boobis, A.; DeWitt, J. C.; Lau, C.; Ng, C.; Smith, J. S.; Roberts, S. M. *Environ. Toxicol. Chem.* **2021**, *40* (3), 606–630.
(82) Cousins, I. T.; Johansson, J. H.; Salter, M. E.; Sha, B.; Scheringer, M. *Environ. Sci. Technol.* **2022**, *56* (16), 11172–11179.
(83) https://echa.europa.eu/restrictions-under-consideration/-/substance-rev/72301/term. Accessed on 6 September 2023.
(84) Wang, Z.; Scheres, L.; Xia, H.; Zuilhof, H. *Adv. Funct. Mater.* **2020**, *1908098*, 1908098.
(85) Li, Y.; Li, L.; Sun, J. *Angew. Chem. Int. Ed.* **2010**, *49* (35), 6129–6133.
(86) Li, L.; Yan, B.; Yang, J.; Chen, L.; Zeng, H. *Adv. Mater.* **2015**, *27* (7), 1294–1299.
(87) Kuroki, H.; Tokarev, I.; Nykypanchuk, D.; Zhulina, E.; Minko, S. *Adv. Funct. Mater.* **2013**, *23* (36), 4593–4600.
(88) Wong, T.-S.; Kang, S. H.; Tang, S. K. Y.; Smythe, E. J.; Hatton, B. D.; Grinthal, A.; Aizenberg, J. *Nature* **2011**, *477* (7365), 443–447.
(89) Xu, H.; Luo, G. *J. Indust. Engin. Chem*. **2018**, *65*, 13–25.
(90) Ren, H.; Zhou, W.; Makowski, M.; Yan, H.; Yu, Y.; Ma, T. *Ann. Oper. Res.* **2021**, *300* (2), 601–620.
(91) Kloxin, C. J.; Scott, T. F.; Adzima, B. J.; Bowman, C. N. *Macromolecules* **2010**, *43* (6), 2643–2653.
(92) Foster, E. M.; Lensmeyer, E. E.; Zhang, B.; Chakma, P.; Flum, J. A.; Via, J. J.; Sparks, J. L.; Konkolewicz, D. *ACS Macro. Lett.* **2017**, *6* (5), 495–499.
(93) Reutenauer, P.; Buhler, E.; Boul, P. J.; Candau, S. J.; Lehn, J. M. *Chem. Eur. J.* **2009**, *15* (8), 1893–1900.
(94) Zhang, G.; Zhao, Q.; Yang, L.; Zou, W.; Xi, X.; Xie, T. *ACS Macro. Lett.* **2016**, *5* (7), 805–808.
(95) Cho, S.; Hwang, S. Y.; Oh, D. X.; Park, J. *J. Mater. Chem.* **2021**, *9* (26), 14630–14655.
(96) van Hurne, S.; Kisters, M.; Smulders, M. M. J. *Front. Chem.* **2023**, *11*.
(97) Black, S. P.; Sanders, J. K. M.; Stefankiewicz, A. R. *Chem. Soc. Rev*. **2014**, *43* (6), 1861–1872.
(98) Ying, H.; Zhang, Y.; Cheng, J. *Nat. Commun.* **2014**, *5*.
(99) Lauer, J. C.; Zhang, W. S.; Rominger, F.; Schröder, R. R.; Mastalerz, M. *Chem. Eur. J.* **2018**, *24* (8), 1816–1820.
(100) Yang, M.; Lu, X.; Wang, Z.; Fei, G.; Xia, H. *J. Mater. Chem. A* **2021**, *9* (31), 16759–16768.
(101) Schoustra, S. K.; Smulders, M. M. J. *Macromol. Rapid Commun.* **2023**, 2200790.
(102) Chin, H. Y.; Wang, D.; Schwartz, D. K. *Macromolecules* **2015**, *48* (13), 4562–4571.
(103) Jones, D. M.; Smith, J. R.; Huck, W. T. S.; Alexander, C. *Adv. Mater.* **2002**, *14* (16), 1130–1134.
(104) Teunissen, L. W.; Kuzmyn, A. R.; Ruggeri, F. S.; Smulders, M. M. J.; Zuilhof, H. *Adv. Mater. Interfaces* **2022**, 2101717.
(105) Ferrand-Drake, G.; Castillo, D.; Kyriakidou, M.; Adali, Z.; Xiong, K.; Hailes, R. L. N.; Dahlin, A. *Angew. Chem.Int. Ed.* **2022**, *61*, e202115745.
(106) Asha, A. B.; Peng, Y. Y.; Cheng, Q.; Ishihara, K.; Liu, Y.; Narain, R. *ACS Appl. Mater. Interfaces* **2022**, *14* (7), 9557–9569.
(107) Van Lijsebetten, F.; Engelen, S.; Bauters, E.; Van Vooren, W.; Smulders, M. M. J.; Du Prez, F. E. *Eur. Polym. J.* **2022**, *176*.
(108) Yang, L.; Li, L.; Li, H.; Wang, T.; Ren, X.; Cheng, Y.; Li, Y.; Huang, Q. *Adv. Healthc. Mater.* **2022**, *11* (12).
(109) Lutz, A.; Van Den Berg, O.; Van Damme, J.; Verheyen, K.; Bauters, E.; De Graeve, I.; Du Prez, F. E.; Terryn, H. *ACS Appl. Mater. Interfaces* **2015**, *7* (1), 175–183.

(110) Kolb, H. C.; Finn, M. G.; Sharpless, K. B. *Angew. Chem. Int. Ed.* **2001**, *40* (11), 2004–2021.
(111) Hoyle, C. E.; Lowe, A. B.; Bowman, C. N. *Chem. Soc. Rev.* **2010**, *39* (4), 1355–1387.
(112) Binder, W. H.; Sachsenhofer, R. *Macromol. Rapid Commun*. **2008**, *29*, 952–981.
(113) Xi, W.; Scott, T. F.; Kloxin, C. J.; Bowman, C. N. *Adv. Funct. Mater.* **2014**, *24* (18), 2572–2590.
(114) Dong, J.; Krasnova, L.; Finn, M. G.; Barry Sharpless, K. *Angew. Chem. Int. Ed.* **2014**, *53* (36), 9430–9448.
(115) Meng, Y. P.; Wang, S. M.; Fang, W. Y.; Xie, Z. Z.; Leng, J.; Alsulami, H.; Qin, H. L. *Synthesis* **2020**, *52* (5), 673–687.
(116) Abdul Fattah, T.; Saeed, A.; Albericio, F. *J. Fluor. Chem.* **2018**, *213* (May), 87–112.
(117) Barrow, A. S.; Smedley, C. J.; Zheng, Q.; Li, S.; Dong, J.; Moses, J. E. *Chem. Soc. Rev.* **2019**, *48* (17), 4731–4758.
(118) Cao, Z.; Zhou, F.; Gu, P. Y.; Chen, D.; He, J.; Cappiello, J. R.; Wu, P.; Xu, Q.; Lu, J. *Polym. Chem.* **2020**, *11* (18), 3120–3124.
(119) Lee, W.; Li, L.; Kim, B. *Catalysts* **2021**, *11* (9).
(120) Liu, W.; Zhang, S.; Liu, S.; Wu, Z.; Chen, H. *Macromol. Rapid. Commun.* **2019**, *40* (20).
(121) Brendel, J. C.; Martin, L.; Zhang, J.; Perrier, S. *Polym. Chem.* **2017**, *8* (48), 7475–7485.
(122) Li, M.; Ma, J. A.; Liao, S. *Macromolecules* **2023**, *56* (3), 806–814.
(123) Oakdale, J. S.; Kwisnek, L.; Fokin, V. V. *Macromolecules* **2016**, *49* (12), 4473–4479.
(124) Yatvin, J.; Brooks, K.; Locklin, J. *Angew. Chem. Int. Ed.* **2015**, *54* (45), 13370–13373.
(125) Durie, K.; Yatvin, J.; Kovaliov, M.; Crane, G. H.; Horn, J.; Averick, S.; Locklin, J. *Macromolecules* **2018**, *51* (2), 297–305.
(126) Liang, D.; Streefkerk, D. E.; Jordaan, D.; Wagemakers, J.; Baggerman, J.; Zuilhof, H. *Angew. Chem. Int. Ed.* **2020**, *59* (19), 7494–7500.
(127) Chao, Y.; Krishna, A.; Subramaniam, M.; Liang, D. D.; Pujari, S. P.; Sue, A. C. H.; Li, G.; Miloserdov, F. M.; Zuilhof, H. *Angew. Chem. Int. Ed.* **2022**, *61* (36).
(128) Kim, H.; Zhao, J.; Bae, J.; Klivansky, L. M.; Dailing, E. A.; Liu, Y.; Cappiello, J. R.; Sharpless, K. B.; Wu, P. *ACS Cent. Sci.* **2021**, *7* (11), 1919–1928.
(129) Park, Y.; Doherty, W. O. S.; Halley, P. J. *Ind. Crops. Prod.* **2008**, *27* (2), 163–167.
(130) Kline, G. M.; Nugroho, K.; Kelly, J. W. *Curr. Opin. Chem. Biol.* **2022**, *67*, 102113.
(131) Zhao, J.; Xiuwen, W.; Hu, J.; Liu, Q.; Shen, D.; Xiao, R. *Polym. Degrad. Stab.* **2014**, *108*, 133–138.
(132) Sainsbury, P. D.; Hardiman, E. M.; Ahmad, M.; Otani, H.; Seghezzi, N.; Eltis, L. D.; Bugg, T. D. H. *ACS Chem. Biol.* **2013**, *8* (10), 2151–2156.
(133) de Gonzalo, G.; Colpa, D. I.; Habib, M. H. M.; Fraaije, M. W. *J. Biotechn* **2016**, *236*, 110–119.
(134) Bugg, T. D. H.; Ahmad, M.; Hardiman, E. M.; Singh, R. *Curr. Op. Biotechn.* **2011**, *22* (3), 394–400.
(135) Mei, J.; Shen, X.; Gang, L.; Xu, H.; Wu, F.; Sheng, L. *Bioresour. Technol.* **2020**, *310*, 123445.
(136) Baiocco, P.; Barreca, A. M.; Fabbrini, M.; Galli, C.; Gentili, P. *Org. Biomol. Chem.* **2003**, *1* (1), 191–197.
(137) D'Acunzo, F.; Baiocco, P.; Fabbrini, M.; Galli, C.; Gentili, P. A *Eur. J. Org. Chem.* **2002**, No. 24, 4195–4201.
(138) D'Acunzo, F.; Baiocco, P.; Galli, C. *New J. Chem.* **2003**, *27* (2), 329–332.
(139) Kawai, S.; Nakagawa, M.; Ohashi, H. *Enzym. Microb. Techn.* **2002**, *30*, 482-489.
(140) Wodrich, M. D.; Corminboeuf, C.; Schreiner, P. R.; Fokin, A. A.; Von Schleyer, P. R. *Org. Lett.* **2007**, *9* (10), 1851–1854.

(141) Pérez-Soto, R.; Besora, M.; Maseras, F. *Org. Lett.* **2020**, *22* (8), 2873–2877.
(142) Hohenberg, P.; Kohn, W. *Phys. Rev.* **1964**, *136* (3B), B864–B871.
(143) Kohn, W.; Sham, L. J. *Phys. Rev.* **1965**, *140* (4A), A1133–A1138.
(144) Becke, A. D. *Phys. Rev. A* **1988**, *38* (6), 3088–3090.
(145) Perdew, J. P.; Burke, K.; Ernzerhof, M. *Phys. Rev. Lett.* **1996**, *77* (18), 3865–3868.
(146) Kresse, G.; Furthmüller, J. *Phys. Rev. B* **1996**, *54* (16), 11169–11186.
(147) Jones, R. O. *Rev. Mod. Phys.* **2015**, *87* (3), 897–923.
(148) Web of Science Core Collection.
(149) Schreiner, E.; Nair, N. N.; Wittekindt, C.; Marx, D. *J. Am. Chem. Soc.* **2011**, *133* (21), 8216–8226.
(150) Brunk, E.; Rothlisberger, U. *Chem. Rev*. **2015**, *115* (12), 6217–6263.
(151) Hansen, T.; Vermeeren, P.; Zijderveld, K. W. J.; Bickelhaupt, F. M.; Hamlin, T. A. *Chem. Eur. J.* **2023**.
(152) Balazs, A. C.; Singh, C.; Zhulina, E. *Macromolecules* **1998**, *31* (23), 8370–8381.
(153) Binder, K.; Paul, W. *J. Polym. Sci. B* **1997**, *35*, 1–31.
(154) Mavrantzas, V. G. *Frontiers in Physics*, **2021**, *9*, 661367.
(155) Ciaccia, M.; Cacciapaglia, R.; Mencarelli, P.; Mandolini, L.; Di Stefano, S. *Chem. Sci.* **2013**, *4* (5), 2253–2261.
(156) Ciaccia, M.; Di Stefano, S. *Org. Biomol. Chem.* **2015**, *13* (3), 646–654.
(157) Rufino, V. C.; Pliego, J. R. *Comput. Theor. Chem.* **2020**, *1191*, 113053.

Chapter 2
Self-healing Antifouling Polymer Brushes: Effects of Degree of Fluorination

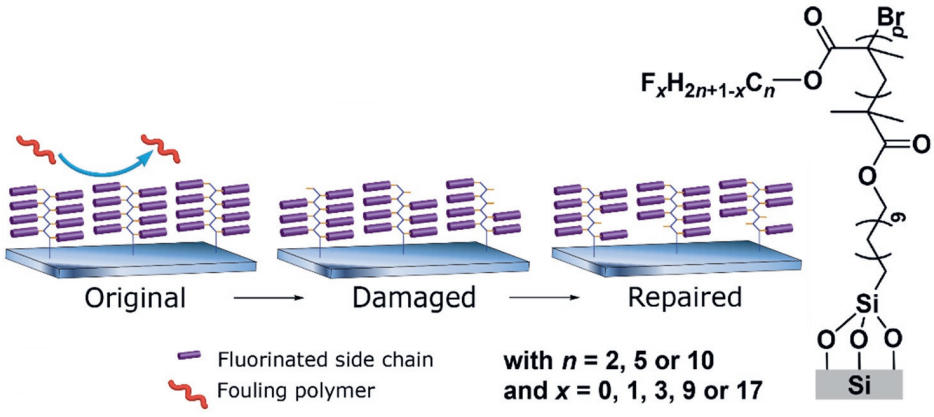

This chapter has been published as:

Annemieke van Dam, Maarten M. J. Smulders, Han Zuilhof, Self-Healing Antifouling Polymer Brushes: Effects of Degree of Fluorination. *Appl. Surf. Sci.* **2022**, *579*, 152264.

https://doi.org/10.1016/j.apsusc.2021.152264.

Abstract

Heavily fluorinated polymeric coatings are used by industry in the prevention of polymeric fouling. However, due to their potential toxicity and lack of durability, there is an increasing demand for sustainable alternatives. In the research described in this chapter, eleven polymer brushes with varying side chain lengths and degrees of fluorination have been developed, and their antifouling and self-healing performances have been compared. In all cases where damage was inflicted by a pH 3 solution, the coatings – including the non-fluorinated ones – showed full restoration of their contact angle upon placement in an oven at 120 °C, confirming the self-healing ability of this range of coatings. One coating, poly(**C10-MAF0**), was unharmed by the acidic conditions, hence no self-healing capability could be established. Investigation with four fluorescently labelled polymer solutions and confocal fluorescent microscopy confirmed that all coatings have antifouling properties towards organic polymers. The more heavily fluorinated polymer brushes performed better than the rest, and not the non-fluorinated, but rather the singly fluorinated brushes showed the least antifouling capability. Determination of the critical surface tension confirmed this trend: the heavily fluorinated polymer brushes have the lowest critical surface tension, and the singly fluorinated polymer brushes have the highest. A lack of alignment of the side chains of the polymer brushes is the proposed reason for this, explaining the contrast with previously reported monolayer experiments. Finally, we explain why both fluorinated and non-fluorinated brushes display self-healing characteristics.

2.1 Introduction

The unwanted deposition of substances on a surface, better known as fouling, has been subject to many investigations in the last few decades. In marine industry,[1,2] water membranes[3,4] or medical implants or sensors,[5,6] the deposition and attachment of biological material to the surface is undesired. Thorough research has led to a deep understanding of the early stages of biofouling, and a large variety of antibiofouling coatings has been designed to prevent it, ranging from fluorinated surfaces,[7,8] polyethylene oxide polymers,[9] via zwitterionic brushes,[10] to *N*-(2-hydroxypropyl) methacrylamide based coatings.[11]

Less known, but not less important, is the prevention of polymeric fouling in non-aqueous media. For example, in high-quality printing, paper manufacturing and food processing, this polymer deposition can severely hamper industrial processes and is therefore costly.[12–14] Traditionally, polytetrafluoroethylene (PTFE, or Teflon) and other heavily fluorinated coatings are used to minimize this type of fouling, but their applicability is often seriously hampered by the stability of their antifouling performance. As the antifouling characteristics are based on having a low surface energy and the surface energy relies on the absence of imperfections of the surface, exposure to an outdoor environment rapidly decreases the antifouling abilities of these coatings. Moreover, while the anti-polymer fouling industry relies heavily on per- or poly-fluorinated compounds such as 1H,1H,2H,2H-perfluorooctyltrichlorosilane (FOTs),[15] more and more of such poly-fluorine-containing chemicals are banned for being potentially toxic and/or environmentally long-term persistent and hazardous.[16]

Non-fluorinated patterned or roughened surfaces can also be used to minimize fouling, relying on their structure to lower the surface energy. This effect is observed in lotus leaves, which are superhydrophobic (water contact angle above 150°) due to their micro- and nanostructure.[17] Many structural designs[18,19] and polymeric nanocomposites[20] have been developed to mimic this lotus effect, yet the lack of self-healing ability hampers application in harsh environments. Durable coatings, without the use of poly-fluorinated moieties, that are both anti-polymer fouling and self-healing are therefore desired, and recently, this topic has gained more attention.[21]

Li *et al.*[22] have developed a porous polyelectrolyte material saturated with fluoroalkyl silanes, that is antifouling and can self-replenish its surface when damage has taken place. Through pores in the material, lower lying silanes are transported to the surface when the top layer has been removed or damaged. In their slippery liquid-infused porous surfaces (SLIPS), Aizenberg and co-workers[23] have employed the same principle, but using a structured porous frame and a liquid lubricant that has saturated the material. Both components are antifouling, but together they are also instantly self-healing as any removed lubricant can be replaced immediately. Although this reduces the healing time to fractions of seconds, leaching of the perfluorinated lubricant remains a potential environmental hazard. By using a covalently bound polymer brush PMAF17 (poly-(perfluorooctyl ethyl methacrylate)), our group[24] has eliminated the liquid elements of the coatings, greatly reducing the environmental impact. The fluorinated polymer brushes can still replenish after repair, as the damaged chains will simply be buried within the polymer chains.

Whereas aqueous fouling can be prevented by high-surface energy materials,[11,25,26] a low-surface energy material is typically required for the prevention of polymer fouling. This can be explained by classical thermodynamics: a process will only take place when there is energy gained, so when the total Gibbs Free energy ($\Delta G = \Delta H - T\Delta S$) is lower than zero. The enthalpic component (ΔH) describes the interactions between the solvent, the foulant and the coating, while the entropic component (ΔS) describes conformational changes that are often temperature dependent. Coatings with a low surface energy gain little enthalpy from interactions with both solvents and fouling agents. In a fully submerged situation, the exchange of solvent by fouling agents will therefore not affect the surface. However, the entropic loss for the fouling agent upon deposition is significant, as it loses the translational freedom that it had in solution. This entropy loss, or more specifically the entropy that can be gained by leaving the surface, will thus effect that any fouling agent will not stay on the coating for long.

Due to what has been labelled 'the fluorophobic effect',[27] fluorinated compounds have an extremely low intrinsic surface energy, explaining their popularity in antifouling coatings. Even in novel, self-healing antifouling materials such as fluorosilane-infused porous polyelectrolyte materials (SLIPS),[23]

or PMAF17,[24] the antifouling property is achieved by the incorporation of fluorine, in most cases relying on a high fluorine content. Recently, monolayer investigations have shown that antifouling properties can actually improve with decreasing amount of fluoride.[28] The increased dipole moment of a terminal CH_2F group, as compared to the CF_3 or the C_8F_{17} group, was proposed to lead to strengthened binding to solvents, thereby further decreasing any enthalpic gain that can offset the lost entropy in case of attachment of the polymer onto the surface.[29]

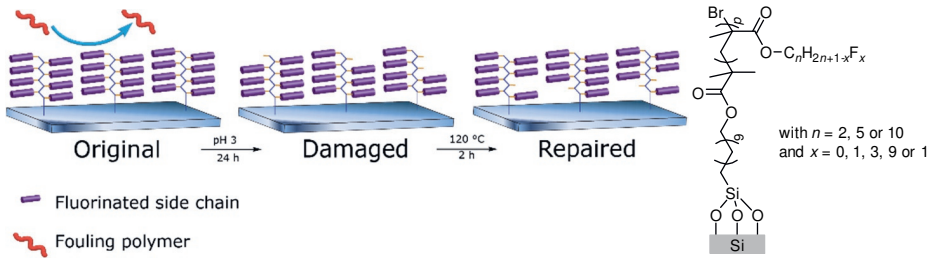

Figure 2.1. Schematic depiction of the self-healing antifouling polymer brushes with fluorinated side chains (left) and general structure of (partially) fluorinated brushes studied herein (right).

In this chapter, we report the preparation and analysis of a range of polymer brushes with varying degrees of fluorination in view of their antifouling characteristics, the environmental demand to reduce the fluorine content in consumer materials, and the encouraging results obtained with low-fluorine materials. To this aim, we report a systematic investigation of the effect of chain length and degree of fluorination on the antifouling and self-healing abilities of methacrylate polymer brushes (Figure 2.1). Taking the C_8F_{17} group in PMAF17 (see Scheme 2.1) as the basis, both the number of fluorine atoms on the methacrylate arms, as well as the length of those arms were varied. In this, we did not limit ourselves to commercially available methacrylates, but instead designed and synthesized a more complete library of monomers. For all polymer brushes, next to standard surface characterization by XPS, ellipsometry and static water contact angle analysis, and polymer fouling studies in four polymer solutions (fluorescently labelled PLGA, PS, PEG and PNIPAM in DCM), the healing ability was studied in ten damage-repair cycles. Finally, the antifouling and self-repair results are discussed in light of each surface's (experimentally determined) critical surface tension and the molecular structure of the brushes.

2.2 Results and discussion

In this investigation on the effect of side chain length and degree of fluorination of methacrylic polymer brushes, we decided to study methacrylates with side chain length of two, five or ten carbon atoms. For each of these chain lengths, zero, one or three fluorine atoms were attached to the final carbon of the chain. To investigate the effect of larger degrees of fluorination, the C_5 and C_{10} side chains were also studied with nine and seventeen F atoms ($–CH_2–C_4F_9$ and $–C_2H_4–C_8F_{17}$, respectively). Our library thus consists of eleven methacrylates (Figure 2.2).

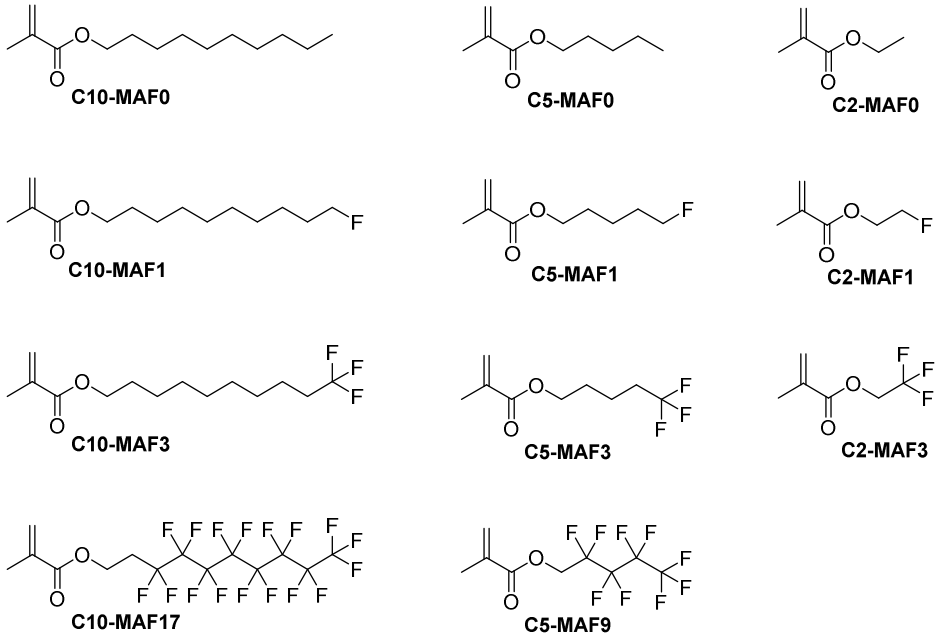

Figure 2.2. Monomers under study as used for the investigated polymer brushes.

Each monomer was labelled according to a naming system that shows the length of the side chain and the degree of fluorination for each of the methacrylates. For example, **C2-MAF3** is the methacrylate (MA) with a side chain of two carbon atoms (C2) and three fluorine atoms (F3). This commercially available compound is also known as TFEMA, or trifluoroethyl methacrylate. In order to keep our nomenclature here consistent and clear, we decided not to use the commercial abbreviations for the polymers.

2.2.1 Synthesis

Five of the desired methacrylates are commercially available, leaving six monomers to be synthesized. For the synthesis of these monomers, three different synthetic routes were used, all on gram scale. **C10-MAF0**, **C5-MAF3** and **C5-MAF°** could be made via the acidic esterification of methacrylic acid and the corresponding alcohols: 1-decanol, 1,1,1-trifluoropentan-5-ol and 1H,1H-perfluoropentan-1-ol, respectively (Scheme 2.1A). For **C10-MAF0** and **C5-MAF3**, this simple Fisher esterification was performed by stirring at room temperature for four and nine days respectively, until NMR analysis showed no more increase in conversion. After work-up (that included extractions and column chromatography) the **C10-MAF0** and **C5-MAF3** monomers could be obtained in a yield of 75% and 84%, respectively. The isolated monomers were subsequently characterized by various NMR methods, mass spectrometry and IR spectroscopy (Supporting Information, sections 2.4.4 and 2.4.5), to assess their purity. The Fisher esterification of **C5-MAF°** was performed with the same reagents as used for **C10-MAF0** but at 110 °C, as the reaction was too slow at room temperature. At this temperature, this esterification was completed in five hours. Also, since purification by column chromatography could not be performed for this monomer due to on-column polymerization of the product (Supporting Information, section 2.4.6), the monomer contained approximately 10% of 1H,1H-perfluoropentan-1-ol. XPS analysis of the eventually resulting polymer brush (see below for details) indicated that this was not incorporated in the coating. The crude yield of C5-MAF9 was 64%.

C10-MAF3 and **C5-MAF1** were made via the esterification of methacrylic acid and the corresponding bromides: 1-bromo-10,10,10-trifluorodecane and 1-bromo-5-fluoropentane, respectively (Scheme 2.1B). This S_N2 reaction was catalyzed by potassium carbonate, and performed overnight under argon at 50 °C in DMF. Following several extraction steps, the desired methacrylates could be isolated, and the products were characterized by mass spectrometry, IR spectroscopy and various NMR techniques. In the **C5-MAF1** product, traces of 1-bromo-5-fluoropentane were found, but these proved not to interfere with polymer brush formation (see below). **C10-MAF3** was produced with 67% yield, and **C5-MAF1** with 82% yield (Supporting Information, sections 2.4.7 and 2.4.8).

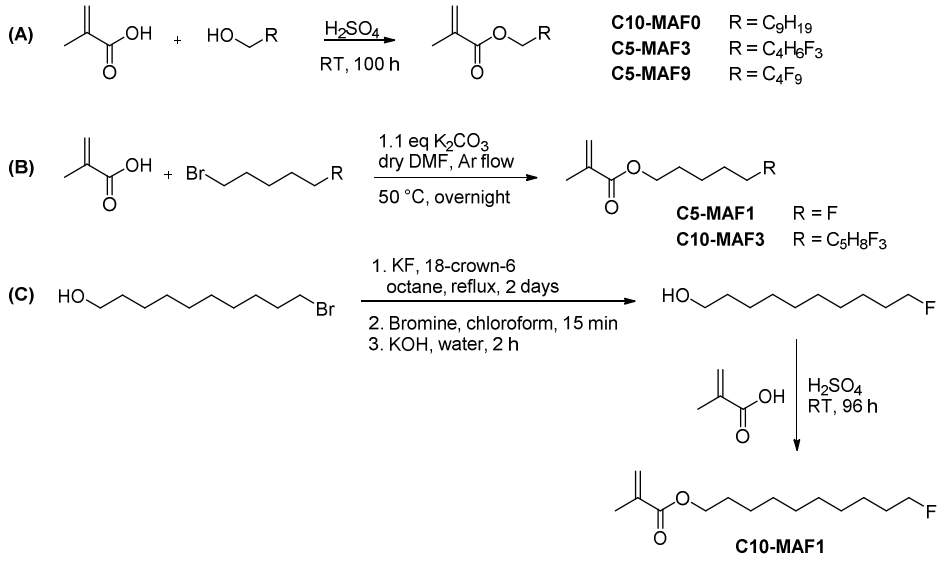

Scheme 2.1. Synthetic pathways to the six non-commercially available methacrylates under study. (A) Fisher esterification for the formation of C10-MAF0, C5-MAF3 and C5-MAF9 (at 100 °C) (B) Esterification for the formation of C10-MAF3 and C5-MAF1. (C) Synthesis of C10-MAF1 in a two-step reaction. For full procedures and characterization: see Supporting Information, sections 2.4.4 – 2.4.10.

For the synthesis of **C10-MAF1**, neither 1-bromo-10-fluorodecane nor 10-fluorodecan-1-ol was commercially available. Therefore, a two-step synthesis was designed (Scheme 2.1C), starting from 10-bromodecan-1-ol. 18-Crown-6 catalyzed the halogen exchange between potassium fluoride and 10-bromodecan-1-ol, which had 7-decen-1-ol and 8-decen-1-ol as byproducts. The C=C bonds were brominated to increase the boiling points of these byproducts, after which the desired 10-fluorodecan-1-ol could be separated via Kügelrohr distillation. This was followed by a Fisher esterification via the same procedure as used for **C10-MAF0**, to produce 10-fluorodecyl methacrylate. Mass spectrometry, IR spectroscopy and various NMR techniques confirmed the formation and purity of the desired **C10-MAF1** monomer, with an overall yield of 32% (Supporting Information, sections 2.4.9 and 2.4.10).

2.2.2 Polymerization

Using the 11 acquired methacrylates, homopolymers were grafted from an initiator-activated silicon surface (Scheme 2.2) by adaptation of a previously reported procedure for a surface-initiated atom transfer radical polymerization (SI-ATRP; see also Supporting Information, section 2.4.3).[30] To this aim, the silicon surface was thoroughly cleaned by sonication in hexane, ethanol and dichloromethane and subsequent oxygen plasma cleaning, after which it was submerged in a solution of 3-(trichlorosilyl)propyl 2-bromo-2-methylpropanoate in toluene at room temperature overnight. After rinsing and drying, the surface was transported to a nitrogen atmosphere glovebox, and the polymer brush growth was started. As all polymer brushes were grown from surfaces produced with this same procedure, a similar grafting density was assumed for all eleven coatings. For poly(**C2-MAF0**), an upper estimate of the grafting density was determined at 1.11 chains per nm^2 (Supporting Information, section 2.4.11). Below we will discuss the required reaction conditions, and polymer brush characterization methods, specifically static water contact angle and XPS.

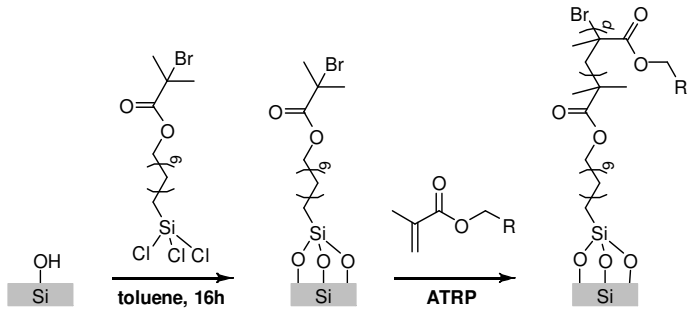

Scheme 2.2. Schematic representation of the attachment of an ATRP initiatior onto a silicon oxide surface, and subsequent grafting of a polymer brush by SI-ATRP.

The polymerization of **C10-MAF17** was previously reported in trifluorotoluene (TFT) at 110 °C, with copper bromide (CuBr) as catalyst and 4,4-dinonyl-bipyridine (dnbpy) as ligand.[24] Using these conditions (Supporting Information, section 2.4.3), a polymerization rate of 1.7 nm/h was reached for **C10-MAF17** (Table 2.1), as could be deduced from ellipsometry measurements. The polymerization of **C10-MAF0** was performed in a similar fashion, but since the monomer is not fluorinated, toluene was used as solvent instead of TFT. A

comparable polymerization rate of 0.8 nm/h was reached (data not shown). When performing the SI-ATRP of **C10-MAF0** in ethanol, the rate increased to 11 nm/h, most likely due to increased solubility of CuBr. Hence, all other polymerizations were performed in ethanol, resulting in polymerization rates ranging from 2.9 nm/h to 25 nm/h (Table 2.1). **C10-MAF17** did not dissolve in ethanol, and no brush growth was observed in this solvent.

In the reaction mixtures of **C10-MAF3**, **C5-MAF°**, **C5-MAF0** and **C2-MAF1**, bipyridine (bpy) was used as a ligand, as dnbpy did not dissolve well. For **C10-MAF3** and **C5-MAF0** this increased the polymerization rates, from 2.3 nm/h to 2.8 nm/h for **C10-MAF3** and from 2.8 nm/h to 5.6 nm/h for **C5-MAF0**. For **C5-MAF°**, polymerization was taking place at 11 nm/h, as opposed to no polymerization when dnbpy was used. Unexpectedly, **C2-MAF1** remained inactive. Only when increasing both the catalyst and bpy concentration tenfold, did this methacrylate start polymerizing, at 1.1 nm/h. Deactivation took place within a day, and no coatings above 30 nm could be grown for **C2-MAF1**.

The polymer brushes were characterized by static water contact angle (WCA) (Table 2.1). The fully fluorinated coatings have a high contact angle: 116° for poly(**C5-MAF°**) and 120° for poly(**C10-MAF17**). When keeping the carbon side chain constant but decreasing the number of fluorine atoms per chain (*e.g.*, from poly(**C10-MAF17**) via poly(**C10-MAF3**) to poly(**C10-MAF1**)), an expected decrease in contact angle was observed, with the singly fluorinated side chains being least hydrophobic. The non-fluorinated side chains showed a slight increase in contact angle with respect to the singly fluorinated ones, which we attribute to more tightly packed side chains of the polymer brush (see also the discussion of critical surface tension below). When keeping the number of fluorine atoms per side chain constant, but decreasing the side chain length (going from poly(**C10-MAF1**) via poly(**C5-MAF1**) to poly(**C2-MAF1**), for example), a decrease in WCA was observed as well.

For industrial purposes where anti-wetting is the main goal, hydrophobic coatings are most relevant. This would imply that from our study, the more fluorinated and/or longer side chains, namely poly(**C10-MAF17**), poly(**C10-MAF0**), poly(**C5-MAF°**), poly(**C5-MAF3**) and poly(**C2-MAF3**), are most interesting for industrial applications.

Table 2.1. Polymer brush formation of methacrylates under study: reaction conditions, average coating thicknesses and static water contact angles (WCA). Reactions were performed at 60 °C with 1 mol% CuBr catalyst, 2 mol% ligand, 50 vol% monomer and 50 vol% solvent.

Monomer	Ligand	Solvent	Reaction time (h)	Coating thickness (nm)	WCA (°)
C10-MAF17	dnbpy	TFT	48[a]	68	120 ± 2
C10-MAF3	dnbpy	Ethanol	16	38	89 ± 1
	bpy	Ethanol	16	59	
C10-MAF1	dnbpy	Ethanol	16	113	83 ± 7
C10-MAF0	dnbpy	Ethanol	17	189	104 ± 4
	dnbpy	Toluene	120[a]	108	
C5-MAF°	bpy	Ethanol	15	209	116 ± 1
C5-MAF3	dnbpy	Ethanol	8	62	92 ± 1
C5-MAF1	dnbpy	Ethanol	24	69	76 ± 1
C5-MAF0	dnbpy	Ethanol	8	30	87 ± 1
	bpy	Ethanol	16	135	
C2-MAF3	dnbpy	Neat	71[a]	47	95 ± 1
	dnbpy	Ethanol	1.5	82	
C2-MAF1	bpy	Ethanol	24[b]	26	69 ± 2
C2-MAF0	dnbpy	Ethanol	6	93	77 ± 1

Notes: [a]: 110 °C. [b]: using 10 mol% catalyst and 12 mol% ligand.

The elemental composition of the coatings was subsequently verified with XPS. In Figure 2.3, the wide XPS spectrum and the C1s narrow scans are shown of the four polymer brushes in the C5 family. The full XPS analysis (wide scan, and C1s, O1s and F1s narrow scans) of all polymer brushes, and of the initiator-activated silicon surface, can be found in the online Supporting Information (section S14).

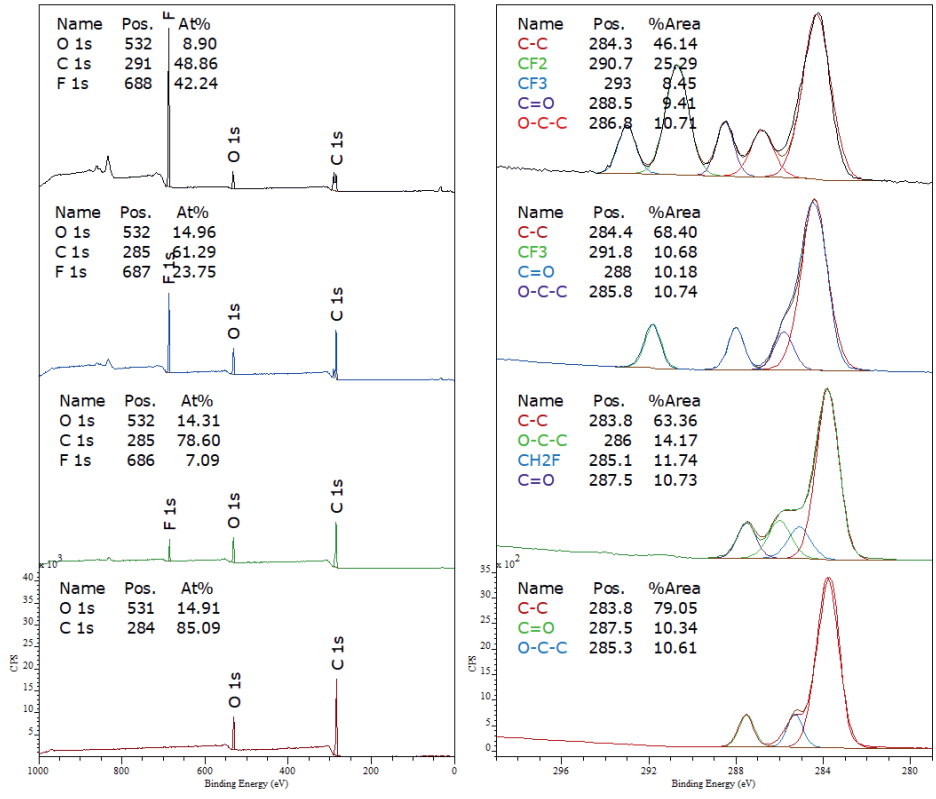

Figure 2.3. XPS wide scan (left) and C1s narrow scans (right) for poly(C5-MAF9) (in black), poly(C5-MAF3) (in blue), poly(C5-MAF1) (in green) and poly(C5-MAF0) (in red).

The XPS data obtained for poly(**C5-MAF°**) serve as an example. The wide XPS spectrum (Figure 2.3, top row) showed a ratio of 9 : 49 : 42 for O : C : F, which is largely in line with the theoretical ratio of 10 : 45 : 45 for a polymer brush consisting solely of **C5-MAF°** monomers; the slightly elevated carbon signal indicates some atmospheric contamination.[31,32] No Si 2p signal was visible, suggesting a polymer layer of at least 20 nm thick that completely covers the silicon surface, which is in line with the ellipsometry results that revealed a thickness of 100 nm. The C 1s narrow scan showed five peaks, indicating five different carbon species. These can be classified as $–CF_3$, $–CF_2–$, –C=O, $O–CH_2–CF_2$ and aliphatic C, going from high to low binding energy. Their theoretical ratio is 11 : 33 : 11 : 11 : 33. We observed an overrepresentation of the aliphatic

carbons (46% instead of 33%), which is in line with the observation of atmospheric carbon contamination in the wide XPS spectrum. The other signals had the correct ratios. The O 1s XPS narrow scan (online Supporting Information, section S14) showed two species occurring in equal amounts, corresponding to the two different oxygen atoms in the ester moiety of each methacrylate. The F 1s XPS narrow scan (online Supporting Information, section S14) showed a single signal, corresponding to carbon-bound fluorine. Together, these spectra indicate a thick, fully surface-covering polymer brush build up from **C5-MAF°** monomers.

When comparing the wide XPS spectra of poly(**C5-MAF°**), poly(**C5-MAF3**), poly(**C5-MAF1**) and poly(**C5-MAF0**), the expected gradual decrease in fluorine content was observed: from 42% in poly(**C5-MAF°**) (theoretical 45%), to 23% in poly(**C5-MAF3**) (theoretical 21%), 7% in poly(**C5-MAF1**) (theoretical 8%) and the expected 0% in poly(**C5-MAF0**). Since the number of oxygens and carbons per monomer remains unchanged, we observed a concomitant increase in their contributions.

The C 1s XPS narrow scans showed a similar trend. Where poly(**C5-MAF°**) had a large contribution of CF_2 carbons, these were absent in the less fluorinated polymer brushes. The signal for the CF_3 group shifted from 293.0 eV to 291.8 eV in poly(**C5-MAF3**), due to the absence of neighboring fluorinated carbons. The signal for the CH_2 group adjacent to the ester moiety shifted from 287 eV in poly(**C5-MAF°**) via 286 eV in poly(**C5-MAF3**) and poly(**C5-MAF1**), to 285 eV in poly(**C5-MAF0**), in line with the reduced influence of electronegative fluorine atoms. The position of the ester carbon remained in all cases more or less unchanged (287.9 ± 0.4 eV).

2.2.3 Self-healing performance

Having synthesized and characterized the polymer brushes, their self-healing capability was analyzed by static water contact angle (WCA) measurements (Figure 2.4), based on a literature procedure[24] (see also Supporting Information, section 2.4.3). Each measurement was repeated on at least five independently prepared surfaces, with at least two drops per surface. By using a damaging solution of pH 3, nearly all polymer brushes were damaged, as evidenced by a decrease in the WCA of 2° to 8° (Figure 2.4; first half cycle). Upon heating in a

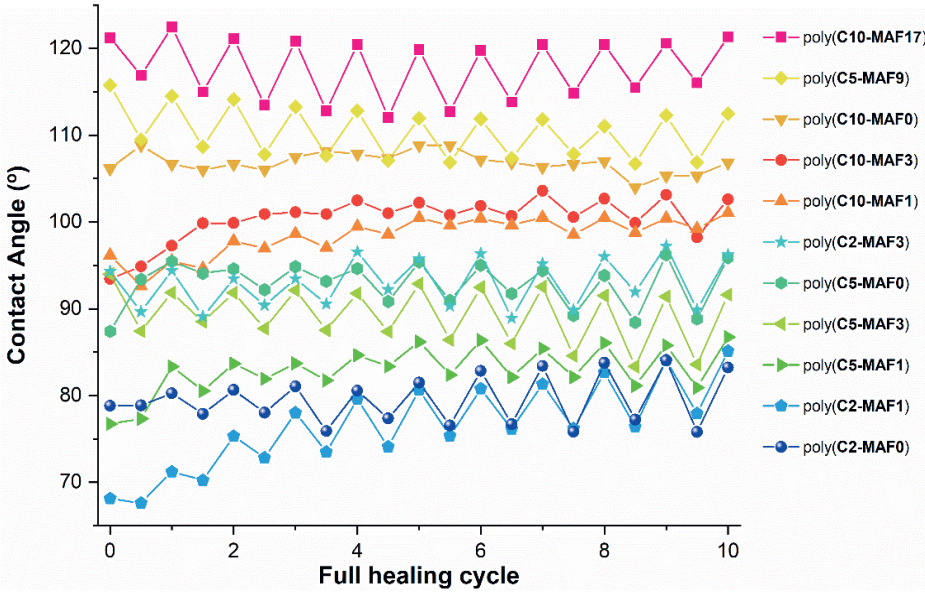

Figure 2.4. Self-healing performance of the polymer brushes under study. The static water contact angle was measured after each damaging step (half cycle points) and after each healing step (whole cycle points). The error margins are < 1° for all points, and are omitted for clarity.

120 °C oven, all polymer brushes showed full recovery of the WCA to their original value, indicating restoration of the outer layer of the coating (Figure 2.4; second half cycle).

The most striking observation from the self-healing results (Figure 2.4) is the zigzag pattern that nearly all coatings showed. The decrease in WCA upon damage indicates a disruption of the surface tension, and can be explained by partial hydrolysis of the acid-sensitive ester bonds in the methacrylates that make up the polymer brush. In this process, the hydrophobic side chains of the polymer brush are released, leaving a hydrophilic acid group behind, which leads to a decrease in WCA. When heating the polymer brush above its glass transition temperature, T_g, rearrangements can occur. The high surface tension is restored, resulting in a restoration of the WCA. As most of these polymers are new, their glass transition temperature is not yet reported in literature. For poly(**C5-MAF0**), poly(**C2-MAF3**) and poly(**C2-MAF0**), values of 3 °C, 75 °C and 65 °C have been reported, respectively.[33,34] To ensure that for all brushes the healing experiments were performed above the T_g, and also to be consistent

with previously reported healing studies,[24] we performed all healing experiments at 120 °C. Nevertheless, healing was also possible at lower temperature: for example, for poly(**C5-MAF0**) (with a T_g of 3 °C) healing at room temperature was feasible (online Supporting Information, section S15). Although, due to the lower temperature, the time for healing increased to around one and a half day.

We also observed a gradual increase of the WCA over the first few cycles in some of the polymer brushes. This "annealing phase" is most likely caused by rearrangement of the polymer brush during the healing steps. Annealing also occurred when the surface was heated to 120 °C without damage first (online Supporting Information, section S16), but at a slower rate: around one day of heating was needed to rearrange a poly(**C10-MAF1**) brush to its critical surface tension, while it takes only four damage-repair cycles (*i.e.*, in total 8 h of heating) to obtain the same result. We attribute this initially counterintuitive observation to the reduction of the density of the top layer of the brush, and a resulting increase in brush flexibility. Initially, the improved repair possibility at the annealing phase more than compensates for the slight damage done during the acid dips.

Until now, it was thought that the low surface energy that resulted from the fluorine atoms, as described by Dalvi and coworkers and named the fluorophobic effect,[27] was the main reason for the this restoration of surface tension.[24,33,34] This would cause the fluorinated side chains to repel each other and the surface, pushing the intact side chains outward to create a low surface tension, thereby burying the damaged side chains deep in the polymer brush. However, if this was the only driving force for the restoration of the surface tension, non-fluorinated polymer brushes such as **C10-MAF0**, **C5-MAF0** and **C2-MAF0** would not restore at all, which they actually also did fully – to our initial surprise. Apparently, also pure aliphatic chains are pushed outwards, burying the acidic groups. One could think that the nature of the substrate has a part in this: as the silicon oxide surface is polar, it attracts the damaged acidic groups, pulling them deep down in the brush. The non-damaged side chains would then remain on the outside of the coating, restoring the low surface tension. In thin coatings this could indeed have an effect, but one would expect this effect to decrease with increasing coating thickness: the further removed the polar

surface is from the damaged top layer, the less it can attract the acidic groups. However, both at 70 nm and at 100 nm thickness, **C5-MAF0** and **C2-MAF0** showed full contact angle restoration after a full damage and anneal cycle (online Supporting Information, section S17). We therefore hypothesize that not the polar surface, but rather the acid groups themselves attract each other, forming hydrophilic, perhaps even hydrogen-bonded clusters. Such clustering deep inside the brush would keep them from the interface with air and pushes the hydrophobic aliphatic chains up, effectively restoring the top layer in the process.

Next to this, we observe in Figure 2.4 that when the amount of fluorine is decreased in the C10 series (going from **C10-MAF17** to **C10-MAF3** to **C10-MAF1** to **C10-MAF0**), the damaging impact of the pH 3 solution is also decreased. Brady has shown that aliphatic side chains of at least eight carbons long have a tendency to aggregate into a tightly packed crystalline layer.[35–37] Such tight packing could hamper acid in reaching the ester moieties near the polymer brush backbone, thereby preventing damage to the coating. Because fluorine is both larger than and electronically different from hydrogen, chains containing both types of atoms are more likely irregular, hampering alignment and tight packing. As a result, whereas the non-fluorinated polymer brush was apparently largely undamaged by repeated submersion in a pH 3 solution, the singly and triply fluorinated polymer brushes did show small but significant signs of damage. As this alignment is only feasible for chains of at least eight carbon atoms,[37] **C5-MAF0** and **C2-MAF0** are not protected in this way, and damage is indeed visible.

2.2.4 Antifouling properties

The antifouling capabilities of the polymer brushes were tested with fluorescently labelled fouling polymers, following a protocol adapted from literature.[24,38] In a petridish, a plasma-treated surface and 11 coated surfaces were placed, face up, and submerged in a fouling solution containing a fluorescently labelled polymer. After 15 min (60 min in case of polystyrene), the surfaces were cleaned by rinsing with fresh solvent, and blown dry. Using confocal fluorescent microscopy, the surface coverage by the fouling polymer was determined (see also Supporting Information, section 2.4.3).

Four fluorescently labelled polymers of varying hydrophobicity were used as fouling agents, with PLGA (poly(lactic-*co*-glycolic acid)) and PS (polystyrene) as hydrophobic polymers and PEG (polyethylene glycol) and PNIPAM (poly(*N*-isopropylacrylamide)) being more hydrophilic (at room temperature). Procedures for the synthesis of fluorescently labelled PS and PNIPAM are based on literature,[39] and can be found in the online Supporting Information (sections S11 and S12, respectively). To prevent solvent effects, all polymers were dissolved in the same solvent, dichloromethane. Using a confocal microscope, the amount of surface covered by the fouling polymers was analyzed for each of the coated surfaces, and the results were normalized against the surface coverage for non-coated, plasma-treated silicon surface (Figure 2.5).

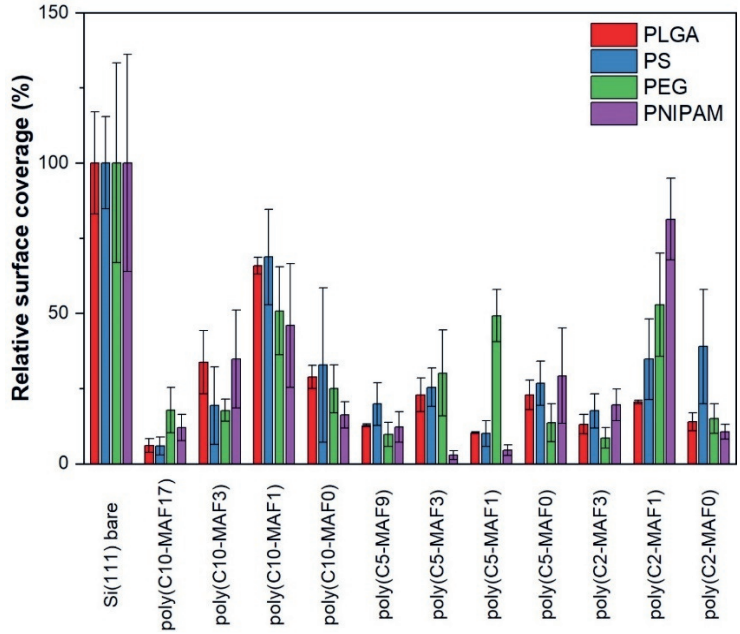

Figure 2.5. Relative surface coverage of fluorescently labelled polymers on 12 types of surfaces, after those surfaces were submerged for 15 min (or 60 min for PS) in a 1 mg/mL polymer solution.

For all coatings and all fouling agents, the degree of fouling was significantly lower than for the non-coated silicon surfaces. Although we observed differences between the four fouling polymers, no clear correlations between antifouling capability of the coatings and the degree of fluorination, the side chain length or the hydrophobicity of the fouling agent were observed.

The antifouling performance was most pronounced in the highly fluorinated polymer brushes poly(**C10-MAF17**), poly(**C5-MAF°**) and poly(**C2-MAF3**), where fouling of all polymers was reduced by at least 80%. Going to less fluorinated polymer brushes, a slight increase in the degree of fouling was observed. The non-fluorinated coatings showed a small reduction in fouling with respect to the single fluorinated ones. This trend is most pronounced in the C10 and the C2 series, and less clear in the C5 series. The observation is in line with the trends observed in the WCA of the coatings, but in contrast to the antifouling monolayers reported by Wang *et al.*,[28] who found that a single fluorine in a hexadecyl monolayer made the coating better antifouling than a non- or fully fluorinated hexadecyl-based monolayer. Wang *et al.* reasoned that a strong dipole interaction between surface and solvent prevents fouling agents from adhering to the surface, as there is only very limited enthalpy to gain by substituting solvent molecules with fouling particles. The DMF contact angle of their F1 coating was lower than those of F0 and F17, explaining why the F1 was best in antifouling.

As we are working in DCM instead of DMF, the interactions of our coatings with the solvent are not directly comparable to those observed by Wang *et al*. To quantify the amount of surface-solvent interaction for our polymer brushes, we determined the critical surface tension of our 11 polymer brushes (Table 2.2, and Supporting Information, section 2.4.3) as described in literature.[40] Using a range of solvents with varying surface tensions, the advancing contact angle θ was determined for each solvent on each coating. Cos θ was plotted against the surface tension, and the critical surface tension was determined by extrapolation to cos θ = 1. As the error margins of the contact angles were about 2–3°, we considered all critical surface tensions within 5 mN/m to be of similar value. This leads to five categories: ultra-low (< 10 mN/m), very low (around 10 mN/m), low (around 20 mN/m), medium (around 30 mN/m) and high (> 40 mN/m). When rearranging the antifouling results from Figure 2.5 in these groups and placing the coatings in ascending order of critical surface tension (Figure 2.6), the correlation between critical surface tension and antifouling capability is quite pronounced. The classification in different categories clearly reflects our previous observations: the fully fluorinated coatings show the best antifouling and have the lowest critical surface tension, while the singly

Table 2.2. Critical surface tensions of polymer brushes. Based on their critical surface tensions, the polymers were categorized in one of five groups (ranging from 'Ultra-low' to 'High'). See section 2.4.3 for full description of the determination of the critical surface tension.

Polymer brush	Critical surface tension (mN/m)	Group
Poly(C10-MAF17)	5	Ultra-low
Poly(C10-MAF3)	28	Medium
Poly(C10-MAF1)	32	Medium
Poly(C10-MAF0)	25	Low
Poly(C5-MAF°)	12	Very low
Poly(C5-MAF3)	22	Low
Poly(C5-MAF1)	32	Medium
Poly(C5-MAF0)	30	Medium
Poly(C2-MAF3)	19	Low
Poly(C2-MAF1)	42	High
Poly(C2-MAF0)	32	Medium

fluorinated coatings, showing the least antifouling capability, have the highest critical surface tension. These critical surface tensions also indicate when a coating is hydrophobic: we observed after polymerization that there were five hydrophobic coatings. These all have a critical surface tension of 25 mN/m or lower. All other coatings have a higher critical surface tension, and are not considered hydrophobic.

It is remarkable, and consistent with lower water contact angles (Table 2.1), that the singly fluorinated polymer brushes show the highest critical surface tension. This indicates the strongest surface-solvent interactions, which we attribute to the dipole moment of – at least somewhat – ordered CH_2F moieties. As the dipole moment of a CF_3 group is stronger than that of a CH_2F moiety, this same dipole moment of a CF_3 group is stronger than that of a CH_2F moiety, this same reasoning could hold for the CF_3-functionalized chains. However, both monolayers and polymer brushes show a weaker effect for the CF_3 than for the CH_2F chains, indicating that another factor needs to be considered as well: the radius of the polar group. Since fluorine is larger than hydrogen, a CF_3 group is sterically more demanding than a CH_2F or a CH_3 group. As a result, the packing

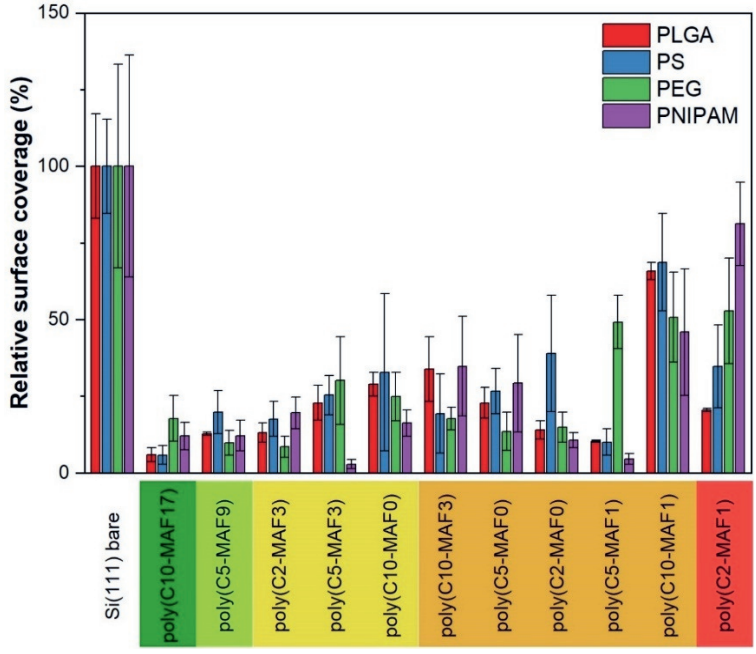

Figure 2.6: Relative surface coverage of fluorescently labelled polymers on 12 types of surfaces, after those surfaces were submerged in a fouling solution. The surfaces are placed in order of increasing critical surface tension, as described in Table 2.2.

of parallelly oriented triply fluorinated chains cannot be as tight as the packing of singly or non-fluorinated chains, which likely disrupts the overall organization of the terminal moieties. This counteracts the effect of the dipole moment.

The fouling observed on singly fluorinated polymer brushes is consistently higher than on the corresponding triply fluorinated polymer brushes. Apparently, the higher critical surface tension is dominant here, even though there are some relatively small differences between the various brushes, which might reflect differences in organization, in water content, and packing density. This observation contrasts findings for monolayers,[28] in which singly fluorinated coatings were consistently best in antifouling but did not show an unusual critical surface tension.[40] We attribute this to the difference in solvents: the antifouling measurements on the polymer brushes were performed in DCM, while the monolayer experiments took place in DMF. As DMF is intrinsically hygroscopic, it will likely have contracted water in the open-to-air experiments,

which can lead to C–F···H–O–H···O=C hydrogen-bonded complexes at the interface. In the DCM experiments, these hydrogen-bonded complexes are less likely to be prominent.

The interplay of polarity and steric irregularity thus appears to be crucial to both the stability and antifouling abilities of a polymer brush. Where a coating with long, regularly packed side chains such as **C10-MAF0** is exceptionally stable in acidic conditions, its lack of fluorine atoms makes for an antifouling coating of intermediate performance. Substitution with one fluorine atom at the end of each side chain (**C10-MAF1**) actually decreases its performance, both in stability and in antifouling capability. In contrast, replacement of 17 hydrogen atoms with 17 fluorine atoms (**C10-MAF17**) makes for an excellent antifouling coating, having the lowest critical surface tension of all 11 investigated coatings. On the other hand, **C10-MAF17** is the most heavily fluorinated of the C10 series, and from environmental perspective there is a clear preference for **C10-MAF0**. Where in monolayer studies, conducted in DMF, a low amount of fluorine was most effective, in polymer brushes the motto seems to be 'all or nothing'. Shortening the side chains to five or two carbons does not influence this trend, yet as a result of the shorter chains, alignment of the chains is less feasible, resulting in lower contact angles and higher critical surface tensions. Depending on the application, one may hence consider **C10-MAF0** (for stability and environmental impact) or **C10-MAF17** (for highest contact angle and best antifouling performance) as the most suitable polymer brush.

2.3 Conclusions

Studies of 11 polymer brushes with a varying fluorine content showed that the self-healing characteristics that are often observed for fluorinated materials actually do not require fluorine atoms at all. Excellent self-healing was also observed for fluorine-free methacrylate polymer brushes. We attribute this initially surprising finding mechanistically to the formation of hydrophilic carboxylic acid moieties upon damage, which can be stabilized in the 'bulk' of the brush and which shy away from the polymer-air interface. The investigated brushes also display antifouling properties with respect to both hydrophilic and hydrophobic polymers, which hinges on their critical surface tension: the most fluorinated polymer brushes having the lowest critical surface tension and the best polymer resistance. The singly fluorinated polymer brushes showed the

highest critical surface tension and performed least in the antifouling tests. Finally, we discovered that long alkyl side chains were best for the stability under acid conditions, and this stability reduces gradually with an increasing fluorine content. The unique behavior of poly(**C10-MAF0**) demands more exploration and will be further discussed in next chapter.

2.4 Supporting Information

This is a selection of the most relevant supporting information. The full supporting information is available online at: https://doi.org/10.1016/j.apsusc.2021.152264.

2.4.1 Materials

All chemicals were used as received, unless specified otherwise. Details on suppliers are provided in the online Supporting Information, section S1.

Decyl methacrylate (**C10-MAF0**), 10-fluorodecyl methacrylate (**C10-MAF1**), 5-fluoropentyl methacrylate (**C5-MAF1**), 1H,1H-perfluoropentyl methacrylate (**C5-MAF°**), 10,10,10-trifluorodecyl methacrylate (**C10-MAF3**), 5,5,5-trifluoropentyl methacrylate (**C5-MAF3**), poly(styrene-co-fluorescein O-methacrylate) and poly(N-isopropylacrylamide-co-fluorescein O-methacrylate) were synthesized in our lab (sections 2.4.4 to 2.4.11, see online Supporting Information for spectra).

2.4.2 Analytical procedures

X-ray Photoelectron Spectroscopy (XPS)

XPS measurements were performed using a JPS-9200 photoelectron spectrometer (JEOL Ltd., Japan), using a focused monochromated Al Kα Xray source (spot size of 300 µm) with radiation at 12 kV and 20 mA and an analyzer energy pass of 10 eV. XPS wide-scan and narrow-scan spectra were obtained under vacuum conditions (base pressure 3×10^{-7} Pa). All narrow-range spectra were corrected with a linear background before fitting. The spectra were fitted with symmetrical Gaussian/Lorentzian [GL(30)] line shapes using CasaXPS, and referenced to the C 1s peak attributed to C−C atoms at 285.0 eV.

Infrared (IR)

IR analyses were performed on a Bruker Tensor 27 spectrometer with a platinum attenuated total reflection accessory.

Static Water Contact Angle Measurements (CA)

The wettability of the modified surfaces was determined by automated static water contact angle measurements with the use of a Kruss DSA 100 goniometer. The volume of a drop of deionized water was 3 µL, per measurement two droplets were taken into account. Contact angles from sessile drops measured by the tangent method were estimated using a standard error propagation technique involving partial derivatives. Advancing contact angles were determined from a growing droplet of solvent, increasing to 20 µL with steps of 0.25 µL, taking one step per second. After each step, a photo was taken, from which the highest contact angle was selected before the droplet propagated outward.

Spectroscopic Ellipsometry

The dry thickness of the brushes was measured using an Accurion Nanofilm EP4 imaging ellipsometer. The ellipsometric data were acquired in air at RT using light in the wavelength range of λ = 400.6−761.3 nm at an angle of incidence of 50°. The data were fitted with EP4 software using a multilayer model. The refractive indices for non-fluorinated, monofluorinated, trifluorinated and perfluorinated polymer brushes were determined at n = 1.470, n = 1.455, n = 1.410 and n = 1.368, respectively. The refractive index for TFEMA is n = 1.400.

Fluorescent microscopy

The degree of fouling was determined through imaging with a Nikon C1 confocal microscope (488 nm CW excitation). Each surface was imaged on five spots of 400 x 400 µm, and at each spot 16 images were taken and overlayed. The resulting images were converted to txt-files using free software ImageJ, after which a threshold of 288 was applied. All pixels with an intensity above this threshold were counted as fouled, all pixels below this intensity were considered non-fouled. The degree of fouling was determined by calculating the percentage of fouled pixels, and this was normalized against the degree of fouling of non-coated silicon surfaces.

Nuclear Magnetic Resonance (NMR)

All NMR were recorded on a Bruker AVANCE III NMR. The ^{1}H NMR and COSY (correlated spectroscopy) spectra were recorded at 400 MHz, the ^{13}C NMR spectra at 101 MHz, the ^{19}F NMR spectrum at 377 MHz. For the ^{1}H–^{13}C HSQC

(heteronuclear single quantum correlation) settings of 400 and 101 MHz were used, and for the $^{1}H–^{19}F$ HMBC (heteronuclear multiple bond correlation) settings of 400 and 377 MHz were used, respectively. Chemical shifts are reported in parts per million (ppm).

Atomic Force Microscopy (AFM)

Atomic Force Microscopy was performed using an Asylum MFP-3D Origin AFM (Oxford Instruments, United Kingdom). The surfaces were gently scratched with a sterile needle to partly remove the polymer brush and expose the silicon surface, after which triplicate dry measurements were done. The instrument was operated in tapping mode and equipped with a silicon cantilever (SCANASYST AIR, k = 0.4 N/m) with a nominal tip radius of about 2 nm.

Swelling measurements were performed by equipping the AFM with a BioHeater Closed Fluid Cell Accessory and Environmental Controller. Measurements were performed in ethanol at room temperature, using a cantilever from the same batch as in the dry measurements, and triplicated to measure the average thickness of the polymeric film. Before measurements, 60 min was taken to obtain AFM thermal stability. Gwyddion software was used to process and analyze the AFM topography images.[19]

Density Functional Theory (DFT)

Density Functional Theory calculations were performed with Gaussian 16,[41] using WB97XD functional and 6-311G(2p,2d) basis set. No solvents or temperatures were taken into account.

2.4.3 Surface chemistry methods

Surface initiation

Samples of 1×1 cm Si(111) were cut from a wafer with a diamond pen. Twelve surfaces were sonicated for 5 min in hexane, ethanol and DCM consecutively, and then blown dry. They were placed face-up in a glass petridish, and exposed to an oxygen plasma for 5 min in a plasma cleaner (100 W; 5 mbar O_2; Diener electronic GmbH, Germany). Next, 10 µL (2-bromo-2-methyl)-isopropionate-decyl trichlorosilane in 4.0 mL dry toluene were added to the petridish, submerging the surfaces. The petridish was covered and left overnight. The

following day, the surfaces were rinsed with fresh toluene, blown dry, and stored under nitrogen.

ATRP surface polymerization

Inside an argon glovebox, 35 mg CuBr and 175 mg 4,4-dinonyl-bipyridine were weighed in a 50 mL Schlenk tube with cap, surface holder and stirring bar (see Figure 2.7). The surfaces were placed face down in the surface holder of the Schlenk tube. 5.0 mL of monomer and 15.0 mL of solvent were added, and the reaction mixture was stirred for a few hours at 60 °C. The vessel was cooled to room temperature and removed from the glovebox. The reaction mixture was removed with a glass pipette and purified for re-use by filtering over a 3 cm silica gel column with heptane as eluent. Up to 80% of the monomer was retained in this way. The surfaces were transferred to a beaker and sonicated in fresh solvent for 5 min, then sonicated in DCM for 5 min and blown dry. Overnight curing was done in the vacuum oven at 50 °C and 100 mbar. After cooling to room temperature, the surfaces were analyzed by contact angle, ellipsometry, AFM and XPS.

Figure 2.7: Picture of the Schlenk tube as used for all polymerization reactions.

Antifouling measurements

The antifouling capabilities of the coatings were measured with a Nikon confocal fluorescence microscope. The polymers that were used for fouling are poly(lactide-co-glycolide)-fluorescein, poly(styrene-co-fluorescein O-methacrylate), poly(ethylene glycol)-fluorescein, and poly(*N*-isopropylacrylamide-co-fluorescein O-methacrylate). To foul the surfaces, they were placed face up in a fouling solution of 1 mg/mL polymer in dichloromethane. After 15 min (for polystyrene 60 min), the surfaces were taken from the fouling solution, rinsed with fresh DCM and blown dry. Confocal fluorescence microscopy pictures were taken the same day, on five spots per surface. For each fouling agent and each polymer brush coating, at least two surfaces were investigated. For each polymer brush and non-coated silicon, also two blanks were measured by placement in a clean DCM solution for 15 min, followed by fluorescence microscopic analysis. These showed 0% fouling in all cases.

Healing measurements

The healing capabilities of the coatings were measured by their static water contact angles. The surfaces were placed in a petridish with a 1 mM HCl solution in MilliQ water (pH 3.0). After exactly 24 hours, the surfaces were rinsed with fresh MilliQ water and blown dry, after which the static water contact angles were measured. Next, the surfaces were placed in another petridish and placed in the oven at 120 °C for exactly 2 h. The petridish was then taken from the oven and left to cool to room temperature, and the contact angles were measured again. This process was repeated ten times. At various points in these damage-repair cycles, but always immediately before a contact angle measurement, the thickness and roughness of some surfaces were measured by ellipsometry and AFM respectively. For each coating, at least five surfaces were tested. To ensure enough thickness for ten repetitions, each polymer brush was at least 60 nm thick, except poly(**C2-MAF1**), which could not be grown higher than 25 nm. To further ensure minimal errors from deviations in acidity, oven temperature or machine settings, the damage-repair cycles of these five surfaces were not synchronized. For a single coating for example, surface A would be in the acidic solution for cycle 8, while surface B would be in the same petridish but for cycle 7, surface C for cycle 6, surface D for cycle 5 and surface E for cycle 4.

Critical surface tension determination

The minimal surface tension of polymer brush-coated surfaces was determined by measurement of the advancing contact angles of a range of solvents, varying in surface tension. For each of the polymer brush coatings, the cosines of the advancing contact angles were plotted against the surface tensions of the solvents. A trendline was added, and the intersection of the trendline with the line cos(θ) = 1 was determined. This surface tension is defined as the minimal surface tension: all solvents with a lower surface tension will have full wettability on the coating.

Contact angles below 20° are very difficult to measure, because the solvent is rapidly wetting the entire surface. As a result, the data points with cos(θ) > 0.9 have a larger inaccuracy than the rest. Next to this, the cosine graph is very steep around cos(θ) = 0. A measurement error of a few degrees therefore has a large impact on the position of its cosine result. Because of this, the root-mean-square value of the trendline is not always as high as desired. The calculated minimal surface tensions (Table 2.3) must therefore be seen as a good estimate, but not an exact determination.

Table 2.3 Minimal surface tension determination for all polymer brushes.

Coating	Trendline	Regression coefficient of trendline, R^2	Minimal surface tension (mN/m)
poly(C10-MAF17)	$y = -0.0395x + 1.2028$	0.9816	5
poly(C10-MAF3)	$y = -0.0319x + 1.8943$	0.9789	28
poly(C10-MAF1)	$y = -0.0311x + 2.0105$	0.9133	32
poly(C10-MAF0)	$y = -0.0315x + 1.7847$	0.9747	25
poly(C5-MAF°)	$y = -0.0478x + 1.5805$	0.9001	12
poly(C5-MAF3)	$y = -0.0234x + 1.5155$	0.9812	22
poly(C5-MAF1)	$y = -0.0241x + 1.7821$	0.9083	32
poly(C5-MAF0)	$y = -0.0286x + 1.8607$	0.9777	30
poly(C2-MAF3)	$y = -0.0240x + 1.4470$	0.9769	19
poly(C2-MAF1)	$y = -0.0336x + 2.4136$	0.9959	42
poly(C2-MAF0)	$y = -0.0235x + 1.7438$	0.9291	32

Example minimal surface tension determination

Advancing contact angle analyses were performed with *n*-hexane (surface tension = 18.43 mN/m), n-heptane (20.14 mN/m), isopropanol (23.00 mN/m), acetone (25.20 mN/m), toluene (28.40 mN/m), aniline (43.40 mN/m), glycerol (64.00 mN/m) and deionised water (72.80 mN/m). The cosine of the resulting angles was calculated, and plotted against the surface tensions of the solvents, from which the trendline was determined: $y = -0.024x + 1.447$. Where $y = 1$, $x = 18.6$. The minimal surface tension of **C2-MAF3** is therefore about 19 mN/m.

2.4.4 Synthesis of decyl methacrylate

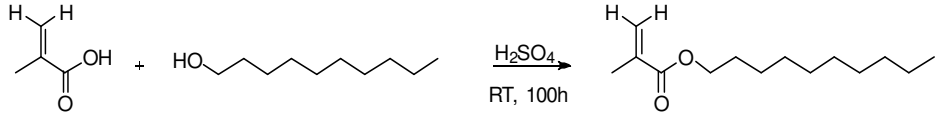

Scheme 2.3: Synthesis of decyl methacrylate (**C10-MAF0**).

Methacrylic acid (66.3 mL, 67.7 g, 786 mmol), 1-decanol (50.0 mL, 41.5 g, 262 mmol) and sulphuric acid (12.9 g, 131 mmol) were combined in a round bottom flask and stirred for seven days at room temperature. 100 mL diethyl ether was added, and an extraction was performed three times with a half-saturated sodium bicarbonate solution. The water layers were not washed with ether to obtain a higher yield, since that would also reintroduce some of the methacrylic acid. The organic layer was dried with sodium sulfate and the solvent was evaporated. The remaining methacrylic acid was removed by column chromatography, using 1% ethyl acetate in heptane. Pure decyl methacrylate was isolated (44.5 g, 197 mmol, 75% yield).

^{1}H NMR (400 MHz, $CDCl_3$): δ 6.05 (d, J = 2.2 Hz, 1H), 5.48 (q, J = 1.9 Hz, 1H), 4.09 (t, J = 6.8 Hz, 2H), 1.95 – 1.85 (m, 3H), 1.62 (p, J = 6.9 Hz, 2H), 1.41 – 1.13 (m, 15H), 0.84 (t, J = 6.7 Hz, 3H). ^{13}C NMR (101 MHz, $CDCl_3$): δ 167.29 (A), 136.52 (B), 124.86 (C), 64.68 (D), 31.84 (E), 29.47 (F, G), 29.24 (H), 29.20 (I), 28.58 (J), 25.93 (K), 22.60 (L), 18.17 (M), 13.96 (N). ESI$^+$ (MeOH): calc.: m/z = 227.20056 $[M+H]^+$, m/z = 249.18250 $[M+Na]^+$; det.: m/z = 227.20041 $[M+H]^+$, m/z = 249.18255 $[M+Na]^+$. ESI$^-$ (MeOH): calc.: m/z = 225.18491 $[M-H]^-$; det.: m/z = 225.18536 $[M-H]^-$.

2.4.5 Synthesis of 5,5,5-trifluoropentyl methacrylate

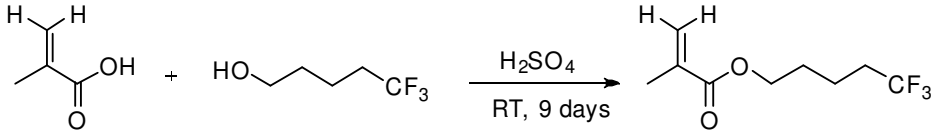

Scheme 2.4: Synthesis of 5,5,5-trifluoropentyl methacrylate (**C5-MAF3**).

5,5,5-Trifluoro-1-pentanol (9.95 g, 70 mmol), methacrylic acid (18.08 g, 210 mmol) and sulphuric acid (3.43 g, 3.5 mmol) were combined in a round bottom flask and stirred for nine days at room temperature until full conversion was reached. 80 mL diethyl ether was added, and the mix was extracted with a half-saturated sodium bicarbonate solution (4× 80 mL). In the fourth extraction cycle, no more carbon dioxide bubbles were visible, indicating that all acid has been neutralized. The water layers were not washed with ether to obtain a higher yield, since that would also reintroduce some of the methacrylic acid. The organic layer was dried with sodium sulfate and the ether was evaporated, yielding 5,5,5-trifluoropentyl methacrylate (12.4 g, 59.0 mmol, 84% yield).

^{1}H NMR (400 MHz, $CDCl_3$) δ 6.07 – 6.02 (m, 1H), 5.51 (q, J = 1.7 Hz, 1H), 4.12 (t, J = 6.3 Hz, 2H), 2.16 – 1.98 (m, 2H), 1.94 – 1.83 (m, 3H), 1.71 (dt, J = 12.7, 6.0 Hz, 2H), 1.67 – 1.56 (m, 2H). ^{13}C NMR (101 MHz, $CDCl_3$) δ 167.16 (A), 136.26 (B), 126.98 (q, J = 276.2 Hz, C), 125.21(D), 63.68 (E), 33.19 (q, J = 28.6 Hz, F), 27.59 (G), 18.62 (q, J = 3.0 Hz, H), 18.01 (I). ESI$^+$ (MeOH): calc.: m/z = 211.09404 $[M+H]^+$, m/z = 233.07599 $[M+Na]^+$; det.: m/z = 211.09391 $[M+H]^+$, m/z = 233.07589 $[M+Na]^+$.

2.4.6 Synthesis of 1H,1H-perfluoropentyl methacrylate

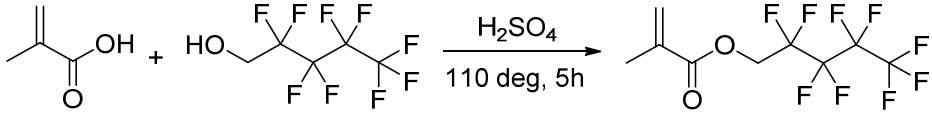

Scheme 2.5: Synthesis of decyl methacrylate (**C5-MAF°**).

1H,1H-Nonafluoro-1-pentanol (10.0 g, 40 mmol), methacrylic acid (10.32 g, 120 mmol) and sulphuric acid (1.96 g, 20 mmol) were combined in a round-bottom flask and stirred at 110 °C for 5 h, when 80% conversion was reached (measured by NMR). After cooling down, 25 mL diethyl ether was added, and the mix was

extracted with a half-saturated sodium bicarbonate solution (5x 40 mL). In the fifth extraction cycle, no more carbon dioxide bubbles were visible, indicating that all acid has been neutralized. The water layers were not washed with ether to obtain a higher yield, since that would also reintroduce some of the methacrylic acid. The organic layer was dried with sodium sulfate and the ether was evaporated. Since full conversion was not reached, some 1H,1H-nonafluoro-1-pentanol remained in the crude product mixture (containing 8.2 g, 25.7 mmol 1H,1H-perfluoropentyl methacrylate (64% crude yield) and 1.0 g, 3.9 mmol 1H,1H-nonafluoro-1-pentanol). Column chromatography was used to remove this, but as 1H,1H-perfluoropentyl methacrylate polymerized on the column, very little pure product was isolated (450 mg, 1.4 mmol, 7% yield). For polymerization purposes, the impure crude product was used, containing 13% 1H,1H-nonafluoro-1-pentanol. Since 1H,1H-nonafluoro-1-pentanol cannot be polymerized via ATRP, we expected that this would not be incorporated into the polymer brush, as confirmed by XPS (section S14, Figure S11).

^{1}H NMR (400 MHz, $CDCl_3$) δ 6.19 (q, J = 1.3 Hz, 1H), 5.66 (dq, J = 3.1, 1.5 Hz, 1H), 4.63 (tt, J = 13.4, 1.6 Hz, 2H), 1.95 (t, J = 2.4 Hz, 2H). ^{13}C NMR (101 MHz, $CDCl_3$) δ 165.39 (d, J = 2.5 Hz, A), 134.77 (B), 127.34 (d, J = 7.0 Hz, C), 117.25 (qt, J = 287.8, 33.1 Hz, G), 115.21 (tt, J = 257.7, 31.3 Hz, F), 111.06 (t quint, J = 266.7, 32.0 Hz, H), 108.54 (m, I), 59.69 (t, J = 27.7 Hz, D), 17.66 (d, J = 5.7 Hz, E). ^{19}F NMR (377 MHz, $CDCl_3$) δ –81.61 (tt, J = 9.8, 2.9 Hz, A), –120.10 (ddtd, J = 15.9, 13.2, 10.5, 2.5 Hz, B), –124.72 (dttt, J = 13.2, 8.3, 7.0, 3.4, 1.7 Hz, C), –126.83 (ddq, J = 16.0, 10.0, 3.4 Hz, D). ESI$^+$ (MeOH): calc.: m/z = 341.01945 $[M+Na]^+$; det.: m/z = 341.01890 $[M+Na]^+$.

2.4.7 Synthesis of 10,10,10-trifluorodecyl methacrylate

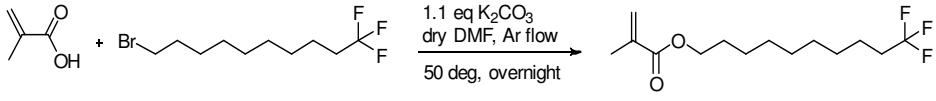

Scheme 2.6: Synthesis of decyl methacrylate (**C10-MAF3**).

Under nitrogen atmosphere, potassium carbonate (3.86 g, 28 mmol) was dissolved in DMF (90 mL) and methacrylic acid (2.18 g, 0.25 mmol) was added. Then 10-bromo-1,1,1-trifluorodecane (6.27 g, 23 mmol) was added dropwise and the reaction was stirred at 50 °C overnight. Diethyl ether (90 mL) was added

and the solution was extracted three times with brine (3× 90 mL) and once with 5% lithium chloride in water. The water layers were not washed with ether to obtain a higher yield, since that would also reintroduce some of the methacrylic acid. The organic layer was dried with sodium sulfate and the solvents were evaporated, to isolate 10,10,10-trifluorodecyl methacrylate (5.2 g, 15.3 mmol, 67% yield).

^{1}H NMR (400 MHz, $CDCl_3$) δ 6.09 (d, J = 1.8 Hz, 1H), 5.54 (t, J = 1.7 Hz, 1H), 4.14 (t, J = 6.7 Hz, 2H), 2.06 (tdd, J = 13.7, 7.9, 4.4 Hz, 2H), 1.94 (t, J = 1.3 Hz, 3H), 1.73 – 1.57 (m, 2H), 1.57 – 1.50 (m, 2H), 1.44 – 1.27 (m, 12H). ^{13}C NMR (101 MHz, $CDCl_3$) δ 167.54 (A), 136.56(B), 127.27 (q, J = 276.3 Hz, C), 125.10 (D), 64.74 (E), 33.70 (q, J = 28.3 Hz, F), 29.19 (H), 29.11 (I), 29.07 (J), 28.64 (K), 28.57 (L), 25.91 (M), 21.82 (q, J = 2.9 Hz, G), 18.29 (N). ESI$^+$ (MeOH): calc.: m/z = 281.17229 $[M+H]^+$, m/z = 303.15424 $[M+Na]^+$; det.: m/z = 281.17203 $[M+H]^+$, m/z = 303.15423 $[M+Na]^+$.

2.4.8 Synthesis of 5-fluoropentyl methacrylate

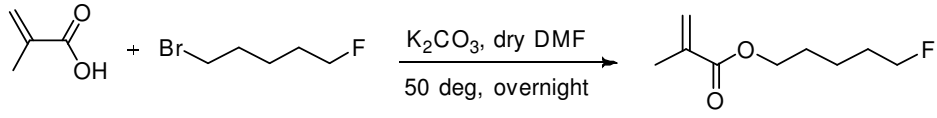

Scheme 2.7: Synthesis of 5-fluoropentyl methacrylate (**C5-MAF1**).

Under nitrogen atmosphere, potassium carbonate (3.87 g, 28 mmol) was dissolved in DMF (90 mL) and methacrylic acid (2.15 g, 0.25 mmol) was added. Then 1-bromo-5-fluoropentane (3.89 g, 23 mmol) was added dropwise and the reaction was stirred at 50 °C overnight. Diethyl ether (90 mL) was added and the solution was extracted three times with brine (3× 90 mL) and twice with 5% lithium chloride in water. The organic layer was dried with sodium sulfate and the solvents were evaporated, to isolate 5-fluoropentyl methacrylate (2.90 g, 16.6 mmol, 72% yield). Trace amounts of 1-bromo-5-fluoropentane were visible with NMR. As the desired product polymerizes on both silica and alumina, column chromatography could not be used to remove these traces. Distillation was not possible for the same reason. Since 1-bromo-5-fluoropentane cannot perform ATRP, we decided to use the methacrylate monomer including its impurity. Analysis of the polymer brush (see later in this supporting information) showed no irregularities, thereby validating this procedure.

^{1}H NMR (400 MHz, $CDCl_3$) 6.06 (d, J = 1.8 Hz, 1H), 5.51 (q, J = 1.6 Hz, 1H), 4.41 (dt, J = 47.3, 6.0 Hz, 2H), 4.12 (t, J = 6.6 Hz, 2H), 1.90 (d, J = 1.8 Hz, 3H), 1.69 (tdd, J = 15.5, 8.9, 6.1 Hz, 4H), 1.48 (qd, J = 10.0, 9.2, 6.0 Hz, 2H). ^{13}C NMR (101 MHz, $CDCl_3$) δ 167.36 (A), 136.42 (B), 125.16 (C), 83.72 (d, J = 164.7 Hz, D), 64.35 (E), 29.97 (d, J = 19.6 Hz ,F), 28.22 (G), 21.83 (d, J = 5.3 Hz, H), 18.21 (I). ESI$^+$ (MeOH): calc.: m/z = 175.11288 $[M+H]^+$, m/z = 197.09483 $[M+Na]^+$; det.: m/z = 175.11262 $[M+H]^+$, m/z = 197.09483 $[M+Na]^+$.

2.4.9 Synthesis of 10-fluorodecan-1-ol

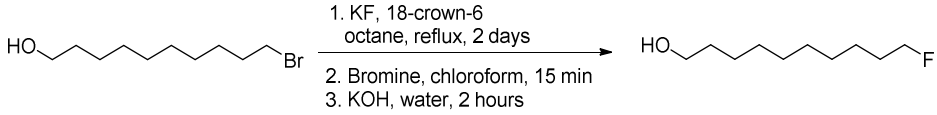

Scheme 2.8: Synthesis of 10-fluorodecan-1-ol.

In a single-neck round-bottom flask, 10-bromodecanol (14.23 g, 60 mmol), anhydrous potassium fluoride (8.70 g, 150 mmol), 18-crown-6 (15.86 g, 60 mmol) and n-octane (60 mL) were combined and refluxed for two days (145 °C). The reaction was quenched with water and extracted with ether. The organic layers were combined, dried with magnesium sulfate and the solvents were evaporated. The crude product was measured with NMR, it showed around 60% crude yield of 10-fluorodecanol and 10% decenol contamination. In order to be able to remove the decenol, its boiling point needed to be increased. This was done by bromination: a stoichiometric amount of bromine (520 µL, 12 mmol) was added dropwise to the mixture of 10-fluoro-1-decanol and decenol. After stirring for 15 min, a solution of potassium hydroxide in water (673 mg, 12 mmol in 7.2 mL) was added and stirred for 2 h. The layers were separated, and the organic layer was washed with water. The solvent was evaporated and then Kugelrohr distillation was performed to obtain pure 10-fluorodecan-1-ol (5.4 g, 30.6 mmol, 51% yield).

^{1}H NMR (400 MHz, $CDCl_3$) δ 4.44 (dt, J = 47.3, 6.2 Hz, 1H), 3.65 (t, J = 6.6 Hz, 1H), 1.69 (ddt, J = 24.9, 8.2, 6.2 Hz, 1H), 1.62 – 1.51 (m, 1H), 1.44 – 1.07 (m, 8H). ^{13}C NMR (101 MHz, $CDCl_3$) δ 84.17 (d, J = 164.3 Hz, A), 33.96 (B), 32.82 (C), 30.40 (d, J = 19.4 Hz, D), 29.38 (E), 29.31 (F), 29.18 (G), 28.72 (H), 28.14 (I), 25.13 (d, J = 5.5 Hz, J).

2.4.10 Synthesis of 10-fluorodecyl methacrylate

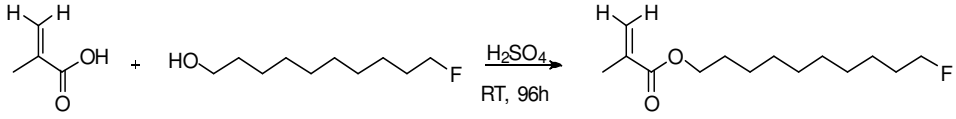

Scheme 2.9: Synthesis of 10-fluorodecyl methacrylate (**C10-MAF1**).

10-Fluorodecyl methacrylate was obtained by performing the synthesis of decyl methacrylate, but using 10-fluoro-1-decanol (5.4 g, 30.6 mmol), methacrylic acid (7.9 g, 91.8 mmol) and sulphuric acid (1.51 g, 15.3 mmol). After 96 h reaction, 86% conversion is reached. Upon purification, 4.6 g (18.8 mmol) 10-fluorodecyl methacrylate was isolated (62% yield).

^{1}H NMR (400 MHz, $CDCl_3$) δ 6.10 (t, *J* = 1.3 Hz, 1H), 5.55 (p, *J* = 1.7 Hz, 1H), 4.44 (dt, *J* = 47.4, 6.2 Hz, 2H), 4.14 (t, *J* = 6.7 Hz, 2H), 1.95 (t, *J* = 1.3 Hz, 3H), 1.69 (ddt, *J* = 19.1, 8.2, 6.2 Hz, 4H), 1.49 – 1.21 (m, 13H). ^{13}C NMR (101 MHz, $CDCl_3$) δ 167.57 (A), 136.58 (B), 125.12 (C), 84.22 (d, J = 164.0 Hz, D), 64.81 (E), 30.40 (d, J = 19.4 Hz, F), 29.39 (d, J = 1.6 Hz, 2C, G), 29.19 (2C, H), 28.60 (I), 25.96 (J), 25.13 (d, J = 5.5 Hz, K), 18.32 (L). ESI$^+$ (MeOH): calc.: m/z = 245.19113 $[M+H]^+$, m/z = 267.17292 $[M+Na]^+$; det.: m/z = 245.19097 $[M+H]^+$, m/z = 267.17292 $[M+Na]^+$.

2.4.11 Grafting density determination

The grafting density of poly(**C2-MAF0**) and poly(**C5-MAF3**) was investigated with AFM. Two coated surfaces were scratched with a surgical needle, after which AFM images were recorded on three places along the scratches (Figure 2.8 top left). The height difference between the scratch and the coating is the dry thickness of the polymer brush (Figure 2.8 bottom left).

Next, the surfaces were measured in a fluid cell filled with ethanol. After submersion, the coatings were left to equilibrate for an hour, after which AFM images were recorded on three places along the scratches (Figure 2.8 top right). The height difference between the scratch and the coating is the wet thickness of the polymer brush (Figure 2.8 bottom right). The swelling ratio was determined by dividing the average wet thickness by the average dry thickness. For poly(**C2-MAF0**), the swelling ratio is 1.33, for poly(**C5-MAF3**), the swelling ratio is 1.07.

To calculate the molecular weight of a polymer brush, a simple DFT calculation was used. We modelled an ethyl methacrylate dimer, placing a tert-butyl group on each end to simulate the steric bulk of the rest of the polymer chain. The average length of a monomer in poly(**C2-MAF0**) was determined by averaging some distances in this optimized geometry (Figure 2.9).

Then, we assumed full stretching of the polymer brush in solvated state. The wet thickness was divided by the monomer length to obtain the number of monomers in a brush, from which the molecular weight of a polymer was calculated using the monomer weight. Following the method of Spencer and coworkers,[42] the grafting density of poly(**C2-MAF0**) was calculated to be 1.11 chains per nm^2.

We acknowledge that the assumption of full stretching in wet conditions results in an underestimation of the polymer chain length, as the chains are never fully stretched. As a consequence, the calculated grafting density is an overestimation.

For poly(**C5-MAF3**), the average dry thickness is 53 nm and the average wet thickness is 56 nm. This led us to believe that, although the ethanol contact angle for poly(**C5-MAF3**) is below 10°, no penetration of ethanol into the polymer took place. The polymer was therefore not swelling, and no reliable chain length calculation could be done.

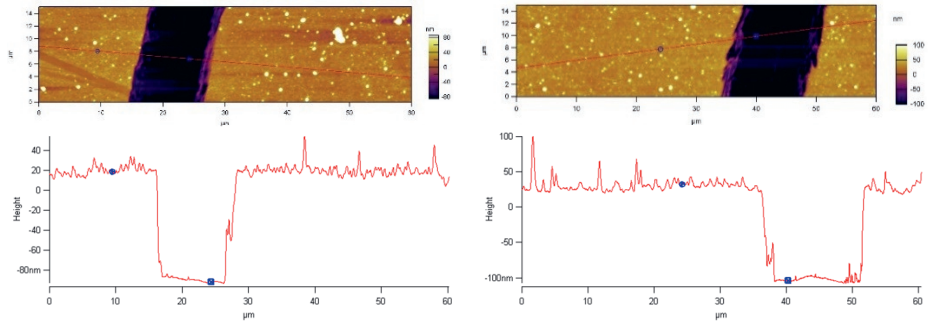

Figure 2.8: Tapping mode AFM images of poly(**C2-MAF0**) in dry (top left) and ethanol (top right) atmosphere, with corresponding height traces (bottom left and right).

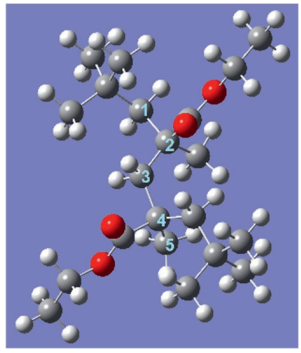

Distance between atoms:	Length (in Å)
C1 and C3	2.54697
C2 and C4	2.73642
C3 and C5	2.56673
C1 and C5	4.49342
Average monomer length	2.52421

Figure 2.9: Optimized geometry of ethyl methacrylate dimer with tert-butyl endcaps. Four carbon-carbon distances have been measured (right table) and the average has been determined. In the calculation of the average monomer length, the distance of C1 and C5 was halved, as this distance covers two monomers.

Example of calculation

For poly(**C2-MAF0**), a wet thickness of 144 nm was obtained. With an average monomer length of 0.25 nm, this implies 569 monomers per polymer. The molecular weight of ethyl methacrylate is 114.14 g/mol, leading to a polymer molecular weight of 64.9 kg/mol.

According to Spencer and coworkers, the surface coverage is equal to the dry thickness multiplied by the bulk density. For poly(**C2-MAF0**), the bulk density is 1.11 g/mL at 25 °C.[43] With an average dry thickness of 108 nm, the surface coverage is then 0.120 g/m^2. Multiplication by Avogadro's number and division by the polymer molecular weight results in a grafting density of 1.11 chains per nm^2.

References

(1) Scardino, A. J.; de Nys, R. *Biofouling* **2011**, *27* (1), 73–86.
(2) Yebra, D. M.; Kiil, S.; Dam-Johansen, K. *Prog. Org. Coat.* **2004**, *50* (2), 75–104..
(3) Gan, D.; Mueller, A.; Wooley, K. L. *J. of Pol. Sci. A: Pol. Chem.* **2003**, *41* (22), 3531–3540.
(4) Rana, D.; Matsuura, T. *Chem. Rev.* **2010**, *110* (4), 2448–2471.
(5) Blaszykowski, C.; Sheikh, S.; Thompson, M. *Chem. Soc. Rev.* **2012**, *41* (17), 5599–5612.
(6) Krishnan, S.; Weinman, C. J.; Ober, C. K. *J. Mater. Chem.* **2008**, *18* (1), 3405–3413.
(7) Molena, E.; Credi, C.; De Marco, C.; Levi, M.; Turri, S.; Simeone, G. *Appl. Surf. Sci.* **2014**, *309*, 160–167.
(8) Wang, Z.; Zuilhof, H. *Langmuir* **2016**, *32* (25), 6310–6318.
(9) Prime, K. L.; Whitesides, G. M. *Science* **1991**, *252* (5009), 1164–1167.
(10) Lange, S. C.; van Andel, E.; Smulders, M. M. J.; Zuilhof, H. *Langmuir* **2016**, *32* (40), 10199–10205.

(11) Wörz, A.; Berchtold, B.; Moosmann, K.; Prucker, O.; Rühe, J. *J. Mater. Chem.* **2012**, *22* (37), 19547–19561.
(12) Mcfadden, D. M.; Wu, R. S. H. EP1024149 B1, **2000**.
(13) Bockstahler, T. E.; Hunt, C. R. US3705190 A, **1972**.
(14) Kuschnerow, J. C.; Dorn, S.; Augustin, W.; Scholl, S. *Proceedings of International Conference on Heat Exchanger Fouling and Cleaning* **2013**, *1* (1), 150–157.
(15) Park, E. J.; Kim, D. H.; Lee, J. H.; Ha, S.; Song, C.; Kim, Y. D. *Mater. Res. Bul.* **2016**, *83*, 88–95.
(16) Https://Eur-Lex.Europa.Eu/Legal-Content/EN/TXT/PDF/?Uri=CELEX:32020R0784; accessed on 18 Feb. 21.
(17) Ensikat, H. J.; Ditsche-Kuru, P.; Neinhuis, C.; Barthlott, W. *Beilstein J. Nanotech.* **2011***, 2* (1), 152–161.
(18) He, Z. R.; Luo, S. T.; Liu, C. S.; Jie, X. H.; Lian, W. Q. *J. Mater. Res. Tech.* **2019**, *8* (5), 3878–3890.
(19) Al-Shimmery, A.; Mazinani, S.; Ji, J.; Chew, Y. M. J.; Mattia, D. *J. Membrane Sci.* **2019**, *574*, 76–85.
(20) Idumah, C. I.; Obele, C. M.; Emmanuel, E. O.; Hassan, A. *Surf. Interf.* **2020**, *21*, 100734.
(21) Wang, Z.; Scheres, L.; Xia, H.; Zuilhof, H. *Adv. Funct. Mater.* **2020**, 1908098.
(22) Li, Y.; Li, L.; Sun, J. *Angew. Chem. Int. Ed.* **2010**, *49* (35), 6129–6133.
(23) Wong, T.-S.; Kang, S. H.; Tang, S. K. Y.; Smythe, E. J.; Hatton, B. D.; Grinthal, A.; Aizenberg, J. *Nature* **2011**, *477* (7365), 443–447.
(24) Wang, Z.; Zuilhof, H. *J. Mater. Chem. A* **2016**, *4* (7), 2408–2412.
(25) Leng, C.; Huang, H.; Zhang, K.; Hung, H.; Xu, Y.; Li, Y.; Jiang, S.; Chen, Z. *Langmuir* **2018**, *34* (22), 6538–6545.
(26) Liu, Y.; Zhang, D.; Ren, B.; Gong, X.; Liu, A.; Chang, Y.; He, Y.; Zheng, J. *Langmuir* **2020**, *36* (11), 2757–2766.
(27) Dalvi, V. H.; Rossky, P. J. *Proc. Natl. Acad. Sci. U.S.A.* **2010**, *107* (31), 13603–13607.
(28) Wang, Z.; Pujari, S. P.; Van Lagen, B.; Smulders, M. M. J.; Zuilhof, H. *Adv. Mater. Int.* **2016**, *3* (4), 1–10.
(29) Wang, Z.; Zuilhof, H. *Langmuir* **2016**, *32* (26), 6571–6581.
(30) Kuzmyn, A. R.; Nguyen, A. T.; Zuilhof, H.; Baggerman, J. *Adv. Mater. Int.* **2019**, *6* (12), 1900351.
(31) Cumpson, P. J.; Zalm, P. C. *Surf. Interf. Anal.* **2000**, *29* (6), 403–406.
(32) Gerenser, L. J. *J. Adh. Sci. Tech.* **1993**, *7* (10), 1019–1040.
(33) Esteves, A. C. C.; Luo, Y.; Van De Put, M. W. P.; Carcouët, C. C. M.; De With, G. *Adv. Funct. Mater.* **2014**, *24* (7), 986–992.
(34) Xie, Y.; Liu, W.; Liang, L.; Liu, C.; He, S.; Zhang, F.; Shi, H.; Yang, M. *Col. Surf. A* **2019**, *579*, 123659.
(35) Brady, G. W. *Acc. Chem. Res*. **1974**, *7* (6), 174–180.
(36) Brady, G. W. *J. Chem. Phys.* **1974**, *60* (9), 3458–3465.
(37) Brady, G. W. *J. Chem. Phys.* **1973**, *58* (9), 3542–3546.
(38) Kuzmyn, A. R.; Nguyen, A. T.; Teunissen, L. W.; Zuilhof, H.; Baggerman, J. *Langmuir* **2020**, *36* (16), 4439–4446.
(39) Li, M.; De Priyadarsi; Gondi, S. R.; Sumerlin, B. S. *Macromol. Rapid Comm.* **2008**, *29* (12–13), 1172–1176.
(40) Pujari, S. P.; Spruijt, E.; Cohen Stuart, M. A.; Van Rijn, C. J. M.; Paulusse, J. M. J.; Zuilhof, H. *Langmuir* **2012**, *28* (51), 17690–17700.
(41) M. J. Frisch, G. W. Trucks, H. B. Schlegel, G. E. Scuseria, M. A. Robb, J. R. Cheeseman, G. Scalmani, V. Barone, G. A. Petersson, H. Nakatsuji, X. Li, M. Caricato, A. V. Marenich, J.

Bloino, B. G. Janesko, R. Gomperts, B. Mennucci, H. P. Hratchian, J. V. Ortiz, A. F. Izmaylov, J. L. Sonnenberg, D. Williams-Young, F. Ding, F. Lipparini, F. Egidi, J. Goings, B. Peng, A. Petrone, T. Henderson, D. Ranasinghe, V. G. Zakrzewski, J. Gao, N. Rega, G. Zheng, W. Liang, M. Hada, M. Ehara, K. Toyota, R. Fukuda, J. Hasegawa, M. Ishida, T. Nakajima, Y. Honda, O. Kitao, H. Nakai, T. Vreven, K. Throssell, J. A. Montgomery, Jr., J. E. Peralta, F. Ogliaro, M. J. Bearpark, J. J. Heyd, E. N. Brothers, K. N. Kudin, V. N. Staroverov, T. A. Keith, R. Kobayashi, J. Normand, K. Raghavachari, A. P. Rendell, J. C. Burant, S. S. Iyengar, J. Tomasi, M. Cossi, J. M. Millam, M. Klene, C. Adamo, R. Cammi, J. W. Ochterski, R. L. Martin, K. Morokuma, O. Farkas, J. B. Foresman, and D. J. Fox, *Gaussian 16, Revision B.01*, Wallingford, CT, **2016**.

(42) Mathis, C. H.; Simič, R.; Kang, C.; Ramakrishna, S. N.; Isa, L.; Spencer, N. D. *Polymer.* **2019**, *169*, 115–123.

(43) https://www.sigmaaldrich.com/NL/en/product/aldrich/182087; accessed on 9 Dec. 21.

Chapter 3
Self-Healing Fluorine-Free Hydrophobic Polymer Brushes

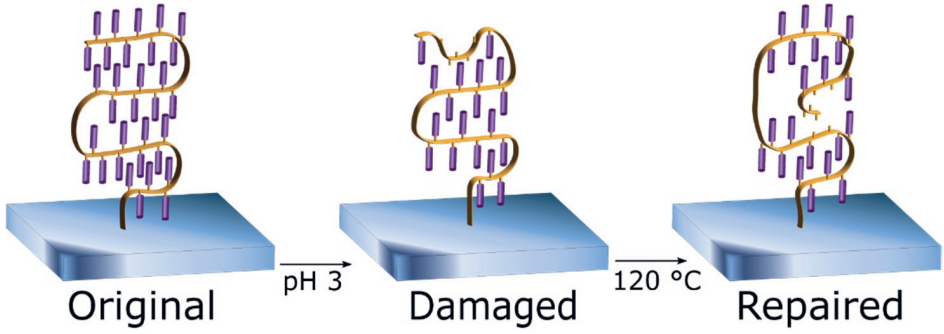

This chapter has been submitted as:

Annemieke van Dam, Maarten M. J. Smulders, Han Zuilhof, Self-Healing Fluorine-Free Hydrophobic Polymer Brushes. *ACS Appl. Nano Mater.* **2024**, *under revision*.

Abstract

Fluorinated hydrocarbons are excellent building blocks for hydrophobic coatings, but also yield undesirable toxicity and environmental persistence. Here, we report that the beneficial properties typically associated with (partially) fluorinated polymer brush coatings, can to a large degree also be achieved with their non-fluorinated counterparts. To this end, we have successfully grafted thirteen poly(alkyl methacrylate) homopolymer brushes from a flat silicon surface using surface-initiated atom transfer radical polymerization (SI-ATRP). These polymer brushes were characterized by XPS, ellipsometry and static water contact angle measurements. They were then shown to be repeatedly self-repairing by thermal treatment at 120 °C after damage by pH 3, with longer side chains being more resistant to damage from the acid. Branching of the side chains did not significantly influence this resistance, but it lowered the static water contact angle. Some polymer brushes with intermediate side chain lengths displayed an increase in contact angle over the first four cycles. This was not caused by impurities, but was the result of an annealing effect that improved the packing of the side chains of the brushes. In all, these coatings are suitable, self-healing, environmentally friendly and fully non-fluorinated alternatives for current fluorine-based hydrophobic coatings.

3.1 Introduction

Hydrophobic surfaces are essential for a smooth operation in, for example, oil processing,[1,2] heat exchangers,[3] ink jet printing and polymer production.[4] The butterfly wing,[5] but also the upper part of a lotus leaf,[6] are well-known, highly attractive natural hydrophobic surfaces: chemically unreactive with water, and both nano- and macro-structured. Most synthetic hydrophobic coatings have taken one or more aspects of the lotus leaf as inspiration. That is, 3D structures have been created to reduce the contact area with a water droplet and thus increasing the contact angle, leading to superhydrophobicity.[7–10] In such cases, the structural integrity of the coating is crucial, and damage leads to significant loss of functionality.[11–13] Furthermore, without the use of a chemical coating, this structural repellence only works for solvents with a high surface tension.

Well-known examples of such coatings are those in which long poly-fluorinated aliphatic chains are used. Examples like polytetrafluoroethylene (PTFE/ Teflon)[14–16] and per-fluorinated silanes[17–20] are often applied as nonreactive coatings on industrial scales, but also for medical purposes and kitchen utensils.[21] However, increasing knowledge on their toxicity and carcinogenicity [22–24] in combination with their environmental persistence display serious drawbacks, and the use of polyfluorinated alkanes (PFAS) should be drastically reduced.[25] In line with this, more and more countries are restricting or forbidding the use of PFAS.[26] In contrast to their environmental persistence, the life-time of such coatings is typically limited, as they lend their antifouling ability to low surface tension which is easily disturbed.

As recently reviewed,[27] many highly elegant approaches have been designed to obtain coatings that are able to withstand damage by the incorporation of a self-repair mechanism.[27–32] However, although the possibility of self-repair after damage may significantly extend the device lifetime, the removed part is still lost to the environment. As all the aforementioned examples are carbon-fluorine-based, release of these fluorine-containing parts has a persistent, negative environmental impact. Finding non-fluorinated hydrophobic coatings is thus urgently needed. The group of Hozumi developed an oil-repellent polymer brush through A(R)GET-ATRP from (dimethylamino) ethyl methacrylate, thus using an environmentally friendly method to create a fluorine-free coating.[33] As polymer brushes are covalently attached to the

surface, a strong, lasting connection is formed.[34] By grafting them from the surface, the thickness can be closely controlled, and precise knowledge of the chemical composition is maintained. Due to this precision, polymer brushes have been developed for various applications, ranging from antibiofouling[35,36] via thermoresponsiveness[37,38] to lubrication.[39] In chapter 2, we reported such a self-repairing polymer brush-based coating as well.[32] In this chapter, we provided preliminary evidence that poly(**decyl methacrylate**) – which is fluorine-free, hydrophobic and polymer repelling – is resistant to damage by pH 3. In contrast, its fluorinated counterparts were damaged by the same solution. Additionally, poly(**pentyl methacrylate**) and poly(**ethyl methacrylate**) were not resistant to the pH 3 solution either, but were repairable by placement in the oven at 120 °C. Although we were positively surprised by this result, we did not have a full explanation.

Intrigued by these initial findings, and in light of the need for robust, fluorine-free hydrophobic coatings, in this chapter, the effect of the alkyl side chain of a poly(alkyl methacrylate) brush on both the stability (in pH 3) and capacity for self-repair is investigated. A range of linear side chains is investigated, from ethyl to hexadecyl (Figure 3.1). As micelle research by Brady[40–42] has shown that alkyl chains can form impenetrable sheets from eight carbons and longer, we expected a change in stability behavior beyond a certain alkyl chain length. In addition, since branching of the alkyl chains may affect such sheet formation, it is highly relevant to also study the effects thereof on the coating stability and self-repair capabilities.

This chapter outlines the synthesis of some, hitherto not reported, alkyl methacrylate monomers, including four with branched alkyl moieties, the polymer brush formation of 14 of these monomers by SI-ATRP, the characterization of the resulting coating by ellipsometry, X-ray photoelectron spectroscopy (XPS) and static water contact angle measurements, and studies of the polymer brush structure after damage by acid (pH 3) and annealing. Finally, it provides an analysis of fluorinated and non-fluorinated polymer brush coatings, and outlines the significant potential of the latter in view of the reported observations.

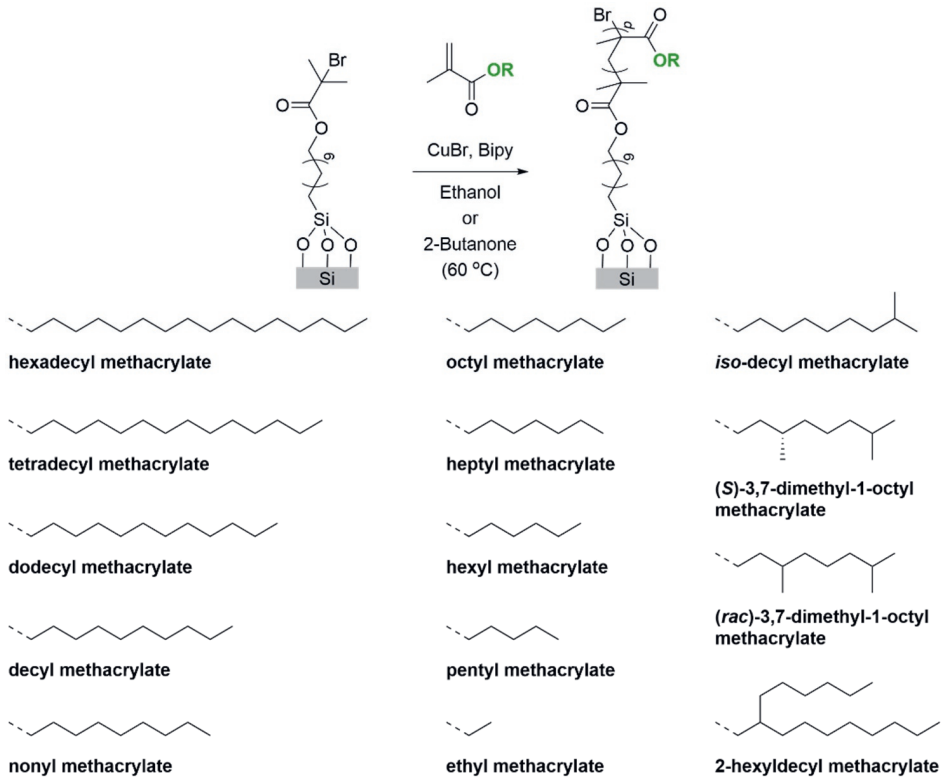

Figure 3.1. Schematic depiction of the self-repairing polymer brushes with side chains accentuated in green (top) and general synthesis and structure of the studied polymer brushes (bottom).

3.2 Results and discussion

3.2.1 Set-up of study and monomers involved

The effect of side chain structure on the self-healing capability of 14 polymer brushes was investigated with a range of homopolymer brushes (Figure 3.1). First, we studied ten methacrylates with linear side chains consisting of two up to sixteen carbons. Then, to also investigate the effect of branching, we studied **decyl methacrylate** and two of its isomers, **iso-decyl methacrylate** and **3,7-dimethyl-1-octyl methacrylate**, the latter both in enantiopure and racemic form. Additionally, we studied **2-hexyldecyl methacrylate**, an isomer of **hexadecyl methacrylate** with ten carbons in its longest chain and therefore displaying two branches of considerable length.

Eight of the monomers under study were commercially available. The other six (**heptyl-, octyl-, nonyl-, (*S*)-3,7-dimethyl-1-octyl-, (*rac*)-3,7-dimethyl-1-octyl- and (*rac*)-2-hexyldecyl methacrylate**) were synthesized on gram scale, via the acid-catalyzed esterification of methacrylic acid, with isolated yields between 75% and 89% (see sections 3.4.1 to 3.4.6, respectively, for details on the synthesis and characterization).

3.2.2 Polymer brush formation

The SI-ATRP protocol that was already presented in previous chapter was again performed on initiator-activated silicon surfaces, to obtain homopolymer brushes of all fourteen methacrylates (section 2.4.3). A batch of silicon surfaces was activated by sonication and oxygen plasma cleaning before being submerged in a solution of 3-(trichlorosilyl)propyl-2-bromo-2-methylpropano-ate in toluene at room temperature for 16 h. Subsequently, the polymerization reaction was performed by placing ten of thus coated silicon surfaces in a reactor in a nitrogen atmosphere glovebox in a polymerization solution (8–48 h at 60 °C ; Table 3.1). The preparation of the polymerization solution was done in the glovebox as well. After the polymerization, the surfaces were placed in a vacuum oven at 50 °C and 50 mbar overnight for further drying. The surfaces were then analyzed by ellipsometry, static water contact angle measurements and XPS, with the characteristic results given in Table 3.1 (XPS results similar to chapter 2, data not shown).

Polymer brush formation was performed until coatings of at least 60 nm thickness were obtained, as we required the brush regime of the tethered polymer chains. We expected similar polymerization rates for all side chain lengths, however we found a large variation in coating thickness after 24 hours (data not shown). We therefore optimized the reaction conditions for each monomer to reach at least 60 nm thickness (Table 3.1). In some instances, double catalyst and ligand concentrations were used, in order to speed up the reaction. The longer methacrylates (C_{10} and higher) did not mix well with ethanol, which we thus substituted with 2-butanone. **Decyl-**, **dodecyl-**, and **tetradecyl methacrylate** polymerized well in this solvent.

Table 3.1. Polymer brush formation of the methacrylates under study: reaction conditions, average coating thickness and static water contact angle (WCA). Reactions were performed at 60 °C with 1 mol% CuBr catalyst, 2 mol% bpy ligand, 25 vol% monomer and 75 vol% solvent.

Monomer	Solvent	Reaction time (h)	Coating thickness (nm)	WCA (°)
Hexadecyl methacrylate	2-Butanone[a]	24	23 ± 11	107 ± 1
Tetradecyl methacrylate	2-Butanone[b]	24	113 ± 5	107 ± 1
Dodecyl methacrylate	2-Butanone	40	125 ± 8	105 ± 3
Decyl methacrylate	2-Butanone	26	114 ± 5	102 ± 3
Nonyl methacrylate	Ethanol[b]	24	139 ± 12	96 ± 3
Octyl methacrylate	Ethanol[b]	20	69 ± 11	94 ± 3
Heptyl methacrylate	Ethanol[b]	24	87 ± 28	90 ± 4
Hexyl methacrylate	Ethanol	20	111 ± 38	87 ± 2
Pentyl methacrylate	Ethanol[b]	46	64 ± 5	86 ± 1
Ethyl methacrylate	Ethanol	8	85 ± 6	76 ± 1
Iso-decyl methacrylate	Ethanol	8	103 ± 26	94 ± 2
(*S*)-3,7-Dimethyl-1-octyl methacrylate	Ethanol	48	143 ± 7	96 ± 1
(*rac*)-3,7-Dimethyl-1-octyl methacrylate	Ethanol	24	65 ± 12	95 ± 1
2-Hexyldecyl methacrylate	2-Butanone	48	61 ± 44	105 ± 3

Notes: [a]with 4,4-dinonyl-bipyridine (dnbpy) as ligand instead of 2,2-bipyridine (bpy); [b]double catalyst and ligand concentration. Thickness variation within a surface was about 5 nm, indicated thickness deviations are between different surfaces of the same batch.

The exception was **hexadecyl methacrylate**, for which use of either ethanol or 2-butanone as solvent did not provide coatings of more than 40 nm, even after reacting for 96 h (section 3.4.7). An average of 23 nm was obtained in 2-butanone after 24 hours. In toluene, 1-pentanol, 1-octanol or 1-decanol, both at

60 °C and at 100 °C and with 4,4-dinonyl-bipyridine as alternative ligand, no more than 15 nm of brush could be grown either. Self-healing results of the thickest poly(**hexadecyl methacrylate**) brushes (section 3.4.7) showed vastly different behavior from poly(**tetradecyl methacrylate**), indicating poor surface coverage. This is most likely caused by poor polymerization due to low solubility of the monomer. Poly(**hexadecyl methacrylate**) should therefore not be included in the series for further experiments. In contrast, polymerization of its branched isomer **2-hexyl-1-decyl methacrylate** was possible under the regular reaction conditions and only slightly longer reaction time. However, a large sample-to-sample variation in thicknesses was observed, indicating that solute-solvent mixing was not ideal for **2-hexyl-1-decyl methacrylate** either.

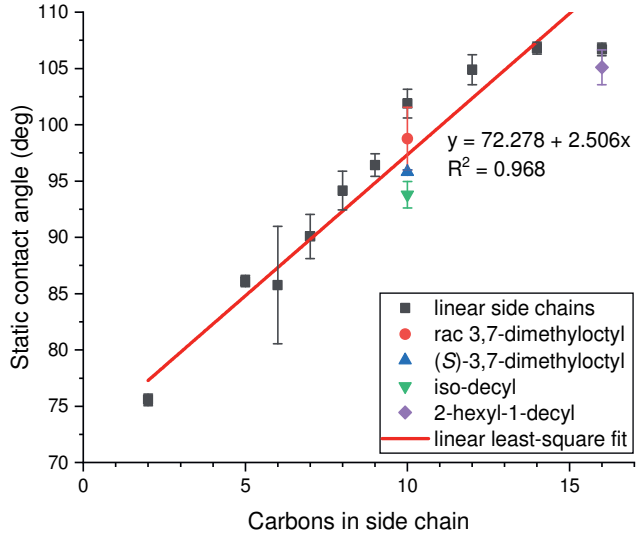

Figure 3.2. Correlation between the number of carbon atoms in the side chain of the polymer brush, and the static water contact angle of this brush (from Table 3.1). A least-square line is fitted through the contact angles of the coatings with linear side chains (black points only), and is described by a linear function.

A clear linear correlation was visible between side chain length and static water contact angle (Figure 3.2). The relatively low static contact angle for the C_{16} brush could be explained by its low thickness, that would make the overall surface somewhat less hydrophobic (as compared to the trendline). For the other brushes, every carbon added to the length of the side chain, added approximately 2.7° to the contact angle on average. The common threshold for

hydrophobicity, 90°, was reached by seven carbon atoms in the alkyl side chains. The branched alkyl moieties did not behave according to their number of carbons, but rather to their longest chain. For example, both racemic and enantiopure poly(**3,7-dimethyloctyl methacrylate**) had a static water contact angle of 95°, similar to the value of 94° for poly(**octyl methacrylate**). This indicated that the cross-section area, determined by the length of the longest linear side chain rather than number of carbon atoms per side chain, dominated the hydrophobicity of the polymer brushes.

3.2.3 Grafting density

Tight-packed polymer brushes have different behavior than surface-bound polymers in the mushroom or pancake regimes.[34] Grafting density is the common measure to describe the tightness of polymer chains in a coating. In order to be able to compare the performance of our polymer brushes with others from literature, we attempted to determine the grafting density. There are three common ways to determine the grafting density of a polymer brush:[43] via swelling in AFM,[44] the gravimetric method, or dry thickness measurement. The method of swelling in AFM was attempted in the work described in chapter 2 (section 2.4.11), but provided no satisfying results, as our hydrophobic polymer brushes did not swell in the solvents that were acceptable for our AFM set-up. The gravimetric method is only suitable for particles and not for flat surfaces. Therefore, we opted for the dry thickness method. In this, three routes are commonly taken for the determination of the molecular weight: degrafting of the polymer,[45,46] single-chain force microscopy,[43] or combined polymerization in solution and on a surface.[47] Of these, the combined polymerization is the only suitable option for our polymers, as there would not be enough material to degraft, and the chain terminus cannot readily be picked up by, *e.g.*, a gold force microscopy tip. We thus intended to determine the grafting density of our polymer brushes by performing a non-grafted, solution polymerization simultaneously to a grafted polymerization and determining the properties of the unbound polymer. The assumption is that the molecular weight of the non-grafted polymer and the grafted polymer are similar, and therefore the properties of the unbound polymer can be transferred to the surface-bound polymer. For structurally similar poly(**methyl methacrylate**), the error of this method has been investigated and shown to be minimal.[48]

Scheme 3.1. Copolymerization of hexyl methacrylate in solution and on a Si(111) surface, both from an isobutyl bromide initiator.

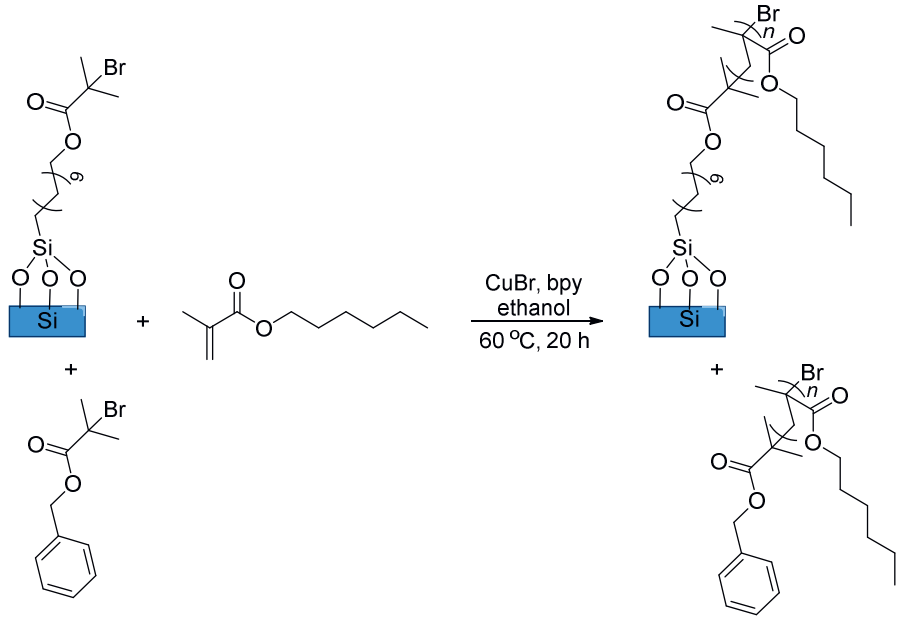

In order to obtain unbound polymer, benzyl-2-bromo-2-methylpropanoate was added to some of the reactors when the surface polymerization was performed (Scheme 3.1). The non-grafted polymer was isolated by precipitation in methanol, redissolving in tetrahydrofuran and precipitation in methanol again. This polymer was then analyzed by NMR and GPC to determine the molecular weight. However, translation of the molecular weight and layer thickness into grafting density led to inconsistent results (section 3.4.8). We observed large variations in grafting density, ranging from 0.54 chains/nm^2 to 2.50 chains/nm^2 for poly(**hexyl methacrylate**). Furthermore, although the radii of gyration are not determined for these polymer brushes, it is safe to assume that they are typically larger than 1 nm^2. Already an **ethyl methacrylate** monomer spans 0.8 nm, thus the radius of gyration of poly(**ethyl methacrylate**) can be estimated to be roughly twice that, *i.e.*, 1.5–1.6 nm (section 2.4.11). For **hexyl methacrylate**, a monomer is 1.3 nm and the radius of gyration thus about 2.5 nm. Therefore, grafting densities above 0.5 chain/nm^2 are physically impossible (cf. ref. 48). This leads us to believe that the solution polymerization rate is slower than SI-ATRP,

resulting in shorter non-grafted polymers and thus in an overestimation of the number of polymer chains on the surface.

Various factors could be at play here. First, we observed inhomogeneous mixing of some monomers with the solvent, leading to concentration gradients. Although this was not always visible by eye, some inhomogeneity cannot be ruled out. A higher concentration near the surface would increase the polymerization rate of SI-ATRP and decrease that of the polymerization in solution. This would be further enhanced by the hydrophobic surface, which attracts monomers and thus intensifies the concentration differences. Furthermore, any differences in reaction rates would be enhanced by the large thickness of the brushes. Michalek and coworkers[49] have calculated that the relative error margins remain constant with the size of the polymer, as long as the grafting density isn't too low or too high. In the extremes, segment density within the tethered brush is no longer equal to bulk density of the non-tethered brush, and the calculations of grafting density no longer hold. Based on our findings, we conclude that our brushes are in a density regime that is too high for the dry measurement calculations, resulting in exorbitantly high error margins. We thus had to conclude that this method was not directly applicable to our situation and that determination of the grafting density was beyond the scope of the current research.

3.2.4 Polymer brush self-repair

The self-repairing ability of the polymer brushes was tested by repeated placement in a pH 3 solution (HCl, for 24 h) and a 120 °C oven (for 2 h), as done in previous research.[32] After each step, the surfaces were blown dry and their static water contact angles were measured (Figure 3.3). The polymers with shorter linear side chains (C_2 until C_7) displayed a clear zigzag pattern. Upon placement in acid, their contact angles decreased. This was most likely caused by acid-catalyzed hydrolysis of the ester bonds in the polymer that removed the aliphatic chain and left only carboxylic acid in the backbone of the polymer. As the carboxylic acid is more hydrophilic than the aliphatic chain, the water contact angle decreased. Upon placement in the oven, full recovery of the original contact angle was observed, indicating that the hydrophobic top layer was restored. We hypothesize that upon heating above the glass transition temperature, the polymer brush rearranges itself in the thermodynamically

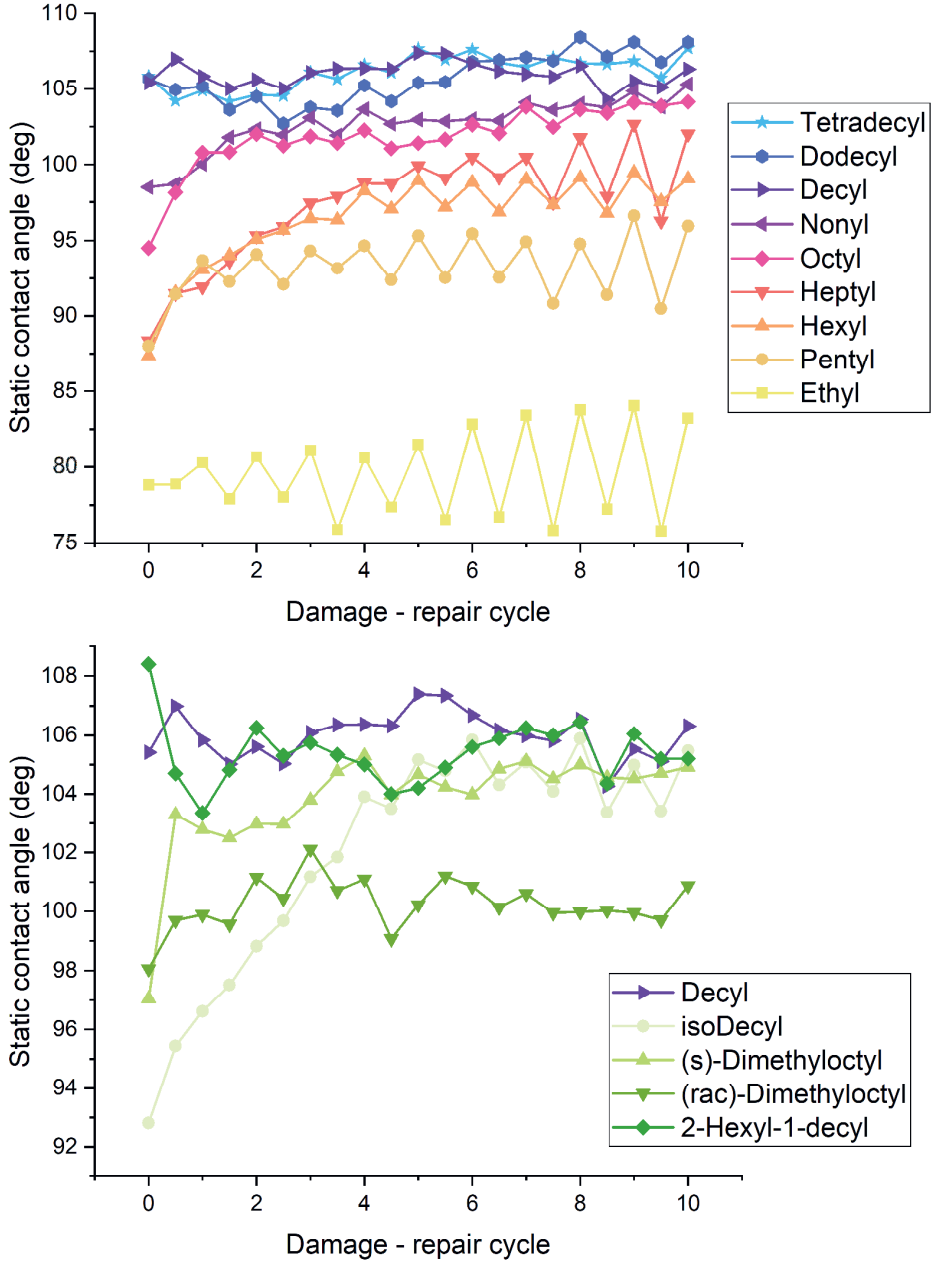

Figure 3.3. Self-repair of the linear polymer brushes (top) and the branched polymer brushes (bottom). The static water contact angle was measured after each damaging step (half cycle points) and after each healing step (whole cycle points). The error margins are around 1° for all points, and are omitted for clarity.

most favorable way. The acidic groups will cluster together, while the hydrophobic side chains will be pushed outwards (Scheme 3.2). A near-pristine top layer reforms, displaying the same hydrophobicity as before the damage took place. As the glass transition temperatures of poly(*n*-alkyl methacrylates) are shown to be lower with each additional carbon,[50] starting with 74 °C for poly(**ethyl methacrylate**),[51] we can assume that at 120 °C, all the studied polymer brushes are well above their glass transition temperature.

Scheme 3.2. The proposed self-repair mechanism:[32] in an acidic environment, some of the ester bonds will be broken and the side chains will be removed. Upon heating, rearrangements occur: the acid groups will cluster together in the bulk of the polymer, and a full top layer returns.

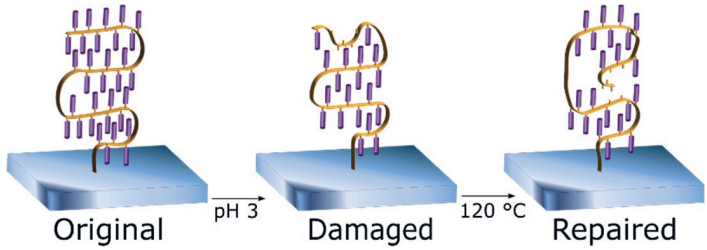

While the polymer brushes with short side chains showed a clear zigzag pattern, the damage of polymer brushes with longer side chains was much less pronounced. In the poly(**octyl methacrylate**) brush some damage and repair could be observed, but poly(**nonyl methacrylate**), poly(**decyl methacrylate**), poly(**dodecyl methacrylate**) and poly(**tetradecyl methacrylate**) brushes even looked mostly unaffected by the acid. We hypothesize that the long linear alkyl chains stack to form a closely packed sheet that is impenetrable by acid. As the acid cannot reach the ester moieties, no hydrolysis takes place and thus no damage to the coating occurs. Already in the '70s such close packing of alkyl chains was mentioned in micelle formation, with a turning point around eight carbons.[41] We now observe a similar turning point for the stability of methacrylate-based polymer brushes with alkyl side chains: clear damage of, *e.g.*, poly(**heptyl methacrylate**) brushes, slight damage of poly(**octyl methacrylate**) brushes and no significant damage of the brushes composed of poly(**nonyl methacrylate**) and longer, linear poly(alkyl methacrylates).

The low stability of the poorly grafted poly(**hexadecyl methacrylate**) (Supporting Information, section 3.4.7) further supports this hypothesis.

Although the side chains are of sufficient length to prevent hydrolysis, the coating is so poorly grafted that no full sheet of alkyl chains was formed, offering no protection against acid hydrolysis. As a result, large changes in contact angle are observed after each damage (around 100°) and repair (around 107°) half-cycle.

We hypothesized that branching of the side chains could impair the tight packing of the side chains, thereby allowing hydrolysis to take place in branched polymer brushes with side chains above eight carbons (Figure 3.3, bottom). Poly(**iso-decyl methacrylate**) displayed some damage and repair after cycle four, indicating that its packing is not as tight as in poly(**decyl methacrylate**). However, both types of poly(**3,7-dimethyloctyl methacrylate**) showed no damage. Apparently, the disruption caused by the methyl on the end of the side chain could be mitigated by the methyl closer to the ester bond, which could provide additional hydrophobic shielding to the nearby ester group. This happened irrespective of the enantiopurity of the side chain.

Disruption of the packing by a larger side chain did not have much effect either. Poly(**2-hexyl-1-decyl methacrylate**) showed the same contact angle and stability as poly(**decyl methacrylate**). No effect of the branching hexyl group was observed. We thus note that although branches close to the ester bond could disrupt the packing of alkyl chains, they remain effective in protecting the ester from acidic hydrolysis, likely by a combination of increased local hydrophobicity and steric hindrance. In contrast, branching at the end of the side chains reduced the robustness of the polymer brush, which we hypothesize to be due to reduction of the interdigitation of alkyl chains inside the brush: branching at the end of the alkyl chain would most affect this interdigitation.

3.2.5 Annealing phase

In the first four damage-repair cycles, the static water contact angle of poly(**hexyl methacrylate**) steadily increased (Figure 3.3). Poly(**heptyl methacrylate**), poly(**octyl methacrylate**) and poly(**iso-decyl methacrylate**) also displayed this behavior. We hypothesized that either contamination (that is released during the immersion in pH 3 solution) or poor packing of the side chains could disrupt the behavior of the polymer brushes at the start of the experiments, leading to a slightly reduced contact angle.

To establish whether the reduction of the contact angle was caused by contamination, we first tried to wash out any contaminations by immersion. To this end, we placed some poly(**hexyl methacrylate**) surfaces in MilliQ for 24 h, then in the oven for 2 h and then again in MilliQ and the oven. This mimicked the first two self-repair cycles, but with pH 7 instead of pH 3, thus doing no damage. After this treatment, we performed ten damage-repair cycles as usual (Figure 3.4, blue line). Although a slight increase of the contact angle in the first cycle could be seen, no significant improvement was found. Contamination that is gradually washed out is thus unlikely to cause the disruption of the contact angle.

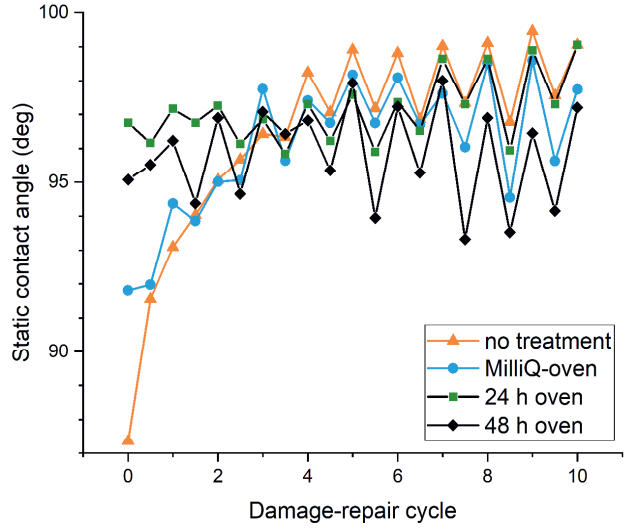

Figure 3.4. Self-repair cycles of poly(hexyl methacrylate) without any treatment (orange), after MilliQ-oven treatment (blue), after 24 h oven treatment (dark green) and after 48 h oven treatment (black).

If the disruption of the contact angle is caused by poor packing, then no damage or solvation steps are necessary to solve the problem, only annealing at an elevated temperature for a specific period of time above the glass transition temperature. To investigate this hypothesis, we placed new surfaces in the oven at 120 °C for 48 h and measured their contact angles (Table 3.2). Indeed, the starting contact angles of most coatings were higher than without the pre-treatment. This supports the hypothesis that the initial coatings do not yet have the most optimal packing, which is only obtained after high-temperature

annealing. It also explains why the shorter, more flexible, chains suffer most from this phenomenon: the longer chains have more driving force for correct packing, and thus will pack in the most stable configuration from the start.

Table 3.2. Static water contact angles of polymer brushes before and after curing for 48 h at 120 °C.

Monomer	WCA (°) before	WCA (°) after
Dodecyl methacrylate	105 ± 3	99
Decyl methacrylate	102 ± 3	99 ± 2
Nonyl methacrylate	96 ± 3	98 ± 2
Octyl methacrylate	94 ± 3	99 ± 2
Heptyl methacrylate	90 ± 4	99 ± 1
Hexyl methacrylate	87 ± 2	95 ± 2
Pentyl methacrylate	86 ± 1	89 ± 2
Ethyl methacrylate	76 ± 1	76 ± 1
Iso-decyl methacrylate	94 ± 2	95 ± 3

Furthermore, poly(**hexyl methacrylate**) surfaces were placed in the oven for 24 h, after which the self-repair experiments were performed (Figure 3.4, dark green line). This proved to be long enough to allow relaxation into the ideal configuration, with no more annealing visible in the first few cycles and a stable, high contact angle throughout the ten cycles. Lastly, self-repair experiments were performed with the poly(**hexyl methacrylate**) surfaces that were placed in the oven for 48 h (Figure 3.4, black line). Although these displayed consistent contact angles, the values were slightly lower than after only 24 h oven treatment or no pre-treatment. As a result, 24 h appears to be the optimal pre-treatment time.

3.3 Conclusions

Fourteen covalently linked non-fluorinated polymer brushes were produced and shown to be self-repairing upon heating after damage by pH 3 in ten damage-repair cycles. Longer linear side chains not only displayed higher hydrophobicity, but were also better able to withstand such damage. With short side chains ($\leq C_8$), an increase in hydrophobicity was observed over the first few cycles,

indicating that the packing of chains was improved with every cycle. Longer chains did not show this: they were packed closely from the start.

The high hydrophobicity, durability and self-healing capability of non-fluorinated polymer brushes is highly desirable, as replacements for fluorinated coatings are urgently needed. In an age where fluorinated compounds have fallen from their throne as ideal coatings, these non-fluorinated counterparts are shown to be worthy heirs.

3.4 Selected supporting information

Materials and methods are described in chapter 2, sections 2.4.1–2.4.3. Further supporting information is provided below.

3.4.1 Synthesis of heptyl methacrylate

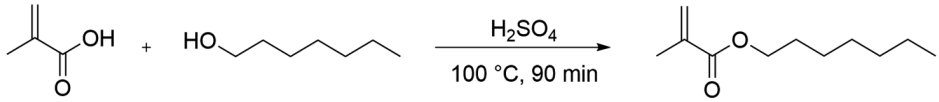

Scheme 3.3. Synthesis of heptyl methacrylate.

Methacrylic acid (25.8 g, 300 mmol), 1-heptanol (11.7 g, 100 mmol) and sulfuric acid (4.9 g, 50 mmol) were combined in a round-bottom flask and stirred at 100 °C for 90 min. 50 mL diethyl ether was added, and an extraction was performed seven times with 75 mL half-saturated sodium bicarbonate solution. The water layers were not washed with ether to obtain a higher yield, since that would also reintroduce some of the methacrylic acid. The organic layer was dried with sodium sulfate and the solvent was evaporated. Pure heptyl methacrylate was isolated (15.8 g, 85.5 mmol, 85% yield).

^{1}H NMR (400 MHz, $CDCl_3$): δ 6.11 (dd, *J* = 1.8, 1.0 Hz, 1H), 5.56 (p, *J* = 1.6 Hz, 1H), 4.16 (t, *J* = 6.7 Hz, 2H), 2.04 – 1.91 (m, 3H), 1.69 (p, *J* = 6.5 Hz, 2H), 1.46 – 1.26 (m, 8H), 0.96 – 0.85 (m, 3H). ^{13}C NMR (101 MHz, $CDCl_3$): δ 167.46 , 136.57, 125.00, 64.78, 31.72, 28.92, 28.62, 25.94, 22.56, 18.26, 13.99. DART-MS: m/z = 185.1533 $[M+H]^+$ (calculated value: 185.1536), m/z = 202.1798 $[M+NH_4]^+$ (calculated value: 202.1802). IR: 2956.62, 2928.25, 2857.90 (all CH_2 and CH_3 stretches), 1718.65 (C=O stretch), 1638.79 (C=C stretch), 1295.71 (C–C–O stretch), 1160.78 (C–O–C stretch), 1012.55 (symmetric C–C), 937.16 (α-CH_3 rocking deformation).

3.4.2 Synthesis of octyl methacrylate

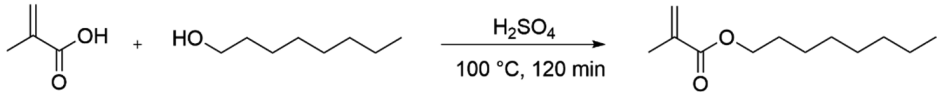

Scheme 3.4. Synthesis of octyl methacrylate.

Methacrylic acid (25.8 g, 300 mmol), 1-octanol (13.0 g, 100 mmol) and sulfuric acid (4.9 g, 50 mmol) were combined in a round-bottom flask and stirred at 100 °C for 120 min. 50 mL diethyl ether was added, and an extraction was performed eleven times with 75 mL half-saturated sodium bicarbonate solution. The water layers were not washed with ether to obtain a higher yield, since that would also reintroduce some of the methacrylic acid. The organic layer was dried with sodium sulfate and the solvent was evaporated. Pure octyl methacrylate was isolated (16.9 g, 85.1 mmol, 85% yield).

^{1}H NMR (400 MHz, $CDCl_3$): δ 6.07 (s, 1H), 5.51 (t, J = 1.8 Hz, 1H), 4.11 (t, J = 6.7 Hz, 2H), 1.95 – 1.90 (m, 3H), 1.71 – 1.59 (m, 2H), 1.26 (q, J = 5.0, 4.2 Hz, 10H), 0.90 – 0.82 (m, 3H). ^{13}C NMR (101 MHz, $CDCl_3$): δ 167.47, 136.55, 125.01, 64.78, 31.75, 29.19, 29.15, 28.59, 25.96, 22.60, 18.25, 14.01. DART-MS: m/z = 199.1692 $[M+H]^+$ (calculated value: 199.1692), m/z = 216.1957 $[M+NH_4]^+$ (calculated value: 216.1958). IR: 2956.22, 2926.51, 2856.50, 1718.86, 1638.71, 1295.98, 1160.64, 1012.73, 937.61.

3.4.3 Synthesis of nonyl methacrylate

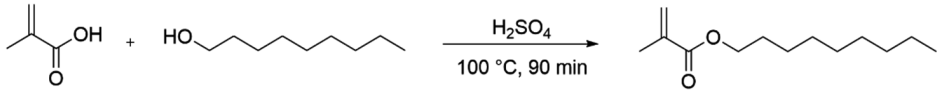

Scheme 3.5. Synthesis of nonyl methacrylate.

Methacrylic acid (25.8 g, 300 mmol), 1-nonanol (14.4 g, 100 mmol) and sulfuric acid (4.9 g, 50 mmol) were combined in a round-bottom flask and stirred at 100 °C for 90 min. 50 mL diethyl ether was added, and an extraction was performed six times with 75 mL half-saturated sodium bicarbonate solution. The water layers were not washed with ether to obtain a higher yield, since that would also reintroduce some of the methacrylic acid. The organic layer was dried with sodium sulfate and the solvent was evaporated. Pure nonyl methacrylate was isolated (16.6 g, 78 mmol, 78% yield).

^{1}H NMR (400 MHz, $CDCl_3$): δ 6.09 (s, 1H), 5.53 (p, J = 1.7 Hz, 1H), 4.13 (t, J = 6.7 Hz, 2H), 1.94 (t, J = 1.4 Hz, 3H), 1.73 – 1.59 (m, 2H), 1.36 – 1.22 (m, 12H), 0.96 – 0.79 (m, 3H). ^{13}C NMR (101 MHz, $CDCl_3$): δ 167.55, 136.58, 125.08, 64.83, 31.84, 29.46, 29.24, 29.21, 28.61, 25.97, 22.65, 18.30, 14.07. DART-MS: m/z = 213.1846 $[M+H]^+$ (calculated value: 213.1849), m/z = 230.2110 $[M+NH_4]^+$ (calculated value: 230.2115). IR: 2955.98, 2925.30, 2855.53, 1719.30, 1638.80, 1295.90, 1160.65, 1011.52, 937.33.

3.4.4 Synthesis of (*S*)-3,7-dimethyl-1-octyl methacrylate

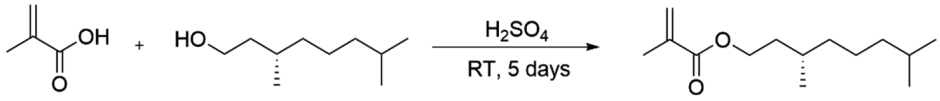

Scheme 3.6. Synthesis of (S)-3,7-Dimethyl-1-octyl methacrylate.

Methacrylic acid (8.13 g, 94.5 mmol), (*S*)-3,7-dimethyl-1-octanol (5.0 g, 31.5 mmol) and sulfuric acid (1.5 g, 15.8 mmol) were combined in a round-bottom flask and stirred at room temperature for 5 days. 50 mL diethyl ether was added, and an extraction was performed six times with 50 mL half-saturated sodium bicarbonate solution. The water layers were not washed with ether to obtain a higher yield, since that would also reintroduce some of the methacrylic acid. The organic layer was dried with sodium sulfate and the solvent was evaporated. Pure (*S*)-3,7-dimethyl-1-octyl methacrylate was isolated (5.35 g, 23.6 mmol, 75% yield).

^{1}H NMR (400 MHz, $CDCl_3$): δ 6.09 (dd, J = 1.9, 1.1 Hz, 1H), 5.54 (p, J = 1.6 Hz, 1H), 4.18 (ddt, J = 11.0, 7.0, 3.9 Hz, 2H), 2.12 – 1.86 (m, 3H), 1.76 – 1.65 (m, 1H), 1.58 – 1.41 (m, 3H), 1.37 – 1.19 (m, 4H), 1.14 (td, J = 7.5, 6.2, 4.3 Hz, 2H), 0.89 (dd, J = 20.8, 6.5 Hz, 9H). ^{13}C NMR (101 MHz, $CDCl_3$): δ 167.56, 136.58, 125.11, 63.29, 39.18, 37.13, 35.49, 29.94, 27.94, 24.62, 22.68, 22.59, 19.58, 18.32. DART-MS: m/z = 227.2005 $[M+H]^+$ (calculated value: 227.2006), m/z = 244.2269 $[M+NH_4]^+$ (calculated value: 244.2271). IR: 2955.09, 2926.93, 2869.79, 1719.43, 1638.89, 1296.05, 1161.64, 1011.25, 937.33.

3.4.5 Synthesis of racemic 3,7-dimethyl-1-octyl methacrylate

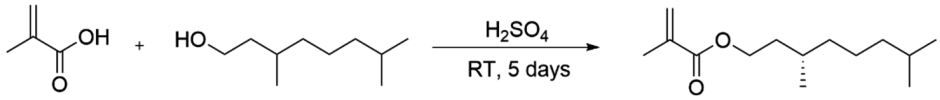

Scheme 3.7. Synthesis of (rac)-3,7-dimethyl-1-octyl methacrylate.

Methacrylic acid (12.91 g, 150 mmol), (*rac*)-3,7-Dimethyl-1-octanol (7.91 g, 50 mmol) and sulfuric acid (2.45 g, 25 mmol) were combined in a round-bottom flask and stirred at room temperature for 5 days. 20 mL water was added, and the acidic aquatic layer was decanted. 50 mL diethyl ether was added, and an extraction was performed five times with 50 mL half-saturated sodium bicarbonate solution. The water layers were not washed with ether to obtain a higher yield, since that would also reintroduce some of the methacrylic acid. The organic layer was dried with sodium sulfate and the solvent was evaporated. Pure (*rac*)-3,7-dimethyl-1-octyl methacrylate was isolated (10.02 g, 44.3 mmol, 89% yield).

^{1}H NMR (400 MHz, $CDCl_3$): δ 6.09 (dq, J = 2.0, 1.0 Hz, 1H), 5.54 (p, J = 1.6 Hz, 1H), 4.18 (ddt, J = 11.0, 7.7, 3.6 Hz, 2H), 1.97 – 1.92 (m, 3H), 1.71 (dtd, J = 13.5, 7.1, 5.0 Hz, 1H), 1.61 – 1.41 (m, 3H), 1.36 – 1.22 (m, 3H), 1.23 – 1.08 (m, 3H), 0.92 (d, J = 6.5 Hz, 3H), 0.87 (d, J = 6.6 Hz, 6H). ^{13}C NMR (101 MHz, $CDCl_3$): δ 167.56, 136.60, 125.07, 63.29, 39.19, 37.14, 35.51, 29.96, 27.94, 24.62, 22.66, 22.58, 19.58, 18.30. DART-MS: m/z = 244.2268 $[M+NH_4]^+$ (calculated value: 244.2271). IR: 2955.20, 2926.96, 2869.83, 1719.18, 1638.88, 1296.02, 1161.17, 1011.26, 937.25.

3.4.6 Synthesis of 2-hexyldecyl methacrylate

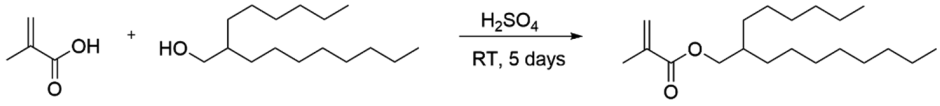

Scheme 3.8: Synthesis of 2-hexyldecyl methacrylate.

Methacrylic acid (6.45 g, 75 mmol), 2-hexyl-1-decanol (6.06 g, 25 mmol) and sulfuric acid (1.23 g, 12.5 mmol) were combined in a round-bottom flask and stirred at ambient conditions. The progress of the reaction was checked with ^{1}H-NMR every few hours. After 48 h, the conversion of alcohol was 80%. This

remained constant, and at 120 h, it was decided to stop the reaction. 50 mL diethyl ether was added, and an extraction was performed six times with 75 mL half-saturated sodium bicarbonate solution. The water layers were not washed with ether to obtain a higher yield, since that would also reintroduce some of the methacrylic acid. The organic layer was dried with sodium sulfate and the solvent was evaporated. The product (6.88 g) consisted of 2-hexyldecyl methacrylate and 10% 2-hexyl-1-decanol. The yield of the methacrylate was 6.38 g (21 mmol, 82% yield). As the research in chapter 2 has shown that free alcohol does not significantly hamper ATRP, and both column chromatography and distillation harm the methacrylate product, no further attempts were done to remove any remaining alcohol.

^{1}H NMR (400 MHz, $CDCl_3$): δ 6.08 (s, 1H), 5.55 – 5.50 (m, 1H), 4.04 (d, J = 5.7 Hz, 2H), 1.93 (s, 3H), 1.66 (q, J = 5.7 Hz, 1H), 1.27 (d, J = 14.1 Hz, 24H), 0.87 (t, J = 6.7 Hz, 6H). ^{13}C NMR (101 MHz, $CDCl_3$): δ 167.56, 136.60, 125.02, 67.45, 37.33, 31.89, 31.79, 31.41, 30.93, 29.93, 29.60, 29.53, 29.29, 26.72, 26.69, 22.66, 22.63, 18.29, 14.07, 14.05. DART-MS: m/z = 311.2939 $[M+H]^+$ (calculated value: 311.2945), m/z = 328.3205 $[M+NH_4]^+$ (calculated value: 328.3210). IR: 2955.72, 2923.91, 2854.78, 1720.27, 1639.18, 1294.95, 1162.77, 1012.07, 937.25.

3.4.7 Polymerization and self-healing performance of poly(hexadecyl methacrylate)

The polymerization of hexadecyl methacrylate was performed as described in previous chapter (section 2.4.3), but on a smaller scale. 1.5 mL solvent (75 vol%), 0.5 mL monomer (25 vol%, 1.40 mmol), and 1 surface were used in a 10 mL tube with micro stirring bar (2 by 4 mm). As catalyst, either 4.0 mg (0.028 mmol) copper(I) bromide (CuBr) and 8.8 mg (0.056 mmol) bipyridine (bpy) were used, or 5.0 mg (0.035 mmol) CuBr and 25 mg (0.061 mmol) 4,4-dinonyl-bypiridine (dnbpy). A variety of solvents was tested at different temperatures (Table 3.3).

The five surfaces with the thickest polymer brushes were used for self-repair experiments (Figure 3.5). A large gap in contact angle could be seen for the damaged and the repaired state. This indicates that the coating is susceptible to hydrolysis by the acid, contrary to what we would expect for a side chain of this length. As the polymerization was quite difficult for this monomer, we suspect that the polymer is poorly distributed over the surface and was not able to form

a thick, impenetrable outer layer. The results of the self-repair experiments are thus not representative for a polymer brush with side chains of this length. We decided to exclude these results from our comparison.

Table 3.3. Reaction conditions and resulting thicknesses of polymerization reactions with hexadecyl methacrylate.

Solvent	Ligand	Temperature (°C)	Time (h)	Number of replicates	Average thickness (nm)
Ethanol	bpy	60	7	2	9
2-butanone	bpy	60	24	9	23
			48	4	35
			168	4	35
2-butanone	dnpby	60	24	3	19
Toluene	dnpby	60	70	3	7
		100		1	5
1-pentanol	dnpby	60	70	1	7
		100		1	9
1-octanol	dnpby	60	96	1	6
		100		1	9
1-decanol	dnpby	60	96	1	9
		100		1	10

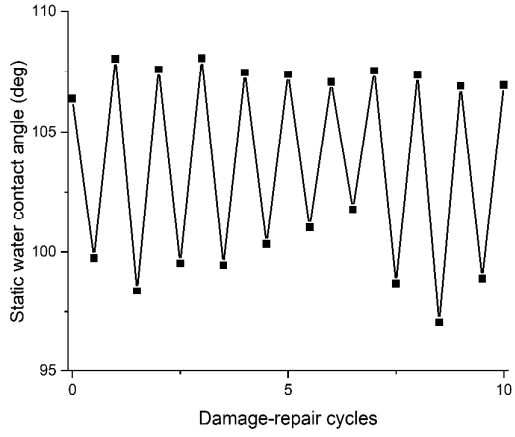

Figure 3.5. Self-repair of poly(hexadecyl methacrylate), as probed by static water contact angle measurements.

3.4.8 Grafting density determination

Procedure

Inside an argon glovebox, 30 mg (0.21 mmol) CuBr and 66 mg (0.42 mmol) 2,2-bipyridine were weighed in a 50 mL Schlenk tube with cap, surface holder and stirring bar. Four surfaces were placed face down in the surface holder of the Schlenk tube. 1.635 mL (10.45 mmol) hexyl methacrylate, 7.5 mL ethanol and 5.0 µL (0.05 mmol) benzyl-2-bromo-2-methyl propanoate were added, and the reaction mixture was stirred for 20 h at 60 °C. The vessel was cooled to room temperature and removed from the glovebox. The surfaces were transferred to a beaker, sonicated in ethanol for 5 min, blown dry, cured overnight in the vacuum oven at 50 °C and 100 mbar and analyzed as usual. The reaction mixture was transferred to a round bottom flask and 2 × 1mL THF was used to rinse the reaction vessel. The solvents were evaporated by rotary evaporation. The residue was dissolved in 2 mL THF and then poured in a beaker containing 80 mL cold methanol. The liquid was filtered, and both the filter and the beaker were placed in the vacuum oven overnight to remove any remaining solvents. The polymer (0.52 g) was analyzed by ^{1}H-NMR and GPC.

Results

The values resulting from these grafting density calculations for poly(hexyl methacrylate) are so high and so widely spread (Table 3.4) that we can only draw the conclusion that this method is not accurate enough. We repeated the procedure once with ethyl methacrylate and once with decyl methacrylate (Table 3.5). Unfortunately, these results were no more plausible.

Table 3.4. Grafting density determination of poly(**hexyl methacrylate**).

Attempt	M_n by NMR	M_n by GPC	Thickness on surface (in nm)	Grafting density by NMR (chains per nm^2)	Grafting density by GPC (chains per nm^2)
#1	18814	32482	75.8	2.498	1.447
#2	10983	16539	14.3	0.808	0.536
#3	11068	-	37.0	2.074	-

Table 3.5. Grafting density determination of poly(ethyl methacrylate) and poly(decyl methacrylate).

Monomer	M_n by NMR	M_n by GPC	Thickness on surface (in nm)	Grafting density by NMR (chains per nm^2)	Grafting density by GPC (chains per nm^2)
Ethyl-MA	6421	11394	16.1	1.752	0.987
Decyl-MA	45527	-	115.0	1.445	-

References

(1) Bockstahler, T. E.; Hunt, C. R. US3705190 A, **1972**.
(2) Feng, L.; Zhang, Z.; Mai, Z.; Ma, Y.; Liu, B.; Jiang, L.; Zhu, D. *Angew. Chem. Int. Ed.* **2004**, *43* (15), 2012–2014.
(3) Kuschnerow, J. C.; Dorn, S.; Augustin, W.; Scholl, S. *Proceedings of International Conference on Heat Exchanger Fouling and Cleaning* **2013**, *1* (1), 150–157.
(4) Mcfadden, D. M.; Wu, R. S. H. EP1024149 B1, **2000**.
(5) Wagner, T.; Neinhuis, C.; Barthlott, W. *Acta Zool.* **1996**, *77* (3), 213–225.
(6) Ensikat, H. J.; Ditsche-Kuru, P.; Neinhuis, C.; Barthlott, W. *Beilstein J. Nanotech.* **2011**, *2* (1), 152–161.
(7) Wang, D.; Sun, Q.; Hokkanen, M. J.; Zhang, C.; Lin, F. Y.; Liu, Q.; Zhu, S. P.; Zhou, T.; Chang, Q.; He, B.; Zhou, Q.; Chen, L.; Wang, Z.; Ras, R. H. A.; Deng, X. *Nature* **2020**, *582* (7810), 55–59.
(8) Haghdoost, A.; Pitchumani, R. *Langmuir* **2014**, *30* (14), 4183–4191.
(9) Shibuichi, S.; Onda, T.; Satoh, N.; Tsujii, K. *J. Phys. Chem.* **1996**, 19512–19517.
(10) Öner, D.; McCarthy, T. J. *Langmuir* **2000**, *16* (20), 7777–7782.
(11) Yamamoto, M.; Nishikawa, N.; Mayama, H.; Nonomura, Y.; Yokojima, S.; Nakamura, S.; Uchida, K. *Langmuir* **2015**, *31* (26), 7355–7363.
(12) Tian, X.; Verho, T.; Ras, R. H. A. *Science* **2016**, *352* (6282), 142–143.
(13) Verho, T.; Bower, C.; Andrew, P.; Franssila, S.; Ikkala, O.; Ras, R. H. A. *Adv. Mater.* **2011**, *23* (5), 673–678.
(14) Sarkar, D. K.; Farzaneh, M.; Paynter, R. W. *Mater. Lett.* **2008**, *62* (8–9), 1226–1229.
(15) Nelson, E.; Kilduff, T. J.; Benderly, A. A. *Ind. Eng. Chem.* **1958**, *50* (3), 329–330.
(16) Dhanumalayan, E.; Joshi, G. M. *Adv. Compos. Hybrid Mater.* **2018**, *1* (2), 247–268.
(17) Denes, A. R.; Tshabalala, M. A.; Rowell, R.; Denes, F.; Young, R. A. *Holzforschung* **1999**, *53*, 318–326.
(18) Akamatsu, Y.; Makita, K.; Inaba, H.; Minami, T. *Thin Solid Films* **2001**, *389*, 138145.
(19) Alessandrini, G.; Aglietto, M.; Castelvetro, V.; Ciardelli, F.; Peruzzi, R.; Toniolo, L. *J. Appl. Polym. Sci.* **2000**, *76* (6), 962–977.
(20) Ivanova, N. A.; Zaretskaya, A. K. *Appl. Surf. Sci.* **2010**, *257* (5), 1800–1803.
(21) Pisani, E.; Tsapis, N.; Galaz, B.; Santin, M.; Berti, R.; Taulier, N.; Kurtisovski, E.; Lucidarme, O.; Ourevitch, M.; Doan, B. T.; Beloeil, J. C.; Gillet, B.; Urbach, W.; Bridal, S. L.; Fattal, E. *Adv. Funct. Mater.* **2008**, *18* (19), 2963–2971.
(22) Fenton, S. E.; Ducatman, A.; Boobis, A.; DeWitt, J. C.; Lau, C.; Ng, C.; Smith, J. S.; Roberts, S. M. *Environ. Toxicol. Chem.* **2021**, *40* (3), 606–630.

(23) Hekster, F. M.; Laane, R. W. P. M.; de Voogt, P. Environmental and Toxicity Effects of Perfluoroalkylated Substances; 2003; 99–121.
(24) Cao, Y.; Ng, C. *Environ. Sci. Process Impacts* **2021**, *23* (11), 1623–1640.
(25) Cousins, I. T.; Johansson, J. H.; Salter, M. E.; Sha, B.; Scheringer, M. *Environ. Sci. Technol.* **2022**, *56* (16), 11172–11179.
(26) https://echa.europa.eu/-/echa-publishes-pfas-restriction-proposal. Accessed on 7 December 2023.
(27) Wang, Z.; Zuilhof, H. *Langmuir* **2016**, *32* (25), 6310–6318.
(28) Li, Y.; Li, L.; Sun, J. *Angew. Chem. Int. Ed.* **2010**, *49* (35), 6129–6133.
(29) Wang, X.; Liu, X.; Zhou, F.; Liu, W. *Chem. Commun.* **2011**, *47* (8), 2324–2326.
(30) Esteves, A. C. C.; Luo, Y.; Van De Put, M. W. P.; Carcouët, C. C. M.; De With, G. *Adv. Funct. Mater.* **2014**, *24* (7), 986–992.
(31) Garcia, S. J. *Eur. Polym. J.* **2014**, *53* (1), 118–125.
(32) van Dam, A.; Smulders, M. M. J.; Zuilhof, H. *Appl. Surf. Sci.* **2022**, *579*, 152264.
(33) Dunderdale, G. J.; Urata, C.; Miranda, D. F.; Hozumi, A. *ACS Appl. Mater. Interfaces* **2014**, *6* (15), 11864–11868.
(34) Zoppe, J. O.; Ataman, N. C.; Mocny, P.; Wang, J.; Moraes, J.; Klok, H. A. *Chem. Rev.* **2017**, *117* (3), 1105–1318.
(35) Kuzmyn, A. R.; Nguyen, A. T.; Teunissen, L. W.; Zuilhof, H.; Baggerman, J. *Langmuir* **2020**, *36* (16), 4439–4446.
(36) Glinel, K.; Jonas, A. M.; Jouenne, T.; Leprince, J.; Galas, L.; Huck, W. T. S. *Bioconjug. Chem.* **2009**, *20* (1), 71–77.
(37) Teunissen, L. W.; Kuzmyn, A. R.; Ruggeri, F. S.; Smulders, M. M. J.; Zuilhof, H. *Adv. Mater. Interfaces* **2022**, 2101717.
(38) Jones, D. M.; Smith, J. R.; Huck, W. T. S.; Alexander, C. *Adv. Mater.* **2002**, *14* (16), 1130–1134.
(39) Kreer, T. *Soft Matter* **2016**, *12* (15), 3479–3501.
(40) Brady, G. W. *Acc. Chem. Res*. **1974**, *7* (6), 174–180.
(41) Brady, G. W. *J. Chem. Phys.* **1974**, *60* (9), 3458–3465.
(42) Brady, G. W. *J. Chem. Phys.* **1973**, *58* (9), 3542–3546.
(43) Michalek, L.; Barner, L.; Barner-Kowollik, C. *Adv. Mater.* **2018**, 1706321.
(44) Gruszkiewicz, A.; Słowikowska, M.; Grześ, G.; Wójcik, A.; Rokita, J.; Fiocco, A.; Wytrwal-Sarna, M.; Marzec, M.; Trzebicka, B.; Kopeć, M.; Wolski, K.; Zapotoczny, S. *Eur. Polym. J.* **2019**, *112*, 817–821.
(45) Kang, C.; Crockett, R. M.; Spencer, N. D. *Macromolecules* **2014**, *47* (1), 269–275.
(46) Patil, R. R.; Turgman-Cohen, S.; Šrogl, J.; Kiserow, D.; Genzer, J. *ACS Macro. Lett.* **2015**, *4* (2), 251–254.
(47) Kuzmyn, A. R.; van Galen, M.; van Lagen, B.; Zuilhof, H. *Polym. Chem.* **2023**, *14*, 3357.
(48) Yu, Y.; Vancso, G. J.; de Beer, S. *Eur. Polym. J*. **2017**, *89*, 221–229.
(49) Kang, C.; Crockett, R.; Spencer, N. D. *Polym. Chem.* **2016**, *7* (2), 302–309.
(50) Beiner, M.; Schröter, K.; Hempel, E.; Reissig, S.; Donth, E. *Macromolecules* **1999**, *32* (19), 6278–6282.
(51) Garwe, F.; Scho, A.; Lockwenz, H.; Beiner, M.; Schro, K.; Donth, E. *Macromolecules* **1996**, *29*, 247–253.

Chapter 4

A DFT Study of Imine Exchange Reactions in Iron(II)-Coordinated Pincers

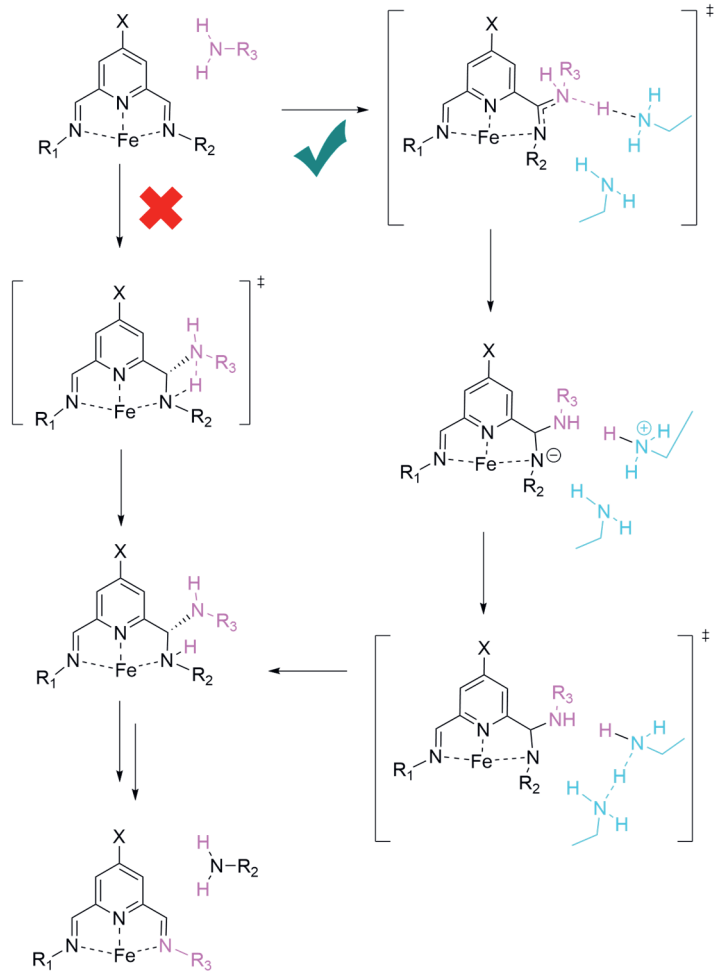

This chapter has been published as:

Annemieke van Dam, Robin van Schendel, Satesh Gangarapu, Han Zuilhof, Maarten M. J. Smulders, *Chem. Eur. J.* **2023**, e202301795.

https://doi.org/10.1016/j.apsusc.2021.152264.

Abstract

The imine bond is among the most applied motifs in dynamic covalent chemistry. Although its uses are varied and often involve coordination to a transition metal for stability, mechanistic studies on imine exchange reactions so far have not included metal coordination. In the research described in this chapter, we investigated the condensation and transimination reactions of an Fe^{2+}-coordinated diimine pyridine pincer, employing wB97XD/6-311G(2d,2p) DFT calculations in acetonitrile. We first experimentally confirmed that Fe^{2+} is strongly coordinated by these pincers, and is thus a justified model ion. When considering a four-membered ring-shaped transition state for proton transfers, the required activation energies for condensation and transimination reaction exceeded values expected for reactions known to be spontaneous at room temperature. The nature of the incoming and exiting amines and the substituents on the *para*-position of the pincer had no effect on this. Replacing Fe^{2+} with Zn^{2+} or removing it altogether did not reduce it either. However, addition of two ethylamine molecules lowered the energy barriers to be compatible with the experiments (19.4 and 23.2 kcal/mol for condensation and transimination, respectively). Lastly, the energy barrier of condensation of a non-coordinated pincer was significantly higher than found for Fe^{2+}-coordinating pincers, underlining the catalyzing effect of metal coordination on imine exchange reactions.

4.1 Introduction

Since the start of the twenty-first century, dynamic covalent chemistry has become increasingly popular.[1] The characteristic combination of reversibility and robustness that defines dynamic covalent bonds has enabled a variety of new concepts and applications in various fields, ranging from dynamic combinatorial libraries to supramolecular chemistry and from molecular machines to materials chemistry.[2-8] For example, in the field of polymer chemistry, covalent adaptable networks (CANs)[9-11] have shown to be a new class of polymers with the robustness of thermosets but the malleability and repairability of thermoplasts,[12-14] bringing degradability and recyclability of network polymers within reach.[15] In the field of supramolecular chemistry, the use of dynamic covalent chemistry has led to the formation of self-assembled cages, largely driven by the possibility of a thermodynamically controlled assembly of large complexes.[16-20] These cages can be used for the transport of small chemicals,[21] but also allow reactions to take place in an artificially high concentration in its confined space.[22] Furthermore, the operation of molecular walkers[23] and the synthesis of metal-organic frameworks[24] hinge on dynamic covalent chemistry.

The dynamic covalent bond motif that is among the most explored is the imine bond, or Schiff base.[25] This imine bond can undergo various dynamic reactions,[26] none of which require a metal catalyst.[27] Imine exchanges have been used in molecular machines, where an aldehyde can 'walk' along a chain of amines.[28] In cages, the imine bond is also vastly popular, as the bond's dynamic nature allows for error-checking during the assembly of the –typically– large number of components that need to come together in a single cage structure.[18, 29-30] Also, within the context of systems chemistry, the imine bond has been used to establish dynamic combinatorial libraries that can collapse upon addition of a suitable target/template.[31-34] Finally, for covalent organic frameworks,[35-38] the dynamic imine bond is crucial to their (equilibrium) synthesis and for their ultimate structure and performance.

Imines are formed reversibly from an aldehyde and an amine. Due to the large variation in commercially available aldehydes and amines, the imine motif offers ample opportunity to create a macrostructure with the desired function or properties. Moreover, exchange of material-bound amines,[39] for example from

an alkylamine or hydrazine to an alkoxyamine, offers the possibility to –post-synthetically– alter a functionality of a material.

A general drawback of imines for materials science is their tendency to hydrolyze.[40] Coordination to a transition metal has been shown to drastically reduce this effect,[41] without hindering the responsive character of the structure. Imine-metal complexes can form stable structures, displaying two orthogonal types of changeability: both the C=N imine bond and the N–M coordination bond can undergo reversible reactions. This so-called "subcomponent self-assembly" has been showcased first by Nitschke and Lehn,[42] and has since then been widely applied in metal-organic cage syntheses.[21, 43-46] Not only cages, but also other types of structures such as grids,[47] macrocycles[48] and metallogels,[49] can be formed by subcomponent self-assembly.[50-51]

Our group has taken the double versatility of imine-metal coordination complexes and applied it to polymeric systems.[52] We created a 2,6-diimine pyridine pincer motif that is connected via a linker to another identical pincer motif. This was shown to create networks with physical properties that could be altered by external stimuli, both via imine exchange reactions and through replacement of the metal center. These networks have been developed in organic solvents, such as acetonitrile. Furthermore, this traditional 2,6-diimine pyridine pincer motif[53] has also been used in cages,[54] knots,[55] tunable gas membranes[56] and other (self-healing) polymer networks.[57-59] While in our previous work, we mostly considered Zn^{2+} for the construction of dynamic coordination polymers,[52] the 2,6-diimine pyridine pincer motif has been combined with a large number of transition metals, including Mn^{2+}, Fe^{2+}, Co^{2+}, Ni^{2+}, Cu^{2+}, Zn^{2+}, Cd^{2+}, Hg^{2+}, and Pd^{2+}.[60-62]

In contrast to the wide range of applications that rely on imine bonds and imine bond exchange reactions, the full mechanistic details of the underlying exchange reactions of imine pincers have received very little attention. It is well-known that Schiff bases can undergo three imine exchange reactions: condensation, with hydrolysis as its reverse reaction, transimination and imine metathesis (Scheme 4.1).[27] In condensation, the amine attacks the aldehyde to first form a carbinolamine, followed by elimination of water. Transimination is the attack of an amine group on the carbon of the imine, creating an aminal,

after which the original amine leaves, and the attacking amine forms an imine bond with the carbon. In imine metathesis, two imine moieties find each other, and through a double [2,2]-metathesis, the carbon and nitrogen atoms of the imines switch partners.

Scheme 4.1. Three reversible reactions of Schiff bases: condensation, with hydrolysis as the reverse reaction, transimination and imine metathesis.

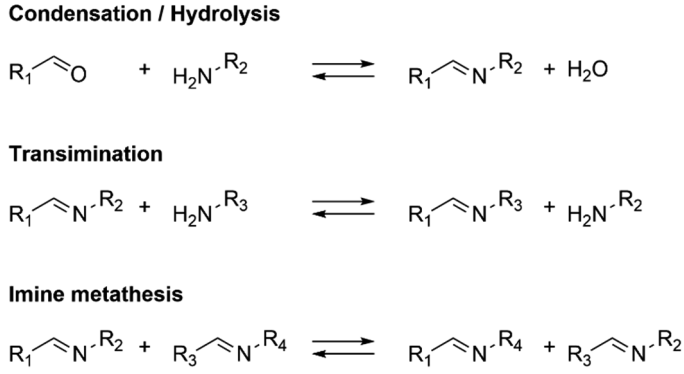

Over the years, insightful computational research has been performed on imine exchange reactions.[27] Ciaccia and co-workers have calculated the transimination and condensation reactions in the presence of primary amines.[63] They suggested a four-membered ring transition state for the proton transfers to be the most likely pathway, as opposed to consecutive protonation and deprotonation. If water is present, the energy of the proton transfer transition states can be lowered by using one or two water molecules as proton shuttles, forming a six- or eight-membered ring, respectively.[64-65] Primary amines can also take up this role, but their effect is less than that of water. Zheng and co-workers have shown that non-covalent interactions of an electron donor with an imine or aldehyde can significantly reduce imine exchange rates.[66] In their case, the interaction was a hydrogen bond. To the best of our knowledge, and in contrast to the rapidly rising amount of experimental work that has been reported,[21, 67-68] the effect of coordination with transition metals on imine exchanges has not yet been studied theoretically, even though it is known that metal coordination alters the electronic and structural shape of a ligand.[69]

In this work, we explore the imine exchange reactions of Fe^{2+}-pincer complexes in acetonitrile by computational means. Using a state-of-the-art functional and

basis set (wB97XD/6-311G(2d,2p)) for our DFT calculations, we investigate the condensation and transimination reactions of a range of pincers. Various amines and imines are considered, and the effect of the pyridine *para*-position's nucleophilicity is included (Figure 4.1). For the final proton transfer from carbinolamine and aminal species to the separate products, both a previously proposed four-membered transition state[63] and two ethylamines as proton shuttles are considered. As pincers drastically reduce the freedom of movement of individual imine moieties, imine metathesis is considered unlikely and therefore not part of the investigation.

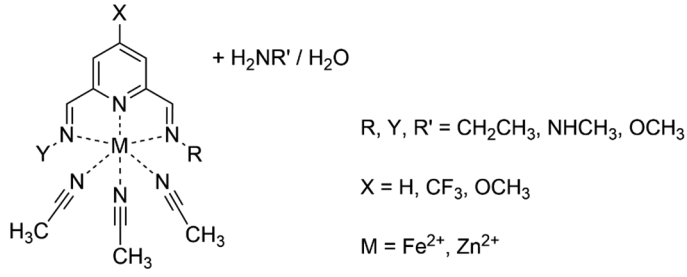

Figure 4.1. Imine pincer complexes under current study that are formed via condensation or transimination.

4.2 Results and discussion

Following our previous report on the use of Zn^{2+} as metal ion to coordinate to a 2,6-diimine pyridine ligand,[52] our current aim was first to see whether a stronger binding metal ion would be available. Following literature on the use of Fe^{2+} as alternative metal ion in polymeric systems featuring a similar pincer motif,[56] and keeping the availability of this innocuous metal in mind, we set out to determine whether the 2,6-diimine pyridine ligand would indeed bind more strongly to Fe^{2+}. As the complexation of the metal ion to the ligand leads to strong coloration of the solution (Figure 4.2a), we performed a UV-vis titration to monitor formation of the metal-ligand complex (details in Supporting Information, section 4.4.4). We plotted the increase in absorption (at 370 nm for Zn^{2+} and at 613 nm for Fe^{2+}) as function of the equivalence of metal ion added (Figure 4.2b). Comparing the results for Zn^{2+} and Fe^{2+} in Figure 4.2B, it can be seen that, while both metal ions can bind strongly to the pincer, the binding for Fe^{2+} is strongest, as is evidenced by the steeper increase in absorption as function of equivalence of metal ion added, and by the fact that the maximum

absorption is reached at lower equivalence of metal for Fe^{2+} than for Zn^{2+}. Our observations are in agreement with earlier work on structurally similar (tridentate) terpyridine-based ligands that also report a higher binding constant for binding to Fe^{2+} than to Zn^{2+}.[70] Given the stronger binding for Fe^{2+} we decided to focus our calculations on this metal ion, and only study the Zn^{2+} ion for specific cases.

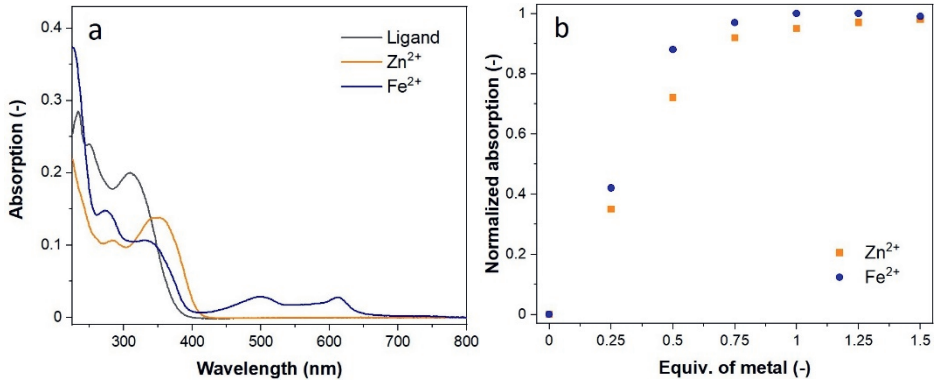

Figure 4.2. (a) UV-vis spectrum of the diiminepyridine ligand, and the diiminepyridine:metal complex (5 equiv. of metal ion). Ligand concentration: $1.0 \cdot 10^{-5}$ M in acetonitrile. Path length: 1.0 cm. (b) Metal titration of Zn^{2+} or Fe^{2+} to the diiminepyridine ligand: the normalized absorption (recorded at 613 nm for Fe^{2+} and at 370 nm at Zn^{2+}) was plotted as function of the equivalence of metal. Ligand concentration: $1.0 \cdot 10^{-5}$ M in acetonitrile.°

4.2.1 Condensation Reaction Without Proton Shuttles

The condensation reaction between [iron(II) 2-methoxo-6-ethylimine pyridine $(NCCH_3)_3]^{2+}$ and ethylamine (Figure 4.3) initially yields a zwitterionic hemiaminal (**B**) at ΔG = –6.5 kcal/mol driving force. In line with previous research,[27] a four-membered ring was taken as the transition state for the proton transfer from the nitrogen to the oxygen, at $\Delta G^{\ddagger}$ = 11.4 kcal/mol (**TS-1**). The resulting hemiaminal (**C**) was found at ΔG = –8.8 kcal/mol. Dihedral rotation from the hemiaminal with alcohol coordination to the one with amine coordination occurred via a transition state of $\Delta G^{\ddagger}$ = 3.0 kcal/mol (**TS-2**). In this transition state, the bond length of Fe–O was significantly elongated from 2.07 Å to 3.00 Å, while the coordination of the amine did not yet start: the bond length is 3.39 Å in the transition state and only 2.08 Å in the resulting hemiaminal (**D**). Due to

this dissociation, the energy barrier was higher than expected for a simple rotation.

The hemiaminal with amine coordinated to the iron center (**D**) was at ΔG = -17.6 kcal/mol significantly more stable than the hemiaminal with alcohol coordination (**C**). The second proton transfer was not followed by another zwitterionic intermediate, but immediately resulted in water elimination. The four-membered ring transition state (**TS-3**) was found with a relative Gibbs free energy of +34.0 kcal/mol, making this the rate-limiting step with a barrier of $\Delta G^{\ddagger}$ = 51.6 kcal/mol. In this four-membered ring, the N–H bond at 1.46 Å and the O–H bond at 1.14 Å were at a strained 118.8°. This means no hydrogen bonding takes place in this transition state, explaining the extremely high energy barrier. The final compound (**E**) was found at ΔG = –16.7 kcal/mol. However, due to the energy barrier of 51.6 kcal/mol, the condensation reaction via this pathway can be ruled out at room temperature in acetonitrile.

To investigate the effect of the metal center, this condensation reaction was also calculated without a metal and with Zn^{2+} as metal (Figure 4.3, in red and blue, respectively). Already in the first step the stabilizing role of the metal becomes very clear, with, *e.g.*, about a 10 kcal/mol difference of the metal-free system compared to the Fe^{2+}-stabilized complex. In addition, for the metal-free system the first proton transfer, yielding **TS-1**, now required 32.0 kcal/mol instead of 17.9 kcal/mol, while the barrier for the second proton transfer **TS-3** was not reduced significantly. In absence of a metal center, there is no rotation of the incoming nitrogen towards the metal center (*i.e.*, **TS-2** does not exist and **D** is equal to **C**). Lastly, the driving force for the overall reaction from aldehyde to imine in the non-coordinated reaction is small, only 3.0 kcal/mol. Thus, without a metal, the barriers are not reduced but the driving force is largely lost.

As experimental work has been carried out with Zn^{2+} as well as Fe^{2+}, we also calculated the condensation reaction with Zn^{2+} as metal center (Figure 4.3, in blue). Adduct **B** formation gained less energy than with Fe^{2+} and the total energy gain is slightly less, both in line with our experimental findings that Fe^{2+} is stronger binding than Zn^{2+}. Proton transfers **TS-1** and **TS-3** have similar energy cost as with Fe^{2+}. However, the rotation **TS-2** required significantly more energy. This higher $\Delta G^{\ddagger}$ for rotation can be explained by the non-symmetrical octahedral

coordination geometry that Zn^{2+} has formed, in which the three acetonitrile ligands are slightly pushed towards the non-reactive amine of the pincer, resulting in stronger binding of the reacting amine. In all, we can conclude that the condensation reaction is most favorable with Fe^{2+}, but also that a different pathway for proton transfer must be found.

It is known that the choice of functional in DFT can have an effect on the energy barriers that are found. To exclude this bias, we recalculated the Gibbs Free energies with B97D and MO6-2X of structures **A**, **D**, **TS-3** and **E** for the condensation reactions with Fe^{2+}, Zn^{2+} and without metal (Supporting information, section 4.4.5, Table 4.1). The condensation reactions were not more likely with these functionals, ruling out any method bias.

The final compound (**E**) was found at ΔG = –16.7 kcal/mol. This value is expected to become more negative (*i.e.*, approximately –22 to –23 kcal/mol) with improved explicit solvation of the released water, which is known to be insufficiently treated using implicit solvent models. Such additional explicit solvation (also relevant for the data in Figures 4.4 – 4.6) was demonstrated for release of water in the imine formation (online Supporting Information, section S4.3), but this larger size due to additional freely 'floating' solvent molecules becomes, however, impractical –especially for the transition state calculations– while it is expected to only play a significant role when water is freely solvable, *i.e.*, after release from the C atom. Therefore, we did not include it in the structures used to construct Figures 4.3 – 4.6, but note that with such additional solvation the imines became the most stable systems, as also found experimentally. However, although thus being thermodynamically attractive, due to the energy barrier of 51.6 kcal/mol, the condensation reaction via this pathway can be ruled out at room temperature in acetonitrile.

4.2.2 Transimination Reaction Without Proton Shuttles

Next to the imine formation (condensation) reaction, we also studied the imine exchange reaction by transimination, in which a free amine attacks an existing imine. Figure 4.4 (in black) shows the energy profile of the transimination reaction between [iron(II) 2,6-bis-ethylimine pyridine $(NCCH_3)_3]^{2+}$ and ethylamine, and (in red) the metal-free system. Both symmetric energy profiles with the four-membered ring transition state of the proton transfer yield

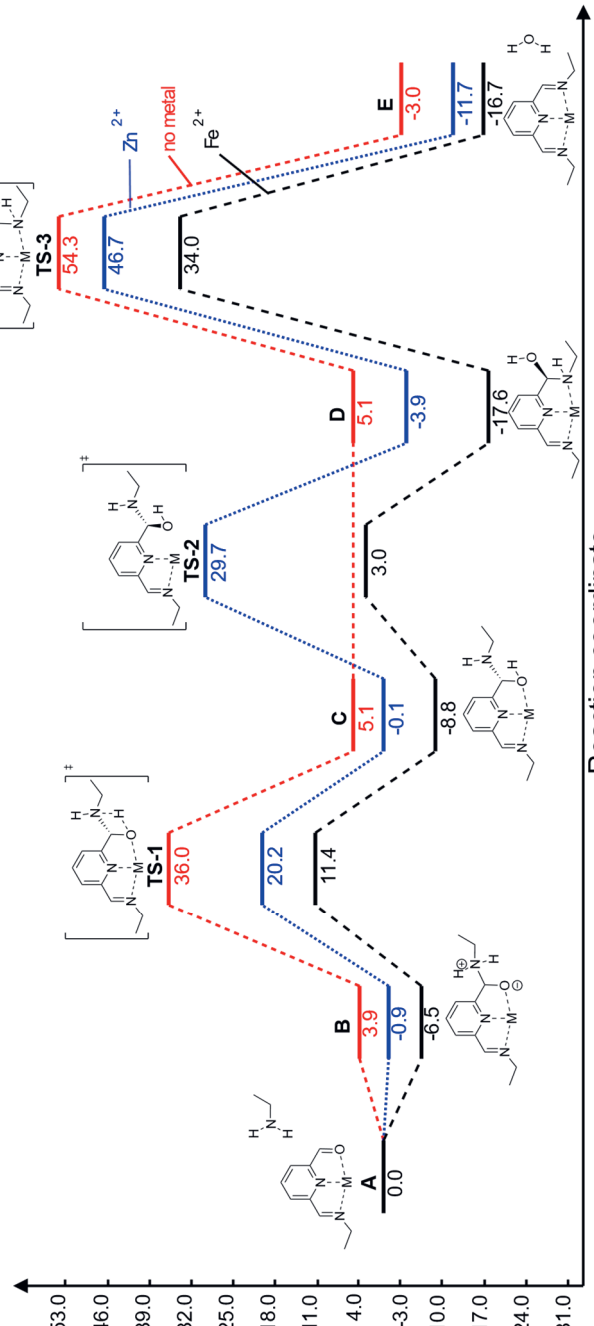

Figure 4.3. Gibbs free energy profile for the condensation reaction between ethylamine and [iron(II) 2-methoxo-6-ethylimine pyridine $(NCCH_3)_3]^{2+}$ (black), [zinc(II) 2-methoxo-6-ethylimine pyridine $(NCCH_3)_3]^{2+}$ (blue), and 2-methoxo-6-ethylimine pyridine (red), calculated without explicit solvation. All energy profiles are produced using free software from Angnes.[71] The second proton transfer, from **D** to **TS-3**, is rate-limiting in all cases with an energy barrier of 51.6, 50.6 and 49.2 kcal/mol, respectively. Note: For both the Fe^{2+} and Zn^{2+}-complex, even an extensive variation in computational parameters did not yield an activation energy of rotation (*i.e.*, structure **TS-2** could not be localized). The maximum energy of the reaction coordinate scan (step size C–C bond torsion of 1°) was taken instead.

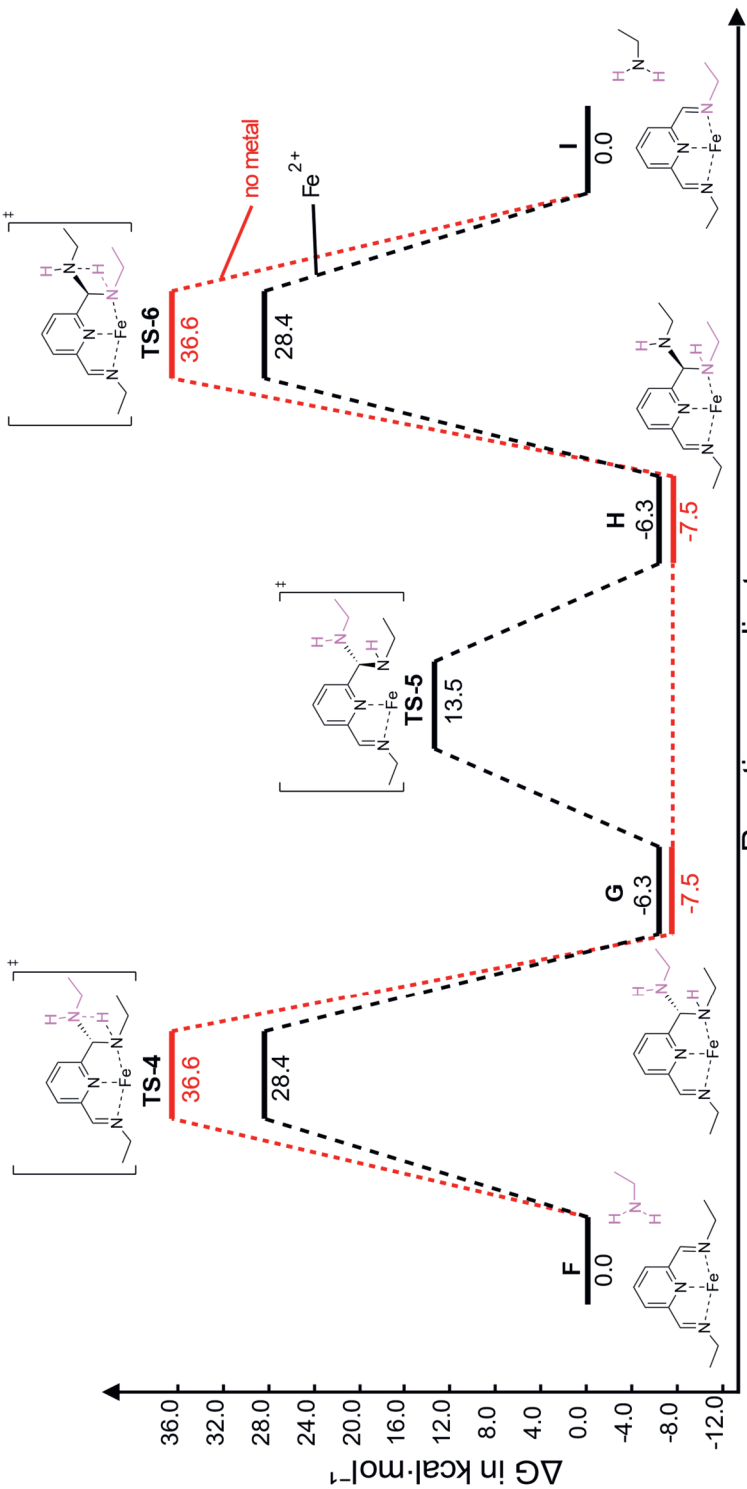

Figure 4. 4. Gibbs free energy profile for the transimination reaction between [iron(II) 2,6-bis-ethylimine pyridine $(NCCH_3)_3]^{2+}$ and ethylamine (black), and between 2,6-bis-ethylimine pyridine and ethylamine (red) , calculated without explicit solvation. The second proton transfer, from **H** to **TS-6**, is rate-limiting with an energy barrier of 34.7 and 44.1 kcal/mol, respectively. Structures of the black pathway are provided. For clarification, the incoming ethylamine has been colored pink.

activation energies of >34 kcal/mol. However, exchanges of imines, hydrazones and oximes occur readily at ambient conditions in acetonitrile. Oximes are more inert in neutral or basic conditions, yet become dynamic in acidic conditions.[72-73] Thus, the four-membered ring TS should be discarded as viable hypothesis, and other mechanistic routes need to be investigated.

4.2.3 Condensation Reaction With Proton-Shuttling Amines

To bypass the high-energy barriers resulting from the four-membered ring TS route, we investigated proton transfers facilitated by proton shuttles, as is known to work in experimental setting[74-76] and has been calculated recently for metal-free dynamic exchanges.[64-65, 77] According to Rufino and Pliego,[65] using two water molecules as shuttle decreases the energy barrier for condensation of acetaldehyde with methylamine from 47.7 to 26.4 kcal/mol (in toluene at 298 K). Using a carboxylic acid group as proton shuttle further reduces the barrier to 15.8 kcal/mol (in acetonitrile or toluene, at 298 K). Kirmizialtin and co-workers[77] have shown that the calculated cost of condensation of oximes in water can be reduced from 31.4 kcal/mol to 12.9 kcal/mol by adding two explicit water molecules. These promising studies enticed us to investigate the role of proton shuttles for the hitherto not-studied case of metal-stabilized pincer molecules. This is especially relevant since here not only the TS might be stabilized by proton shuttles, but the starting materials, of course, also by metal ions (and, *e.g.*, inverting the equilibrium between aldehydes and imines from 'towards aldehydes' without metal coordination to 'towards imines' with metal coordination).[78] In the dynamic polymer systems that form the experimental basis for our calculations,[52] only trace amounts of water are present, whereas free amines are present in excess. Therefore, two ethylamines were used as proton shuttles in the calculation of the condensation reaction between [iron(II) 2-methoxo-6-ethylimine pyridine $(NCCH_3)_3]^{2+}$ and ethylamine (Figure 4.5, in black). The two hydrogen transfers (turning R–NH_2 into R–N=C) were thereby transformed to multistep processes involving eight-membered rings.

Starting from adduct **K**, a proton was transferred from the incoming ethylamine to the first mediating ethylamine, leading to intermediate **L** (+1.9 kcal/mol). Then, another proton on that ethyl amine is moved from the first to the second mediating ethylamine, requiring another 5.9 kcal/mol (transition state **TS-8**). Finally, a similar, third proton movement from the second mediating ethylamine

to the aldehyde on the pincer completed the first transfer into hemiaminal **M**. Various scans and IRC calculations showed that there is no intermediate between transition state **TS-8** and hemiaminal **M**. Rotation of the hemiaminal from one coordination to the other, thus from **M** to **N**, required an additional 14.9 kcal/mol. The proton-shuttling amines are not involved in this step. This rotation **TS-9** is rate-determining with $\Delta G^{\ddagger}$ 19.4 kcal/mol. The second mediated proton transfer followed an analogous path, but now the proton moves backwards. Starting at hemiaminal **N**, a proton is moved from the donating ethylimine to the first mediating ethylamine, followed immediately by a second proton transfer from the first mediating ethylamine to the second. This transition state **TS-10** required 16.9 kcal/mol, and only showed the movement of the second proton; multiple scans and IRCs did not yield a stable intermediate with an ammonium-like structure for the bottom amine molecule (see molecular structures in Figure 4.5) between hemiaminal **N** and **TS-10**. After **TS-10**, we found stable intermediate **O** at 15.7 kcal/mol, in which the top ethylamine had the extra proton. A final proton transfer lead to water elimination, resulting in the product **P** at –1.9 kcal/mol. Compared to the non-mediated pathway, the gain is significant, reducing the energy barrier from more than 50 kcal/mol to just 19.4 kcal/mol. The ethylamine-mediated route can thus be considered a viable reaction at room temperature.

This mediated condensation reaction was also calculated in the absence of a metal center (Figure 4.5, in red). The first proton transfer now required less energy in the absence of Fe^{2+}, and the hemiaminal **M** without metal center was very stable (–14.1 kcal/mol), much more than the Fe^{2+}-coordinated hemiaminal **M** (4.5 kcal/mol). Although the energies of **TS-10** of both systems were in the same range, the energy barrier for condensation without metal was much larger (32.8 kcal/mol), due to the higher stability of the hemiaminal **N**. Imine pincer **P** is more stable as well (–10.5 kcal/mol instead of –1.9 kcal/mol). As a consequence, backwards reaction from imine pincer **P** to adduct **K** has an energy barrier of 29.2 kcal/mol in its first two proton transfers, with hemiaminal **M** as most stable structure.

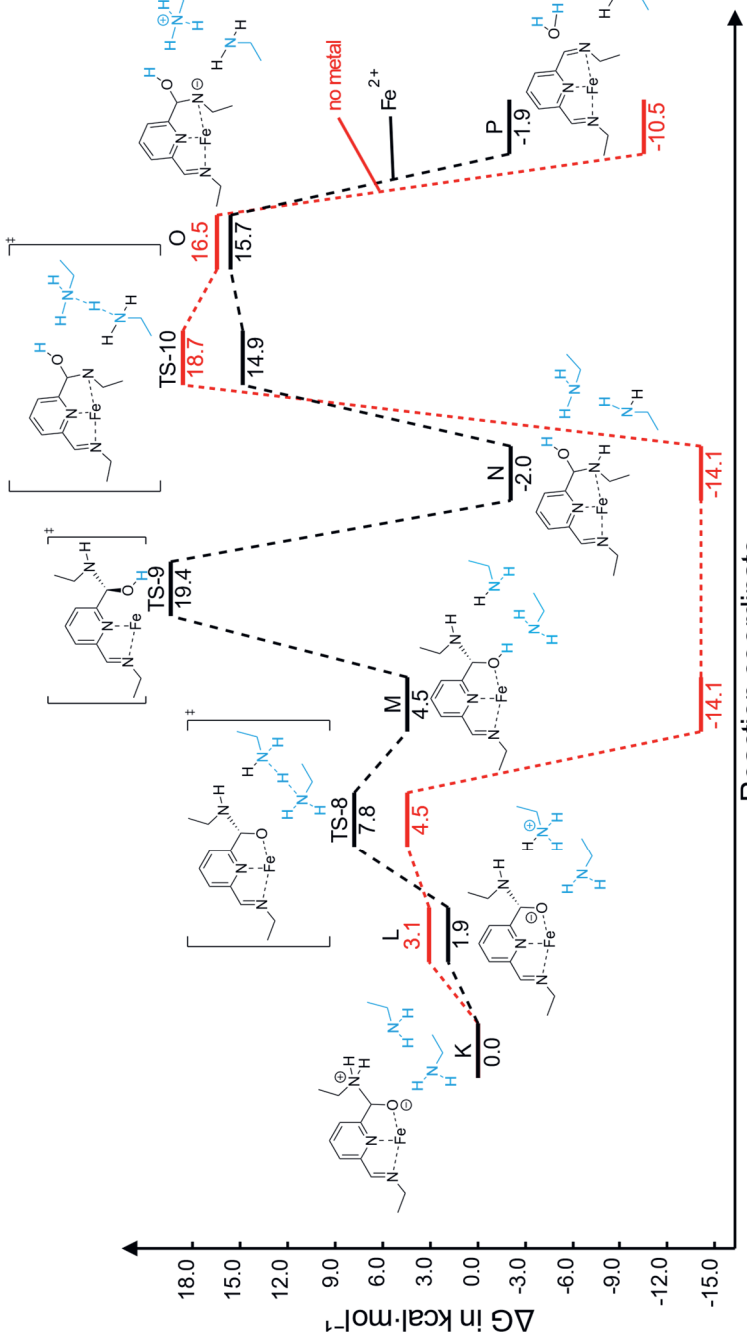

Figure 4.5. Gibbs free energy profile for the condensation reaction between ethylamine and [iron(II) 2-methoxo-6-ethylimine pyridine (NCCH3)3]2+ (black), and 2-methoxo-6-ethylimine pyridine (red), both with two additional ethylamines acting as proton shuttles, calculated without explicit solvation. At 19.4 kcal/mol, the rotation TS-9 is rate-limiting if Fe2+ is present. In absence of a metal, the barrier of 32.8 kcal/mol from N to TS-10 is rate-limiting. Structures of the black pathway are provided. For clarification, the mediating ethylamines have been colored blue.

In this amine-mediated condensation reaction, we have thus again shown the catalyzing effect of Fe^{2+}-coordination. It lowers the energy barrier from 32.8 kcal/mol to 19.4 kcal/mol, and provides the driving force to push the condensation from hemiaminal to pincer complex to completion.

4.2.4 Transimination Reaction With Proton-Shuttling Amines

Subsequently, the transimination reaction was also calculated for [iron(II) 2,6-bis-ethylimine pyridine $(NCCH_3)_3]^{2+}$ and ethylamine with two extra ethylamines acting as proton shuttles. As the transimination reaction is symmetrical, the reaction is only calculated until the rotation of the aminal (Figure 4.6).

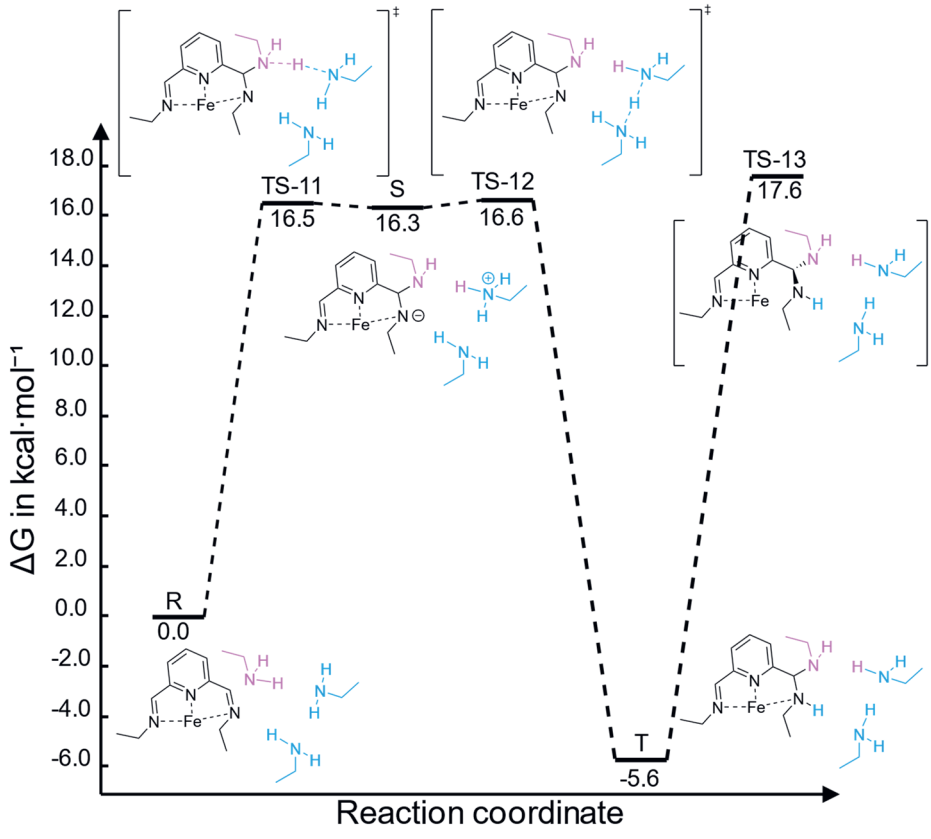

Figure 4.6. Gibbs free energy profile for the mediated transimination reaction between [iron(II) 2,6-bis-ethylimine pyridine $(NCCH_3)_3]^{2+}$ and ethylamine, calculated without explicit solvation. With 23.3 kcal/mol, rotation of the aminal (**T** to **TS-13**) is rate-limiting. For clarification, the incoming ethylamine has been colored pink and the mediating ethylamines are blue.

The amine-mediated proton transfer yields two transition states **TS-11** and **TS-12** and an intermediate **S**, all around 16.5 kcal/mol. The formed aminal **T** was found at –5.6 kcal/mol compared to the starting materials, and the rotation of the aminal **TS-13** at 17.6 kcal/mol. Analogously to the condensation reaction, the proton-shuttling lowered the activation energy of the proton transfer to such an extent that the rotation is now rate-determining. With a total energy barrier of 23.2 kcal/mol, we can conclude that this mediated transimination reaction is plausible at room temperature.

4.2.5 Condensation Reaction With Two Pincer ligands

In all calculations, we have – for reasons of computational efficiency – assumed coordination of a single pincer and three acetonitrile molecules to the metal center. However, we know from experimental work that double pincers (*i.e.*, the pincers exist as 1:2 metal to ligand complex) are predominant.[52] To validate the computational approach taken, we also performed the calculation of the condensation reaction of Fe^{2+} with two pincer ligands (Supporting Information, section 4.4.6). This reaction displayed an energy path similar to the one with a single pincer and three acetonitrile ligands, with only slightly higher energy barriers for the proton transfers via the four-membered ring TS. Following this result, we considered our use of single pincer complexes as a valid computational simplification.

4.2.6 Structural Variations in The Non-Amine-Mediated Condensation Reaction

The exchange reactions under current study can be readily varied using different nucleophiles and changing various electronic factors of possible importance, as has indeed been done experimentally to quite some detail.[28, 52, 79-80] We have thus compared the condensation reactions of the aldehyde pincer with ethylamine, methylhydrazine or methoxyamine as nucleophiles (online Supporting Information, section S4.5). As we have taken the four-membered ring transition state for proton transfer, $\Delta G^{\ddagger}$ remains high (>47.8 kcal/mol).

In non-coordinated aromatic imines, substituents on the ring have strong influence on the reactivity of the imine, as they alter the electron density of the imine.[39] In the presence of a metal, this could be different. The condensation reaction was therefore calculated for pincers in which the X and Y positions were

altered (Figure 4.1, online Supporting Information, section S4.6). Substitution of the hydrogen atom on the X-position by the electron-withdrawing $–CF_3$ group or the electron-donating $–OCH_3$ group resulted in less than 2 kcal/mol change in any step, regardless of the nature of the imine and amine of the system. Additionally, when changing the non-reactive imine of a double pincer from ethylimine to hydrazone or methoxime (position Y in Figure 1), no changes in energy were observed either (Table S4.2). Substitutions of the R', X and Y positions in the transimination reaction showed similar results (online Supporting information, sections S4.7 and S4.8) We can therefore conclude that neither meta-position is relevant to our imine exchanges. Neither factor is expected to change in character when considering the amine-mediated reactions, suggesting that rotation of the (hemi-)aminal is indeed the energetically most relevant process.

4.3 Conclusions

We studied the condensation reaction of a metal-coordinated aldehyde pincer with ethylamine, via either a four-membered ring transition state for the proton transfers, as previously proposed in literature, or via an unstrained transition state involving two proton shuttles. The former activation barrier was calculated to be much higher (52 kcal/mol) than experimentally observed (the reaction proceeds readily at room temperature), making such a strained transition state unlikely. In contrast, with the involvement of two ethyl amines as proton shuttles the calculated activation energy dropped to 19 kcal/mol, which is compatible with experiments. This confirmed our hypothesis that the imposed ring strain of the four-membered transition state unnecessarily increased the energy barrier. While this insight was previously known for single proton shuttles,[65] here we demonstrated its viability in acetonitrile with multiple amines in the presence of a metal center.

For the transimination reaction a similar reduction in activation energy was found: the non-mediated pathways required 34–43 kcal/mol depending on the nature of studied amine, whereas the amine-mediated proton transfer required only 23 kcal/mol. These calculations thus explain the advantages of the experimentally common addition of a small excess of free amine in the production of dynamic imine/amine-based vitrimer materials in order to speed up the exchange.[81-82]

Titration experiments showed that Fe^{2+} binds stronger to the studied pincers than Zn^{2+}. Calculation of the condensation reaction without proton shuttles further confirmed that the Fe^{2+} is better suited for these imine exchange reactions. Finally, our calculations also provide – for the first time – theoretical support for the stabilizing effect of coordination of the imine to the metal center, which was already experimentally found in cage formations[43] and other subcomponent self-assemblies.[51]

4.4 Supporting information

The full supporting information is available with the published paper online at: https://doi.org/10.1002/chem. 202301795.

4.4.1 Computational methods

Density functional calculations (DFT) – geometry optimization, vibrational frequency calculations and IRC calculations – were performed using the Gaussian 16 suite of programs,[83] with the wB97XD functional[84-85] and 6-311G(2d,2p) basis set as implemented in there. Although transition metals such as iron are well-defined in this basis set, geometry connectivity was added to ensure coordination to the iron where desired. All (natural population) charges and Wiberg bond orders were calculated using the NBO 3.1 program as implemented in Gaussian 16. Generic solvent effects were incorporated by using the universal solvation model based on density (SMD)[86]. Acetonitrile was chosen as the model solvent, as experimental work on imine pincer-based polymers has been reported for acetonitrile.[52] Gibbs free energies are reported in a standard state: at 298 K and 1 bar pressure. Output of all geometry optimizations is provided in the online Supporting Information (sections S4.9 and S4.10).

In each reaction step in which more than one molecule is involved (for example, structures **A** and **E** in Figure 4.3), all molecules were calculated as part of a single computation at a minimum 3.6 Å distance. In the mediated pathways however, all starting and ending molecules were calculated separately. For crucial transition states, full IRC analysis was performed, confirming the nature of the transition state. The rotational transition state of the transimination reaction (**TS-2** in Figure 4.3) required multiple extensive rotational scans, followed by a transition state search involving IOp(1/8=2). For computational simplicity, only

a single pincer was coordinated to an iron(II) center. The other three coordination sites were occupied by explicit acetonitrile ligands (Figure 4.1).

4.4.2 Materials and Methods

^{1}H NMR and ^{13}C NMR spectra were recorded on a Bruker Avance III 400 spectrometer (observation of ^{1}H nucleus at 400 MHz, and of ^{13}C nucleus at 101 MHz). Chemical shifts are reported in parts per million (ppm), calibrated on the residual peak of the solvent, whose values are referred to tetramethylsilane (TMS, δ_{TMS} = 0 ppm), as the internal standard. ^{13}C NMR spectra were performed with proton decoupling. High-resolution ESI mass spectra were recorded on a Thermo Scientific Q Exactive High-Resolution mass spectrometer. UV-vis spectra were recorded on a Varian Cary 50 spectrophotometer.

4.4.3 Synthesis of the diiminepyridine pincer

2,6-pyridinedicarboxaldehyde (5.2 mmol, 700 mg) was dissolved in 35 mL absolute methanol, containing molecular sieves. Aniline (10.4 mmol, 975 µL) was added to the solution and the reaction mixture was stirred under reflux for 2 hours. The hot reaction mixture was filtered, over a normal filter and washed with hot methanol (50 °C). The solvent was removed *in vacuo*. The product was dried in the oven overnight and obtained as yellowish powder in 1.22 g yield (82%). ^{1}H NMR (400 MHz, Chloroform-d) δ 8.70 (s, 2H), 8.31 (d, J = 7.8 Hz, 2H), 7.96 (t, J = 7.8 Hz, 1H), 7.44 (dd, J = 8.4, 7.2 Hz, 4H), 7.36 – 7.28 (m, 6H). ^{13}C NMR (101 MHz, Chloroform-d) δ 160.14, 154.66, 150.84, 137.30, 129.26, 129.25, 126.90, 123.23, 123.19, 121.18, 121.16, 77.21. High-res. MS (ESI): Expected for $[M+H]^+$ 286.1339, found 286.1339.

4.4.4 Titration

For the metal-to-ligand titration two solutions were prepared. A: ligand (*i.e.*, diiminepyridine) solution (without metal salt) in acetonitrile ($1.0\cdot10^{-5}$ M), and B: ligand solution with 5 equivalent of metal salt in acetonitrile. Ligand concentration was $1.0\cdot10^{-5}$ M, while metal concentration was $5.0\cdot10^{-5}$ M. As metal salt, $Fe(OTf)_2$ and $Zn(OTf)_2$ were used.

Mixing solutions A and B in the appropriate ratio allowed for the titration curve of each metal to be recorded by UV-vis spectrometry. After mixing, 30 min of equilibration time was allowed. Figure 4.2A shows the UV-vis spectra of the

ligand without metal, and with either Fe^{2+} or Zn^{2+}. Figure 4.2B shows the (normalized) absorption as function of equivalence of metal added (recorded at 613 nm for Fe^{2+} and at 370 nm at Zn^{2+}).

4.4.5 DFT functionals

For structures **A**, **D**, **TS-3** and **E** of the condensation reactions with Fe^{2+}, Zn^{2+} and without metal center (see Figure 3 of the main text), the energies were also calculated with B97D and MO6-2X in single point calculations. The tables below display the Gibbs Free energies with all three functionals. From these tables, we conclude that with B97D and MO6-2X, the condensation reaction is as unlikely as it was with wB97xD. It is not merely a result of our choice of functional.

Table 4.1. Gibbs Free energies of selected structures in the condensation reaction with four-membered ring proton transfers, calculated with three DFT functionals.

M = Fe^{2+}	wB97xD	B97D	MO6-2X
A	0.00	0.00	0.00
D	–17.62	–14.31	–19.44
TS-3	33.95	30.43	32.45
E	–16.70	–20.34	–17.79

M = Zn^{2+}	wB97xD	B97D	MO6-2X
A	0.00	0.00	0.00
D	–3.88	2.78	–6.54
TS-3	46.68	68.98	64.33
E	–11.66	–8.15	–13.73

M = nothing	wB97xD	B97D	MO6-2X
A	0.00	0.00	0.00
D	5.10	4.75	–3.32
TS-3	54.26	48.95	46.82
E	–3.03	–6.93	–9.56

4.4.6 One versus two pincer ligands

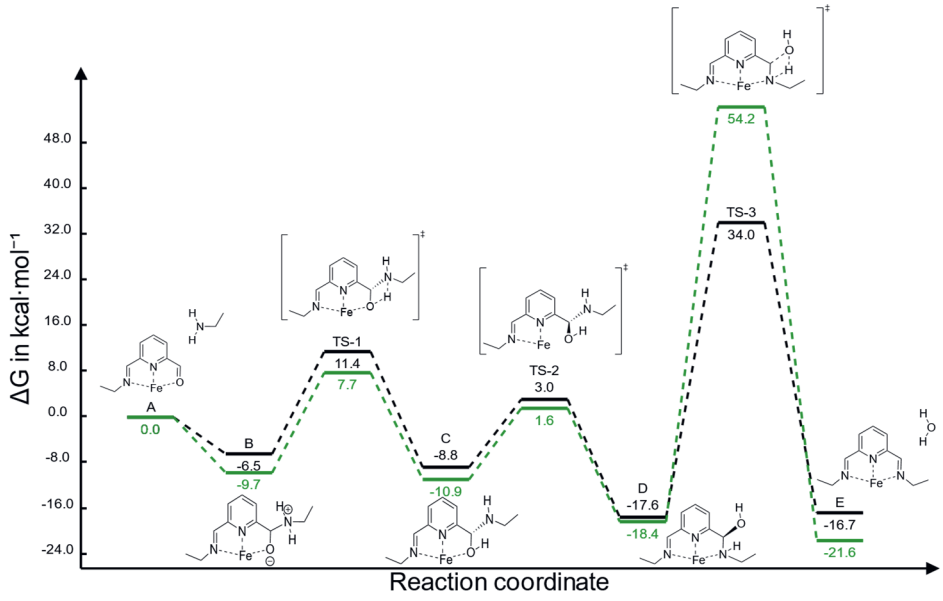

Figure 4.7. The Gibbs Free Energy diagrams of the condensation reactions of the iron complexes with one (black) or two (green) pincers coordinated. Where one pincer is coordinated, three explicit acetonitriles are used to occupy the remaining coordination sites of the octahedral Fe^{2+}. Only the reacting pincer is drawn for clarity.

The condensation reaction was calculated for a complex with one pincer and three acetonitrile ligands coordinating to iron(II), and for a complex with two pincers. As shown in Figure 4.7, the Gibbs Free energy of these pathways was similar, except for the transition state of the second four-membered ring proton transfer. This was significantly higher in energy for the double pincer complex than for the single pincer complex, most likely due to steric hindrance. As the double pincer pathway had a 72.7 kcal/mol energy barrier, the pathway was even less likely than the single pincer pathway that was used for further comparison in the rest of the article.

Exchange of the second pincer with three acetonitriles costed –17.4 kcal/mol for Fe^{2+} and –24.3 kcal/mol for Zn^{2+} (Scheme 4.2). As two pincer complexes are lower in energy, most complexes will have two pincers. However, these exchange energies showed that single pincer complexes can be formed at room temperature. The use of a single pincer complex in calculations is thus justified.

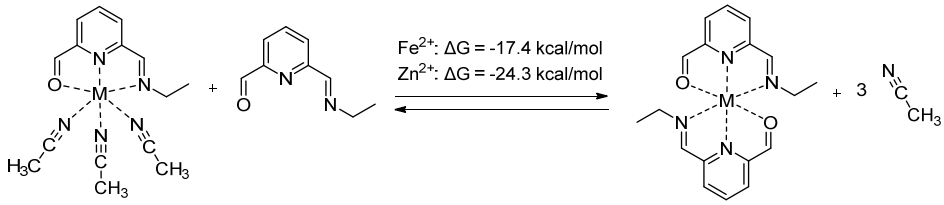

Scheme 4.2. Coordination of a second 2-methoxo-6-ethylimine pyridine moiety to a metal pincer complex, in exchange of three acetonitrile molecules. The metal is either Fe^{2+} or Zn^{2+}, as used in experimental work.

References

(1) S. J. Rowan, S. J. Cantrill, G. R. L. Cousins, J. K. M. Sanders, J. F. Stoddart, *Angew. Chem. Int. Ed.* **2002**, *41*, 898.

(2) *Dynamic Covalent Chemistry: Principles, Reactions, and Applications* (Eds: W. Zhang, Y. Jin), John Wiley & Sons Ltd., Chichester, UK, **2017**.

(3) A. Herrmann, *Chem. Soc. Rev.* **2014**, *43*, 1899.

(4) F. García, M. M. J. Smulders, *J. Polym. Sci., Part A: Polym. Chem.* **2016**, *54*, 3551.

(5) J. W. Sadownik, R. V. Ulijn, *Curr. Opin. Biotechnol.* **2010**, *21*, 401.

(6) N. Zheng, Y. Xu, Q. Zhao, T. Xie, *Chem. Rev.* **2021**, *121*, 1716.

(7) M. Mondal, A. K. H. Hirsch, *Chem. Soc. Rev.* **2015**, *44*, 2455.

(8) Y. Chao, A. Krishna, M. Subramaniam, D.-D. Liang, S. P. Pujari, A. C.-H. Sue, G. Li, F. M. Miloserdov, H. Zuilhof, *Angew. Chem. Int. Ed.* **2022**, *61*, e202207456.

(9) C. J. Kloxin, C. N. Bowman, *Chem. Soc. Rev.* **2013**, *42*, 7161.

(10) M. Podgórski, B. D. Fairbanks, B. E. Kirkpatrick, M. McBride, A. Martinez, A. Dobson, N. J. Bongiardina, C. N. Bowman, *Adv. Mater.* **2020**, *32*, 2070158.

(11) N. J. Van Zee, R. Nicolaÿ, *Prog. Polym. Sci.* **2020**, 101233.

(12) G. M. Scheutz, J. J. Lessard, M. B. Sims, B. S. Sumerlin, *J. Am. Chem. Soc.* **2019**, *41*, 16181.

(13) M. Guerre, C. Taplan, J. M. Winne, F. E. Du Prez, *Chem. Sci.* **2020**, *11*, 4855.

(14) P. Chakma, D. Konkolewicz, *Angew. Chem. Int. Ed.* **2019**, *58*, 9682.

(15) J. Zheng, Z. M. Png, S. H. Ng, G. X. Tham, E. Ye, S. S. Goh, X. J. Loh, Z. Li, *Materials Today* **2021**.

(16) K. R. West, K. D. Bake, S. Otto, *Org. Lett.* **2005**, *7*, 2615.

(17) S. M. Elbert, N. I. Regenauer, D. Schindler, W.-S. Zhang, F. Rominger, R. R. Schröder, M. Mastalerz, *Chem. Eur. J.* **2018**, *24*, 11438.

(18) K. Acharyya, P. S. Mukherjee, *Angew. Chem. Int. Ed.* **2019**, *58*, 8640.

(19) A. J. McConnell, *Chem. Soc. Rev.* **2022**, *51*, 2957.

(20) E. N. Keyzer, A. Sava, T. K. Ronson, J. R. Nitschke, A. J. McConnell, *Chem. Eur. J.* **2018**, *24*, 12000.

(21) D. Zhang, T. K. Ronson, J. R. Nitschke, *Acc. Chem. Res.* **2018**, *51*, 2423.

(22) Y. Fang, J. A. Powell, E. Li, Q. Wang, Z. Perry, A. Kirchon, X. Yang, Z. Xiao, C. Zhu, L. Zhang, F. Huang, H.-C. Zhou, *Chem. Soc. Rev.* **2019**, *48*, 4707.

(23) M. von Delius, E. M. Geertsema, D. A. Leigh, *Nat. Chem.* **2010**, *2*, 96.

(24) J. Hu, S. K. Gupta, J. Ozdemir, M. H. Beyzavi, *ACS Appl. Nano Mater.* **2020**, *3*, 6239.

(25) M. E. Belowich, J. F. Stoddart, *Chem. Soc. Rev.* **2012**, *41*, 2003.

(26) E. H. Cordes, W. P. Jencks, *J. Am. Chem. Soc.* **1962**, *84*, 826.

(27) M. Ciaccia, S. Di Stefano, *Org. Biomol. Chem.* **2015**, *13*, 646.

(28) P. Kovaříček, J.-M. Lehn, *J. Am. Chem. Soc.* **2012**, *134*, 9446.
(29) J. C. Lauer, W.-S. Zhang, F. Rominger, R. R. Schröder, M. Mastalerz, *Chem. Eur. J.* **2018**, *24*, 1816.
(30) B. P. Benke, T. Kirschbaum, J. Graf, J. H. Gross, M. Mastalerz, *Nat. Chem.* **2023**, *15*, 413.
(31) O. Storm, U. Lüning, *Chem. Eur. J.* **2002**, *8*, 793.
(32) K. Ziach, J. Jurczak, *Org. Lett.* **2008**, *10*, 5159.
(33) N. Giuseppone, J.-L. Schmitt, J.-M. Lehn, *Angew. Chem. Int. Ed.* **2004**, *43*, 4902.
(34) N. Giuseppone, J.-L. Schmitt, J.-M. Lehn, *J. Am. Chem. Soc.* **2006**, *128*, 16748.
(35) P. Pandey, A. P. Katsoulidis, I. Eryazici, Y. Wu, M. G. Kanatzidis, S. T. Nguyen, *Chem. Mater.* **2010**, *22*, 4974.
(36) A. Natraj, W. Ji, J. Xin, I. Castano, D. W. Burke, A. M. Evans, M. J. Strauss, M. Ateia, L. S. Hamachi, N. C. Gianneschi, Z. A. Alothman, J. Sun, K. Yusuf, W. R. Dichtel, *J. Am. Chem. Soc.* **2022**, *144*, 19813.
(37) F. J. Uribe-Romo, J. R. Hunt, H. Furukawa, C. Klöck, M. O'Keeffe, O. M. Yaghi, *J. Am. Chem. Soc.* **2009**, *131*, 4570.
(38) E. Dautzenberg, M. Lam, G. Li, L. C. P. M. de Smet, *Nanoscale* **2021**, *13*, 19446.
(39) S. K. Schoustra, J. A. Dijksman, H. Zuilhof, M. M. J. Smulders, *Chem. Sci.* **2021**, *12*, 293.
(40) C. Godoy-Alcántar, A. K. Yatsimirsky, J. M. Lehn, *J. Phys. Org. Chem.* **2005**, *18*, 979.
(41) P. Mal, D. Schultz, K. Beyeh, K. Rissanen, J. R. Nitschke, *Angew. Chem. Int. Ed.* **2008**, *47*, 8297.
(42) J. R. Nitschke, J.-M. Lehn, *Proc. Natl. Acad. Sci. U. S. A.* **2003**, *100*, 11970.
(43) D.-H. Ren, D. Qiu, C.-Y. Pang, Z. Li, Z.-G. Gu, *Chem. Commun.* **2015**, *51*, 788.
(44) J. R. Nitschke, *Acc. Chem. Res.* **2007**, *40*, 103.
(45) D. Schultz, J. R. Nitschke, *J. Am. Chem. Soc.* **2006**, *128*, 9887.
(46) J. Anhäuser, R. Puttreddy, L. Glanz, A. Schneider, M. Engeser, K. Rissanen, A. Lützen, *Chem. Eur. J.* **2019**, *25*, 12294.
(47) J. I. van der Vlugt, S. Demeshko, S. Dechert, F. Meyer, *Inorg. Chem.* **2008**, *47*, 1576.
(48) T. J. Burchell, R. J. Puddephatt, *Inorg. Chem.* **2005**, *44*, 3718.
(49) H. Bunzen, Nonappa, E. Kalenius, S. Hietala, E. Kolehmainen, *Chem. Eur. J.* **2013**, *19*, 12978.
(50) C. D. Meyer, C. S. Joiner, J. F. Stoddart, *Chem. Soc. Rev.* **2007**, *36*, 1705.
(51) S. Kitagawa, R. Kitaura, S.-i. Noro, *Angew. Chem. Int. Ed.* **2004**, *43*, 2334.
(52) F. García, J. Pelss, H. Zuilhof, M. M. J. Smulders, *Chem. Commun.* **2016**, *52*, 9059.
(53) P. E. Figgins, D. H. Busch, *J. Am. Chem. Soc.* **1960**, *82*, 820.
(54) R. Lavendomme, T. K. Ronson, J. R. Nitschke, *J. Am. Chem. Soc.* **2019**, *141*, 12147.
(55) C. D. Pentecost, K. S. Chichak, A. J. Peters, G. W. V. Cave, S. J. Cantrill, J. F. Stoddart, *Angew. Chem. Int. Ed.* **2007**, *46*, 218.
(56) G. Nasr, T. Macron, A. Gilles, Z. Mouline, M. Barboiu, *Chem. Commun.* **2012**, *48*, 6827.
(57) D.-P. Wang, J.-C. Lai, H.-Y. Lai, S.-R. Mo, K.-Y. Zeng, C.-H. Li, J.-L. Zuo, *Inorg. Chem.* **2018**, *57*, 3232.
(58) Y. Zhang, M. Barboiu, *ChemistryOpen* **2019**, *8*, 1345.
(59) I. Kocsis, D. Dumitrescu, Y.-M. Legrand, A. van der Lee, I. Grosu, M. Barboiu, *Chem. Commun.* **2014**, *50*, 2621.
(60) L. Hogg, D. A. Leigh, P. J. Lusby, A. Morelli, S. Parsons, J. K. Y. Wong, *Angew. Chem. Int. Ed.* **2004**, *43*, 1218.
(61) D. A. Leigh, P. J. Lusby, S. J. Teat, A. J. Wilson, J. K. Y. Wong, *Angew. Chem. Int. Ed.* **2001**, *40*, 1538.
(62) C. Browne, T. K. Ronson, J. R. Nitschke, *Angew. Chem. Int. Ed.* **2014**, *53*, 10701.
(63) M. Ciaccia, R. Cacciapaglia, P. Mencarelli, L. Mandolini, S. Di Stefano, *Chem. Sci.* **2013**, *4*, 2253.

(64) R. Pérez-Soto, M. Besora, F. Maseras, *Org. Lett.* **2020**, *22*, 2873.
(65) V. C. Rufino, J. R. Pliego, *Comput. Theor. Chem.* **2020**, *1191*, 113053.
(66) H. Zheng, H. Ye, X. Yu, L. You, *J. Am. Chem. Soc.* **2019**, *141*, 8825.
(67) G. Olivo, O. Lanzalunga, S. Di Stefano, *Adv. Synth. Catal.* **2016**, *358*, 843.
(68) S. K. Schoustra, M. M. J. Smulders, *Macromol. Rapid Commun.* **2023**, *44*, 2200790.
(69) C. Fonseca Guerra, P. J. Sanz Miguel, A. Cebollada, F. M. Bickelhaupt, B. Lippert, *Chem. Eur. J.* **2014**, *20*, 9494.
(70) R. H. Holyer, C. D. Hubbard, S. F. A. Kettle, R. G. Wilkins, *Inorg. Chem.* **1966**, *5*, 622.
(71) R. A. Angnes, *GitHub repository* **2020**, *DOI 10.5281/zenodo.4065333*.
(72) L. Shen, N. Cao, L. Tong, X. Zhang, G. Wu, T. Jiao, Q. Yin, J. Zhu, Y. Pan, H. Li, *Angew. Chem. Int. Ed.* **2018**, *57*, 16486.
(73) T. Jiao, G. Wu, Y. Zhang, L. Shen, Y. Lei, C.-Y. Wang, A. C. Fahrenbach, H. Li, *Angew. Chem. Int. Ed.* **2020**, *59*, 18350.
(74) F. Schaufelberger, K. Seigel, O. Ramström, *Chem. Eur. J.* **2020**, *26*, 15581.
(75) A. Dirksen, T. M. Hackeng, P. E. Dawson, *Angew. Chem. Int. Ed.* **2006**, *45*, 7581.
(76) N. Wilhelms, S. Kulchat, J.-M. Lehn, *Helv. Chim. Acta* **2012**, *95*, 2635.
(77) S. Kirmizialtin, B. S. Yildiz, I. Yildiz, *J. Phys. Org. Chem.* **2017**, *30*, e3711.
(78) D. Schultz, J. R. Nitschke, *Angew. Chem. Int. Ed.* **2006**, *45*, 2453.
(79) F. Schaufelberger, O. Ramström, *J. Am. Chem. Soc.* **2016**, *138*, 7836.
(80) Y. R. Hristova, M. M. J. Smulders, J. K. Clegg, B. Breiner, J. R. Nitschke, *Chem. Sci.* **2011**, *2*, 638.
(81) A. Liguori, M. Hakkarainen, *Macromol. Rapid Commun.* **2022**, *43*, 2100816.
(82) F. Van Lijsebetten, K. De Bruycker, Y. Spiesschaert, J. M. Winne, F. E. Du Prez, *Angew. Chem. Int. Ed.* **2022**, *61*, e202113872.
(83) M. J. Frisch, G. W. Trucks, H. B. Schlegel, G. E. Scuseria, M. A. Robb, J. R. Cheeseman, G. Scalmani, V. Barone, G. A. Petersson, H. Nakatsuji, X. Li, M. Caricato, A. V. Marenich, J. Bloino, B. G. Janesko, R. Gomperts, B. Mennucci, H. P. Hratchian, J. V. Ortiz, A. F. Izmaylov, J. L. Sonnenberg, Williams, F. Ding, F. Lipparini, F. Egidi, J. Goings, B. Peng, A. Petrone, T. Henderson, D. Ranasinghe, V. G. Zakrzewski, J. Gao, N. Rega, G. Zheng, W. Liang, M. Hada, M. Ehara, K. Toyota, R. Fukuda, J. Hasegawa, M. Ishida, T. Nakajima, Y. Honda, O. Kitao, H. Nakai, T. Vreven, K. Throssell, J. A. Montgomery Jr., J. E. Peralta, F. Ogliaro, M. J. Bearpark, J. J. Heyd, E. N. Brothers, K. N. Kudin, V. N. Staroverov, T. A. Keith, R. Kobayashi, J. Normand, K. Raghavachari, A. P. Rendell, J. C. Burant, S. S. Iyengar, J. Tomasi, M. Cossi, J. M. Millam, M. Klene, C. Adamo, R. Cammi, J. W. Ochterski, R. L. Martin, K. Morokuma, O. Farkas, J. B. Foresman, D. J. Fox, *Gaussian 16 Rev. C.01*, Wallingford, CT, **2016**.
(84) J.-D. Chai, M. Head-Gordon, *Phys. Chem. Chem. Phys.* **2008**, *10*, 6615.
(85) Y. Minenkov, Å. Singstad, G. Occhipinti, V. R. Jensen, *Dalton Trans.* **2012**, *41*, 5526.
(86) A. V. Marenich, C. J. Cramer, D. G. Truhlar, *J. Phys. Chem. B* **2009**, *113*, 6378.
(87) S. Kulchat, M. N. Chaur, J.-M. Lehn, *Chem. Eur. J.* **2017**, *23*, 11108.
(88) M. He, J.-M. Lehn, *J. Am. Chem. Soc.* **2019**, *141*, 18560.

Chapter 5
A DFT Study On Chain-Growth SuFEx Polymerization

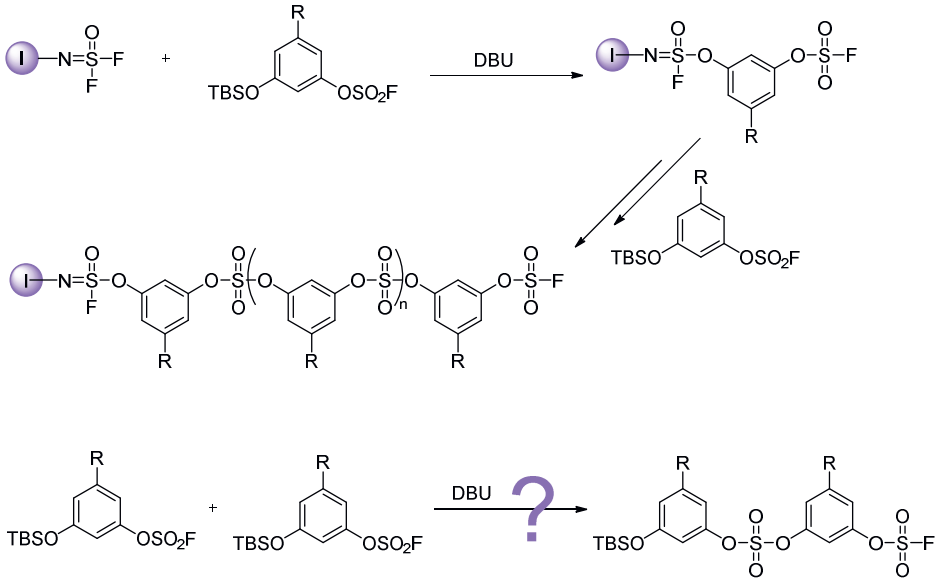

The research in this chapter has been done in collaboration with J. Escorihuela.

Abstract

In 2021, a SuFEx polymerization by an unusual chain-growth mechanism was presented by Sharpless and Wu. Long polymer chains with low polydispersity were produced in the presence of (4-nitrophenyl)-sulfur imidoyl difluoride, and no polymers were observed without this initiator. In their experiments, the electron-withdrawing nature of various substituents was proposed to prevent self-polymerization, allowing a monomer to become prone to SuFEx reacting only when attached to an electron-donating polymer chain. Self-polymerization of the monomers with the least electron-withdrawing substituents supported this claim.

To provide further mechanistic insight into this unusual chain-growth polymerization, chain-growth SuFEx polymerizations of (3-fluorosulfonyl)-5-substituted phenyl hydrogen sulfate were investigated with DFT calculations in this chapter, using NH_4^+ as a computationally efficient mimic of $DBUH^+$. As the leaving fluoride anion required an electrophile, the reactions without NH_4^+ were difficult to compute and led to unrealistic results. The initiation and propagation reaction with the other monomers were calculated in the presence of NH_4^+ and showed no significant electronic substituent effects. Furthermore, the self-reaction of all four monomers required activation energies between 15.5 and 17.1 kcal/mol, again displaying no substituent effects, suggesting self-polymerization is accessible for all monomers. This contrasts experimental findings, and we thus assume that not all experimental factors were sufficiently taken into account in our calculations. For future work, the use of explicit solvent molecules is suggested to more properly simulate solvent interactions.

5.1 Introduction

Polymers are essential for our way of living in recent decades, and well-defined polymers are in high demand. For photonic devices, only well-defined polymers are conductive enough to be applicable.[1] In coatings, tuning of specific material properties is desired, and can, for example, be achieved using polymer brushes.[2,3] Polymers that are to be used as substrates must be well-defined as well, to ensure proper post-modification.[4] Efficient production of these well-defined polymers requires fast chemical reactions with high conversion and few side reactions. In 2001, Sharpless coined a category of chemical reactions that fit these criteria: click reactions.[5] Reactions like the Copper-catalyzed Azide–Alkyne Cycloaddition (CuAAC), Strain-Promoted Azide–Alkyne Cycloaddition (SPAAC), Diels-Alder, and thiol-ene reactions are not only fast and high yielding, but also modular, water tolerant, and feasible in one pot. Their use in material chemistry is multifold, for example in linear polymers, branched polymers and crosslinked networks.[6–9]

In 2014, Sharpless[10] added a new click reaction to the toolbox: the Sulfur(IV) Fluoride Exchange (SuFEx). In this reaction, a phenolate or amine group attacks a sulfonyl fluoride group, eliminating the fluoride and forming a sulfate or sulfonamide moiety. The fluorine is commonly captured by a silicon group, forming the extremely stable Si–F bond. Being first discovered in the 1920s[11] and rediscovered in 2008,[12] it was only when Sharpless outlined its full potential in 2014 that the reaction started receiving widespread attention.

The SuFEx reaction can been used as a synthetic tool to produce synthetically demanding moieties such as sterically hindered amides,[13] bifluoride ionic liquids,[14] triflates and triflamides.[15] Memory devices[16] and organic frameworks[17] can be made as well. The reaction is biocompatible, [18–21] even for double SuFEx on the same sulfur hub,[20] and can be performed on a surface.[22–24] Moreover, SuFEx reactions can be enantiospecific.[25,26] Finally, Si-free,[26] fluorine-free [27] and reversible[27,28] sulfur(VI) exchange reactions have all been demonstrated.

Like all click reactions, the SuFEx reaction has been explored as polymerization method. The SuFEx reaction was applied in step-growth polymerization, mostly to couple disulfonyl fluoride monomers to disilyl ethers or amides, forming AB-type polymers.[29–32] Those polymers could then be further functionalized, either

with non-SuFEx click reactions [33] or with a second SuFEx reaction. [25,34] An AB-type polymer could also be obtained by combining SuFEx with another click reaction such as CuAAC. [35]

For a bifunctional SuFEx monomer, containing both the sulfonyl fluoride and the silyl ether or amide, step-growth polymerization is to be expected as well. If no catalyst is required for the reaction, as is the case in SuFEx reactions, monomers will react upon collision, resulting in dimers and gradually in longer chains: step-growth polymerization. Chain-growth polymerization only occurs when an extra factor is required for reacting which prevents uncontrolled polymerization, such as a catalyst. This control results in lower polydispersity (Đ), even at higher molecular weight (M_n), which is often desirable.

It is therefore noteworthy that in 2021, the groups of Sharpless and Wu[36] were able to perform a chain-growth polymerization with the SuFEx reaction. By using aryl silyl ether-fluorosulfate monomers, an iminosulfur oxydifluoride-containing initiator and DBU as catalyzing base, they were able to produce polymers with a remarkable low polydispersity of below 1.4 (Figure 5.1). When an electron-withdrawing group was present on the monomer, they confirmed the absence of self-polymerization, thus confirming chain-growth polymerization. Although the resulting polymers were stable in a range of temperatures, only mild acidic or basic conditions were needed for full degradation.

Given the unusual nature of the chain-growth polymerization reaction, we have explored the mechanism of this promising polymerization reaction by DFT calculations in this chapter. Some DFT calculations have already been performed on SuFEx reactions, focused on the general mechanism[26] and on the effect of the accompanying base[37] or an additive such as Ca^{2+}.[38] Our calculations describe the initiation and propagation reaction of this chain-growth polymerization (Figure 5.2), both in the presence and absence of NH_4^+, which acts as electrophile to capture the leaving fluoride and was selected to mimic the experimentally used but much larger $DBUH^+$ of the reaction mixture. Furthermore, the effects of various electron-withdrawing and donating monomer-substituents on these steps, and the possibility of self-polymerization of those monomers are investigated.

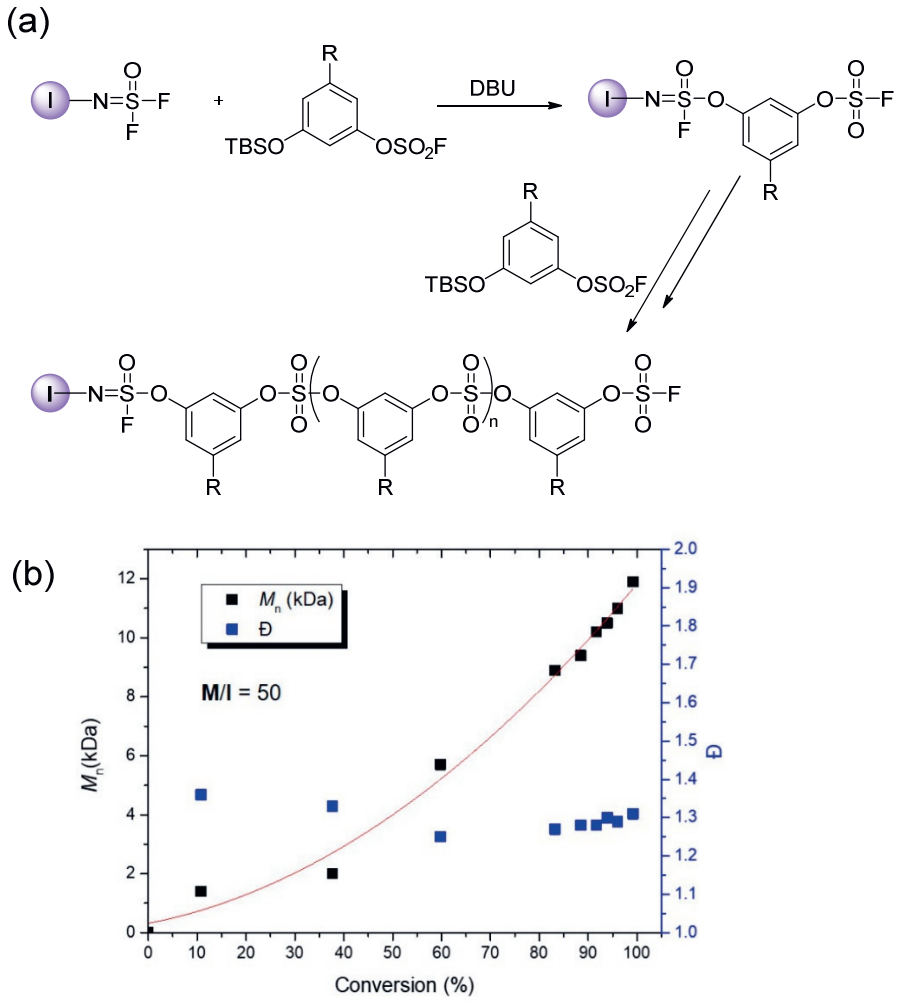

Figure 5.1. (a) Chain-growth polymerization of aryl silyl ether-fluorosulfates,[36] and (b) M_n and Đ (M_w/M_n) as a function of conversion at a monomer-to-initiator ratio of 50.

5.2 Results

In order to find the energy paths for initiation, propagation and self-polymerization of the four chosen monomers, density functional calculations (DFT) were performed. Geometry optimization, vibrational frequency calculations and IRC calculations were executed with the ωB97XD functional[39,40] and the 6-311G(2d,2p) basis set as implemented in the Gaussian 16 suite of programs.[41] All (natural population) charges and Wiberg bond orders were calculated using the NBO 3.1 program as implemented in there as well. Generic

solvent effects were incorporated by using the universal solvation model based on density (SMD).[42] Butyronitrile was chosen as the model solvent, as the experimental work by Sharpless and Wu[36] was performed in butyronitrile. Gibbs free energies are reported in a standard state: at 298 K and 1 bar pressure.

We calculated three stages of polymerization: initiation, propagation and self-polymerization (Figure 5.2). All stages were calculated for four monomers (Figure 5.2d): 3-((fluorosulfonyl)oxy)-phenolate (hereafter called **mon-H**), 3-((fluorosulfonyl)oxy)-5-(methoxycarbonyl)phenolate (**mon-MeEst**), 3-((fluoro-sulfonyl)oxy)-5-methoxyphenolate (**mon-OMe**), and 3-fluoro-5-((fluorosulfo-nyl)oxy)phenolate (**mon-F**). **Mon-MeEst**, **mon-OMe** and **mon-F** were used in the reported experimental work,[36] with various results, while **mon-H** was chosen for ease of calculation.

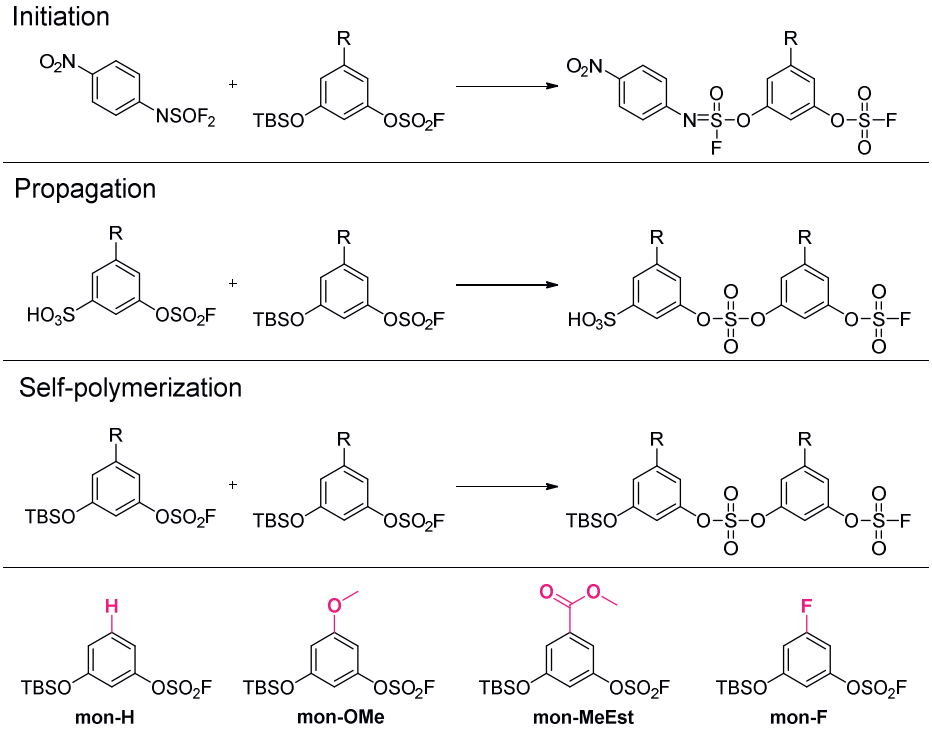

Figure 5.2. The initiation, propagation and self-polymerization reactions as calculated with DFT in this paper, as well as the four investigated monomers.

5.2.1 Initiation reaction

As the TBS protecting group on the phenol does not take part in the SuFEx reaction,[26] we calculated the initiation reaction between (4-nitrophenyl)-sulfurimidoyl difluoride (**initiator**) and **mon-H** (Figure 5.3, in grey). The initiation reaction followed the profile of a typical addition-elimination reaction, starting with the addition of the phenolate onto the sulfur atom. This addition required 6.3 kcal/mol and led to a stable intermediate at 3.1 kcal/mol. The removal of F^- was rate-determining at 12.6 kcal/mol, and without a counterion to connect to, the fluoride ion positioned itself near the aromatic ring. If the product is calculated in absence of F^-, and the energy of F^- is calculated from the difference of TBS-F and TBS^+ connected to **mon-H** (Supporting Information, section 5.5.1), the product energy is found at –15.1 kcal/mol.

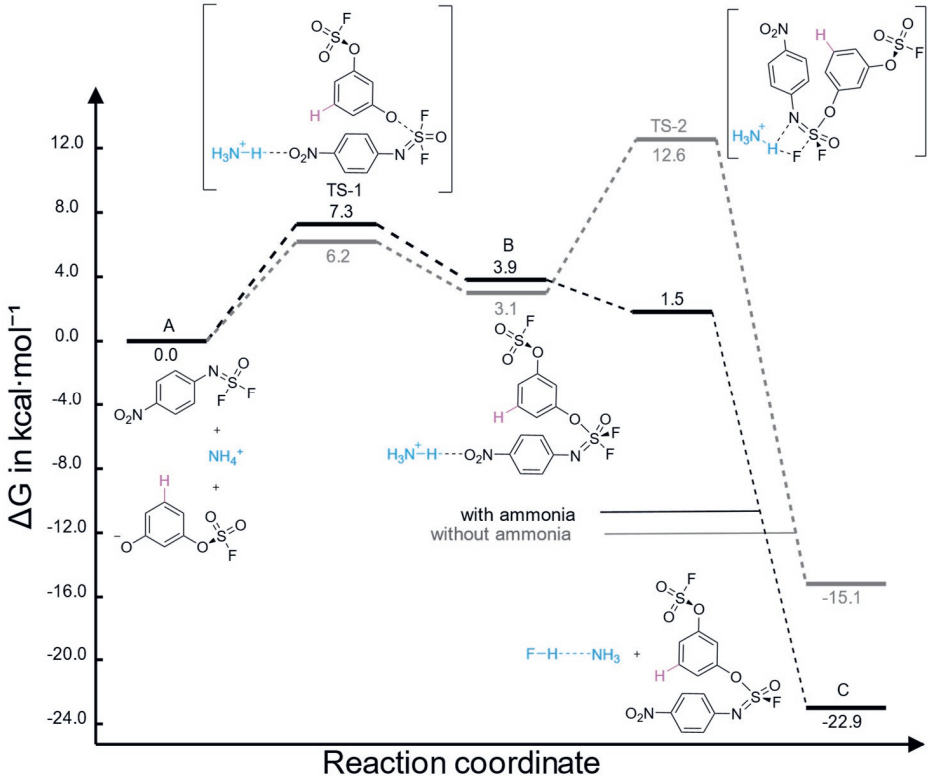

Figure 5.3. Gibbs free energy profiles of the initiation reaction (Figure 5.2) of **mon-H**, in presence (black lines) and absence (grey lines) of NH_4^+. All energy profiles are produced using free software from Angnes.[43]

However, in the experimental setting, DBU is present in a solvent that will likely attract some water. We therefore expect that $DBUH^+$ can act as fluoride abstractor. We thus recalculated the initiation reaction, taking NH_4^+ as a mimic for $DBUH^+$ for ease of calculation (Figure 5.3, in black). Remarkably, the phenolate addition (TS-1) required 7.3 kcal/mol in presence of NH_4^+ as opposed to 6.3 kcal/mol without NH_4^+. One would expect a decrease of this barrier, as coordination of NH_4^+ to the sulfur could decrease electron density on sulfur and thereby increase susceptibility to nucleophilic attack. However, as NH_4^+ is not located near the sulfur hub but instead is forming a hydrogen bond with the NO_2 group of the initiator molecule (Figure 5.4a), its interaction with the sulfur hub is simply too weak to be of any influence on bond lengths and electron densities. Placement of the ammonia near the sulfur hub immediately resulted in the product, without any transition states or intermediates: multiple scans from the product to the start showed only uphill energy paths.

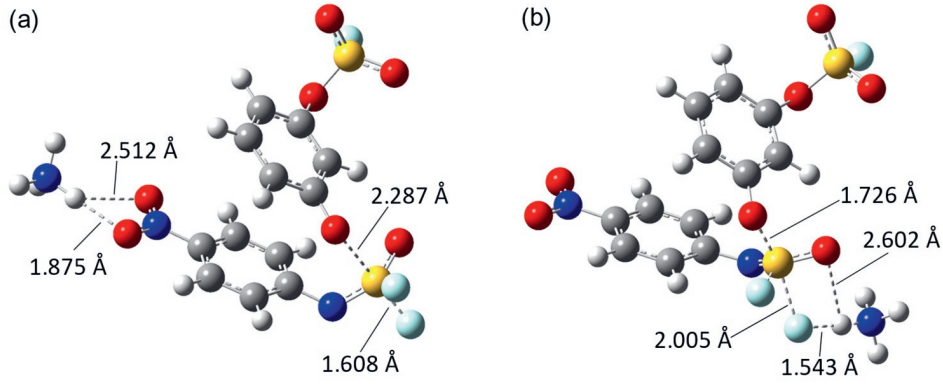

Figure 5.4. Geometry of (a) TS-1 and (b) TS-2 of the initiation reaction of **mon-H** in presence of NH_4^+. The reaction coordinate in TS-1 is along the 2.287 Å non-covalent bond between sulfur and oxygen. The reaction coordinate in TS-2 is elongation of the 2.005 Å S–F bond and shortening of the 1.543 Å F–H bond.

An intermediate was found at 3.9 kcal/mol with the NH_4^+ near the sulfur hub. A second transition state was found in a scan from intermediate to product (Figure 5.4b), yet at 1.5 kcal/mol it was lower than the intermediate. Indeed, IRC calculations could not confirm its true transition state character. We can thus conclude that barrierless elimination resulted in the product at –22.9 kcal/mol. This demonstrates that the rate-determining elimination step as found previously, in which 12.6 kcal/mol was required to remove F^- from the sulfur

hub without any electrophile to go to, was the result of the absence of a fluoride-abstractor. Incorporation of the fluoride abstractor removed this barrier, as the F^- now transferred effortlessly to the NH_4^+. The 7.8 kcal/mol lower Gibbs free energy of the product was another result from this incorporation: the NH_4–F formed two extra hydrogen bonds with the solvent.

5.2.2 Propagation reaction

The propagation reaction between ((3-fluorosulfonyl)oxy)phenyl hydrogen sulfate (**pol-H**) and ((3-fluorosulfonyl)oxy)phenolate (**mon-H**) was calculated in the absence and presence of NH_4^+ (Figure 5.5). In both cases, the polymer chain was represented by a sulfate group. Calculation of the propagation with full polymer chain showed that this simplification was justified – a difference in Gibbs free energy of at most 2.2 kcal/mol was found for all reaction steps in the presence of NH_4^+ (Figure 5.5, full discussion in Supporting Information, section 5.5.2). In the absence of NH_4^+, no transition states or intermediates could be obtained for the full polymer chain, as the energy profile of the reaction was upwards only (Supporting Information, section 5.5.2).

Propagation in the absence of NH_4^+ (Figure 5.5 in grey) was difficult to calculate. Although the electronic energy of the first transition state was 0.07 kcal/mol higher than the intermediate, causing the calculation to finish, an IRC of this transition state only led back to the substrates and failed in the forward direction. With both the Gibbs Free energy and the enthalpy lower than the intermediate (Table 5.1), this transition state is not an actual transition state but merely a shoulder on the energy profile. TS-2 was a proper transition state at 11.9 kcal/mol, however, it showed only movement of the fluoride away from the sulfur, and no change in the phenolate – sulfur distance. It was therefore clearly not the only transition state of this reaction. This is similar to the silicon-free SuFEx reactions of sulfonimidoyl fluorides,[44] where the addition of phenolate and the elimination of fluoride were also found to be separate, yet one of the two processes was near spontaneous. These SuFEx reactions are thus clearly not S_N2 reactions, yet not traditional addition-eliminations either, as they have no stable intermediate with both bonds fully formed. The product was found at –17.5 kcal/mol, with the F^- forming a hydrogen bond with one of the

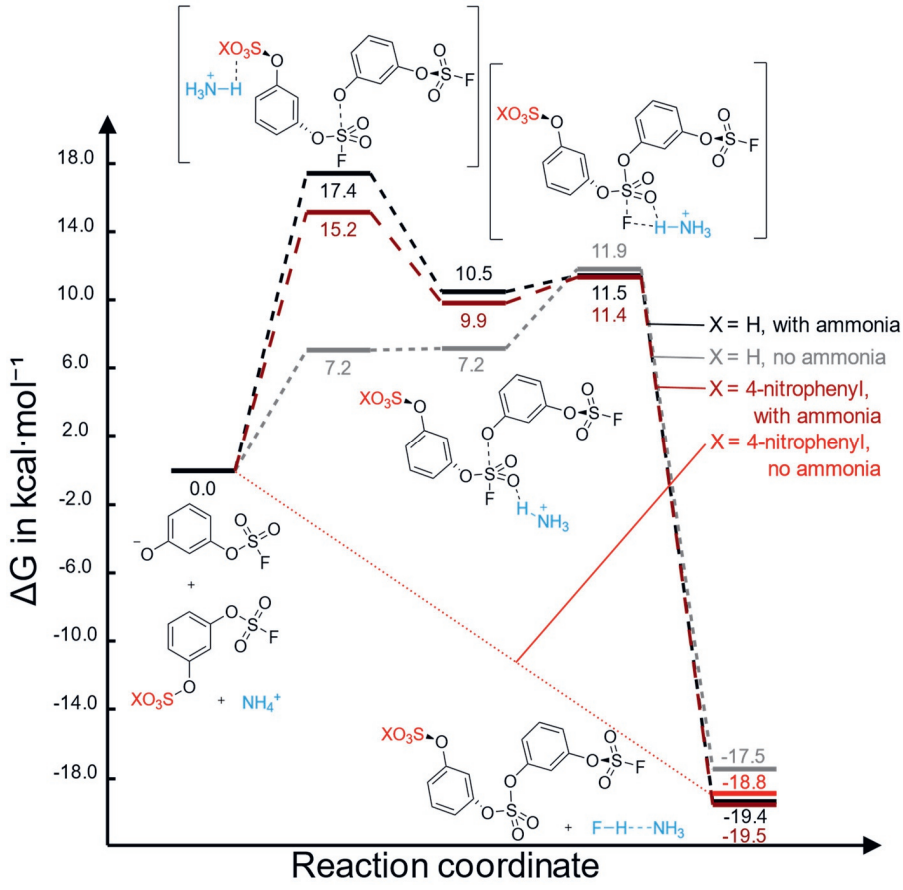

Figure 5.5. Gibbs free energy profiles of the propagation reaction of **pol-H** with **mon-H**, in presence (black) and absence (grey) of NH_4^+, and the propagation reaction with (4-nitrophenyl) sulfate and **mon-H**, in presence (dark red) and absence (red) of NH_4^+.

Table 5.1. Electronic energy, and electronic energy with Gibbs corrections and enthalpy corrections of the five steps in the propagation reaction of **mon-H** without ammonia. A second decimal is added to ease discussion of the results.

	ΔEE (kcal/mol)	ΔG (kcal/mol)	ΔH (kcal/mol)
Substrates	0.00	0.00	0.00
TS-1	5.53	7.16	4.99
Intermediate	5.47	7.22	5.70
TS-2	7.95	11.87	7.80
Products	–6.19	–17.47	–7.42

protons from a phenyl ring. These difficulties further underlined the importance of a proper electrophile for F^- capture, as without it the calculations could not mimic experimental results. In the rest of this chapter, we therefore primarily calculated the SuFEx reactions in the presence of NH_4^+.

The propagation reaction of **mon-H** in presence of NH_4^+ displayed a typical addition-elimination energy profile (Figure 5.5, in black). An initial activation energy of 17.4 kcal/mol was needed for the addition of the phenolate to the sulfur hub. In this addition, NH_4^+ was not near the sulfur hub, but instead formed a hydrogen bond with the sulfate group of the polymer representative above the aromatic ring of **pol-H** (Figure 5.6a). Placement of NH_4^+ near the sulfur hub (Figure 5.6b) complicated the finding of a proper transition state, requiring a change of basis set to 6-311G(d,p) and use of iop(1/8=2) to get the transition state search to converge. Single point energy calculation with our regular basis set located this transition state at 19.2 kcal/mol. It can thus be concluded that NH_4^+ is not involved near the sulfur hub for the addition of the phenolate.

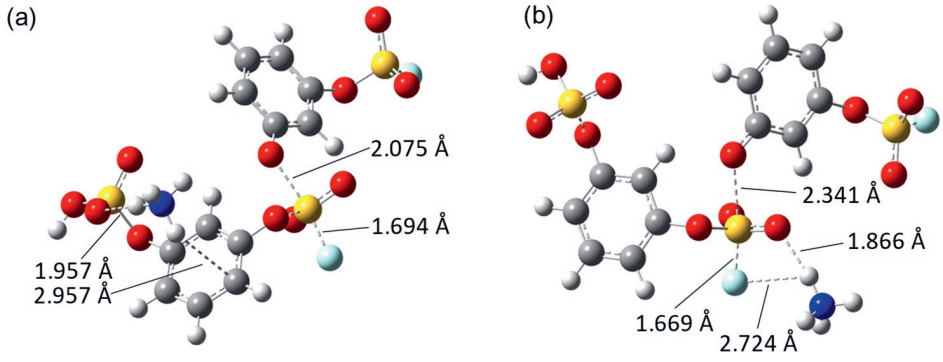

Figure 5.6. Geometry of TS-1 of the propagation reaction of **mon-H** in presence of NH_4^+, with (a) ammonia near the aromatic ring of **pol-H**, and (b) near the fluoride.

A stable intermediate was found at 10.5 kcal/mol. At this stage, NH_4^+ formed a hydrogen bond with the leaving fluoride, thereby easing elimination of F^-. This transition state was found at 11.5 kcal/mol and displayed the movement of F^- from the sulfur towards NH_4^+. The products were found at –19.4 kcal/mol.

5.2.3 Initiation with experimentally relevant substituents

To relate our findings to the experimental work from Sharpless and Wu,[36] the reaction was also calculated for **mon-MeEst** (Figure 5.7, in green), **mon-OMe** (in

red), and **mon-F** (in blue) monomers. The experimental work indicated rapid initiation and propagation for all these monomers. While these polymerization reactions were experimentally performed with $DBUH^+$, in our calculations NH_4^+ was again included in all pathways.

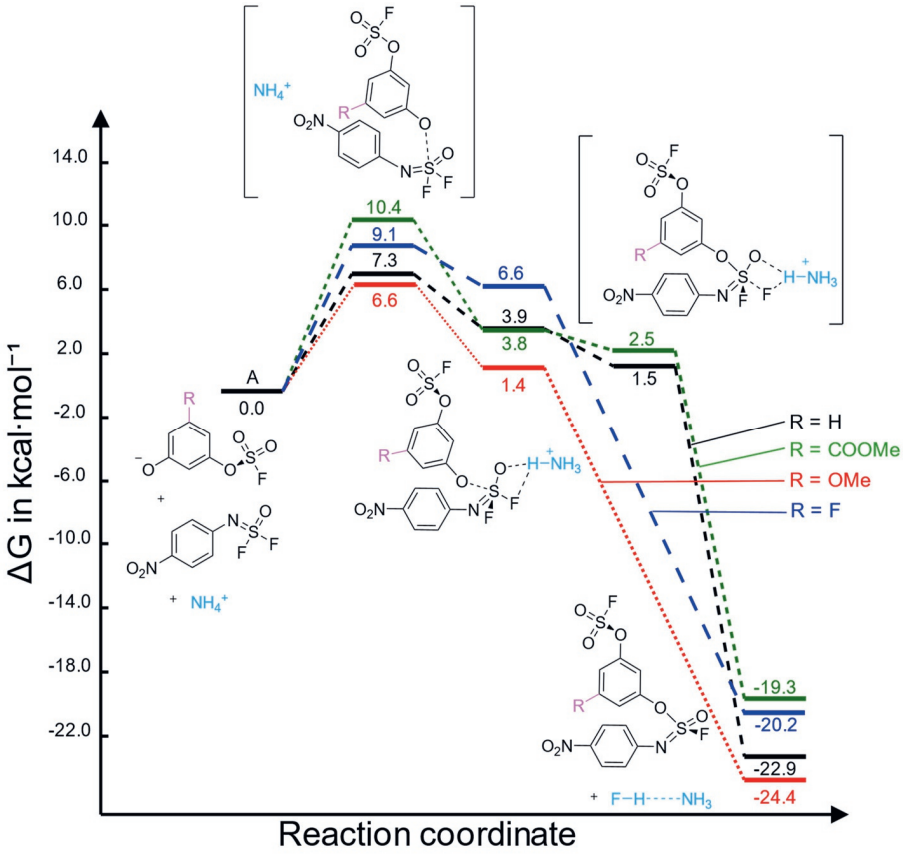

Figure 5.7. Gibbs free energy profiles of the initiation reaction in presence of NH_4^+ with **mon-H** (black), **mon-MeEst** (green), **mon-OMe** (red) and **mon-F** (blue) as monomer.

Substitution of the *meta*-position led to only minor changes in the activation energy for all three substituents. In the first transition state, which displayed a clear addition of the phenolate to the sulfur, the NH_4^+ formed hydrogen bonds with the NO_2 group. Intermediates were found in which both phenolate and fluoride were connected to the sulfur. With the NH_4^+ now nearby, forming a hydrogen bond with the oxygen on the sulfur, the second transition state did not require any energy. The second transition state displayed movement of the

ammonia to the fluoride, after which fluoride elimination from the sulfur was instantaneous. For two monomers, this transition state could be located, but an IRC could not confirm the validity. For the other two, a scan along the reaction coordinate did not indicate any true transition state.

Manual placement of the NH_4^+ near the sulfur hub in TS-1 led to immediate product formation for **mon-H**, and we investigated whether this would be similar for the other three monomers . For **mon-F**, immediate product formation was indeed observed, yet for **mon-MeEst** and **mon-OMe** an increased activation barrier in TS-1 was found (13.8 kcal/mol for **mon-MeEst** and 12.1 kcal/mol for **mon-OMe**). As the NH_4^+ was now in position to form a hydrogen bond with the leaving fluoride, the position of TS-1 moved to much earlier in the reaction path than when the NH_4^+ was near the NO_2 (Figure 5.8). This is seen from a longer S–O distance, smaller C–C–N–S dihedral and reduced charge on the imine of the sulfur hub, together indicating that more charge delocalization took place around the sulfur hub when the NH_4^+ was near the sulfur hub. This promoted fluoride abstraction, which next forced phenolate addition to take place at an earlier stage where it needed to cover more distance, which required more energy.

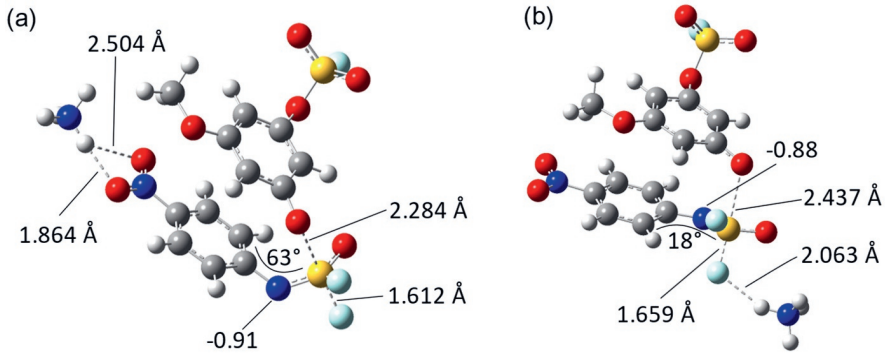

Figure 5.8. Geometry of TS-1 of initiation reaction with **mon-OMe**, with (a) NH_4^+ near the NO_2 group, and (b) NH_4^+ near the leaving fluoride.

An increase of 2.7 kcal/mol was observed for the intermediate of **mon-F** with respect to **mon-H**, and also the TS-1 and the product were 2–3 kcal/mol higher in energy. This increase is fully ascribed to the enthalpic component (Supporting Information, section 5.5.3). We suspect that this energy difference is due to repulsion between the electrophilic NO_2 group of the initiator and the

electrophilic fluorine substituent of the **mon-F** monomer. Bringing the two starting components together with these substituents resulted in a relative increased energy of 2–3 kcal/mol that remained throughout the reaction. This phenomenon was not observed in the propagation reaction (Section 5.2.4, Figure 5.10), where no NO_2 group is present. However, as the NPA charges in the intermediates of the initiation reaction with **mon-H** and **mon-F** showed no differences, and the distance between the substituent and the NO_2 group was more than 5 Å, the repulsion and thus energy increase was minimal (Figure 5.9).

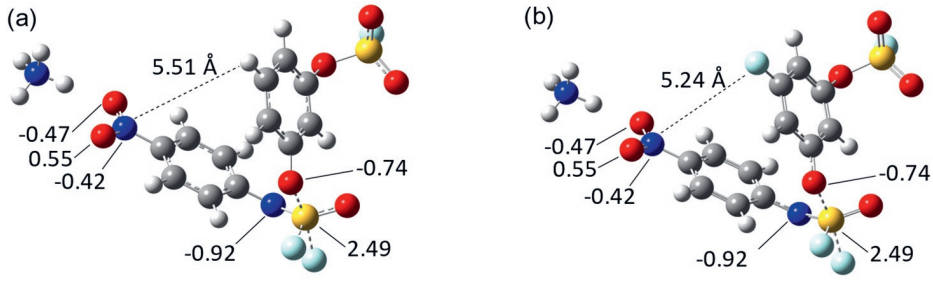

Figure 5.9. Geometries of intermediates of initiation reactions with (a) **mon-H**, and (b) **mon-F**, both with NH_4^+ near the NO_2 group. NPA charges are indicated of selected atoms and the distance from the substituent to the oxygen of the NO_2 group is indicated.

5.2.4 Propagation with relevant substituents

Where the energies of the initiation reaction were already close together, the propagation reaction had even less conformational differences between substituents (Figure 5.10). The first transition states of **mon-OMe** and **mon-F** required similar activation energy to that of **mon-H**. The intermediates of all monomers were similar in conformation as well. The **mon-H** and **mon-OMe** intermediates were 0.02 Å further along the reaction coordinate (with S–O distance at 1.78 Å and S–F distance at 1.80 Å) than **mon-F** and **mon-MeEst**. As a result, the charge on the leaving F^- was 0.01 larger for **mon-H** and **mon-OMe**. However, this did not influence the relative energies of the intermediates. Where the second transition state for **mon-H** had an energy barrier of 1.0 kcal/mol, the energy of the second transition state was lower than the intermediate for **mon-OMe** and **mon-F**, indicating that fluoride elimination was barrierless. This was similar to the initiation reaction, where these two substituents also had spontaneous fluoride elimination. For **mon-MeEst**, the second transition state could not even be located.

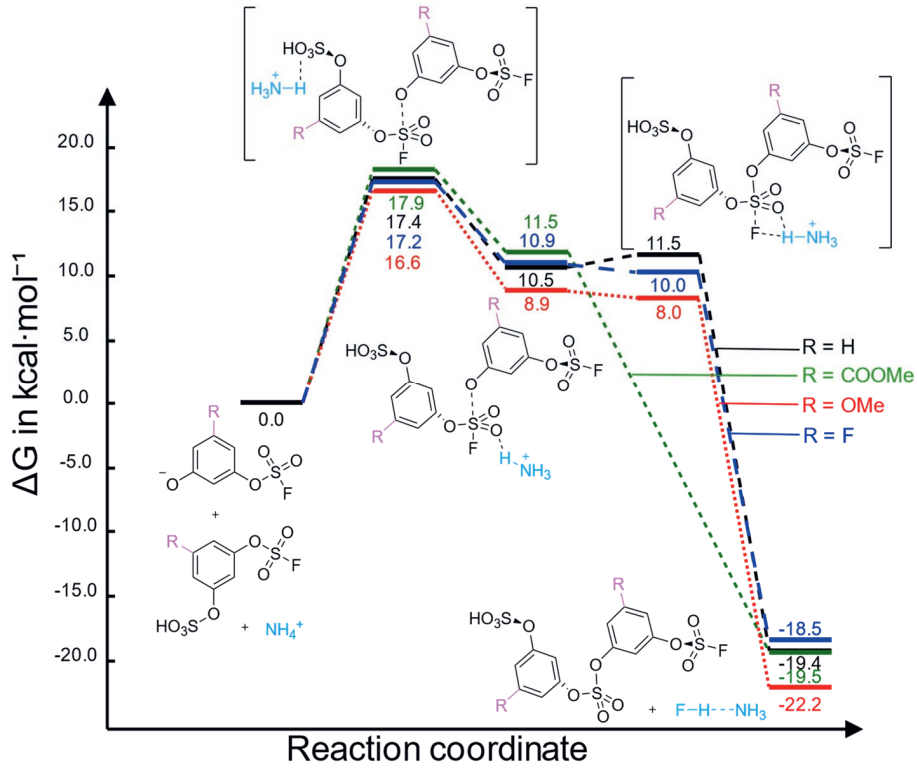

Figure 5.10. Gibbs free energy profiles of the propagation reaction of the SuFEx-based chain-growth polymerization in presence of NH_4^+, with **mon-H** (black), **mon-MeEst** (green), **mon-OMe** (red) and **mon-F** (blue) monomers. The polymer chain is represented by ((3-fluorosulfonyl)oxy)-5-substituted phenyl hydrogen sulfate.

5.2.5 Self-polymerization

By experimentally demonstrating that no polymerization occurred in absence of the initiator, Sharpless and Wu[36] excluded step-growth polymerization as plausible alternative for their proposed chain-growth polymerizations. Most monomers, among which were **mon-MeEst** and **mon-F**, did not undergo self-polymerization under regular SuFEx conditions and in the presence of 20 mol% DBU. However, **mon-OMe** was found to form considerable polymers under these conditions. This was attributed to the electron-donating nature of the methoxy group, as quantified through the Hammett parameter. Although our **mon-H** was not investigated experimentally, based on the Hammett parameters of the various meta-substituents (Table 5.2), self-polymerization is to be expected.

Table 5.2. Hammett parameters[45] of various substituents on the *meta*-position as investigated experimentally by Sharpless and Wu.[36]

Meta-substituent	Hammett parameter	Observed self-polymerization?
H	0.00 (defined)	-
OMe	0.12	Yes
F	0.34	No
MeEst	0.37	No
Acetyl	0.38	No
Cyano	0.56	-

We calculated the self-polymerization of the four monomers in presence of NH_4^+. In the SuFEx reaction between two **mon-H** monomers (Figure 5.11, in black), the addition of the phenolate required 15.5 kcal/mol and lead to a stable intermediate at 11.8 kcal/mol. In agreement with the initiation and propagation reaction, NH_4^+ is already interacting with the leaving F^- in the intermediate. The elimination of the fluorine atom required an additional 1.8 kcal/mol, which is marginally higher than in the propagation reaction and in contrast to the initiation reaction, where elimination occurred spontaneously for **mon-H**. Similar to the initiation and propagation reaction, products were found at -21.2 kcal/mol. With a total barrier of 15.5 kcal/mol, self-polymerization of **mon-H** at room temperature is thus deemed feasible.

The other three monomers displayed very similar pathways, with the first and second transition state and intermediate close in energy. The product of **mon-F** is 4.3 kcal/mol higher, presumably the absence of one hydrogen bond with the solvent. Similarly, with one hydrogen bond extra, the product of **mon-MeEst** is 4.8 kcal/mol lower.

In stark contrast to experimental findings, our results thus indicated no significant difference in reactivity between the four monomers, allowing self-polymerization in all cases. Although the paper[36] suggests that differences between monomers are due to their electron-withdrawing capability, our results do not indicate this.

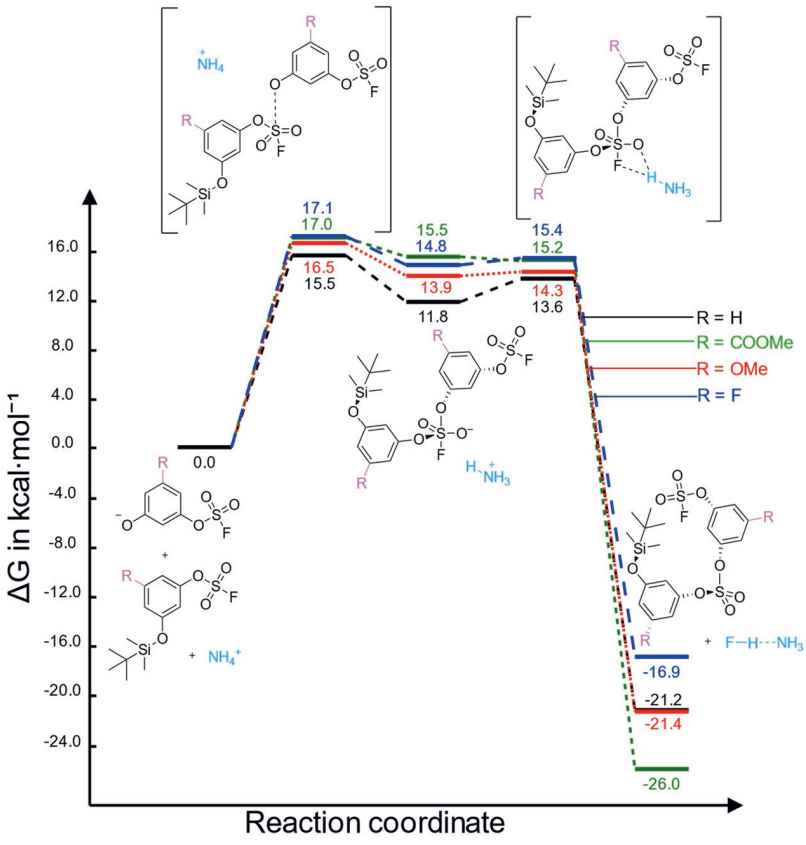

Figure 5.11. Gibbs free energy profile of the self-polymerization of **mon-H** (black), **mon-MeEst** (green), **mon-OMe** (red) and **mon-F** (blue) monomers, in presence of NH_4^+.

5.3 Discussion

It appears we are missing an essential aspect in our simulation of the experimental set-up. We should thus closer inspect our computational method. Given the significant size of our basis set (6-311G(2d,2p)) that includes ample polarization options, we highly doubt that the basis set is at fault. If the basis set would be insufficient, the electron-withdrawal of the methyl ester would be incorrectly accounted for, which would result in significantly different energy values. Similarly, our functional ωB97XD is expected for this type of interactions to be close to the current benchmark[46] and we would thus estimate that this combination is more than sufficient for our system.

However, we might have oversimplified our description in other directions. Misrepresentation of the solvent interactions is the most likely cause of the discrepancy between experiments and computations. In the initiation reaction, we observed a 2 kcal/mol increase for all structures for **mon-F** as compared to **mon-H**, which we ascribed both to the favorability of hydrogen bond formation with the solvent in the substrates. Furthermore, in the self-polymerization reaction, we observed a 4.3 kcal/mol increase for the product energy for **mon-F** as compared to **mon-H** and a 4.8 kcal/mol decrease for **mon-MeEst**, which we ascribed to hydrogen bond formation with the solvent as well. As we have indicated that the interaction with the solvent is relevant, our calculations would benefit from explicit solvent modelling. Such modelling should involve multiple explicit solvent molecules near the sulfur hub and near the substituents, to properly account for all solvent interactions that will likely change over the course of the SuFEx reaction. While this was beyond the scope of this chapter, it will need to be incorporated in future research.

Additionally, the experimental procedures could be repeated with alternative solvents. Our calculations seem to exclude electronic effects as the primary reason for the lack of self-polymerization for **mon-F** and **mon-MeEst** monomers. If this were true, the absence of self-polymerization for those two monomers is probably due to interactions with the solvent which stabilize the starting materials, such as hydrogen bonding. This hydrogen bonding increases the activation barriers and hinders self-polymerization. A less polar solvent, such as toluene, would not be able to form hydrogen bonds with the starting materials and could thus facilitate self-polymerization. Of course, the solvent must be polar enough to allow solvation and TBS abstraction by the DBU, in order for any SuFEx reaction to take place. Furthermore, as self-polymerization is undesired for chain-growth polymerization, these non-polar solvents would not be suitable for chain-growth polymerizations. They would help to clarify the mechanistic details that are currently out of view.

5.4 Conclusions

According to high-level DFT calculations, all investigated SuFEx reactions with the four chosen monomers are feasible in the presence of protonated ammonia. Both the initiation and propagation reaction showed slight substituent effects on the activation energies, which were attributed to conformational differences

and hydrogen bond formation of the substrates with the solvent. The feasibility of the initiation and propagation SuFEx reactions is in agreement with the experimental findings of Sharpless and Wu,[36] who described rapid polymerization for all substituents in the presence of initiator. In our calculations, however, the self-polymerization reaction is likely as well for all substituents and displayed less than 2 kcal/mol difference in activation energy between the various substituents. These results are remarkable, as they contradict experimental findings where no self-polymerization occurred for the **mon-MeEst** and **mon-F** monomers, while the **mon-OMe** does self-polymerize. More calculations are thus required, including explicit solvent interactions.

5.5 Supporting Information

5.5.1 Energy of the fluoride ion

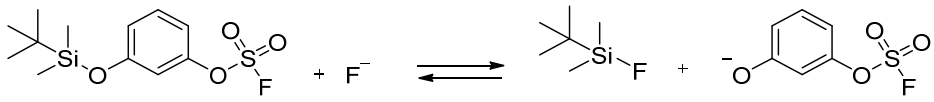

Figure 5.12. Reaction scheme of a TBS-group from **mon-H** to a fluoride anion.

In order to calculate the energy of an F^- in a similar environment as in our SuFEx reactions (Figure 5.12), we calculated the Gibbs free energy values of TBS-protected ((3-fluorosulfonyl)oxy)phenolate, non-protected ((3-fluorosulfonyl)oxy)phenolate and TBS-fluoride. By subtracting the TBS-protected ((3-fluorosulfonyl)oxy)phenolate from ((3-fluorosulfonyl)oxy)phenolate and TBS-fluoride, we obtained the Gibbs free energy of a 'naked' F^- (Table 5.3). Hence for F^-, G = –100.0054 Hartree.

Table 5.3. Gibbs free energy values for the calculation of a 'naked' F^-.

Compound	EE+Gcorr (in Hartree)
TBS-F	–626.982777
(3-fluorosulfonyl)phenolate	–1029.982763
TBS-(3-fluorosulfonyl)phenolate	–1556.960182

5.5.2 Propagation with full polymer chain and with $-SO_3H$

In presence of NH_4^+, the substitution of hydrogen sulfate by (4-nitrobenzene) sulfate slightly lowers the activation energy of the first transition state (Figure 5.5, in black and deep red respectively). However, the 2.2 kcal/mol difference is small enough to justify simplification of the polymer representation by hydrogen sulfate.

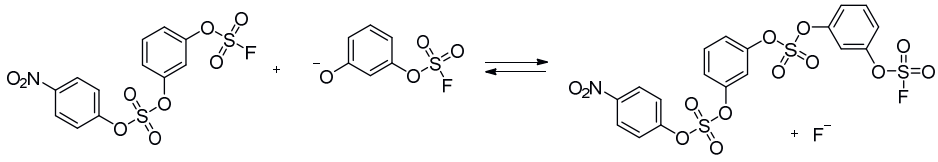

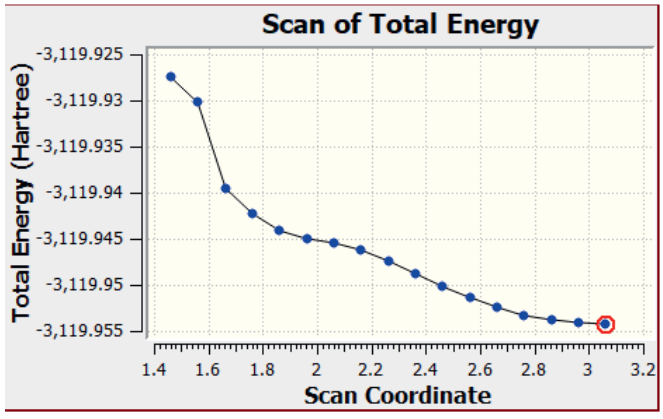

Figure 5.13. Reaction scheme of the propagation reaction between ((3-fluorosulfonyl)oxy)phenolate and ((3-fluorosulfonyl)oxy)phenyl (4-nitrophenyl) sulfate, and the total energy (without Gibbs free energy corrections) as function of the reaction coordinate (S–O distance) of this reaction.

In absence of NH_4^+, substitution of hydrogen sulfate by (4-nitrobenzene) sulfate rendered the reaction impossible. A scan of the reaction coordinate decreasing the S–O distance (between the sulfur hub and the phenolate) showed a continuous increasing energy, yielding no transition states or intermediate (Figure 5.13). Only by calculating the separate components of the product, did we obtain an energy value. This value was in agreement with the energy for the hydrogen sulfate pathway, supporting our claim that the simplification was justified. Furthermore, it indicates once more that the presence of an electrophile for the capture of F^- is essential for proper representation of the SuFEx reaction.

5.5.3 Gibbs Free energy and enthalpy values

Table 5.4: Gibbs free energy and enthalpy of the initiation reaction including NH_4^+ for (a) **mon-H**, (b) **mon-MeEst**, (c) **mon-OMe**, and (d) **mon-F**.

(a)	EE+Gcorr	EE+Hcorr
Reactants	0.00	0.00
TS-1	7.30	–13.47
Intermediate	3.88	–17.66
TS-2	1.54	–21.39
Products	–22.92	–32.88

(b)	EE+Gcorr	EE+Hcorr
Reactants	0.00	0.00
TS-1	6.62	–18.50
Intermediate	3.85	–19.89
TS-2	2.53	–22.30
Products	–19.30	–32.36

(c)	EE+Gcorr	EE+Hcorr
Reactants	0.00	0.00
TS-1	10.35	–15.90
Intermediate	1.41	–20.61
TS-2	0.02	–22.67
Products	–24.41	–35.40

(d)	EE+Gcorr	EE+Hcorr
Reactants	0.00	0.00
TS-1	9.12	–12.87
Intermediate	6.57	–14.93
TS-2	3.23	–18.59
Products	–20.16	–29.54

References

(1) Sze, S. M.; Morkoç, H.; Mohammad, S. N.; Tomozawa, H. ; J.; Fung, A. W. P.; Katz, H. E.; Yang, Y.; Heeger, A. J.; Pei, Q.; Yu, G.; Zhang, C.; Pakbaz, K. *Phys. Semicond. Dev.* **1981**, *267* (1), 35.

(2) van Dam, A.; Smulders, M. M. J.; Zuilhof, H. *Appl. Surf. Sci.* **2022**, *579*, 152264.

(3) Yang, W.; Zhang, R.; Wu, Y.; Pei, X.; Liu, Y.; Zhou, F. *J. Appl. Polym. Sci.* **2018**, *135* (22), 46231-46239.

(4) Gauthier, M. A.; Gibson, M. I.; Klok, H. A. *Angew. Chem. Int. Ed.* **2009**, *48* (1), 48–58.

(5) Kolb, H. C.; Finn, M. G.; Sharpless, K. B. *Angew. Chem. Int. Ed.* **2001**, *40*, 2004–2021.

(6) Briou, B.; Améduri, B.; Boutevin, B. *Chem. Soc. Rev.* **2021**, *50* (19), 11055–11097.

(7) Döhler, D.; Michael, P.; Binder, W. H. *Acc. Chem. Res.* **2017**, *50* (10), 2610–2620.

(8) Lowe, A. B. *Polym. Chem.* **2010**, *1* (1), 17–36.

(9) Tasdelen, M. A. *Polym.Chem.* **2011**, *2*, 2133–2145.

(10) Dong, J.; Krasnova, L.; Finn, M. G.; Barry Sharpless, K *Angew. Chem. Int. Ed.* **2014**, *53* (36), 9430–9448.

(11) Steinkopf, W. *J. Prakt. Chem.* **1927**, *117*, 1–82.

(12) Gembus, V.; Marsais, F.; Levacher, V. *Syn. Lett.* **2008**, *10*, 1463–1466.

(13) Smedley, C. J.; Barrow, A. S.; Spiteri, C.; Giel, M. C.; Sharma, P.; Moses, J. E. *Chem. Eur. J.* **2017**, *23* (42), 9990–9995.

(14) Hmissa, T.; Zhang, X.; Dhumal, N. R.; McManus, G. J.; Zhou, X.; Nulwala, H. B.; Mirjafari, A. *Angew. Chem. Int. Ed.* **2018**, *57*, 16005–16009.

(15) Li, B. Y.; Voets, L.; van Lommel, R.; Hoppenbrouwers, F.; Alonso, M.; Verhelst, S. H. L.; de Borggraeve, W. M.; Demaerel, J. *Chem. Sci.* **2022**, *13* (8), 2270–2279.

(16) Xiao, X.; Zhou, F.; Jiang, J.; Chen, H.; Wang, L.; Chen, D.; Xu, Q.; Lu, J. *Polym. Chem.* **2018**, *9* (8), 1040–1044.

(17) Wan, H.; Xu, Q.; Wu, J.; Lian, C.; Liu, H.; Zhang, B.; He, J.; Chen, D.; Lu, J. *Angew. Chem. Int. Ed.* **2022**, *61* (33), e202208577.

(18) Kline, G. M.; Nugroho, K.; Kelly, J. W. *Curr. Opin. Chem. Biol.* **2022**, *67*, 102113.

(19) Wilson Lucas, S.; Zijian Qin, R.; Rakesh, K. P.; Sharath Kumar, K. S.; Qin, H. L. *Bioorg. Chem.* **2023**, *130*, 106227.

(20) Liu, F.; Wang, H.; Li, S.; Bare, G. A. L.; Chen, X.; Wang, C.; Moses, J. E.; Wu, P.; Sharpless, K. B. *Angew. Chem. Int. Ed.* **2019**, *58* (24), 8029–8033.

(21) Cheng, M.; Guo, C.; Gross, M. L. *Angew. Chem. Int. Ed.* **2020**, *59* (15), 5880–5889.

(22) Yatvin, J.; Brooks, K.; Locklin, J. *Angew. Chem. Int. Ed.* **2015**, *54* (45), 13370–13373.

(23) Gahtory, D.; Sen, R.; Pujari, S.; Li, S.; Zheng, Q.; Moses, J. E.; Sharpless, K. B.; Zuilhof, H. *Chem. Eur. J.* **2018**, *24* (41), 10550–10556.

(24) Durie, K.; Yatvin, J.; Kovaliov, M.; Crane, G. H.; Horn, J.; Averick, S.; Locklin, J. *Macromolecules* **2018**, *51* (2), 297–305.

(25) Liang, D. D.; Pujari, S. P.; Subramaniam, M.; Besten, M.; Zuilhof, H. *Angew. Chem. Int. Ed.* **2022**, *61*, e202116158.

(26) Liang, D. D.; Streefkerk, D. E.; Jordaan, D.; Wagemakers, J.; Baggerman, J.; Zuilhof, H. *Angew. Chem. Int. Ed.* **2020**, *59* (19), 7494–7500.

(27) Chao, Y.; Krishna, A.; Subramaniam, M.; Liang, D. D.; Pujari, S. P.; Sue, A. C. H.; Li, G.; Miloserdov, F. M.; Zuilhof, H. *Angew. Chem. Int. Ed.* **2022**, *61*, e202207456.

(28) Cao, Z.; Zhou, F.; Gu, P. Y.; Chen, D.; He, J.; Cappiello, J. R.; Wu, P.; Xu, Q.; Lu, J. *Polym. Chem.* **2020**, *11* (18), 3120–3124.

(29) Dong, J.; Sharpless, K. B.; Kwisnek, L.; Oakdale, J. S.; Fokin, V. V. *Angew. Chem. Int. Ed.* **2014**, *53* (36), 9466–9470.

(30) Yatvin, J.; Brooks, K.; Locklin, J. *Chem. Eur. J.* **2016**, *22* (46), 16348–16354.

(31) Kulow, R. W.; Wu, J. W.; Kim, C.; Michaudel, Q. *Chem. Sci.* **2020**, *11* (30), 7807–7812.
(32) Lee, W.; Li, L.; Kim, B. *Catalysts* **2021**, *11* (9), 1044.
(33) Wang, H.; Zhou, F.; Ren, G.; Zheng, Q.; Chen, H.; Gao, B.; Klivansky, L.; Liu, Y.; Wu, B.; Xu, Q.; Lu, J.; Sharpless, K. B.; Wu, P. *Angew. Chem. Int. Ed.* **2017**, *56* (37), 11203–11208.
(34) Li, S.; Li, G.; Gao, B.; Pujari, S. P.; Chen, X.; Kim, H.; Zhou, F.; Klivansky, L. M.; Liu, Y.; Driss, H.; Liang, D. D.; Lu, J.; Wu, P.; Zuilhof, H.; Moses, J.; Sharpless, K. B. *Nat. Chem.* **2021**, *13* (9), 858–867.
(35) Yang, C.; Flynn, J. P.; Niu, J. *Angew. Chem. Int. Ed.* **2018**, *57* (49), 16194–16199.
(36) Kim, H.; Zhao, J.; Bae, J.; Klivansky, L. M.; Dailing, E. A.; Liu, Y.; Cappiello, J. R.; Sharpless, K. B.; Wu, P. *ACS Cent. Sci.* **2021**, *7* (11), 1919–1928.
(37) Luy, J. N.; Tonner, R. *ACS Omega* **2020**, *5* (48), 31432–31439.
(38) Han, B.; Khasnavis, S. R.; Nwerem, M.; Bertagna, M.; Ball, N. D.; Ogba, O. M. *Inorg. Chem.* **2022**, *61* (25), 9746–9755.
(39) Chai, J. Da; Head-Gordon, M. *Phys. Chem. Chem. Phys.* **2008**, *10* (44), 6615–6620.
(40) Minenkov, Y.; Singstad, Å.; Occhipinti, G.; Jensen, V. R. *Dalton Trans.* **2012**, *41* (18), 5526–5541.
(41) Frisch, M. J.; Trucks, G. W.; Schlegel, H. B.; Scuseria, G. E. ; Robb, M. A.; Cheeseman, J. R.; Scalmani, G.; Barone, V. ; P.; G. A.; Nakatsuji, H.; Li, X.; Caricato, M.; Marenich, A. V.; Bloino, J. ; Janesko, B. G.; Gomperts, R.; Mennucci, B.; Hratchian, H. P.; Ortiz, J.; V.; Izmaylov, A. F.; Sonnenberg, J. L.; Williams-Young, D.; Ding, F. ; Lipparini, F.; Egidi, F.; Goings, J.; Peng, B.; Petrone, A. ; H.; T.; Ranasinghe, D.; Zakrzewski, V. G.; Gao, J.; Rega, N.; Zheng, G. ; Liang, W.; Hada, M.; Ehara, M.; Toyota, K.; Fukuda, R.; Hasegawa, J. ; Ishida, M.; Nakajima, T.; Honda, Y.; Kitao, O.; Nakai, H.; Vreven, T. ; Throssell, K.; Montgomery, J. A., Jr.; Peralta, J. E.; Ogliaro, F. ; Bearpark, M. J.; Heyd, J. J.; Brothers, E. N.; Kudin, K. N. ; S.; V. N.; Keith, T. A.; Kobayashi, R.; Normand, J.; Raghavachari, K. ; Rendell, A. P.; Burant, J. C.; Iyengar, S. S.; Tomasi, J.; Cossi, M. ; Millam, J. M.; Klene, M.; Adamo, C.; Cammi, R.; Ochterski, J. W. ;; Martin, R. L.; Morokuma, K.; Farkas, O.; Foresman, J. B.; Fox, D. J. *Gaussian 16, Revision C.01*, Wallingford, CT, **2016**.
(42) Marenich, A. V.; Cramer, C. J.; Truhlar, D. G. *J. Phys. Chem. B* **2009**, *113* (18), 6378–6396.
(43) Angnes, R. A. *GitHub repository* **2020**, *DOI 10.5281/zenodo.4065333*.
(44) Liang, D.; Streefkerk, D. E.; Jordaan, D.; Wagemakers, J.; Baggerman, J.; Zuilhof, H. *Angew. Chem. Int. Ed.* **2020**, *59* (19), 7494–7500.
(45) Hansch, C.; Leo, A. Substituent Constants for Correlation Analysis in Chemistry and Biology; Wiley-Interscience: NY, 1979.
(46) Santra, G.; Calinsky, R.; Martin, J. M. L. *J. Phys. Chem. A* **2022**, *126* (32), 5492–5505.

Chapter 6
Controlling the Competition: Boosting Laccase/HBT-Catalyzed Cleavage of a *β*-O-4′ Linked Lignin Model

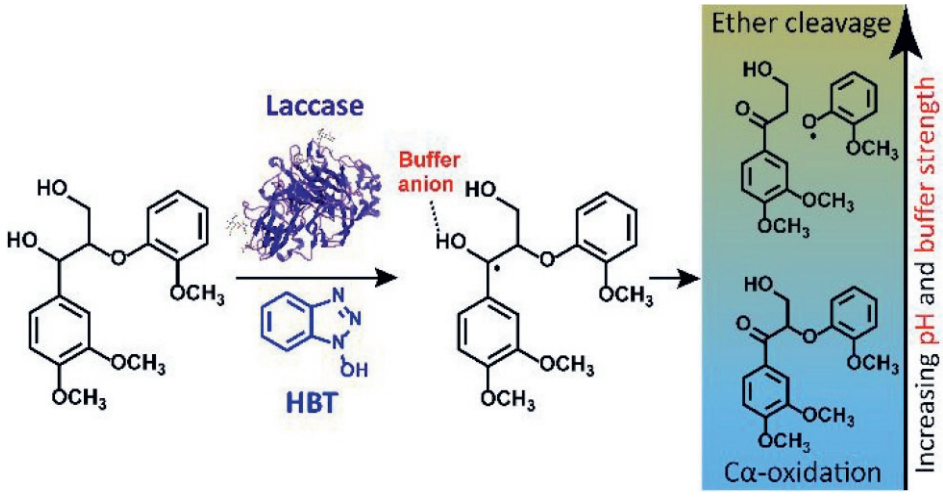

This chapter has been published as:

Roelant Hilgers, Annemieke van Dam, Han Zuilhof, Jean-Paul Vincken, Mirjam A. Kabel, *ACS Catal.* **2020**, 10, 8650−8659.

https://doi.org/10.1021/acscatal.0c02154

Abstract

Over the past years, laccase/mediator systems (LMS) have received a lot of attention as potential sustainable tools for biocatalytic lignin degradation. Nevertheless, it has often been reported that C_α-oxidation, rather than ether bond cleavage, is the main result of LMS treatments, which limits the overall efficiency and effectiveness. Remarkably few studies have attempted to influence this product profile and thereby enhance the effectivity of LMS-catalyzed lignin degradation. In the research described in this chapter, we studied the influence of buffer properties on the product profile of a *β*-O-4' linked lignin model dimer upon conversion by a laccase/hydroxybenzotriazole system. We show that the ratio between *β*-O-4' ether cleavage and C_α-oxidation can be substantially increased by using unconventional buffer properties (*i.e.*, highly concentrated buffers at near-neutral pH). Whereas <10% ether cleavage was obtained in a conventional buffer (*i.e.*, weak buffer at pH 4), as much as 80% ether cleavage was obtained in highly concentrated buffers at pH 6. In addition, this alteration of buffer properties was found to improve the stability of both laccase and mediator. The underlying reactions were further studied by experimental and computational (density functional theory, DFT) approaches. Based on the outcomes, we propose detailed reaction mechanisms for the reactions underlying ether cleavage and C_α-oxidation. We propose that increasing buffer pH or increasing buffer strength enhances hydrogen bonding between the lignin model and buffer anions, which drives the overall reaction outcome toward ether cleavage. These insights may pave the way for more efficient and effective biocatalytic lignin degradation.

6.1 Introduction

Lignin is a highly abundant aromatic polymer in plant cell walls, and its selective degradation is a major challenge in biorefinery. Lignin mainly consists of syringyl (S), guaiacyl (G), and p-hydroxyphenyl (H) units, coupled via a variety of interunit linkages, of which the *β*-O-4′ linkage is most abundant (45−94% of the total interunit linkages).[1] The polymer consists of phenolic subunits (10−30%), mainly being the end-caps of the polymer, and nonphenolic subunits (70−90%), forming the backbone.[2] Although lignin can be degraded by using thermochemical treatments, green alternatives are preferred and are receiving increasing attention.

A potential green approach for selective lignin degradation is the use of laccase/mediator systems (LMS). Laccases (EC 1.10.3.2) are oxidases with redox potentials of <800 mV[1] that use molecular oxygen to perform one-electron oxidations of aromatic substrates. Laccases can oxidize the phenolic lignin subunits, which have sufficiently low redox potentials, but oxidation of the nonphenolic subunits, having redox potentials up to 1500 Mv, is hampered.[3] To overcome the inertness of nonphenolic subunits, a mediator can be added to form a LMS. In such a system, laccase oxidizes the mediator, which subsequently oxidizes the nonphenolic lignin structure. The most widely used mediator is 1-hydroxybenzotriazole (HBT). Other commonly used mediators are TEMPO ((2,2,6,6-tetramethylpiperidin-1-yl)oxyl) and ABTS (2,2′-azino-bis(3-ethylbenzo-thiazoline-6-sulfonic acid)).

These mediators oxidize lignin substructures via different mechanisms. For TEMPO, an ionic mechanism has been proposed.[4] ABTS has been suggested to operate via electron transfer (ET), although this has not been unambiguously demonstrated.[5] HBT is generally assumed to oxidize nonphenolic lignin structures via hydrogen atom transfer (HAT),[5,6] although it has been suggested that electron transfer (ET) may also occur in the case of relatively electron-rich lignin substructures.[7] Oxidation of lignin substructures via HAT and ET results in the formation of benzylic radicals and radical cations, respectively. These radicals react further (nonenzymatically) via several routes, depending on the structure of the substrate.[8–12] Studies on LMS treatments of nonphenolic *β*-O-4′ linked lignin model compounds mainly report C_α-oxidation[13] and bond cleavage as outcomes,[8,11,12,14,15] and it has been suggested that their formation occurs via

competing routes.[1,10] Typically, C_α-oxidation is the major reaction outcome, whereas cleavage products are only formed in minor amounts.[12,14,15] Obviously, when LMS treatments are performed with the aim to degrade lignin, this product distribution is undesirable and should be shifted in favor of bond cleavage.

In principle, to increase the efficiency of LMS-catalyzed lignin degradation, two strategies could be followed: (i) maximizing the total extent of oxidation by increasing the catalytic performance of the LMS or (ii) steering the nonenzymatic follow-up reactions toward bond cleavage (at the cost of C_α-oxidation). Whereas multiple studies have been published related to the catalytic performance of different laccases and mediators (in line with the first approach),[16-20] to the best of our knowledge, no studies have been published that follow the second approach. In addition, as LMS treatments are often performed at those conditions under which the laccase is optimally active, it is largely unknown whether and how reaction conditions can affect the reaction product profile. In this chapter, we show that altering buffer pH and buffer strength can dramatically enhance degradation of a nonphenolic lignin model, veratrylglycerol-*β*-guaiacyl ether (VBG), by a laccase/HBT system (Figure 6.1). Furthermore, based on additional experiments and a computational (DFT) study, we provide new insights into the competition between C_α-oxidation and ether bond cleavage and the underlying mechanisms.

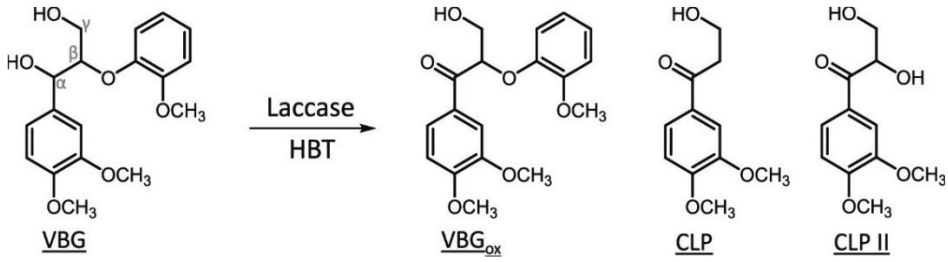

Figure 6.1. Reaction products of VBG formed upon incubation with the laccase/HBT system, as described in section 6.2.1.

6.2 Results and discussion

6.2.1 Conversion of VBG by the Laccase/HBT System

Incubations of VBG with laccase/HBT were performed in citrate/phosphate buffers at pH 3−7. In all cases, three reaction products were detected: The C_{α}-ketone analogue of VBG (VBG_{ox}) and two ether cleavage products (CLP and CLP II; Figures 6.1 and 6.2; see Table S6.1 and Figure S6.1−6.3 of the online Supporting Information for UHPLCMS and NMR based identification). VBG_{ox} was found to be the major product, which is in line with previous findings in the literature.[12,14,15]

During the incubation, HBT was partly converted to benzotriazole (BT) (23−86% based on UV peak ratio, Table S6.2). It should be noted that, upon formation of CLP and CLP II, other cleavage products should have been formed as well (*i.e.*, products containing the other aromatic ring of VBG). These products were not detected, most likely because they reacted further to other products.

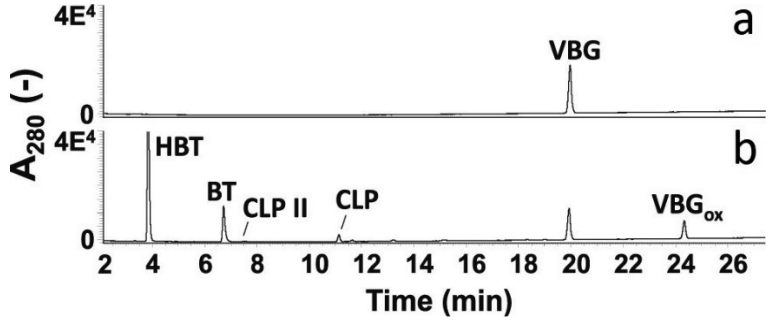

Figure 6.2. RP-UHPLC-UV_{280} chromatograms of VBG (a) and VBG incubated for 48 h with laccase/HBT in a 20/40 mM citrate/phosphate buffer at pH 6 (b). BT = benzotriazole. Other chromatograms and data used for product identification can be found in the online Supporting Information.

6.2.2 Effect of pH and Buffer Strength on Product Distribution

Laccase/HBT incubations performed at pH 3−7 in 20/40 mM citrate/phosphate buffers were followed over time (Figure S6.4). Regarding the extent of VBG conversion, pH 4 and 5 were found to be the optimum pH values, showing 45 and 54% conversion, respectively, after 48 h (Figure 6.3).

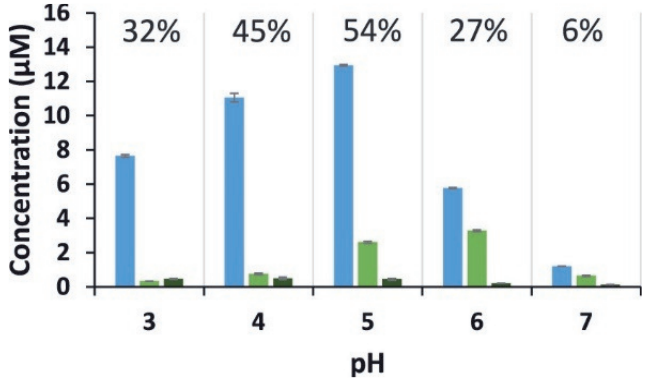

Figure 6.3. Concentration of the reaction products VBG_{ox} (blue), CLP (green), and CLP II (dark green) after incubation with laccase/HBT for 48 h in 20/40 mM citrate/phosphate buffers. Percentages refer to the conversion of VBG. The error bars represent the standard deviation of two independent incubations.

The relatively high conversion may justify why most lignin and lignin model compound incubations in literature are performed at these, for the laccase more optimal, pH values.[11,12,21–25] Nevertheless, the pH was shown to strongly affect the product distribution. At pH 3 and 4, mainly VBG_{ox} was formed and the cleavage products were only formed to a minor extent (*i.e.*, both <6% of the reaction products). At higher pH values, the product distribution shifted in favor of the cleavage products, mainly due to an increased formation of CLP (Figure 6.3). At pH 6 and 7, the cleavage products together accounted for 38% of the reaction products. The product ratios did not show a strong dependence on incubation time (data not shown). Regarding absolute amounts, the optimal pH for cleavage of VBG was pH 6, due to a higher laccase activity at pH 6 than at pH 7. The formation of CLP II was highest at low pH values, but rather low yields (≤1%) were found in all incubations, indicating that cleavage of the *O*-4' bond occurs only to a very limited extent. Therefore, in further investigations, we focused on the formation of VBG_{ox} and CLP.

Although it seemed that the pH influenced the reaction product profile, it is important to note that by increasing the buffer pH, also the phosphate/citrate ratio and the dissociation of citrate and phosphate increased. Therefore, we investigated whether the observed differences in product ratios (see Figure 6.3) were effects of pH or (also) of the concentration of specific ions. To this end, the incubations of VBG were repeated in 5/10 mM, 40/80 mM and 80/160 mM citrate/phosphate buffers. Interestingly, the molar ratio CLP/VBG_{ox} was found

to increase not only with increasing pH but also with increasing buffer strength (Figure 6.4). In absence of a buffer, a pH effect was still observed, although the ratio CLP/VBG_{ox} was significantly lower than in buffered incubations. These results indicate that the product ratio is not determined by a "simple" pH dependence but that the ratio CLP/VBG_{ox} is considerably affected by the presence of buffer ions.

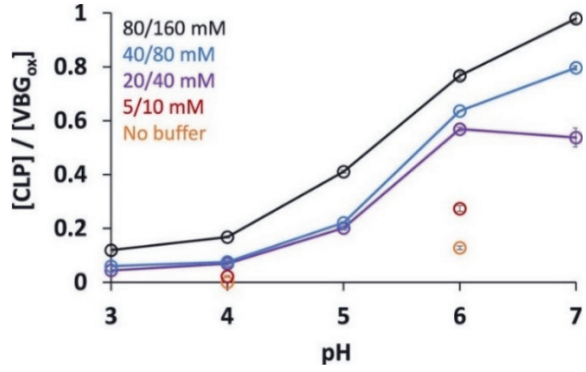

Figure 6.4. Molar ratios between CLP and VBGox after incubation of VBG for 48 h with laccase/HBT in buffers prepared from 5/10 mM (red), 20/40 mM (purple), 40/80 mM (blue), and 80/160 mM citrate/phosphate (black) or nonbuffered solutions of which the pH was adjusted using NaOH and HCl (yellow). The error bars represent the standard deviation of two independent incubations.

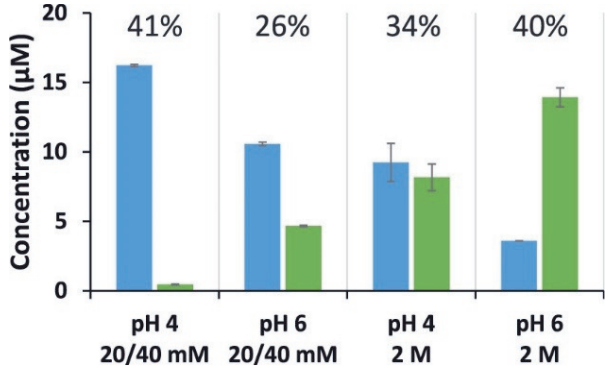

Figure 6.5. Concentrations of the reactions products VBG_{ox} (blue) and CLP (green) after incubation of VBG with laccase/HBT in 20/40 mM citrate/phosphate or 2 M citrate buffers for 48 h. Percentages refer to the conversion of VBG. The error bars represent the standard deviation of two independent incubations.

Based on the insights described above, we attempted to further enhance ether cleavage of VBG by performing incubations in highly concentrated (2 M) citrate buffers at pH 4 and 6. After 48 h, 34−40% of the VBG was converted, and CLP/VBGox ratios as high as 0.9 and 3.9 were obtained at pH 4 and 6, respectively (Figure 6.5).

The latter ratio is 138 times higher than that obtained in the control experiment (20/40 mM citrate/phosphate buffer at pH 4), and demonstrates the enormous impact of the buffer properties on the reaction outcome. Interestingly, after 48 h of incubation, the residual laccase activity was larger in the concentrated citrate buffers than in the weak citrate/phosphate buffers, and substantially less HBT was degraded to BT (Table S6.2). Hence, the increased extent of ether bond cleavage does not occur at the cost of enzyme stability.

6.2.3 Experimental Insights into the Effect of Reaction Conditions on Product Distribution

Competing or Sequential Formation of VBG_{ox} and CLP?

Our next step was to understand in more detail how the buffer properties affect the product distribution in laccase/HBT incubations. First, we verified that the two dominant reaction products (*i.e.*, VBG_{ox} and CLP) are true end products of the incubation, and that they are formed through competing, rather than sequential reactions. To this aim, purified VBG_{ox} and CLP were incubated with laccase/HBT at pH 4 and 6. After 24 h, no conversion was found for both products, confirming that both VBG_{ox} and CLP are end products of the laccase/HBT treatment, formed via competing reaction pathways (Figure S6.5).

Role of Laccase Activity

As the results shown in Figure 6.3 were obtained from incubations with the same amount (and not activity) of laccase at all pH values, we checked whether the observed pH effects were caused indirectly by the effect of pH on laccase activity toward HBT. Although laccase loading slightly affected the ratio CLP/VBG_{ox} (Figure S6.6), the differences were too small to explain the results shown in Figure 6.3. Based on these verifications, it was concluded that CLP and VBG_{ox} should be formed from laccase-independent, competing reactions.

Buffer or Salt Effects in the Competing Reactions?

The ratio CLP/VBG_{ox} was found to increase with increasing pH and buffer strength. As both buffer strength and pH are positively correlated with ionic strength, due to increased concentration and dissociation of ions, respectively, we investigated whether the ratio CLP/VBG_{ox} could also be enhanced by increasing the ionic strength with a non-buffer salt (*i.e.*, KNO_3). As can be observed from Figure 6.6, the addition of 0.5 M KNO_3 did not significantly affect the product ratio. From this, it can be inferred that the product ratio is not affected by the ionic strength of the reaction medium but rather by the concentration of specific buffer ions.

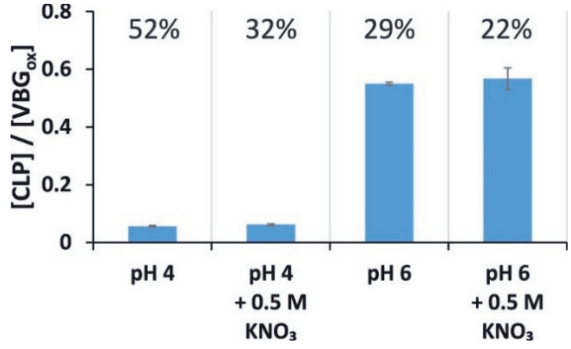

Figure 6.6. Molar product ratios (CLP/VBG_{ox}) after incubation of VBG for 48 h with laccase/HBT in buffers at pH 4 and 6 prepared from 20/40 mM citrate/phosphate, and in the same buffers supplemented with 0.5 M KNO_3. The error bars represent the standard deviation of two independent incubations. The percentages refer to the conversion of VBG.

Do Buffer pH and Strength Affect the Oxidation Mechanism?

To define the exact starting point of the observed competition reactions, we investigated whether oxidation of VBG by the HBT radical would result in the formation of benzylic radicals (via HAT) and/or radical cations (via ET). Although it is generally assumed that the laccase/HBT system operates via a HAT mechanism, evidence for this has only been obtained by using monomeric lignin model substrates and only at pH 5.[5,26] In another study, in which a dimeric lignin model was used, it has been suggested that laccase/HBT can operate via both HAT and ET.[7] We, therefore, investigated whether a HAT or an ET mechanism would be more plausible in the case of VBG oxidation and whether a shift in oxidation mechanism could occur when changing the buffer pH. To this end, we

determined the kinetic isotope effect (KIE) of VBG and its C_α-deuterated analogue ($VBG_{C\alpha\text{-}D}$) in intermolecular competition experiments in 20/40 mM citrate/phosphate buffers at pH 3, 4, 5, and 6 (see Figure 6.7).

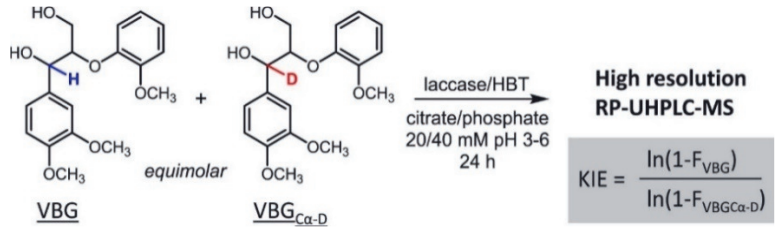

Figure 6.7. Schematic overview of the kinetic isotope effect (KIE) determination. The KIE was determined by comparing conversion rates of VBG and its C_α-deuterated analogue $VBG_{C\alpha\text{-}D}$ in an intermolecular competition experiment. The KIE was then determined by using the formula shown in the figure, wherein *F* = fraction of substrate converted.[27]

In case of a HAT mechanism, a substantial primary KIE can be expected, as cleavage of the C_α-H/D bond occurs at the rate-limiting step. In contrast, no substantial KIE is expected in the case of ET, as the C_α-H/D bond is not involved in the rate limiting step.[5] Relatively large KIEs (4.1−6.3) were found for all pH values (Table 6.1).

As these KIE values clearly point into the direction of a HAT mechanism, and as no clear increasing or decreasing trend in KIE was observed with increasing pH, a shift in oxidation mechanism seems implausible. Thus, we concluded that the competition between CLP and VBG_{ox} formation starts after formation of a VBG benzylic radical.

Table 6.1. Kinetic Isotope Effects Obtained from an Intermolecular Competition between Oxidation of VBG and C_α-Deuterated VBG ($VBG_{C\alpha\text{-}D}$) upon Incubation with Laccase/HBT for 48 h.[a]

pH	KIE (H/D)
3	5.1 ± 0.7
4	5.1 ± 0.3
5	6.3
6	4.1 ± 0.5

[a]Averages and standard deviations of two independent incubations are shown.

6.2.4 Computational Insights

To gain further insights into the competing reactions of the VBG benzylic radical, we zoomed in on the reaction mechanisms underlying C_α-oxidation and C_β-O' ether cleavage. Mechanisms have been suggested for both reactions, although few efforts have been made to provide evidence for these mechanisms.[7,28] To check the plausibility of the suggested mechanisms and to obtain more insights into the structures of the transition states (TS) and intermediates, we performed a Density Functional Theory (DFT) study to determine the relative enthalpies of all structures involved.

C_α-Oxidation

For C_α-oxidation, a mechanism has been suggested in literature that involves addition of O_2 to the benzylic radical, after which the C_α-ketone is formed by splitting off a hydroperoxyl radical (Figure 6.8, pathway A).[7,28] As the energy-minimized starting point of this step (*i.e.*, structure 1 + O_2) has quartet spin, while the resulting peroxyl radical intermediate (structure 3) has doublet spin, TS 2 is likely to have a blended spin state. Therefore, we started out by potential energy scans assuming either quartet spin (coming from structure 1 and O_2) or doublet spin (coming from structure 3). The quartet-state trajectory yielded a clear TS upon specific geometric restrictions (Figure 6.9), while the doublet trajectory did not yield a TS. Since the quartet trajectory was higher in energy than the doublet one, this was analyzed in detail, so as to obtain an upper limit to the TS energy. The resulting (quartet) TS structure (Figure 6.9) has a relative energy of 29.7 kcal/mol compared to the starting materials. As O_2-addition is overall exothermic by 52.6 kcal/mol, it was concluded that O_2-addition is irreversible.

The second step of pathway A involves splitting off a hydroperoxyl radical. For this step, a clear transition state (structure 4) containing a five-membered ring was found, indicating that the hydroperoxyl radical leaving group is formed through intramolecular hydrogen transfer. The activation energy of this second step equals 17.5 kcal/mol. Thus, depending on how much doublet spin character is involved in TS 2, the activation energy of pathway A is predicted to be in the range of 17.5−29.7 kcal/mol. Although the calculated enthalpy gain of splitting of a hydroperoxyl radical is essentially zero, the reaction is probably driven forward by entropy gain and/or further reactions of the hydroperoxyl radical.

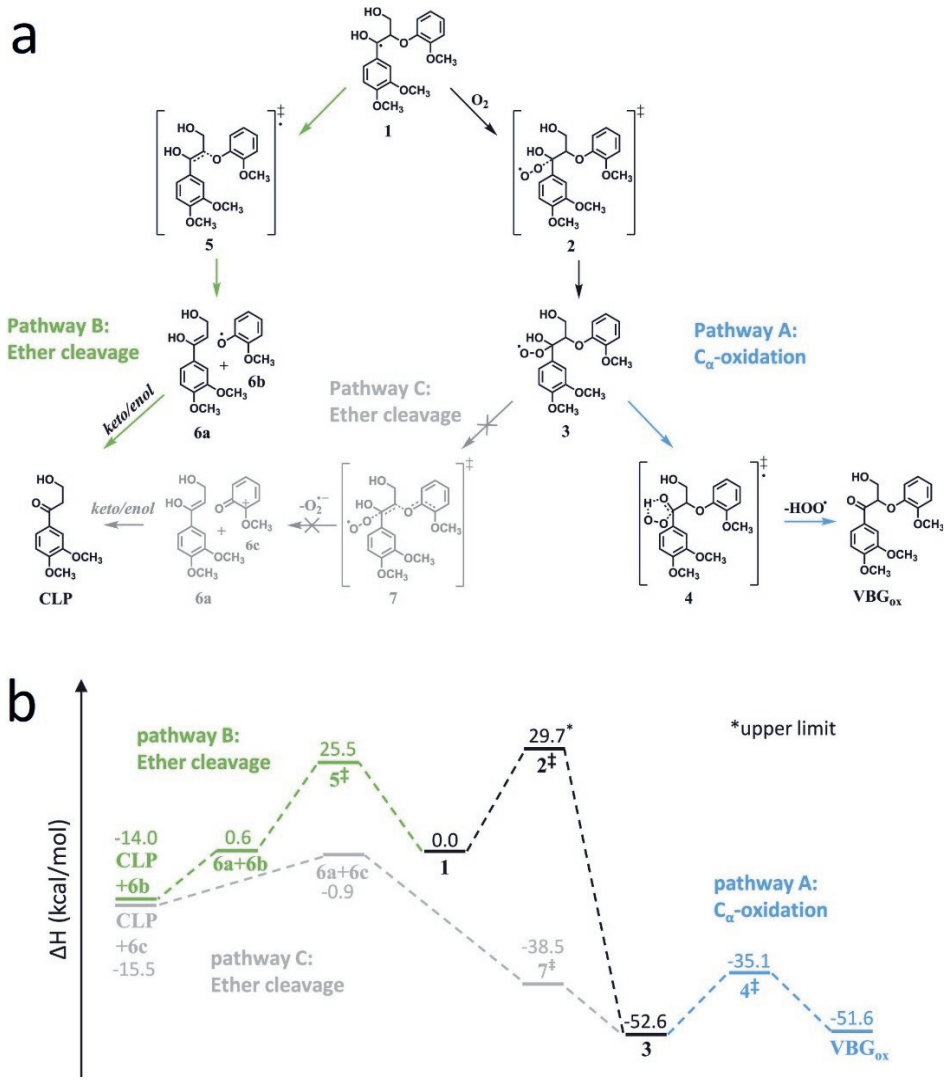

Figure 6.8. Reaction mechanisms (top) for C_α-oxidation (pathway A) and C_β-O' cleavage (pathways B and C) of the VBG benzylic radical, with calculated relative enthalpies of intermediates, transition states, and products (bottom). As structure 6b and 6c rapidly react further, the final relative enthalpies of the cleavage pathways (B and C) are expected to be significantly lower than the presented values. *This enthalpy should be interpreted as an upper limit.

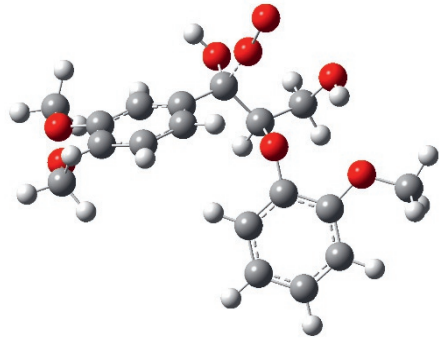

Figure 6.9. Optimized geometry of the transition state (TS) of O2 addition to the VBG benzylic radical, assuming quartet spin (TS 2 in Figure 6.8). The quartet spin trajectory yielded a clear TS only if the O-O bond length in the incoming O2 molecule was restricted at 1.57 Å and the H-O bond of the secondary hydroxyl group was restricted at 0.97 Å. Without doing so, TS 4 instead of TS 2 was found (Figure 6.8).

C_β-O′ Ether Cleavage

For C_β-O′ ether cleavage, two different mechanisms have been reported in literature. The first mechanism involves a homolytic cleavage of the C_β-O′ bond directly from the benzylic radical (Figure 6.8, pathway B), whereas the second mechanism involves O_2 addition followed by heterolytic cleavage of the C_β-O′ bond (Figure 6.8, pathway C).[7,28]

In pathway B, the relative enthalpy of the TS for the C_β-O′ bond cleavage was calculated to be 25.5 kcal/mol (structure 5). As the subsequent keto−enol tautomerization is expected to be very fast, and thus not rate-limiting,[29] no further TS was calculated. The overall activation energy of pathway B, thus, equals 25.5 kcal/mol. Although the calculated enthalpy gain of pathway B only equals 14.0 kcal/mol, it should be noted that the formed guaiacol radical (structure 6b) rapidly reacts further, which is expected to further decrease the relative enthalpy of its products. Based on the overall energy gain, and a surmountable activation energy, pathway B seems to be a plausible route.

Pathway C has a slightly higher overall energy gain than pathway B. However, the intermediate after splitting off the superoxide (structure 6c) lies 51.5 kcal/mol higher than its precursor (structure 3), making this pathway unlikely to occur.

Toward an Explanation for the Buffer-Dependent Competition

Based on the DFT study, a competition between pathway A and pathway B seems possible. However, based on the reactions shown in Figure 6.8, it is not directly clear how this competition would be influenced by the buffer pH and/or strength. Theoretically, as O_2 solubility decreases at high salt levels,[30] pathway A could be slowed down at increased buffer strength and pH. Nevertheless, no significant effects of buffer salts on O_2 solubility are expected in weak buffers, nor did we find any significant differences in O_2 concentrations between buffers at pH 3 and 7 using Oxygraph measurements (data not shown). In addition, if the O_2 solubility would have been the main reason underlying the observed buffer effects, it would be expected that also high concentrations of other salts would affect the product profile. As can be clearly observed from Figure 6.6, this was not the case.

Since it was found that only buffer ions, and not KNO_3, affected the product ratio, a more plausible scenario is that specific buffer ions interact with the lignin model during the course of the reaction, and thereby influence the competition between ether cleavage and C_α-oxidation. The pK_a equalization principle [31] states that hydrogen bond donors and acceptors of similar pK_a form stronger bonds than donors and acceptors with a large difference in pK_a. Based on this principle, strong hydrogen bonding can be expected between the secondary alcohol proton in structure 1 and 3 (Figure 6.8) and the citrate trianion or phosphate dianion. As the concentrations of these anions increase with increasing pH (in the used pH range) and buffer strength, it is plausible that these anions are indeed involved in the observed buffer effect.

Furthermore, we investigated whether hydrogen bonding between the VBG benzylic radical (structure 1) and citrate would be more favorable for the citrate trianion than for the dianion. Although in both cases such intermolecular hydrogen bonding would require disruption of the intramolecular hydrogen bond between the C_α-OH and C_γ–OH groups of structure 1, we found that hydrogen bonding between structure 1 and the citrate trianion is favorable by 3.9 kcal/mol (Figure 6.10, left). In contrast, bonding to the citrate dianion would require an additional 1.9 kcal/mol as compared to intramolecular hydrogen bonding (Figure 6.10, right). This finding strengthens our suggestion that only specific anions are involved in hydrogen bonding to the lignin model. Two

scenarios can be described via which such hydrogen bonding between anions and lignin could affect the observed competition (Figure 6.11).

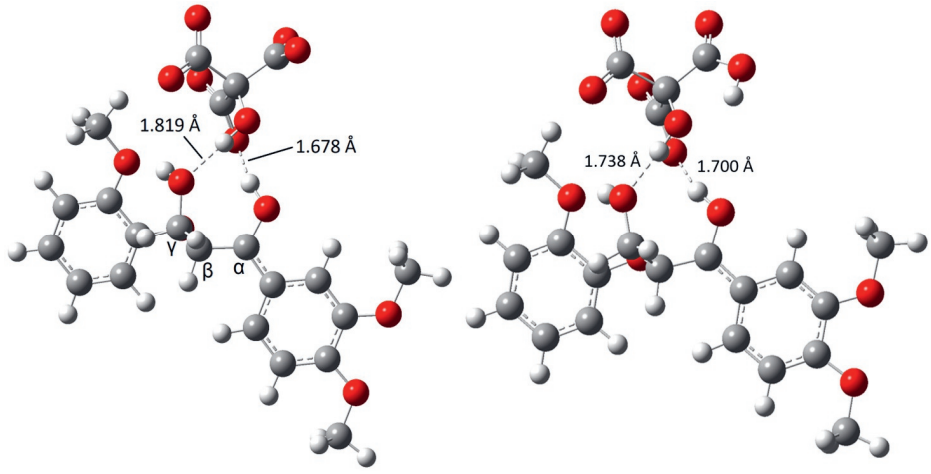

Figure 6.10. (left) Optimized geometry of the VBG benzylic radical (structure 1) and the citrate^{3-}. The molecules are linked via two H-bonds: one between the C_α-OH proton of the VBG radical and a citrate carboxylate group (bond length = 1.678 Å), and one between the C_γ–OH oxygen and the tertiary alcohol proton of citrate (bond length = 1.819 Å). It should be noted that the O atom of the aryl-ether is present but largely hidden behind the C_γ-atom. (right) Optimized geometry of the VBG benzylic radical (structure 1) and the citrate^{2-}.

First, it has been shown that the rate of O_2-addition to (benzylic) radicals can be substantially diminished by, *e.g.*, steric or electronic stabilization of the radical.[32,33] As hydrogen bonding of buffer anions to the secondary alcohol proton brings the anions in close proximity of the radical-bearing carbon atom (Figure 6.9), and this it is not inconceivable that such hydrogen bonding somehow increases the stability of the radical and thereby decreases the rate of O_2-addition. A lower O_2-addition rate would slow down pathway A but not pathway B, resulting in relatively more ether cleavage (Figure 6.11, top). As there is currently no good model to predict O_2-addition rates to radicals, it remains to be investigated whether hydrogen bonding between buffer anions and lignin radicals indeed slows down O_2-addition. αβγ

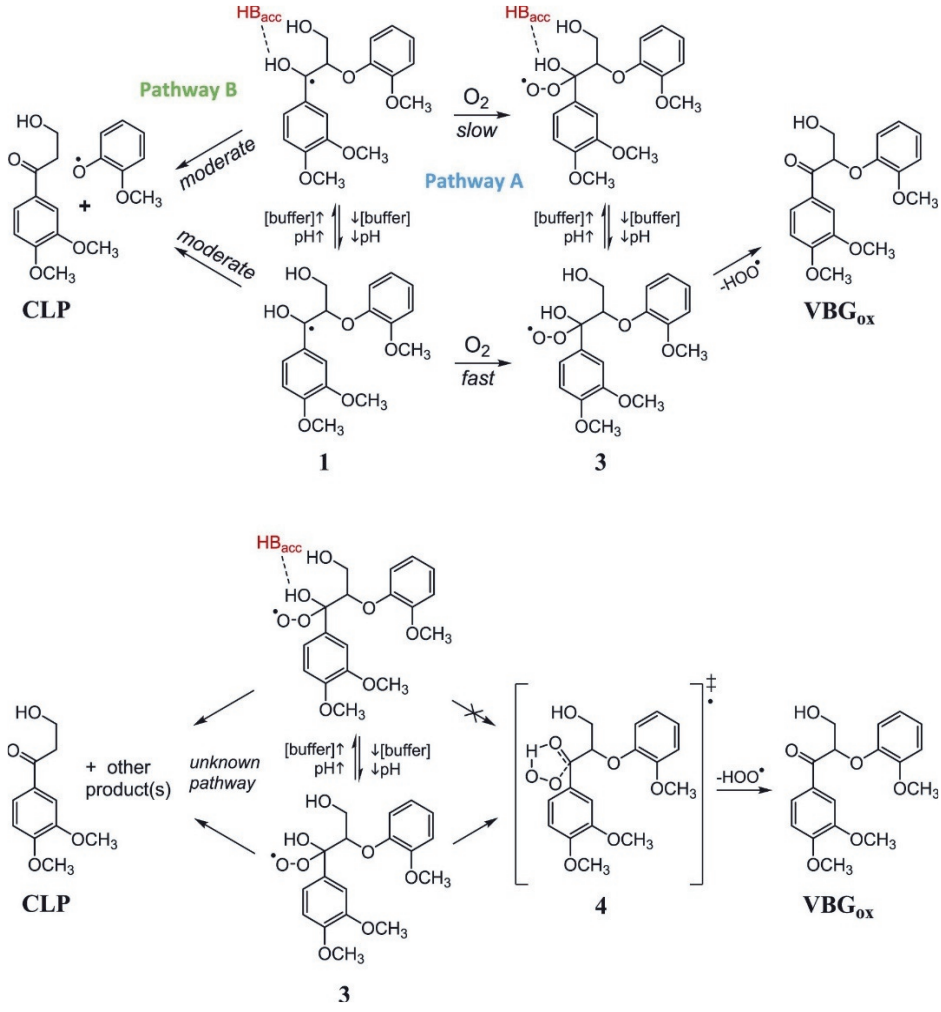

Figure 6.11. Two possible scenarios for the effect of hydrogen bonding on the competition between C_{β}-O' ether cleavage and C_{α}-oxidation.

The second possibility is that the competition between C_{β}-O' ether cleavage and C_{α}-oxidation takes place after the addition of O_2. Although our chosen pathway C was shown to be implausible, it could be speculated that there is an alternative and more favorable ether cleavage pathway, starting from the peroxyl intermediate (structure 3 in Figure 6.8). If that is the case, it is highly conceivable that hydrogen bonding between buffer anions and structure 3 would affect the competition, in favor of ether cleavage. As the second step of pathway A involves an intramolecular hydrogen transfer (TS 4 in Figure 6.8), strong

hydrogen bonding of the secondary alcohol proton to buffer anions would slow down this reaction step by impairing the formation of TS 4 (Figure 6.11, bottom). Valgimigli et al. reported previously that the rate of a comparable reaction is indeed decreased by hydrogen bond formation between substrate and solvent.[34] Whether an alternative and favorable ether cleavage pathway exists after O_2 addition remains to be investigated.

6.3 Conclusions

In conclusion, we have shown that the competition between ether cleavage and C_α-oxidation of a nonphenolic *β*-O-4′ linked lignin model in LMS incubations is highly dependent on the reaction conditions. Both the relative and absolute extent of ether cleavage can be dramatically enhanced by increasing buffer pH and buffer strength. Furthermore, based on both experimental and computational efforts, we have provided new insights into the reaction mechanisms underlying C_α-oxidation and ether cleavage, and proposed that increased hydrogen bonding between buffer anions and the C_α-OH group of the lignin model structure drives the outcome of LMS treatment toward ether bond cleavage. We expect that these insights will be useful in further studies and optimizations of oxidative lignin degradation in industrial settings. Our results showed that laccase-induced degradation of HBT was substantially lower at increased buffer strength and pH. Nonetheless, as still a significant portion of HBT was degraded, future research should focus on finding more stable mediating compounds that can be used at lower concentrations.

6.4 Supporting Information

Further supporting information, materials and methods are available online at: https://doi.org/10.1021/acscatal.0c02154.

Computational Analysis

All quantum chemical calculations were performed with the B97D functional and 6-311+G(d,p) basis set, as implemented in Gaussian 16 (version B1).[35] (natural population) charges and Wiberg bond orders were calculated using the NBO 3.1 program as implemented in Gaussian 16. Generic solvent effects were incorporated by using the universal solvation model based on density (SMD), with water as the model solvent.[36] Enthalpic energies are reported in a standard state: at 298 K and 1 bar pressure.

References

(1) Munk, L.; Sitarz, A. K.; Kalyani, D. C.; Mikkelsen, J. D.; Meyer, A. S. *Biotechnol. Adv.* **2015**, *33* (1), 13–24.

(2) Lundquist, K.; Parkås, J. *Bioresources* **2011**, *6* (2), 920–926.

(3) Rodríguez Couto, S.; Toca Herrera, J. L. *Biotechnol. Adv.* **2006**, *24* (5), 500–513.

(4) D'Acunzo, F.; Baiocco, P.; Fabbrini, M.; Galli, C.; Gentili, P. *European J. Org. Chem.* **2002**, *24,* 4195–4201.

(5) Baiocco, P.; Barreca, A. M.; Fabbrini, M.; Galli, C.; Gentili, P. *Org. Biomol. Chem.* **2003**, *1* (1), 191–197.

(6) D'Acunzo, F.; Baiocco, P.; Galli, C. New Journal of Chemistry **2003**, 27 (2), 329–332.

(7) Kawai, S.; Nakagawa, M.; Ohashi, H. *Enzyme Microb. Technol.* **2002**, *30,* 482–489.

(8) Kawai, S.; Umezawa, T.; Higuchi, T. *Arch. Biochem. Biophys.* **1988**, *262* (1), 99–110.

(9) Kawai, S.; Nakagawa, M.; Ohashi, H. *FEBS Letters* **1999**, *446* (2–3), 355–358.

(10) Kawai, S.; Umezawa, T.; Shimada, M.; Higuchi, T. *FEBS Letters* **1988**, *236* (2), 309–311.

(11) Kawai, S.; Asukai, M.; Ohya, N.; Okita, K.; Ito, T.; Ohashi, H. *FEMS Microbiology Letters* **1999**, *170* (1), 51–57.

(12) Srebotnik, E.; Hammel, K. E. J. *Biotechnol.* **2000**, *81* (2–3), 179–188.

(13) Although ether cleavage may eventually also result in the formation of ketone groups at the C_α-position, in this paper the term C_α-oxidation is used to describe the conversion of C_α-OH to a C_α=O without concomitant ether cleavage.

(14) Heap, L.; Green, A.; Brown, D.; Van Dongen, B.; Turner, N. *Catal. Sci. Technol.* **2014**, *4* (8), 2251–2259.

(15) Hilgers, R.; Twentyman-Jones, M.; van Dam, A.; Gruppen, H.; Zuilhof, H.; Kabel, M. A.; Vincken, J.-P. *Catal. Sci. Technol.* **2019**, *9* (6), 1535–1542.

(16) Fabbrini, M.; Galli, C.; Gentili, P. *J. Mol. Catal. B. Enzym.* **2002**, *16* (5–6), 231–240.

(17) Moldes, D.; Díaz, M.; Tzanov, T.; Vidal, T. *Bioresour. Technol.* **2008**, *99* (17), 7959–7965.

(18) Ibarra, D.; Romero, J.; Martínez, M. J.; Martínez, A. T.; Camarero, S. *Enzyme Microb. Technol.* **2006**, *39* (6), 1319–1327.

(19) Barreca, A. M.; Fabbrini, M.; Galli, C.; Gentili, P.; Ljunggren, S. *J. Mol. Catal. B. Enzym.* **2003**, *26* (1–2), 105–110.

(20) Li, K.; Xu, F.; Eriksson, K.-E. L. *Appl. Environ. Microb.* **1999**; *65* (6), 2654–2660.

(21) Shleev, S.; Persson, P.; Shumakovich, G.; Mazhugo, Y.; Yaropolov, A.; Ruzgas, T.; Gorton, L. *Enzyme Microb. Technol*. **2006**, *39* (4), 841–847.

(22) Camarero, S.; Ibarra, D.; Martínez, Á. T.; Romero, J.; Gutiérrez, A.; del Río, J. C. *Enzyme Microb. Technol.* **2007**, *40* (5), 1264–1271.

(23) Gutiérrez, A.; Rencoret, J.; Cadena, E. M.; Rico, A.; Barth, D.; del Río, J. C.; Martínez, Á. T. *Bioresour. Technol.* **2012**, *119*, 114–122.

(24) Rencoret, J.; Pereira, A.; del Río, J. C.; Martínez, A. T.; Gutiérrez, A. *Bioenergy Res.* **2016**, *9* (3), 917–930.

(25) Kawai, S.; Iwatsuki, M.; Nakagawa, M.; Inagaki, M.; Hamabe, A.; Ohashi, H. *Enzyme Microb. Technol.* **2004**, *35* (2–3), 154–160.

(26) D'Acunzo, F.; Baiocco, P.; Fabbrini, M.; Galli, C.; Gentili, P. *New Journal of Chemistry* **2002**, *26* (12), 1791–1794.

(27) Mel; er, L. C. S.; Saunders, W. H. Reaction Rates of Isotopic Molecules *R.E. Krieger Pub. Co.,* **1987**.

(28) Ten Have, R.; Teunissen, P. J. M. *Chem. Rev*.**2001**,*101*,3397−3413.

(29) Clayden, J.; Greeves, N.; Warren, S.; Wothers, P. Organic Chemistry, 2nd ed. *Oxford University Press,* **2012**.

(30) Geng, M.; Duan, Z. *Geochim. Cosmochim. Acta* **2010**, *74* (19), 5631–5640.

(31) Gilli, P.; Pretto, L.; Bertolasi, V.; Gilli, G. *Acc. Chem. Res.* **2009**, *42* (1), 33–44.
(32) Bejan, E. V.; Font-Sanchis, E.; Scaiano, J. C. *Org. Lett.* **2001**, *3* (25), 4059–4062.
(33) Wright, J. S.; Shadnia, H.; Chepelev, L. L. *J. Comput. Chem.* **2009**, *30* (7), 1016–1026
(34) Valgimigli, L.; Amorati, R.; Fumo, M. G.; DiLabio, G. A.; Pedulli, G. F.; Ingold, K. U.; Pratt, D. A. *J. Org. Chem.* **2008**, *73* (5), 1830–1841.
(35) Frisch, M. J.; Trucks, G. W.; Schlegel, H. B.; Scuseria, G. E. ; Robb, M. A.; Cheeseman, J. R.; Scalmani, G.; Barone, V. ; P.; G. A.; Nakatsuji, H.; Li, X.; Caricato, M.; Marenich, A. V.; Bloino, J. ; Janesko, B. G.; Gomperts, R.; Mennucci, B.; Hratchian, H. P.; Ortiz, J.; V.; Izmaylov, A. F.; Sonnenberg, J. L.; Williams-Young, D.; Ding, F. ; Lipparini, F.; Egidi, F.; Goings, J.; Peng, B.; Petrone, A. ; H.; T.; Ranasinghe, D.; Zakrzewski, V. G.; Gao, J.; Rega, N.; Zheng, G. ; Liang, W.; Hada, M.; Ehara, M.; Toyota, K.; Fukuda, R.; Hasegawa, J. ; Ishida, M.; Nakajima, T.; Honda, Y.; Kitao, O.; Nakai, H.; Vreven, T. ; Throssell, K.; Montgomery, J. A., Jr.; Peralta, J. E.; Ogliaro, F. ; Bearpark, M. J.; Heyd, J. J.; Brothers, E. N.; Kudin, K. N. ; S.; V. N.; Keith, T. A.; Kobayashi, R.; Normand, J.; Raghavachari, K. ; Rendell, A. P.; Burant, J. C.; Iyengar, S. S.; Tomasi, J.; Cossi, M. ; Millam, J. M.; Klene, M.; Adamo, C.; Cammi, R.; Ochterski, J. W. ;; Martin, R. L.; Morokuma, K.; Farkas, O.; Foresman, J. B.; Fox, D. J. Gaussian 16, Revision B.01: Gaussian, Inc.: Wallingford CT, **2016**.
(36) Marenich, A. V.; Cramer, C. J.; Truhlar, D. G. *Journal of Physical Chemistry B* **2009**, *113* (18), 6378–6396.

Chapter 7
General Discussion

7.1 A general discussion…

The coatings industry and bulk polymer industry rely heavily on polluting methods and toxic chemicals. The main motivation to perform the research described in this thesis, is to deepen molecular insights in these current practices in an effort to help reduce the environmental impact[1] of these industries. The research described in chapters 2 and 3 on self-healing antifouling polymer brushes was performed to find alternatives for heavily fluorinated antifouling coatings, as they are toxic and persistent chemicals.[2] Dynamic covalent networks, for example those hinging on the versatile reactivity of the imine bond described in chapter 4, form potential recyclable alternatives[3] to thermoset polymers that currently have no sustainable end-of-life-plan. Novel chemical reactions, such as the SuFEx reaction modelled in chapter 5, can potentially replace[4] industrially complicated processes. Polymers coming from a natural source, like lignin, have limited environmental impact upon production. They are thus perfect candidate resources for basic chemicals, if their depolymerization can be controlled and optimized, as has been reported in chapter 6. The chapters describe in detail the content of the research and its contribution to the reduction of environmental impact. Nonetheless, a few principal remarks can be made and suggestions for future research can be given.

7.2 … on the applicability of polymer brushes,

In chapters 2 and 3 of this thesis, polymer brushes were reported that could be grafted from a surface using Surface Initiated Atom Transfer Radical Polymerization (SI-ATRP). In this polymerization technique (Figure 7.1), typically a copper(I) catalyst abstracts a halogen from the end of a polymer chain or initiator group, generating a radical on the polymer chain end and thereby activating it. A monomer with a suitable double bond will react with that radical, opening its double bond to propagate the polymer chain. Return of the halogen from the catalyst caps the polymer and temporarily deactivates it, until the next time a copper catalyst abstracts the halogen and polymerization (with the same or another type of monomer) can continue. As this polymerization technique gives precise control over the grow speed and composition of the polymer, it is one of the more popular techniques in academic research.[5–7]

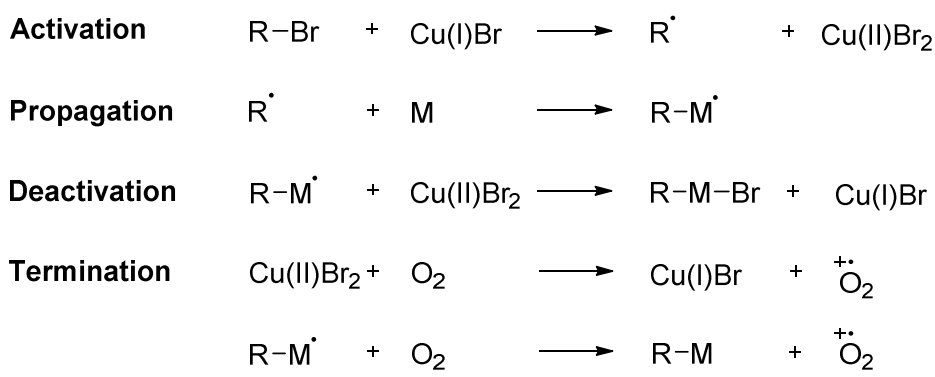

Figure 7.1: Activation, polymerization, deactivation and termination mechanism of Atom Transfer Radical Polymerization (ATRP) in which R is the polymer chain and M a monomer.

However, standard ATRP requires an oxygen-free environment.[8] Oxygen could oxidize the catalyst, rendering it inactive. Less frequently, oxygen can take up a radical from a growing polymer chain, thereby ending the polymerization and poisoning the catalyst, which cannot return the halogen and thus cannot activate another polymer chain (Figure 7.1). Either way, the oxygen halts polymerization. Absence of oxygen is thus essential, hence most ATRP are performed in Schlenk glassware or in glovebox. While this is acceptable in research, scalability and thereby industrial applicability is limited.

Various approaches have been taken by the group of Matyjaszewski to allow oxygen in an ATRP reaction. With ARGET-ATRP, trace amounts of oxygen are tolerated, as reducing agents regenerate the catalyst when it is oxidized.[9] Alternatively, enzymes such as glucose oxidase and horseradish peroxidase can deoxygenate reaction mixtures in open reaction vessels with the use of a mediator, preventing oxidation of the catalyst or polymer.[10,11] Most recently, they discovered that the mediator sodium pyruvate triggers polymerization under UV irradiation in the presence of oxygen, without the need for enzymes or other reducing agents.[12] This is the first oxygen-tolerant small molecule-based photoinduced ATRP.

For industrial relevance, not only oxygen tolerance is convenient, but also the absence of expensive or toxic metals as copper. A wide range of transition metals has been tested for ATRP and indeed some suitable alternatives have

been found, such as iron.[13] Metal-free light-triggered SI-ATRP has also been reported,[14] as well as microliter-scale ATRP,[15] which reduces the amount of required catalyst simply by reducing the reaction scale. Unfortunately, the combination of a cheap and benign ATRP catalyst with high oxygen-tolerance has not been found. As a result, few industrial applications of SI-ATRP exist.

Some initial attempts at industrializing SI-ATRP have been made. For 2-(dimethylamino)ethyl methacrylate (DMAEMA), AGRET-ATRP allowed "paint on" polymer brushes, using low monomer concentrations in a water-based reaction mixture to create hydrophilic, oleophobic coatings that only cost $17 per m^2.[16] However, these results have not been reproduced with any hydrophobic monomers. Furthermore, thermoresponsive poly(*N*-isopropylacrylamide) polymer brushes have been applied by SI-ATRP on glassware, which was then used to grow cell cultures.[17] By changing the temperature, the affinity of the polymer to the cells was reduced, cleaving the cells from the glassware without the common invasive treatments. This is very effective for a small group of cell lines, however specific (expensive) adaptations must be made to accommodate other cell lines, hampering widespread use of the technique.[18] Therefore, although these examples are promising, further research is required for large-scale industrialization of SI-ATRP.

For reversible addition fragmentation chain-transfer polymerization (RAFT), the combination of a cheap catalyst with high oxygen-tolerance is the norm. While RAFT has the same control over the radical polymerization by capping the polymer chain with a RAFT agent, this group contains no metal but typically only sulfur, carbon, oxygen and hydrogen.[19] It is thus less expensive to produce. Additionally, RAFT is much more oxygen-tolerant and can be applied in water.[20] When using a photo-initiator as in SI-PET-RAFT,[21] the polymerization can be minutely controlled, resulting in even better defined polymer brushes suitable for industrial applications.[22] If the RAFT moiety is not removed, depolymerization is possible as well,[23] a highly desirable property from a sustainability point of view. However, as an external radical initiator is needed to start the polymerization, RAFT has a higher chance of uncontrolled free radical polymerization as side reaction.[24] Furthermore, the practical challenges of growing polymer brushes from large scale or non-flat surfaces remain. Thus, the industrial applicability of SI-RAFT is no further developed than SI-ATRP.

A more scalable method of polymer brush application is grafting-to polymerization. In this procedure, the polymer brush is produced in solution, after which it is attached onto the surface. Scalability issues and oxygen-sensitivity are hereby circumvented, as the polymer can be grown on a different location than where it needed to be applied. However, steric hindrance and poor solubility generally result in thin coatings (5 to 8 nm)[25] with low grafting densities.[26–29]

The polymer brushes described in chapters 2 and 3 of this thesis are potentially relevant for industry. For example in inkjet printing, perfluorinated silanes are currently used as antiwetting and antifouling coating.[30–32] We have shown in chapter 2 that the antifouling performance of our non-fluorinated polymer brushes is not less than the fully fluorinated ones, hence they would form a suitable fluorine-free alternative. In chapter 3 we have further explored the capabilities of these fluorine-free polymer brushes and confirmed their antiwetting property. They even have the added feature of self-healing upon heating. With industrially applicable polymerization processes such as SI-PET-RAFT[21] or µL-ATRP,[15] these coatings could form a more environmentally friendly alternative to the perfluorinated silanes that are soon to be banned.[33] By grafting the polymer brushes onto the surface, the process could be made industrially feasible.

7.3 … on the reduction of fluorine,

The need for fluorine reduction is clear. Where PTFE-coated non-stick pans were proudly advertised in the 1960s (Figure 7.2), we have learned since then the negative effects of producing products with such “forever chemicals”, as Perfluorinated Alkyl Substances (PFAS) have been branded. They are toxic, carcinogenic and disrupting the reproductive system.[2,34,35] Health and safety guidelines have been sharpened, yet alarming levels of PFAS have been found in, for example, Western Scheldt fish,[36] mother milk[37] and brains.[38]

As the current safety guidelines of PFAS use are clearly providing insufficient protection to the environment of industrial plants where PFAS is used, the European Union is contemplating a full ban on all PFAS substances.[33] According to the current definition of this EU legislation, almost any compound containing a $–CF_3$ or a $–CF_2$ group is a PFAS substance and may not be used in any lab in the

Figure 7.2: Advertisements from Dupont in 1960 (left) and 1965 (right) for non-stick cookware with Teflon (PTFE) coating.

EU. This undoubtedly will lead to production problems of many small drugs containing a trifluoride,[39] as precursors may not be produced or imported. Additionally, as the ban also involves (precursors of) common solvents, all chemical labs will need to adapt, including the academic labs. A cry from European academic chemists to stop this generic PFAS ban is thus the result.[40]

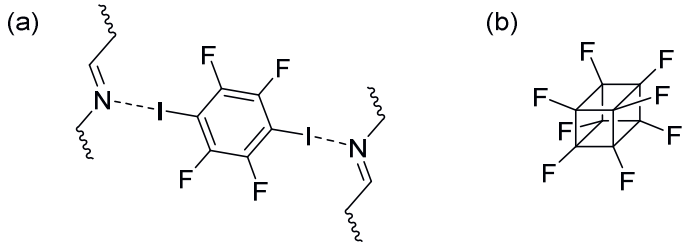

Figure 7.3: (a) Halogenated benzene rings as supramolecular bridges between imine-based macromolecules, and (b) perfluorocubane, voted favorite molecule of the year 2022 by readers of C&EN.

Although significant research is done to reduce negative effects of PFAS,[41] outcries like this can make one wonder how sincere the chemical academic world is in its claims to work towards a more sustainable future.[42] Recently, a heavily fluorinated linker (Figure 7.3a) was presented as 'excellent method to post-modify imine-based materials'.[43] Although the presented chemistry is certainly novel, the applicability and desirability is questionable in light of the toxicity and environmental impact of fluorinated compounds. A popular vote from Chemical & Engineering News showed perfluorocubane (Figure 7.3b) as

the favorite molecule of 2022,[44] demonstrating once more that environmental impact was not taken into consideration when the chemical engineers voted for this structurally intriguing compound. A distance from chemical academia to society can be observed, which is highly undesirable in light of the current environmental crises that are unfolding. Scientists should lead by example, making educated choices in their research that place the needs of the world above scientific curiosity.

7.3.1 SuFEx and SuPhenEx

The rapid development of SuFEx click chemistry is another example where a fluorinated compound is lauded by academia, yet its environmental impact is overlooked. In the last decade, SuFEx has gained tremendous attention[45] and has frequently been claimed to be one of the most promising reaction of the future, perhaps even better than the copper click reaction due to its oxygen-tolerance. However, production of the sulfur hubs for the starting materials is often dangerous, with highly reactive and polluting reagents (*e.g.*, sulfuryl fluoride[46,47] (SO_2F_2), thiazyl trifluoride[48] (NSF_3), and ethenesulfonyl fluoride[49] (CH_2=CH-SO_2F)). The sulfur hubs are generally harmful as well and have been used for decades as insecticides and as protein inhibitors in biochemistry.[50] One can thus wonder whether the SuFEx system as a whole is actually sustainable, and if it would in fact be a an improvement upon the CuAAC reaction.

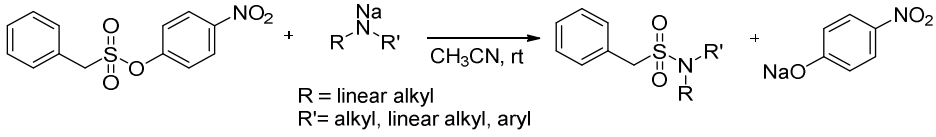

Figure 7.4: Schematic representation of the SuPhenEx reaction as presented by Van den Boom *et al.*[51]

Fortunately, an alternative has been found. In Sulfur Phenolate Exchange (SuPhenEx),[51] a fluoride-free counterpart of the SuFEx reaction, the leaving group, F^-, of SuFEx has been replaced by a phenol (Figure 7.4). Herein, the dangerous sulfur-fluorinated precursors of SuFEx are circumvented, and no fluorinated side products are formed. The reaction proceeds in a similar fashion as SuFEx, with the added feature of reversibility.[52] As such, it is a feasible alternative to SuFEx, worthy of more investigation. The research performed in chapter 5 of this thesis can be translated to SuPhenEx, as the reaction

mechanism is similar. Both reactions were found be addition-elimination reactions involving a cation (Na^+,[52] Ca^{2+} [53,54] or NH_4^+ [55]), with activation energies depending on the entering phenolate. SuPhenEx is thus certainly a candidate for chain-growth polymerization similar to the SuFEx system described by Sharpless and Wu.[56]

7.3.2 Reducing PFAS

More research is performed on the reduction of environmental PFAS amounts.[57] Various waste removal treatments have been developed such as removal by coagulation,[58,59] adsorption on carbon nanomaterials,[60] and adsorption on air by foam fractionation.[61] Preliminary work of our own group shows selective capture of perfluorooctyl carboxylic acid over non-fluorinated carboxylic acid by pillar-[5]-arenes.[62]

Degradation of the removed PFAS has been attempted in various ways.[57] Bacterial degradation is effective, but slow.[63,64] Singly-fluorinated benzene can be defluorinated by a ruthenium catalyst under mild conditions.[65] Dichtel and co-workers recently mineralized perfluoro carboxylic acids with sodium hydroxide into to fluoride, sodium trifluoroacetate, and nonfluorinated carbon-containing products.[66] Although these methods (and many others) are successful, either their scope is too small or their applicability too limited (either in time or in acceptable chemical environments) to be of significant industrial relevance.

The most sustainable way to prevent PFAS pollution is by simply not using it. Instead of a pan with a PFAS coating, one could use a ceramic or cast-iron pan. Fluorine-containing flame retardants and cooling agents are replaced by halogen-free alternatives.[67] In cases where hydrophobicity is required, physical instead of chemical water repulsion is investigated, creating hydrophobicity through an increase in surface roughness instead of the fluorophobic effect.[68] Chapters 2 and 3 of this thesis show that fluorine-free polymer brushes with side chains of seven or more carbons in the side chain are hydrophobic, and have the same self-healing ability as those used by Wang *et al.*[69] Use of our fluorine-free polymer brushes would thus be an ecofriendly improvement without loss of functionality.

7.4 … and on the use of DFT in chemical research.

Another way to make chemical research itself more sustainable is by replacing some of the experimental work by calculations. This costs electricity and computer components, but requires no solvents or catalysts. In toxicology, computational predictions are already common practice as replacement for animal testing,[70] and also in small chemical production, calculations like DFT are frequently used to support experimental searches. For example, prediction of which cycloadditions with fluorinated compounds lead to which products allows us to only follow those procedures that lead to the desired pharmaceutical.[71] This greatly reduces the use of fluorinated starting materials.

In polymer chemistry, the use of DFT is still limited. A major drawback of DFT is the long calculation time, as a DFT calculation scales at least quadratically with the number of atoms involved. Drastic measures, such as electron localization,[72] can reduce it to linear scaling, yet for polymers this still rapidly surmounts practicality. Other calculation methods that do not consider single atoms but instead consider larger scale physical interactions between subunits, for example molecular dynamics (MD)[73] or dissipative particle dynamics (DPD),[74] are thus more appropriate for studying a polymer as a whole. However, the small-scale interactions between individual atoms are hereby ignored.

DFT calculations could play a much larger role in materials science, for example in imine chemistry. Imine chemistry is old and well-established, with many experimental[75,76] and computational studies[77–79] confirming its robustness. Yet when imines are applied in larger structures, forming porous networks, cages or polymers, computational support is missing. The oldest report of an imine coordinated to a metal is 63 years old,[80] yet chapter 4 of this thesis is the first theoretical paper published on the effect of this metal coordination on the reactivity of the imine. In contrast, the more novel field of materials for energy storage already incorporates DFT.[81] In the early stages of the design process, possible materials are calculated with DFT to predict their energy storing ability, after which the most promising materials are selected and produced. Specifically with carbon-nitride based materials, this strategy has proven fruitful.[82]

7.4.1 Reporting of DFT results

For efficient use of DFT in other fields, proper reporting of the DFT results is crucial. Most chemists know how to translate an activation energy in kcal/mol or kJ/mol to experimental settings, but an activation energy reported in Hartree will raise eyebrows. It is thus up to the computational chemist to translate the raw DFT results into widely accepted units. Similarly, an energy profile reported with the zero-point energies of a reaction might be most trustworthy and thus preferred by a computational chemist, yet translating it into experimental conditions is less than straight-forward. Incorporation of enthalpy corrections or free energy corrections is thus preferred, even though these corrections significantly increase the error margins of the calculations.

Especially when solvent interactions are expected, as with hydrogen bonding in protic solvents, but only implicit solvent interactions are modelled, the Gibbs free energy can stray multiple hydrogen bonds (each with an expected 3.3–4.9 kcal/mol energy loss).[83] The inclusion of explicit solvent molecules could reduce this error, but is computationally not always feasible. Figure 7.5 clearly displays the inconsistency between the electronic energy, enthalpy and Gibbs free energy of a SuFEx propagation reaction from chapter 5. Where the DFT calculation minimized the electronic energy to find the intermediate, addition of the zero-point, enthalpy and free energy corrections place its energy above that of TS1, making it a false intermediate. Additionally, as the Gibbs free energy corrections falsely exclude three hydrogen bonds in the implicit solvent interactions, the total energy gain of the reaction is 11 kcal/mol lower than in the other energy models.

Presentation of such DFT results should thus always come with a proper explanation, warning the experimental chemist of the flaws of the chosen model. Furthermore, the appropriate energy must be communicated. For example, for the lignin degradation in water of chapter 6, we decided to avoid misrepresentation of the many hydrogen bonds between solvent and lignin, and provided enthalpy values instead.

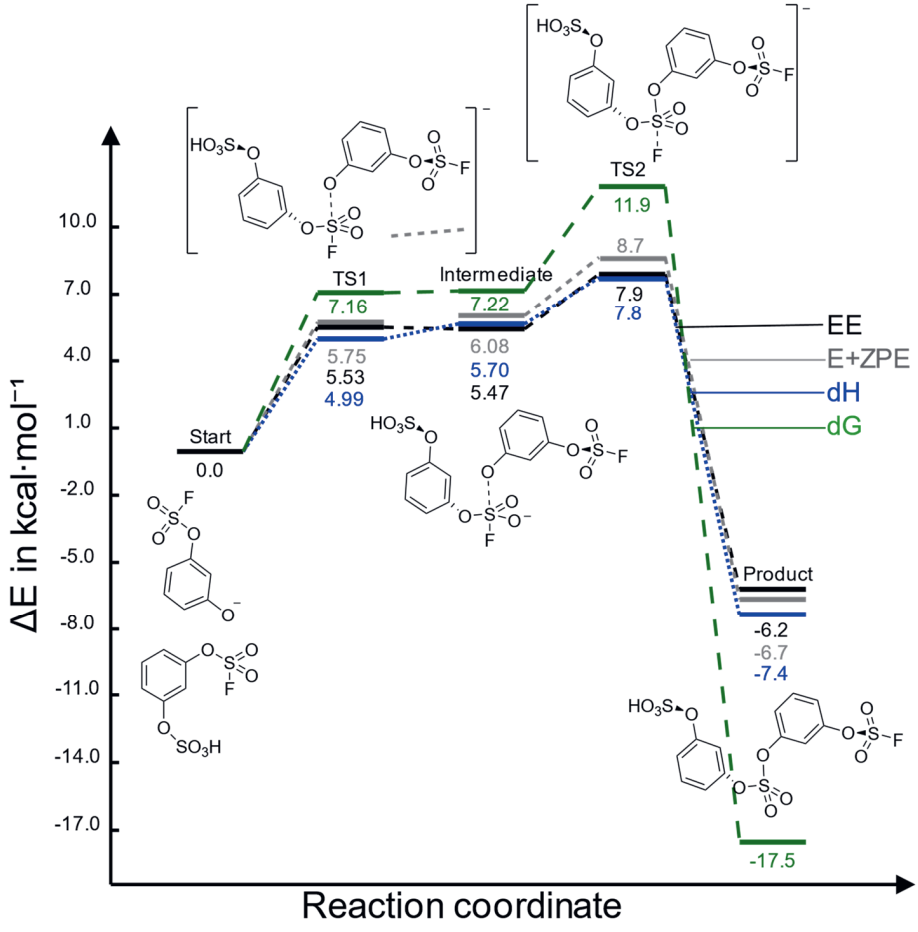

Figure 7.5: Electronic energy (black), zero-point energy (grey), enthalpy (blue) and Gibbs free energy (green) profile of a SuFEx reaction, calculated as in chapter 5 of this thesis. Implicit solvent interactions in butanonitrile are included. See chapter 5 for all computational details. For discussion purposes, an extra decimal is included for TS1 and Intermediate.

7.4.2 DFT parameters

In conversations between theoretical chemists, a reappearing question is 'what functional and basis set did you use?'. Similar to solvents for a synthetic chemist, the choice of functional and basis set has a large impact on the result of the endeavor. They must be able to accommodate all atoms under investigation, and take the relevant electronic interactions into account. They should preferably do so within an acceptable time frame. As with solvent choice, there

is not a single correct option. There are many obvious wrong options, plenty acceptable options, and a few preferred options, of which most are out of reach as they would be too time-expensive or are not included in the available software packages. Next to suitability, the compatibility with literature is relevant as well. It would be preferred if the results of the calculations could be compared to existing literature. Therefore, one prefers to use benchmark parameters. However, as computers are becoming faster and computational costs are rapidly decreasing, more elaborate basis sets become accessible and replace the old basis sets, while more intricate functionals allow for better simulation of the available orbitals. The benchmark is thus constantly changed, further complicating the choice of parameters. Especially when a project spans a few years, the relevancy of the chosen functional and basis set must be evaluated.

The project described in chapter 4 was initially calculated with B97D[84] and 6-311+G(d,p). As they included empirical dispersion corrections and diffuse functions, they accommodated the transition metal interactions of interest. However, as the range-separated hybrid functional ωB97XD[85] is superior in simulating the long-range behavior to the semi-local GGA B97D, we updated our functional to ωB97XD. Simultaneously, the basis set was improved to 6-311G(2d,2p), as we saw that we could better accommodate the ionic interactions with an extra set of polarization functions than with the inclusion of diffuse functions. Increased computer power allowed these changes.

A recent comparison of 91 functionals[86] indicated that ωB97M-V[87] or ωB97M(2)[88] would provide marginally more accurate values for barrier heights and reaction energies than ωB97XD. By applying machine learning and large data sets, these 12- and 14-parameter functionals were optimized to be at the top of their field. Unfortunately, ωB97M-V and ωB97M(2) are not included in Gaussian 16 yet, and were therefore not available to us. Furthermore, for proton transfer, as investigated in chapter 4, and halogen atom transfer, as reported in chapter 5, their performance is similar to ωB97XD.[86] Recalculation with ωB97M-V or ωB97M(2) is therefore not required at the moment.

7.5 The end?

Although this thesis is completed, the research described within is not. IR measurements of the coatings described in chapter 3 could support the hypothesis of acid resistance by tight packing of the side chains. Explicit solvent molecules might be added to the calculations of chapter 5 to support the hypothesis of solvent interactions hindering self-polymerization in selected monomers. The optimized pH and buffer concentrations from chapter 6 were applied in further research for efficient grass delignification.[89]

On a larger scale, the applicability of the investigated polymer brushes should be investigated. By changing the polymerization method to SI-PET-RAFT, industrial applicability can be greatly increased. Evolving the method into a grafting-to approach would ease industrialization even more.

Furthermore, to increase sustainability and productivity of the materials industry, the incorporation of DFT in materials chemistry should be enhanced. This can be promoted by the organization of multidisciplinary conferences, like CHAINS, where various topics are presented at a level that is understandable to chemists from other topics. Additionally, a DFT course could be added to the curriculum of the studies Applied Chemistry and Materials Science, to provide future material chemists with a basic knowledge of DFT, which will ease collaborations. Theoretical chemists, on their part, should acquaint themselves with common terminology of materials chemistry.

We have full confidence that the various topics brushed upon in this thesis will continue to develop, growing from hypothesis via proof of principle to industrial application, using this thesis as one of the monomers in their intellectual chains.

References

(1) Rockström, J.; Steffen, W.; Noone, K.; Persson, Å.; Chapin, F. S.; Lambin, E. F.; Lenton, T. M.; Scheffer, M.; Folke, C.; Schellnhuber, H. J.; Nykvist, B.; de Wit, C. A.; Hughes, T.; van der Leeuw, S.; Rodhe, H.; Sörlin, S.; Snyder, P. K.; Costanza, R.; Svedin, U.; Falkenmark, M.; Karlberg, L.; Corell, R. W.; Fabry, V. J.; Hansen, J.; Walker, B.; Liverman, D.; Richardson, K.; Crutzen, P.; Foley, J. A. *Nature* **2009**, *461* (7263), 472–475.

(2) Cousins, I. T.; Johansson, J. H.; Salter, M. E.; Sha, B.; Scheringer, M. *Environ. Sci. Technol.* **2022**, *56* (16), 11172–11179.

(3) Zheng, J.; Png, Z. M.; Ng, S. H.; Tham, G. X.; Ye, E.; Goh, S. S.; Loh, X. J.; Li, Z. *Mater. Today* **2021**, *51*, 586–625.

(4) Dong, J.; Krasnova, L.; Finn, M. G.; Barry Sharpless, K. *Angew. Chem. Int. Ed.* **2014**, *53* (36), 9430–9448.
(5) Matyjaszewski, K. *Macromolecules* **2012**, *45* (10), 4015–4039.
(6) Matyjaszewski, K.; Miller, P. J.; Shukla, N.; Immaraporn, B.; Gelman, A.; Luokala, B. B.; Siclovan, T. M.; Kickelbick, G.; Vallant, T.; Hoffmann, H.; Pakula, T. *Macromolecules* **1999**, *32* (26), 8716–8724.
(7) Ran, J.; Wu, L.; Zhang, Z.; Xu, T. *Progr. Pol. Sci.* **2014**, 124–144.
(8) Szczepaniak, G.; Fu, L.; Jafari, H.; Kapil, K.; Matyjaszewski, K. *Chem. Res.* **2021**, *54* (7), 1779–1790.
(9) Matyjaszewski, K.; Hongchen, D.; Jakubowski, W.; Pietrasik, J.; Kusumo, A. *Langmuir* **2007**, *23* (8), 4528–4531.
(10) Enciso, A. E.; Fu, L.; Russell, A. J.; Matyjaszewski, K. *Angew. Chem. Int. Ed.* **2018**, *57* (4), 933–936.
(11) Enciso, A. E.; Fu, L.; Lathwal, S.; Olszewski, M.; Wang, Z.; Das, S. R.; Russell, A. J.; Matyjaszewski, K. *Angew. Chem. Int. Ed.* **2018**, *57* (49), 16157–16161.
(12) Szczepaniak, G.; Łagodzińska, M.; Dadashi-Silab, S.; Gorczyński, A.; Matyjaszewski, K. *Chem. Sci.* **2020**, *11* (33), 8809–8816.
(13) di Lena, F.; Matyjaszewski, K. *Prog. Polym. Sci.* **2010**, *35* (8), 959–1021.
(14) Yan, J.; Pan, X.; Schmitt, M.; Wang, Z.; Bockstaller, M. R.; Matyjaszewski, K. *ACS Macro. Lett.* **2016**, *5* (6), 661–665.
(15) Ślusarczyk, K.; Flejszar, M.; Chmielarz, P. *Polymer* **2021**, *233*, 124212.
(16) Dunderdale, G. J.; Urata, C.; Miranda, D. F.; Hozumi, A. *ACS Appl. Mater. Interfaces* **2014**, *6* (15), 11864–11868.
(17) Nagase, K.; Watanabe, M.; Kikuchi, A.; Yamato, M.; Okano, T. *Macromol. Biosci.* **2011**, *11* (3), 400–409.
(18) Nash, M. E.; Healy, D.; Carroll, W. M.; Elvira, C.; Rochev, Y. A. *J. Materi. Chem.* **2012**, *7*, 19376–19389.
(19) Keddie, D. J.; Moad, G.; Rizzardo, E.; Thang, S. H. *Macromolecules* **2012**, *45* (13), 5321–5342.
(20) Cho, W. K.; Son, K. S.; Kim, C. S.; Cho, S.; Lee, J. H. *Langmuir* **2020**, *36* (39), 11538–11545.
(21) Li, M.; Fromel, M.; Ranaweera, D.; Rocha, S.; Boyer, C.; Pester, C. W. *ACS Macro. Lett.* **2019**, *8* (4), 374–380.
(22) Poisson, J.; Polgar, A. M.; Fromel, M.; Pester, C. W.; Hudson, Z. M. *Angew. Chem. Int. Ed.* **2021**, *60* (36), 19988–19996.
(23) Wang, H. S.; Truong, N. P.; Pei, Z.; Coote, M. L.; Anastasaki, A. *J. Am. Chem. Soc.* **2022**, *144* (10), 4678–4684.
(24) Veloso, A.; García, W.; Agirre, A.; Ballard, N.; Ruipérez, F.; De La Cal, J. C.; Asua, J. M. *Polym. Chem.* **2015**, *6* (30), 5437–5450.
(25) Brittain, W. J.; Minko, S. *J. Polym. Sci. A. Polym. Chem.* **2007**, *45* (16), 3505–3512.
(26) Bergbreiter, D. E.; Tao, G.; Franchina, J. G.; Sussman, L. *Macromolecules* **2001**, *34* (9), 3018–3023.
(27) Ginzburg, M.; Galloro, J.; Jakle, F.; Power-Billard, K. N.; Yang, S.; Sokolov, I.; Lam, C. N. C.; Neumann, A. W.; Manners, I.; Ozin, G. A. *Langmuir* **2000**, *16* (24), 9609–9614.
(28) Ebata, K.; Furukawa, K.; Matsumoto, N. *J. Am. Chem. Soc.* **1998**, *120* (29), 7367–7368.
(29) Crooks, R. M.; Ricco, A. J. *Acc. Chem. Res.* **1998**, *31* (5), 219–227.
(30) Mcfadden, D. M.; Wu, R. S. H. EP1024149 B1, **2000**.
(31) Bockstahler, T. E.; Hunt, C. R. US3705190 A, **1972**.
(32) Kuschnerow, J. C.; Dorn, S.; Augustin, W.; Scholl, S. *Proceedings of International Conference on Heat Exchanger Fouling and Cleaning* **2013**, *1* (1), 150–157.

(33) https://echa.europa.eu/restrictions-under-consideration/-/substance-rev/72301/term. Accessed on 6 September 2023.
(34) Hekster, F. M.; Laane, R. W. P. M.; de Voogt, P. Environmental and Toxicity Effects of Perfluoroalkylated Substances, **2003**, 99–121.
(35) Fenton, S. E.; Ducatman, A.; Boobis, A.; DeWitt, J. C.; Lau, C.; Ng, C.; Smith, J. S.; Roberts, S. M. *Environm. Tox. Chem.* **2021**, *40* (3), 606–630.
(36) Zwartsen, A.; Boon, P. Consumptie van Producten Verontreinigd Met PFAS Uit de Westerschelde, *RIVM rapport 2022-0020*.
(37) LaKind, J. S.; Naiman, J.; Verner, M.-A.; Lévêque, L.; Fenton, S. *Environ. Res.* **2023**, *219*, 115042.
(38) Cao, Y.; Ng, C. *Environ. Sci. Process Impacts* **2021**, *23* (11), 1623–1640.
(39) Inoue, M.; Sumii, Y.; Shibata, N. *ACS Omega* **2020**, *5* (19), 10633–10640.
(40) Tyrrell, N. D. *Org. Process. Res. Dev.* **2023**, *27*, 1422−1426.
(41) Evich, M. G.; Davis, M. J. B.; McCord, J. P.; Acrey, B.; Awkerman, J. A.; Knappe, D. R. U.; Lindstrom, A. B.; Speth, T. F.; Tebes-Stevens, C.; Strynar, M. J.; Wang, Z.; Weber, E. J.; Henderson, W. M.; Washington, J. W. *Science* **2022**, *375* (6580).
(42) Flerlage, H.; Slootweg, J. C. Nat Rev Chem 2023, 7 (9), 593–594.
(43) Nieland, E.; Komisarek, D.; Hohloch, S.; Wurst, K.; Vasylyeva, V.; Weingart, O.; Schmidt, B. M. *Chem. Commun.* **2022**, *58* (34), 5233–5236.
(44) https://cen.acs.org/education/science-communication/CENs-Year-Chemistry-2022/100/i44. Version of 15 December 2022.
(45) Homer, J. A.; Xu, L.; Kayambu, N.; Zheng, Q.; Choi, E. J.; Kim, B. M.; Sharpless, K. B.; Zuilhof, H.; Dong, J.; Moses, J. E. *Nature Rev. Methods Primers* **2023**, *3* (1).
(46) Mühle, J.; Huang, J.; Weiss, R. F.; Prinn, R. G.; Miller, B. R.; Salameh, P. K.; Harth, C. M.; Fraser, P. J.; Porter, L. W.; Greally, B. R.; O'Doherty, S.; Simmonds, P. G. J. *Geophys. Res. Atmosph.* **2009**, *114* (5).
(47) Veryser, C.; Demaerel, J.; Bieliunas, V.; Gilles, P.; De Borggraeve, W. M. *Org. Lett.* **2017**, *19* (19), 5244–5247.
(48) Li, B.-Y.; Su, K.; Meervelt, V.; Verhelst, S. H. L.; Ismalaj, E.; De Borggraeve, W. M.; Demaerel, J. *Angew. Chem. Int. Ed.* **2023**, *62*, e20230509.
(49) Meng, Y. P.; Wang, S. M.; Fang, W. Y.; Xie, Z. Z.; Leng, J.; Alsulami, H.; Qin, H. L. *Synthesis* **2020**, *52* (5), 673–687.
(50) Chinthakindi, P. K.; Arvidsson, P. I. *Eur. J. Org. Chem.* **2018**, 3648–3666.
(51) van den Boom, A. F. J.; Zuilhof, H. *Org. Lett.* **2023**, *25* (5), 788–793.
(52) Chao, Y.; Krishna, A.; Subramaniam, M.; Liang, D. D.; Pujari, S. P.; Sue, A. C. H.; Li, G.; Miloserdov, F. M.; Zuilhof, H. *Angew. Chem. Int. Ed.* **2022**, *61*, e202207456.
(53) Mahapatra, S.; Woroch, C. P.; Butler, T. W.; Carneiro, S. N.; Kwan, S. C.; Khasnavis, S. R.; Gu, J.; Dutra, J. K.; Vetelino, B. C.; Bellenger, J.; Am Ende, C. W.; Ball, N. D. *Org. Lett.* **2020**, *22* (11), 4389–4394.
(54) Mukherjee, P.; Woroch, C. P.; Cleary, L.; Rusznak, M.; Franzese, R. W.; Reese, M. R.; Tucker, J. W.; Humphrey, J. M.; Etuk, S. M.; Kwan, S. C.; Am Ende, C. W.; Ball, N. D. *Org. Lett.* **2018**, *20* (13), 3943–3947.
(55) Chapter 5 of this thesis.
(56) Kim, H.; Zhao, J.; Bae, J.; Klivansky, L. M.; Dailing, E. A.; Liu, Y.; Cappiello, J. R.; Sharpless, K. B.; Wu, P. *ACS Cent. Sci.* **2021**, *7* (11), 1919–1928.
(57) Leung, S. C. E.; Shukla, P.; Chen, D.; Eftekhari, E.; An, H.; Zare, F.; Ghasemi, N.; Zhang, D.; Nguyen, N.-T.; Li, Q. *Sci. Total Environ.* **2022**, *827*, 153669.
(58) Xiao, F.; Simcik, M. F.; Gulliver, J. S. *Water. Res.* **2013**, *47* (1), 49–56.

(59) Bao, Y.; Niu, J.; Xu, Z.; Gao, D.; Shi, J.; Sun, X.; Huang, Q. *J. Colloid Interface Sci.* **2014**, *434*, 59–64.
(60) Liu, L.; Liu, Y.; Gao, B.; Ji, R.; Li, C.; Wang, S. *Crit. Rev. Environ. Sci. Technol.* **2020**, *50* (22), 2379–2414.
(61) Buckley, T.; Xu, X.; Rudolph, V.; Firouzi, M.; Shukla, P. *Sci. Technol.* **2022**, *57* (6), 929–958.
(62) Gao T-N, Huang S, Nooijen R, Zhu Y, Kociok-Köhn G, Stuerzer T, et al. Rim-Based Binding of Perfluorinated Acids to Pillararenes Purifies Water. ChemRxiv. Cambridge: Cambridge Open Engage; 2023; This Content Is a Preprint and Has Not Been Peer-Reviewed.
(63) Chetverikov, S. P.; Loginov, O. N. *Microbiology* **2019**, *88* (1), 115–117.
(64) Chetverikov, S. P.; Sharipov, D. A.; Korshunova, T. Y.; Loginov, O. N. *Appl. Biochem. Microbiol.* **2017**, *53* (5), 533–538.
(65) Baumgartner, R.; McNeill, K. *Environ. Sci. Technol.* **2012**, *46* (18), 10199–10205.
(66) Trang, B.; Li, Y.; Xue, X.-S.; Ateia, M.; Houk, K. N.; Dichtel, W. R. *Science* **2022**, *377* (6608), 839–845.
(67) Ravichandran, S.; Bouldin, R. M.; Kumar, J.; Nagarajan, R. *J. Clean. Prod.* **2011**, *19* (5), 454–458.
(68) Bell, M. S.; Shahraz, A.; Fichthorn, K. A.; Borhan, A. *Langmuir* **2015**, *31* (24), 6752–6762..
(69) Wang, Z.; Zuilhof, H. *Langmuir* **2016**, *32* (25), 6310–6318.
(70) Kostal, J.; Voutchkova-Kostal, A. *Chem. Res. Toxicol.* **2020**, *33* (4), 880–888.
(71) Su, R.; Xie, K.; Liang, Y.; Houk, K. N.; Liu, F. *J. Org. Chem.* **2023**, *88* (2), 893–900.
(72) Fabian, M. D.; Shpiro, B.; Baer, R. *J. Chem. Theory. Comput.* **2022**, *18* (4), 2162–2170.
(73) Binder, K.; Horbach, J.; Kob, W.; Wolfgang, P.; Fathollah, V. *J. Phys. Cond. Matt.* **2004**, *16* (5), 429–453.
(74) Español, P.; Warren, P. B. *J. Chem. Phys.* **2017**, *146*, 150901.
(75) Nitschke, J. R.; Lehn, J. M. *Proc. Natl. Acad. Sci. USA* **2003**, *100* (21), 11970–11974.
(76) Kulchat, S.; Chaur, M. N.; Lehn, J. M. *Chem. Eur. J.* **2017**, *23* (46), 11108–11118.
(77) Ciaccia, M.; Cacciapaglia, R.; Mencarelli, P.; Mandolini, L.; Di Stefano, S. *Chem. Sci.* **2013**, *4* (5), 2253–2261.
(78) Ciaccia, M.; Di Stefano, S. *Org. Biomol. Chem.* **2015**, *13* (3), 646–654.
(79) Rufino, V. C.; Pliego, J. R. *Comput. Theor. Chem.* **2020**, *1191*, 113053.
(80) Figgins, P. E.; Busch, D. H. *J. Am. Chem. Soc.* **1960**, *82* (4), 820–824.
(81) Jain, A.; Shin, Y.; Persson, K. A. *Nature Rev. Mater.* **2016**, *1* (1), 15004.
(82) Adekoya, D.; Qian, S.; Gu, X.; Wen, W.; Li, D.; Ma, J.; Zhang, S. *Nano-Micro Letters* **2021**, *13* (1), 13.
(83) Yu, Z.; Jacobson, M. P.; Josovitz, J.; Rapp, C. S.; Friesner, R. A. *J. Phys. Chem. B* **2004**, *108* (21), 6643–6654.
(84) Becke, A. D. *J. Chem. Phys.* **1997**, *107* (20), 8554–8560.
(85) Chai, J. Da; Head-Gordon, M. *Phys. Chem. Chem. Phys.* **2008**, *10* (44), 6615–6620.
(86) Santra, G.; Calinsky, R.; Martin, J. M. L. *J. Phys. Chem. A* **2022**, *126* (32), 5492–5505.
(87) Mardirossian, N.; Head-Gordon, M. *J. Chem. Phys.* **2016**, *144* (21), 214110.
(88) Mardirossian, N.; Head-Gordon, M. *J. Chem. Phys.* **2018**, *148* (24), 241736.
(89) Hilgers, R.; Van Erven, G.; Boerkamp, V.; Sulaeva, I.; Potthast, A.; Kabel, M. A.; Vincken, J. P. *Green Chem.* **2020**, *22* (5), 1735–1746.

Acknowledgements & About the Author

Acknowledgements

In the seven years of my PhD, there were many people that touched my life and my work in one way or another. While I would love to thank you all by name, there were simply too many of you. I have thus made a small selection, as I would feel worse for leaving one name out by accident than a hundred by choice.

First of all, let me thank my promotor, prof. dr. Han Zuilhof, for giving me the opportunity to do a PhD. It was a bumpy road. When I informed you of my first pregnancy, you told me that I wasn't your first PhD student to get pregnant, yet none of the others now had a PhD title. I accepted this challenge. As the research, my personal life, the pandemic and your sabbatical developed, it proved to be a real challenge indeed. Yet we made it work, and here we are, with me defending my thesis at last.

Secondly, a big thanks to my co-promotor dr. ir. Maarten Smulders. Maarten, I don't know where to begin. Thank you for the nice conversations that we had. Thank you for the interesting research discussions and for giving me new insights and ideas when I was stuck. Thank you for putting up with the pregnancy hormones at work, while you were also having your fair share of child issues at home. Thank you for diving into DFT in order to understand my research. Thank you for standing by me through the slow ups and steep downs. Most of all, thank you for always making time, even when you actually didn't have any.

Thirdly, I would like to thank my opponents. You have been part of the most recent stage in my education, without which I would not have been able to obtain the doctors title. Prof. Leermakers, dear Frans, although our intended collaboration wasn't fruitful, I am glad that you remain a part of my PhD track. Prof. Bitter, prof. Palmans and prof. Schenning, thank you for taking the time to read and evaluate my thesis. I am confident we will have an interesting discussion.

Fourthly, thanks to my collaborators and sponsors. Marc, thank you for setting up this project from the side of Océ/Canon, and thank you for your continued interest after your retirement. Harald and Yulia, thank you for facilitating that

collaboration through M2i. Roelant, your passion and curiosity drove our collaboration, and I'm sure they will drive your career far. Sateesh and Robin, thank you for the continuation of the imine project, and for guiding me through your results afterwards. Jorge, your computational expertise helped the SuFEx project further and I am convinced it is in good hands with you.

I would also like to thank all colleagues from ORC. I cannot name you all (there have been more than 120 of you!), but I would like to thank everyone for the friendly conversations that we've had over tea, cake, lunch, or just when passing in a hallway. In particular, I would like to thank Simon for being my office friend. Whatever the situation, we could talk about it. We have very different lives, yet that did not stop you from listening to and sometimes advising me on my parenting issues. Dieuwertje, you provided a connection to my old chemistry life in Amsterdam and we discussed many (non-work) things in the open and honest style that is so common there. Esther and Esther, thank you for teaching me surface chemistry, grown-up fashion and work ethos all at once. Learning to drink coffee was a bridge too far though. Alice, thank you for being your sparkling, bubbly, loud, loving self. Sjoerd, thank you for making me feel at home in ORC and for showing me that having a lot of boardgames is a relative clause. Kaustub, thank you for our unprofessional but highly refreshing conversations. I wish you all the best in your bright future. Barend, thank you for saving my experiments when I was suddenly needed elsewhere. Loes and Wouter, thank you for doing your projects with me. You have taught me a lot on how to be a proper supervisor (or not) and I wish you all the best in your careers.

Furthermore, I would like to thank my friends, family and church acquaintances. These seven years haven't been easy, and I have often complained about one aspect or another. Thank you for helping and supporting me where possible, and for showing me that there is more to life than work. Tobias and Emma, thank you for your unconditional love and your faith that I can do anything.

Lastly, of course, I would love to thank Michiel. Thank you for sticking by me and for making the sacrifices that were needed to finish this PhD. Thank you for being a loving husband and a great father. I couldn't have done it without you.

About the author

Annemieke grew up in Apeldoorn. After finishing secondary school in 2009, she studied Chemistry at the Radboud University Nijmegen, where she obtained the BSc. degree in 2012. She then moved to Delft University of Technology, where she took two years of the BSc. Applied Mathematics. In the second year of this bachelor's degree, she also enrolled in the MSc. program Chemistry at the University of Amsterdam. The Bachelor of Applied Mathematics was dropped in favour of the Master in Chemistry. Within this Master, she did an internship in the Homogeneous Catalysis group under supervision of dr. Colet te Grotenhuis and prof. dr. Bas de Bruin, which focussed on cobalt – catalysed coupling – cyclisation reactions. In 2016 she graduated as a Master of Science in Chemistry from the University of Amsterdam.

In 2017, Annemieke started her PhD at Wageningen University in the Laboratory of Organic Chemistry under the supervision of dr. ir. Maarten Smulders and prof. dr. Han Zuilhof and in collaboration with Canon printing company. She studied the self-healing and antifouling behaviour of polymer brushes grafted from silicon surfaces, aiming to reduce the use of perfluorinated compounds in antifouling coatings in inkjet printing without reducing the coating's performance. Two pregnancies steered her away from experiments in the lab, due to safety issues, and towards computational chemistry. She also collaborated with WUR's Food Chemistry group, which resulted in two publications and chapter 6 of this thesis.

List of Publications

A. van Dam, J. Escorihuela, H. Zuilhof, A DFT Study on Chain-Growth SuFEx Polymerization, *manuscript in preparation*.

A. van Dam, M. M. J. Smulders, H. Zuilhof, Self-Healing Fluorine-Free Polymer Brushes, *manuscript submitted*.

A. van Dam, R. van Schendel, S. Gangarapu, H. Zuilhof, M. M. J. Smulders, A DFT Study of Imine Exchange Reactions in Iron(II)-Coordinated Pincers, *Chem. Eur. J.* **2023**, e202301795.
https://doi.org/10.1002/chem.202301795

A. van Dam, M. M. J. Smulders, H. Zuilhof, Self-Healing Antifouling Polymer Brushes: Effects of Degree of Fluorination. *Appl. Surf. Sci.* **2022**, *579*, 152264.
https://doi.org/10.1016/j.apsusc.2021.152264.

R. Hilgers, A. van Dam, H. Zuilhof, J.-P. Vincken, M. A. Kabel, Controlling the Competition: Boosting Laccase/HBT-Catalyzed Cleavage of a β-O-4′ Linked Lignin Model. *ACS Catalysis* **2020**, *10* (15), 8650–8659.
https://doi.org/10.1021/acscatal.0c02154.

R. Hilgers, M. Twentyman-Jones, A. van Dam, H. Gruppen, H.Zuilhof, M. A. Kabel, J.-P. Vincken, The Impact of Lignin Sulfonation on Its Reactivity with Laccase and Laccase/HBT. *Catal Sci Technol* **2019**, *9* (6), 1535–1542.
https://doi.org/10.1039/C9CY00249A.

Overview of Completed Training Activities

Discipline specific activities	Organizing institute	Year
Advanced Organic Chemistry	VLAG, ORC	2017–2021
Wageningen Molecular Life Sciences Seminar Series	WUR	2017–2018
CHAINS*	KNCV	2017, 2018, 2019, 2020, 2021, 2022**, 2023
Dutch Polymer Days*	NWO, KNCV, PTN	2017, 2018, 2021, 2023**
M2i conference*	M2i	2017, 2019, 2020**, 2022, 2023**

*Poster presentations at all attendances in 2017 – 2021.

**Oral presentations.

General courses	Organizing institute	Year
VLAG PhD week	VLAG	2017
Scientific Artwork with Photoshop and Illustrator	WGS	2017
COMSOL introduction course	PCC	2017
Brain-friendly writing	WGS	2019
Career orientation	WGS	2020
Scientific Writing	In'to Languages	2022

Other activities	Organizing institute	Year
Group meetings and colloquia	ORC	2017–2023
M2i cluster meetings	M2i	2017–2023
Research proposal	ORC	2017
PhD study tour to Denmark and Sweden	ORC	2017
PhD study tour to Israel	ORC	2019

Total: 43.6 ECTS

Teaching activities	**Year**
ORC-31806 Bio-organic Chemistry at Surfaces	2017, 2019, 2020
ORC-13803 Organic Chemistry for Life Sciences	2017
Exam supervision	2018
ORC-12803 Organic Chemistry 1	2018
ORC-11806 Analytical Methods in Organic Chemistry	2019
Supervising BSc and MSc thesis students	2019-2020

This research was carried out under project number S62.3.15577 in the framework of the Partnership Program of the Materials innovation institute M2i (www.m2i.nl) and the Technology Foundation TTW (www.stw.nl), which is part of the Dutch Research Council (www.nwo.nl).

Financial support from Wageningen University and M2i for printing this thesis is gratefully acknowledged.

Cover design by proefschriftmaken.nl.

Printed by proefschriftmaken.nl on FSC-certified paper.